Performance Effects and Causal Mechanisms of Mid-Channel Congestion in Diesel Particulate Filters

by

Ian Patrick Tracy

S.B. Mechanical Engineering (2011), S.B. Aerospace Engineering (2011)
S.M. Technology & Policy (2015), S.M. Mechanical Engineering (2015)
Massachusetts Institute of Technology

Submitted to the Department of Mechanical Engineering
in Partial Fulfillment of the Requirements for the Degree of

Doctor of Philosophy

at the

Massachusetts Institute of Technology

February 2021

Signature of Author……
Department of Mechanical Engineering
January 8th, 2021

Certified by……
Wai Cheng
Professor of Mechanical Engineering; Director, Sloan Automotive Laboratory
Thesis Supervisor

Accepted by……...
Nicolas Hadjiconstantinou
Professor of Mechanical Engineering
Chairman, Department Committee on Graduate Theses

[This page is left intentionally blank.]

Performance Effects and Causal Mechanisms of Mid-Channel Congestion in Diesel Particulate Filters

by

Ian Patrick Tracy

Submitted to the Department of Mechanical Engineering
on January 8th, 2021 in Partial Fulfillment of the
Requirements for the Degree of
Doctor of Philosophy

Abstract

The diesel particulate filter (DPF) is a ~$5,000-$50,000 USD critical component of aftertreatment systems installed in diesel engine-powered vehicles. The device is designed to trap particles emitted by the diesel combustion process in order to prevent their release into the surrounding environment, thereby reducing pollution levels and mitigating greenhouse gas emissions. Increasing stringency of emissions regulations has progressively necessitated the installation of DPFs on diesel-powered vehicles over the past few years, with the DPF market expected to remain significant in size at least through 2025.

While DPFs nominally operate by trapping and accumulating incoming PM continuously in the far downstream plug region of the filter channels so that no gaps form between trapped particulate matter (PM) agglomerates, both real-world field and laboratory bench tests have demonstrated that channel-spanning ash agglomerates form well upstream of the end plug region, prematurely clogging the mid-channel region. This effectively renders useless the remaining open space in the channel downstream of the blockage location. In addition to mid-channel congestion, this adverse phenomenon is referred to in the literature interchangeably as mid-channel collapse (MCC), mid-channel clogging, and mid-channel deposits (MCD).

MCC, due to accelerated filling of the filter channels, often results in significantly reduced DPF lifetime and performance (i.e. increased backpressure yielding depressed fuel economy), both of which prove costly for diesel vehicle operators. Existing hypotheses regarding causality of MCC are largely based on inconclusive empirical observations, and not substantiated by fundamental quantitative analysis. The primary contributions of this dissertation include: 1) summarizing hypothesized causal mechanisms of MCC with an emphasis on sintering as a primary driver thereof, 2) introducing a method by which to analyze X-Ray CT scans that show MCC in DPF channels, 3) assessing the performance penalty associated with MCC by correspondingly extending the industry standard model for pressure drop across a DPF, and 4) suggesting modifications to the DPF regeneration process in order to prevent sintering of ash agglomerates to the DPF side walls, based on an efficient reformulation of the prevalent temperature history model of the DPF that solves for both flow and temperature conditions inside filter channels over time during active regeneration.

Thesis Supervisor: Professor Wai Cheng
Tile: Professor of Mechanical Engineering; Director, Sloan Automotive Laboratory

[This page is left intentionally blank.]

Acknowledgements

I would like to take this opportunity to thank some folks who have meant a lot to me over the past several years and have in no small part contributed to enabling me to achieve my goals.

First, this thesis is dedicated to the late Dr. Victor Wong, my thesis advisor for over seven years since our memorable and amicable first interview back in the spring of 2013. Without him and his unrelenting advocating for me and my abilities, I would likely not be here completing my PhD at MIT today. It was a real joy working and bonding with Victor, and I miss him dearly. The trips to Thailand were incredible, as were many of our Royal East lunches in Cambridge, and his senses for business and applying common sense to approaching engineering problems were truly enlightening. Rest in peace, my friend. I will do my best to pay it forward to the next generation of scholars and leaders.

I am particularly appreciative of Wai Cheng for taking me under his wing at the eleventh hour and providing significant assistance in helping me bring my work to fruition, Bill Green and Sili Deng for patiently and supportively serving on my committee, as well as Tian Tian for serving as a de facto committee member and providing a morale boost with useful feedback at especially critical times. I want to thank Kamal Youcef-Toumi and Nancy Leveson for being wonderful advisors and giving me a chance in your labs, Ali for your postdoctoral advice and guidance, Pierre and Evelyn of MIT MechE for your undying passion and enthusiasm for your work and genuinely caring for your students in the department, Yuesen for all of your hard work and generally being a great person, and of course Leslie Reagan, without whom the all-important administrative arm of the MechE department simply would not function nearly as well as it does.

I would also like to thank Monica for having provided the inspiration and motivation for my applying to graduate school at MIT, Sofia and Yoonjin for being my close friends during graduate school, my brother Tommy for always being there whenever I needed him, David and Petek for imploring me to at all times keep it real, David #2 for the true friendship and days running through parks and golf courses chasing Charizards while playing Pokémon Go at the oddest of hours, and the Gilbertson twins for inspiring me and showing me that if you can dream it you can truly do it.

Thank you Nori Lietz for believing in me and encouraging me to "get the ball over the goal line," James Vanek for making me believe that I can achieve anything to which I set my mind, Anita Elberse and Linda Schukman for teaching me never to take things for granted and that only with hard work will you achieve your dreams, Flavia Frierson and Bruce Palmer for instilling in me that I am responsible for my own actions, David Fubini for being a trusted advisor and empathetic friend, and Matt Weinzierl for showing me how true excellence looks.

Lastly, thank you to my incredible parents and many brothers for their unconditional love and always being there for me, whatever the situation.

[This page is left intentionally blank.]

Table of Contents

List of Figures

List of Tables

[This page is left intentionally blank.]

1 Problem Motivation and Background Information

The purpose of this dissertation is to explain the current understanding of the anomalous mid-channel congestion (MCC) phenomenon that is known to hinder the performance of diesel particulate filters (DPFs), which are critical components of aftertreatment systems (ATSs) installed in diesel vehicles. The ATS exists for two primary reasons: first, to convert harmful greenhouse gases to less harmful compounds (e.g., NO_x and CO to N_2, O_2, and CO_2) and second, to trap toxic particulate matter (e.g., soot and lubricant-derived ash) so that it is not released unabated into the atmosphere. After all, diesel engine exhaust is considered 100 times more hazardous to human health than exhaust from gasoline combustion, as diesel produces more aldehydes, NO_x, and particulate matter [31]. Its untreated release into the surrounding environment substantially increases the concentration of greenhouse gases emissions and airborne pollutants that have plagued the skies of urban and extra-urban centers around the world. Effective operation of the DPF and ATS in general are therefore vitally important as humans continue to consume billions of barrels of distillate fuel on an annual basis.

In this opening chapter, we describe historical data related to both the greenhouse effect and air pollution, which provide motivation for seeking to improve the diesel engine aftertreatment device that forms the basis of discussion for this dissertation. We correlate the release of both greenhouse gases and soot from diesel combustion to the development of global warming and worsening of air pollution, elucidate the projected impact of further global warming and persistent air pollution on the human condition, and thereby underscore the importance of further reducing greenhouse gas and soot emissions. We subsequently describe a related anomaly that is been observed to occur in a device commonly used in diesel vehicles for trapping toxic particulate matter—especially soot—that results in decreased effective lifetime of the device and reduced fuel economy of the corresponding vehicle. In doing so, we motivate and introduce the observed, associated problem of premature mid-channel congestion (MCC) in monolith honeycomb DPFs that forms the basis of discussion for this dissertation.

1.1 Global Warming

As of 2020, global warming continues to threaten a sustainable future for humans on planet Earth and has already contributed to a one-degree Celsius rise in surface temperatures on our beloved planet over just the past fifty years, as depicted in Figure 1-1.

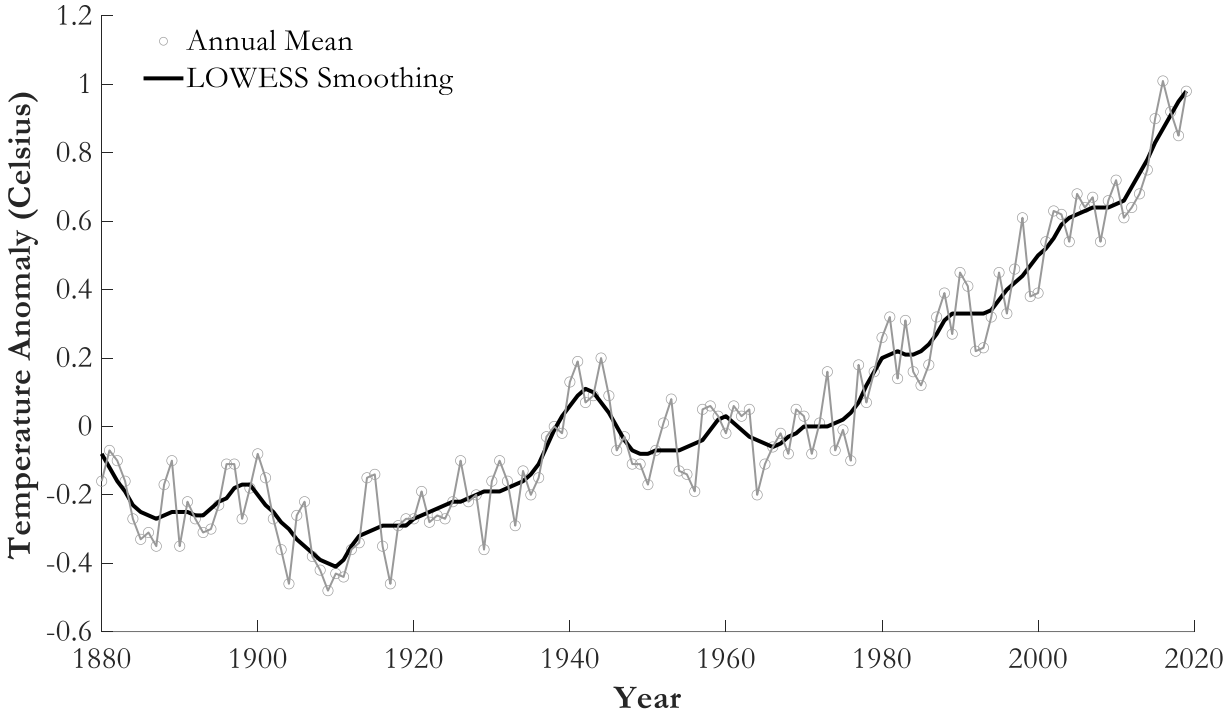

Figure 1-1: Average annual global temperatures since 1880 compared to average temperatures over the period 1951-1980. The light gray circles represent annual data points for temperature anomaly, whereas the dark plot is generated using the LOWESS locally weighted linear regression model [1].

Moreover, per Figure 1-2, the distribution of temperature change over the past ~50 years has not been geographically uniform throughout Earth, and instead is more pronounced at northern latitudes, which significantly elevates the risk of rising global sea levels due to the rapid melting of arctic glaciers and associated icebergs.

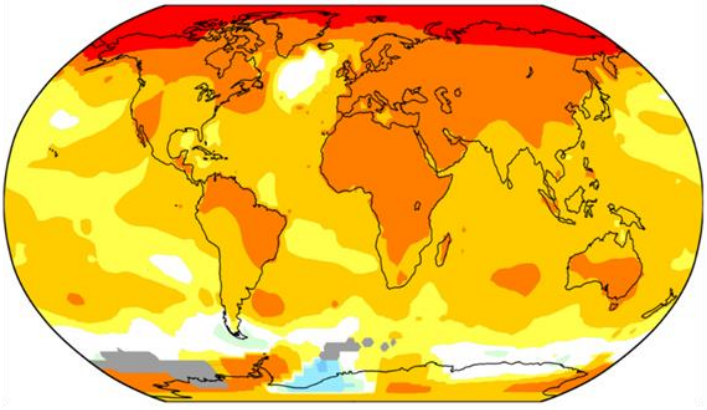

Figure 1-2: The distribution of Earth's surface temperature fluctuation over the past ~50 years, indicating the greatest increase in temperatures on land and especially in the northernmost latitudes [2].

Consequences of achieving a rise in global temperature of 1.5 degrees Celsius above baseline values include significant risks to human health and safety, increasing food insecurity, threats to global water supplies, and severely constrained economic growth, all of which become even more pronounced at two degrees of global warming [32]. NASA has specifically indicated that reaching just 1.5 degrees Celsius above nominal values will likely result in the following adverse effects [32]:

- several hundred million more people susceptible to climate-induced poverty risks;
- over 10 percent of people on Earth experiencing severe heatwaves once every five years or more;
- much higher propensity for drought to wreak havoc across most, increasing stress on water supply stability for up to 50 percent of the world's population and up to 270 million additional people without access to enough water by 2050;
- increased instances of heavy rainfall and flooding around the world;
- over 50% of geographic range reduced for 6 percent insects, 8 percent of plants, and 4 percent of the vertebrates;
- increased risks from forest fires, extreme weather events, and invasive species;
- multiple meters rise in sea levels across the planet; and
- geographic shift to higher latitudes among several marine species with significant damage to marine ecosystems.

This list of effects due to global warming is not exhaustive and becomes both significantly longer and exponentially more intense in magnitude as global surface temperature increases rise above 1.5 degrees Celsius to 2 degrees and beyond. Unsurprisingly then, the ultimate goal espoused by NASA and climate scientists is to limit the upward shift in global temperature to no more than 1.5 degrees Celsius [32].

The two primary causal mechanisms of global warming are thought to be greenhouse gas (GHG) emissions and the release of black carbon—or soot—into the atmosphere [33, 34]. GHGs are widely considered to be the primary contributor to global warming, and in 2001 Jacobson published in *Nature* that soot may be responsible for 15-30% of the temperature increase experienced by the planet post-industrial age due in part to their prolonged lingering in the atmosphere, reflection of heat back down onto the Earth's surface, and propensity to serve as nucleation points for condensation of atmospheric moisture that generates heat-reflecting clouds [33, 35]. Similarly, in 2013 a study conducted by the University of Washington suggested that black carbon aerosols are the second greatest contributor to global warming behind GHGs [34]. These findings relate to the aftertreatment system core to this thesis because greenhouse gas emissions increase as engine fuel economy decreases because more fuel must be consumed (and exhaust generated) for a given number of miles driven. Furthermore, substantial volume of soot is produced during the diesel combustion process. If filters fail to trap this toxic particulate matter prior to it exiting the tailpipe, then emitted black carbon particles enter the atmosphere and may contribute significantly to air pollution and global warming.

1.2 The Greenhouse Effect and Transportation

GHGs are responsible for promoting the greenhouse effect, in which they trap heat that would otherwise escape the Earth's atmosphere, thereby warming the planet. It has been reliably determined that human activities are responsible for virtually all increases in GHG release into the atmosphere over the past 150 years. Figures 1-1 through 1-4 suggest that human-derived greenhouse emissions are responsible for the one-degree Celsius increase in global temperature rise that Earth has already experienced since the pre-industrial era.

The volume of global GHGs has been exponentially increasing since 1900, with an inflection point in 1950 marking an increase in growth rate of GHG emissions to the approximately twentyfold above pre-industrial levels that the Earth is currently experiencing, per Figure 1-3 [4,5]. Only in the past few years have we seen a slight reduction in the annual rate of growth of GHG

emissions, and to prevent Earth from reaching either a 1.5- or 2-degree Celsius increase in global surface temperature, GHG emissions must continue to be markedly reduced, and on a global scale.

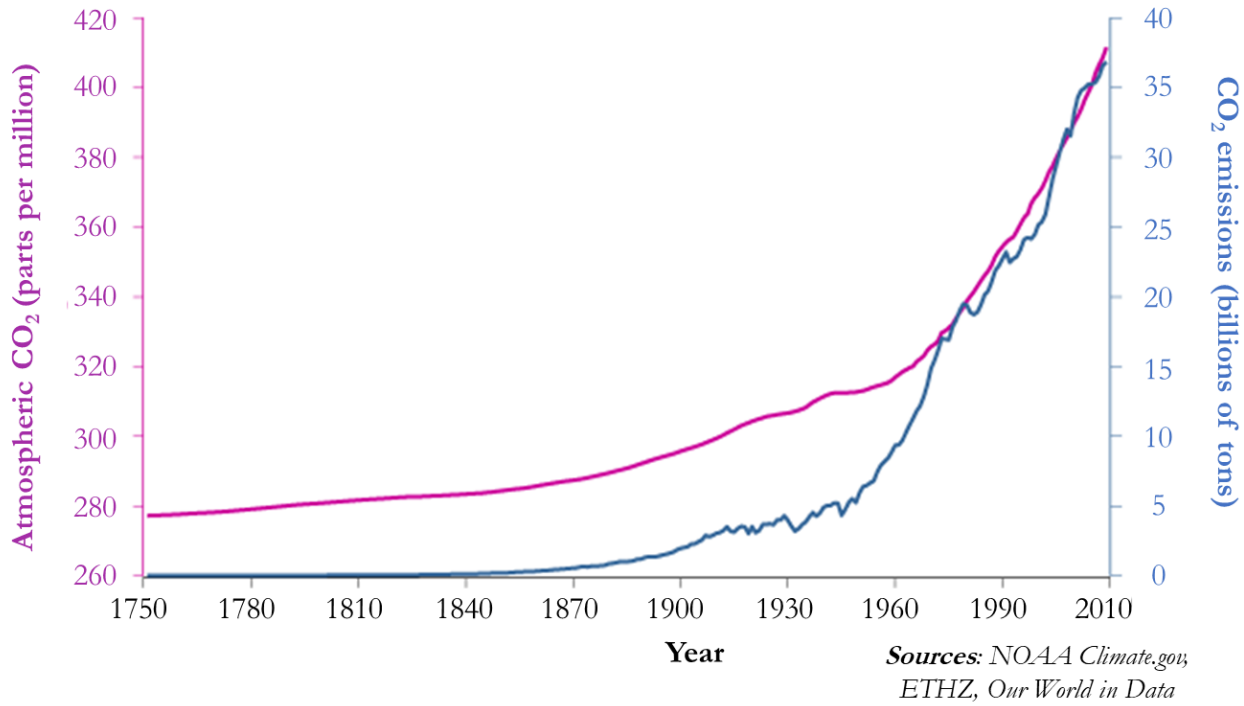

Figure 1-3: Global CO_2 emissions (billions of tons) and atmospheric CO_2 concentration (in parts per million) over the past 270 years, to illustrate the acceleration of greenhouse gas emissions since the Industrial Revolution [3].

As demonstrated in Figures 1-3 and 1-4, planet Earth has seen an over 35% increase in atmospheric carbon dioxide compared to the peak concentration thought to exist over the past 800,000 years, rising to over 410ppm as of 2020 from a pre-industrial era high of 300ppm [3]. Note that atmospheric carbon dioxide abundance was only approximately 330ppm as of 1975, representing a marked, steady growth in CO_2 concentration just within the past 45 years [3]! Without significant, sustained efforts to abate carbon emissions, this figure is surely to continue to rise, along with an undesirable, concomitant rise in temperatures across the globe.

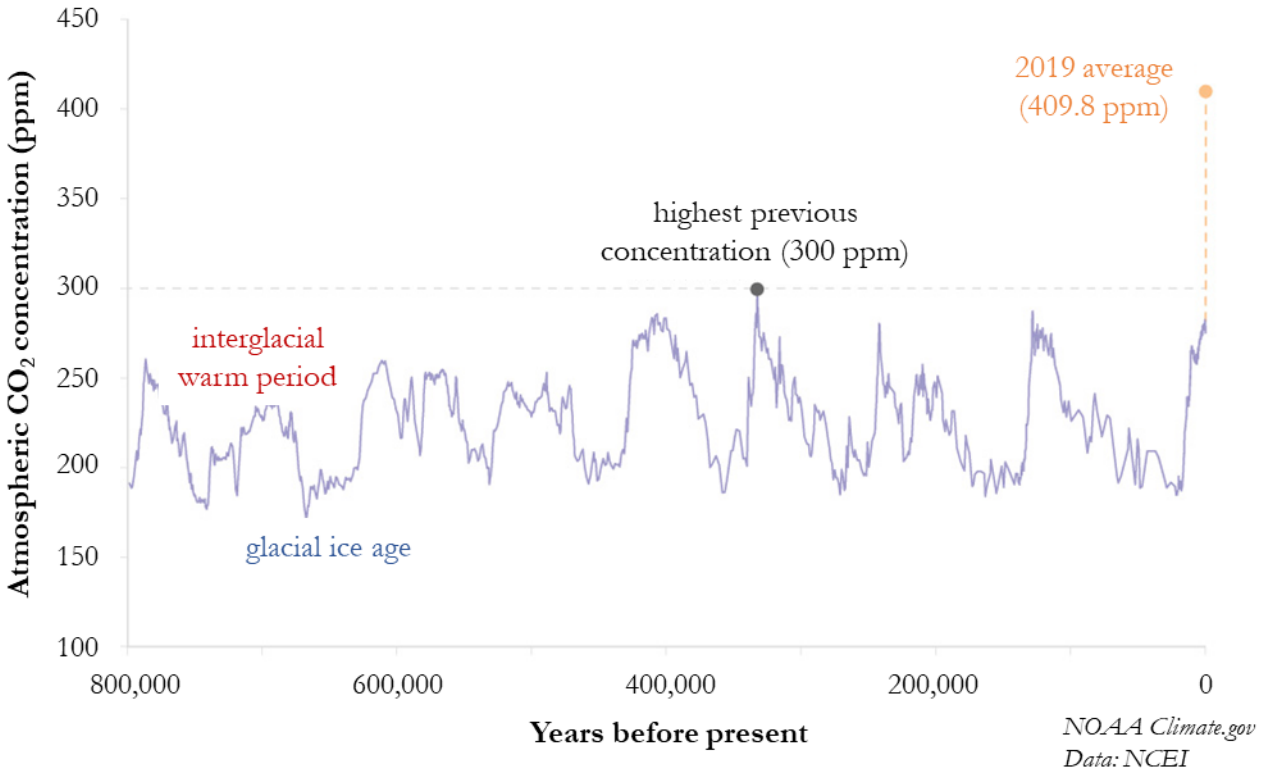

Figure 1-4: Concentration of CO_2 in Earth's atmosphere over the past 800,000 years in parts per million [3].

As of 2010, transportation accounts for 14% of global greenhouse gas (GHG) emissions, almost 95% of which are derived from petroleum based-fuels—largely gasoline and diesel [4]. However, if we take the perspective of GHGs by gas type, 65% of global emissions are the result of carbon dioxide generated via the combustion of fossil fuels and industrial processes, which is staggering. Another 11% of GHGs are carbon dioxide emitted in forestry and various other land use applications, elaborated in Figure 1-5 [4].

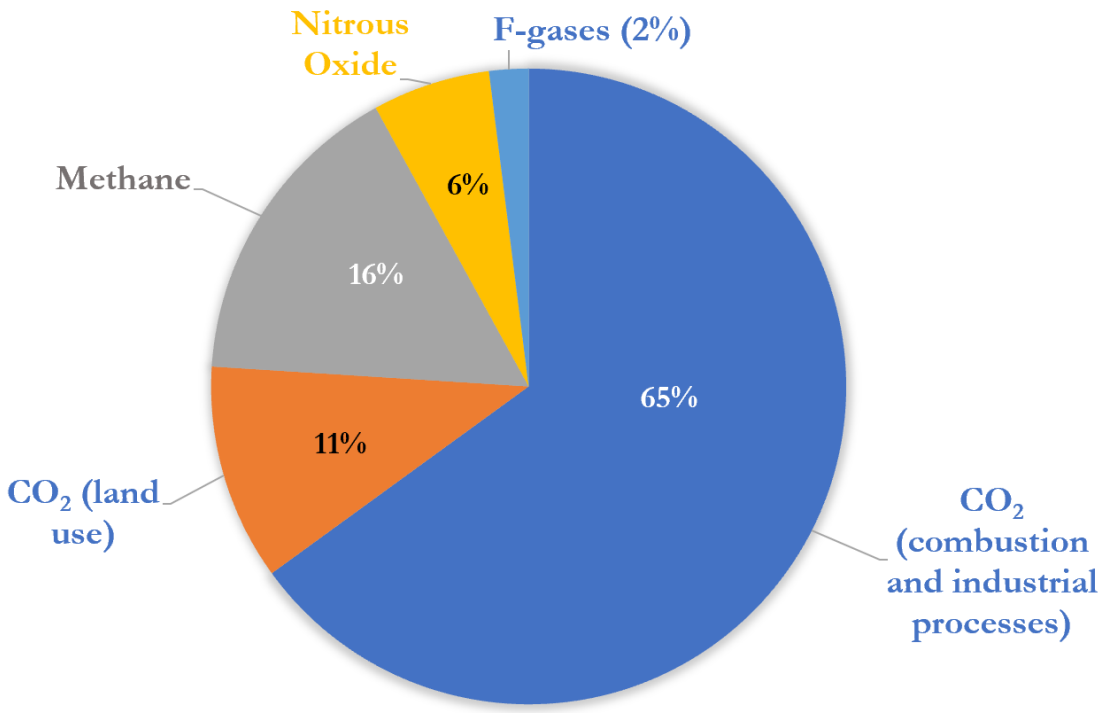

Figure 1-5: Greenhouse gas emissions by type and origin of gas [4].

In terms of geographic distribution, as of 2014 some 30% of carbon dioxide emissions from combustion and industrial processes are thought to emanate from China, 15% from the U.S., and 9% from the EU-28 [4]. Additional data is readily available for the United States, as follows.

According to the United States Environmental Protection Agency (EPA), transportation is the top greenhouse gas emitting generating sector in the United States, having recently overtaken electricity generation as the leading source of GHGs, expressed in Figure 1-6. Transportation accounts for over 28 percent of all 2018 U.S. emissions and consists of exhaust from trucks, ships, trains, planes, and automobiles. According to the EPA, as of 2018, 82% of transportation-related GHG emissions are attributable to ground vehicles: light-duty vehicles (at 59%) and medium- and heavy-duty trucks (23%). Ground vehicles are thus responsible for almost ¼ of all GHG emissions produced in the United States, which is substantial [36].

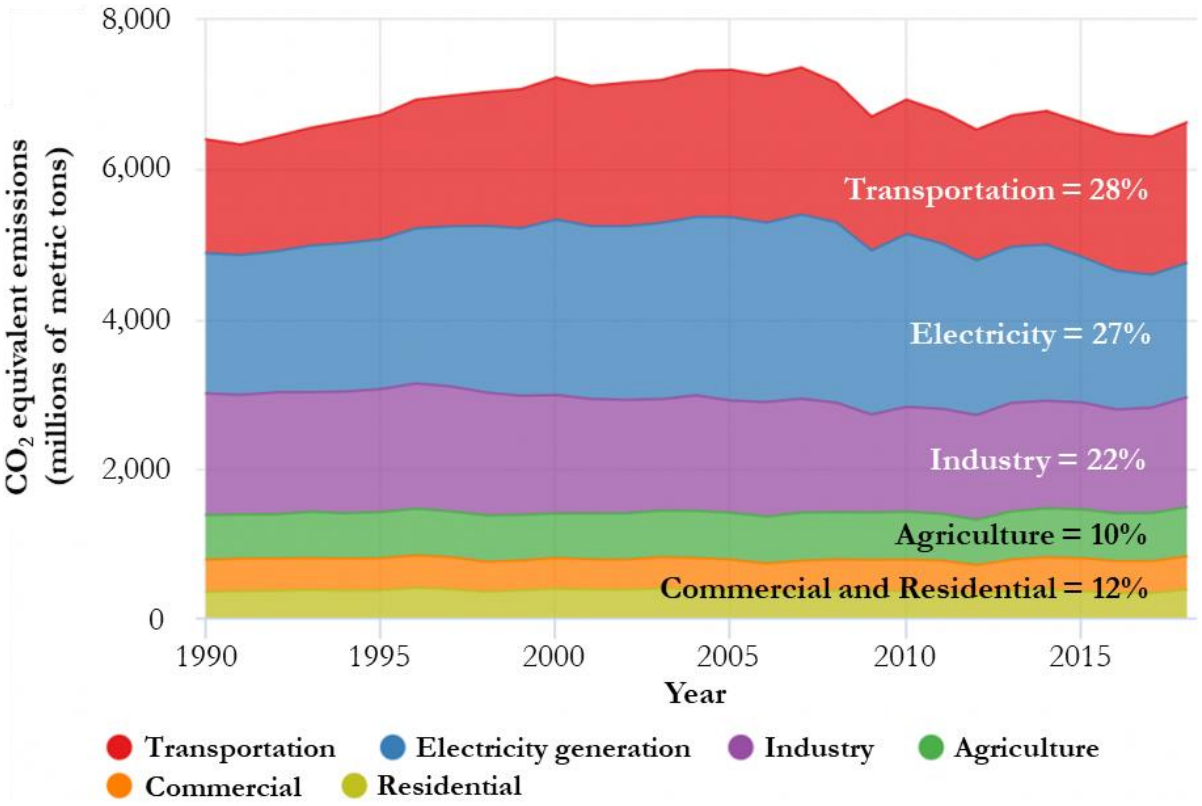

Figure 1-6: U.S. greenhouse gas emissions by economic sector, 1990-2018. Total Emissions in 2018 = 6,677 Million Metric Tons of CO_2 equivalent. Percentages may not add up to 100% due to independent rounding. Note that the 12 percent greenhouse gas emissions offset by land use and forestry has not been included [5].

Over 90 percent of the fuel used for transportation is petroleum-based and includes primarily gasoline and diesel (distillate) [5]. The U.S. Energy Information Administration has estimated that in 2018 alone, the consumption of diesel fuel by the U.S. transportation sector produced nearly 500 million metric tons of CO_2, accounting for around ¼ of total transportation sector CO_2 almost 9% of total U.S. CO_2 emissions in the energy space [37].

Since transportation will continue to represent a critical need of not only the American people but generally the ever-increasing supply and wealth of humans around the world, the EPA has outlined four major opportunities for GHG reduction in transportation [5]. They include [38]:

1) developing alternative fuel sources such as biofuels, hydrogen, and electricity from renewable energy sources;
2) improving the efficiency of existing vehicle types with new technology and designs;
3) implementing more efficient operating protocols; and
4) reducing demand for travel.

This thesis focuses on the second point: specifically, contributing knowledge toward a technical flaw inherent in the current implementation of particulate filters in diesel vehicle aftertreatment systems.

1.3 Soot Generation, Public Health, and Transportation

Operating with engine aftertreatment systems does adversely affect the environment by reducing fuel economy via the backpressure the systems introduce by virtue of their presenting resistance to the exhaust flow. However, they of course do so to serve their primary purpose: that of preventing harmful particulate matter from escaping unabated into the atmosphere. Not only is black carbon—the primary component of soot, a major contributor to global warming (responsible for some 15-30% of global temperature rise, as previously mentioned); soot is also directly responsible for adversely impacting the health and safety of humans across the globe [33]. Small airborne particulate matter is often classified by its characteristic size, or effective diameter. The most consequential (or hazardous) particles are those referred to as $PM_{2.5}$ or PM_{10}, which indicates characteristic size in microns. Sources of $PM_{2.5}$ and PM_{10} include both man-made (i.e. anthropogenic, including combustion and industrial processes) and natural (i.e. non-anthropogenic, including soil and dust re-suspension in arid areas) contributors. The California Air Resources Board (CARB) states that the majority of $PM_{2.5}$ is derived from the products of combustion [39].

Consisting of carbonaceous soot particles on the order of 30 to 500nm (so less than 1 micron) in diameter, diesel PM presents a particularly egregious hazard to human health not only due to its small size, but also because it is known to contain over 40 carcinogenic compounds, most of which are readily absorbed onto soot particles [11, 12]. In fact, over the years government research institutions have bolstered the claim that soot is carcinogenic—e.g., via the following timeline:

- in 1998, California Environmental Protection agency classified diesel PM as a toxic air contaminant because of its potential to cause cancer [40];
- in 2000 the National Toxicology Program (NTP) listed diesel exhaust particles as "reasonably anticipated to be a" carcinogen to humans [40];
- in 2002 the United States EPA stated that diesel emissions are "likely to be carcinogenic to humans" [40];
- in 2009 the same institution stipulated a causal relationship between particulate matter (like diesel PM) and premature mortality; and

- in 2012 the International Agency for Research on Cancer (IARC)—part of the World Health Organization—classified diesel as "carcinogenic to humans," with enough evidence having been accumulated to declare diesel exhaust a cause of lunch cancer [40].

As far as quantifiable impact on human health and safety, CARB suggests that diesel emissions are attributable to around 70% of the cancer risk derived from air contaminants in California. The organization goes on to explain that diesel PM comprises around 8% of outdoor $PM_{2.5}$, a known health hazard linked to several medical ailments such as heart and respiratory diseases that ultimately result in increased hospitalizations and premature death [40]. CARB specifically estimates that diesel emissions are responsible for around 1,500 annual premature deaths due to cardiovascular disease in California [40]. A popular experiment conducted from 1974 to 2009 known as the Harvard Six Cities Study tracked adults across six major United States cities in an attempt to link the impact of air pollution on excess mortality in humans [41]. The study associated a 2.5 $\frac{\mu g}{m^3}$ decrease in $PM_{2.5}$ (from a baseline of around 15 $\frac{\mu g}{m^3}$) to a 3.5% reduction in "all-cause mortality" [41]. A related experiment concluded that a reduction in fine PM pollution in the United States during the 1980s and 1990s is attributable to some 15% of the nearly 3-year increase in life expectancy experienced during that period [41].

Unfortunately, the vast majority of the world's population continues to be exposed to fine PM in excess of the amounts recommended by WHO in their air quality guideline (AQG), which in the case of PM_{10} is a threshold atmospheric concentration of 20 $\frac{\mu g}{m^3}$ [41]. The perhaps surprisingly high degree of global PM exposure is illustrated in Figure 1-7 below. One observes that almost the entire population of every country in the world is exposed to excessive concentrations of PM_{10}. In Europe, for instance, over 80% of the cities for which PM data exists experience PM_{10} levels in excess of those prescribed by WHO guidelines.

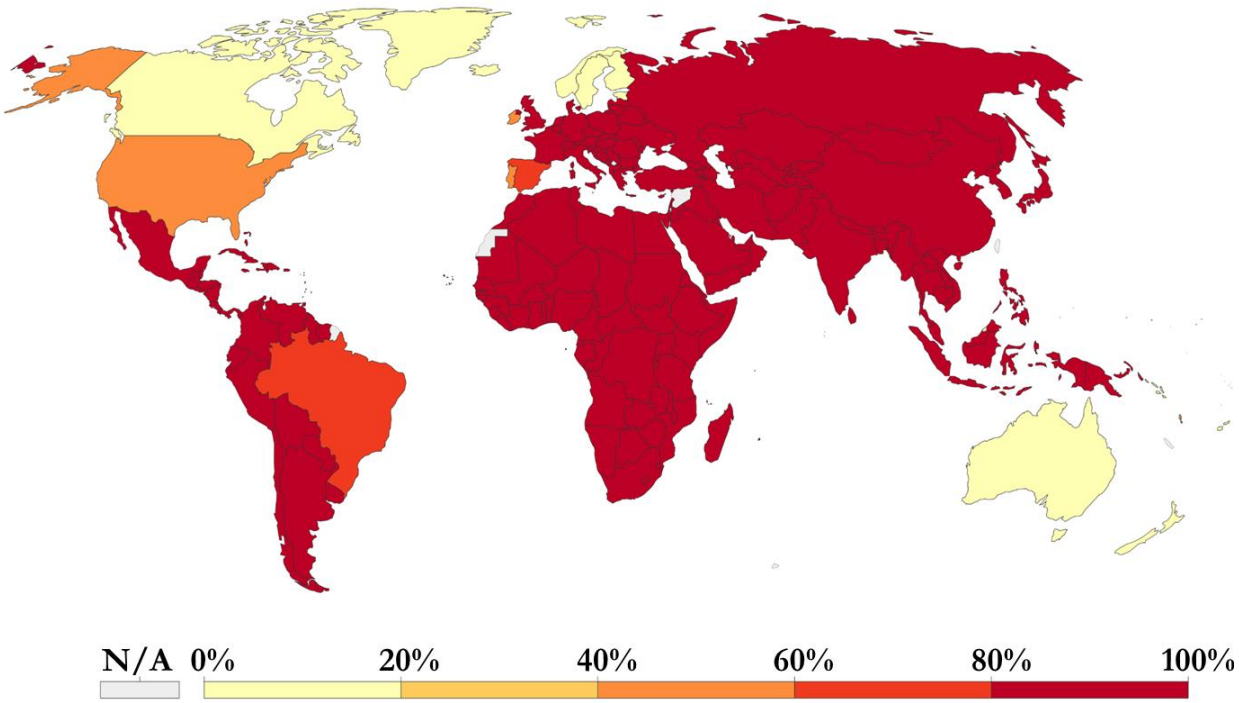

Figure 1-7: The share of the world's population exposed to $PM_{2.5}$ levels above the WHO guidelines espoused in 2016 [6].

In China, the world's most populous country as of 2020—containing some 1.4 billion humans—the picture is particularly grim, with over 90% of the vast quantities of PM emissions there attributable to diesel vehicles, which account for less than 10% of China's vehicle population as of 2020 [42]. While according to a 2020 study air quality across 338 cities in China had been improving over the prior 5 years, the average annual $PM_{2.5}$ concentration across the cities under study ranged from 9 to 74 $\frac{\mu g}{m^3}$, averaging around 40 $\frac{\mu g}{m^3}$, and the average annual PM_{10} concentration spanned from 23 to 154 $\frac{\mu g}{m^3}$, with an average of over 70 $\frac{\mu g}{m^3}$ [43]. These values are is clearly well above the 20 $\frac{\mu g}{m^3}$ air quality guideline set by the WHO for PM_{10} levels, and still exceeds the "second-level concentration limit" related to the Blue Sky Defense Battle set by China itself [43]. In 2015, average levels of $PM_{2.5}$ in Beijing (population ~22 million) were found to range from a low seasonal value of 65 $\frac{\mu g}{m^3}$ in the summer to around 90 $\frac{\mu g}{m^3}$ in the fall, with PM_{10} values approximately double, which implies an average annual sub-10-micron particle air density—exceeding the WHO AQG by a factor of 8 [44]! Average seasonal $PM_{2.5}$ values were found to vary from 40 to 75 $\frac{\mu g}{m^3}$ in Shanghai (population ~24 million) and from 30 to 60 $\frac{\mu g}{m^3}$ in Guangzhou, with PM_{10} values again approximately double in both locations [44]. There is widespread consensus that both on- and off-road diesel

engine emissions plays a major role in the sustained high PM concentrations suspended over many Chinese cities in thick, hazy, toxic clouds.

1.4 Diesel Engines and Aftertreatment Systems

As the focus of this dissertation is to investigate causality of an adverse phenomenon transpiring in the (exhaust) aftertreatment system of diesel engines that results in increased greenhouse gas and (potentially also) soot release into the atmosphere, it is appropriate to review these engines and systems. Recall that diesel (or compression-ignition) engines differ from their gasoline counterparts in a few important ways, and while they generate both better fuel economy and higher thermal efficiency, the relatively large amount of particulate matter they generate necessitates the use of filtration and catalytic converters. The first major difference between the engine types is that diesels do not use spark plugs to ignite the air-fuel mixture in the power cylinder. Instead glow plugs are used to warm the combustion cylinder and the air-fuel mixture spontaneously ignites (or undergoes autoignition) to initiate the combustion process. More specifically, at around 20 degrees before top-dead center, a liquid fuel jet is injected into the cylinder where it atomizes into droplets, then evaporates into vapor and mixes with entrained air until proportions amenable to combustion are achieved. Temperature and pressure rise to exceed the fuel's ignition point, and autoignition commences after a brief "delay period" [45]. A second major difference between spark-ignition (gasoline) and autoignition (diesel) engines is that, for diesel engines, only air is inducted into the cylinder, as the fuel spray is injected just before combustion is required to commence [45]. Diesel engines are generally categorized as either direct-injection or indirect-injection depending on whether the combustion chamber consists solely of a single open region or instead also an additional chamber called the prechamber in which more rapid air-fuel mixing is promoted.

Diesel fuel combustion products consist mostly of nitrogen (N_2), carbon dioxide, water, and oxygen. Since diesel engines operate substantially leaner than stoichiometric with equivalence ratios (quotient of actual fuel/air ratio divided by stoichiometric fuel/air ratio) of $\phi \leq 0.8$, the diesel combustion process is effectively complete with a combustion inefficiency of ≤ 2 percent [46]. Diesel exhaust gas composition is therefore relatively straightforward, with CO_2 and O_2 essentially trading off until all oxygen is converted into carbon dioxide at a fuel/air equivalence ratio of around unity, where the mole fraction of CO_2 is approximately 15% [46]. It is generally agreed upon that emissions of CO and unburned hydrocarbons are low for diesel engines [46].

While diesel combustion has high efficiency and runs virtually to completion, it is also characterized by nonuniform fuel distribution given the means of fuel injection applied and the simultaneous entrainment of lubricant into the combusting air-fuel mixture. Figure 1-8 illustrates the relative composition of diesel exhaust.

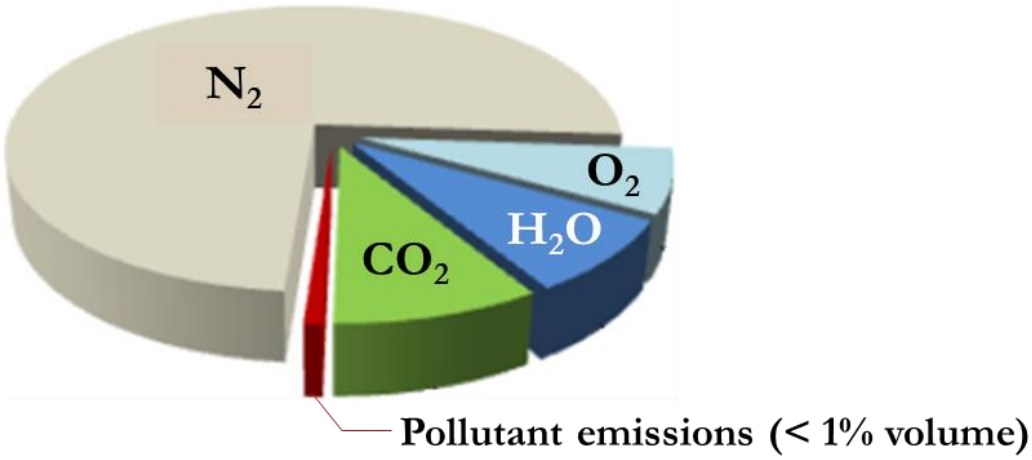

Figure 1-8: Chemical composition of diesel exhaust emissions. Note that while pollutants represent less than 1% of diesel exhaust volume, its unabated release into the environment is highly deleterious human health [7].

It is known that pollutant formation during combustion depends largely on the evolution of fuel distribution during mixing, which in the case of diesel results in exhaust that is composed of significant quantities of NO_x (mostly NO with some NO_2), unburned hydrocarbons, and soot. It is the general consensus that over 99% of the particle mass emitted by modern diesel engines is soot, which is combustible and comprised of primarily carbon but also sulfate and other organic compounds; the remaining 1% of consists of incombustible ash [21].

Figure 1-9 shows that NO_x forms in the nonuniform burned gas regions characterized by high temperatures, especially where the mixture is close to stoichiometric [8]. NO is generated primarily when atmospheric N_2 is oxidized, though NO may also form via the oxidation of nitrogen contained in diesel fuel, which for heavy distillates can constitute over 2% of the weight of the fuel [8]. NO is thought to be formed by way of the Zeldovich mechanism in the case of stoichiometric fuel-air mixtures [8]:

$$O + N_2 \rightarrow NO + N \quad (1.1)$$

$$N + O_2 \rightarrow NO + O \quad (1.2)$$

$$N + OH \rightarrow NO + H \quad (1.3)$$

While the presence of NO_2 is sometimes considered trivial compared to that of NO, NO_2 can represent up to 30% of total nitrogen exhaust oxide emissions. NO is rapidly converted to NO_2 by way of reactions like [8]:

$$NO + HO_2 \rightarrow NO_2 + OH \tag{1.4}$$

Per Figure 1-9, soot (also known as carbonaceous material) forms in the core regions of the fuel sprays that contain rich, unburned fuel vapor that is heated by mixing with hot unburned gases and oxidized in the flame zone when encountering oxygen. This occurs between about 1000 and 2800K, at pressures of 50 to 100 bar, with sufficient air oxidizing all of the fuel. Most diesel particulate matter consists of soot to which some other organic compounds are attached [8]. The bulk of soot consists of additives contained in lubricating oils and, to a lesser extent, metals (e.g., iron oxide) resulting from engine wear, exhaust system corrosion byproducts, and trace metals cerium and iron contained in diesel fuel [47, 48]. Lubricant-derived ash is thus the term often used to describe ash that is accumulated in the aftertreatment system. It consists primary of calcium, zinc, manganese, phosphorus, and sulfur compounds that are intrinsic to lubricant formulations, as shown in Table 1-1 based on analysis of field ash samples [47]. Fuel-borne metals are more prominent when fuel-borne catalysts are used.

Table 1-1: Elemental composition of six different samples of field ash by mass [17, 49].

% Composition of Ash Samples by Mass							
Element	**Ash A**	**Ash B**	**Ash C**	**Ash D**	**Ash E**	**Ash F**	**Ash G**
Calcium	28	21.56	16.18	20.37	22.04	17.9	33.5
Zinc	15	9.94	10.72	10.05	10.01	11	23.5
Magnesium	-	0.2	5.31	0.35	0.25	1.8	1.5
Iron	1.8	1.43	1.52	1.34	1.95	0.56	2.5
Sulfur	-	14.64	11.36	14.58	15.65	-	10.5
Phosphorus	1.3	6.95	9.79	6.92	6.91	7.44	21
Potassium	-	0.05	-	0.14	0.06	0.23	1
Sodium	-	0.69	0.23	0.88	0.93	0.2	-
Oxygen	-	41.51	43.49	41.7	37.05	-	-
Silicon	-	-	-	-	-	-	2.5
Aluminum	-	-	-	-	-	-	3
Total	***46.1***	***96.97***	***98.6***	***96.33***	***94.85***	***39.13***	***99***

Hydrocarbons (HCs) and aldehydes are generated where the flame quenches along the cylinder walls, where dilution with air prevents complete oxidation of the fuel and where fuel vaporizes in the

nozzle sac volume region late in combustion [8]. Unburned HC emissions are thought to increase with increase as deposits accumulate along the wall of the combustion chamber [8].

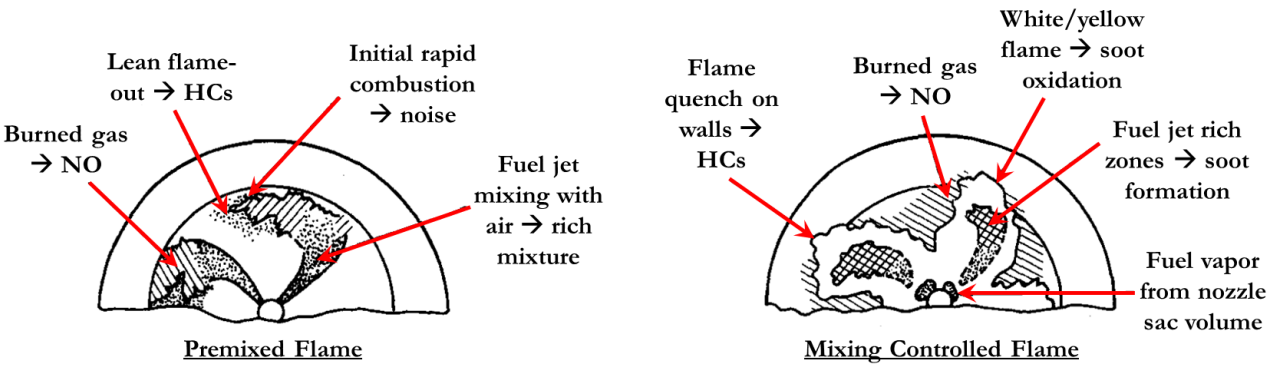

Figure 1-9: Pollutant formation in a direct-injection diesel engine during two combustion approaches. Air and fuel mix prior to entering the combustion zone in the premixed case [8, 9].

The aftertreatment system for diesel engines consists of exhaust pipes, catalytic converters, and particulate filters. The three most prominent components of the system are: a diesel oxide catalyst (DOC), a diesel particulate filter (DPF), and the Selective Catalytic Reduction (SCR) system, illustrated below in Figure 1-10. Other components sometimes include ammonia oxidation (AMOX) catalyst and lean NO_x traps (LNTs) [13, 14]. A common integrated aftertreatment system model involves variable configurations of the three major components, such as SCR forward (DOC-SCR-DPF) and DPF forward (DOC-DPF-SCR) systems, to name two such configurations [50]. The DPF forward configuration is illustrated in Figure 1-10 immediately below.

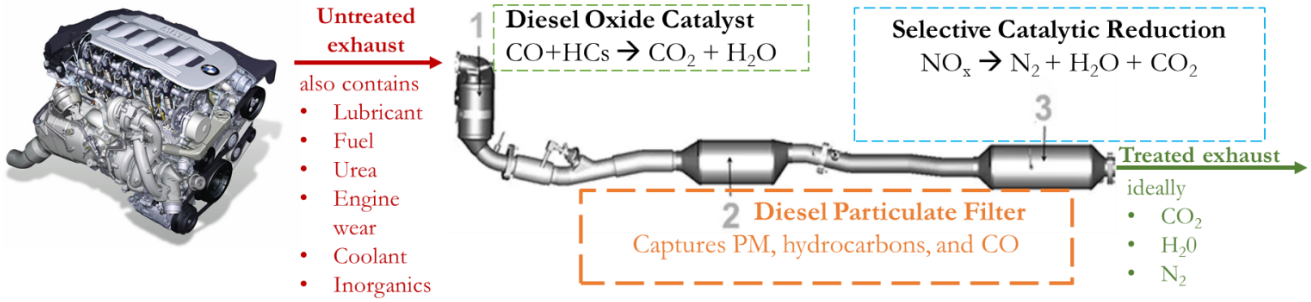

Figure 1-10: Key aftertreatment components through which the incoming engine exhaust passes prior to escaping the vehicle and entering the ambient atmosphere.

The DOC's main purpose is to covert carbon monoxide and other hydrocarbons into CO_2 and water, in addition to converting NO to NO_2. It is often assumed that the DOC oxidizes all soluble organic fractions (SOFs) of PM so that only the elemental carbon fraction (i.e. soot) is passed through to be filtered and oxidized downstream in the DPF [50]. The purpose of the SCR system is

to facilitate the conversion of NO_x to N_2, as well as promote ammonia adsorption, desorption, and oxidation [50]. The DPF is designed to physically trap solid particulate matter entrained in the exhaust flow, and further oxidize soot so that virtually all incompletely combusted matter is converted to ash, which occupies much smaller volume such that the volume ratio of ash to the corresponding pre-oxidized soot is on the order of 1 to 100, respectively [21].

1.5 Diesel Particulate Filters

The intent of this research effort is to help identify the primary causal mechanisms of (premature) mid-channel congestion (MCC) in diesel particulate filters (DPFs). A general illustration of a DPF is provided in Figure 1-11.

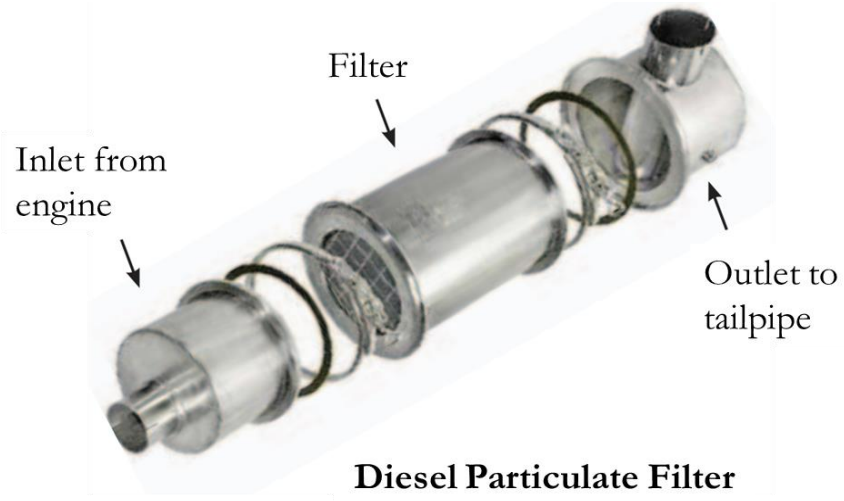

Figure 1-11: A classically cylindrical diesel particulate filter (DPF) enclosed in its metal encasing.

The device itself has grown significantly in popularity since it was first introduced in the 1980s, in no small part due to its effectively required use across several diesel vehicle classes in many global markets due to increased stringency of vehicle emissions standards, as expressed in Figure 1-12.

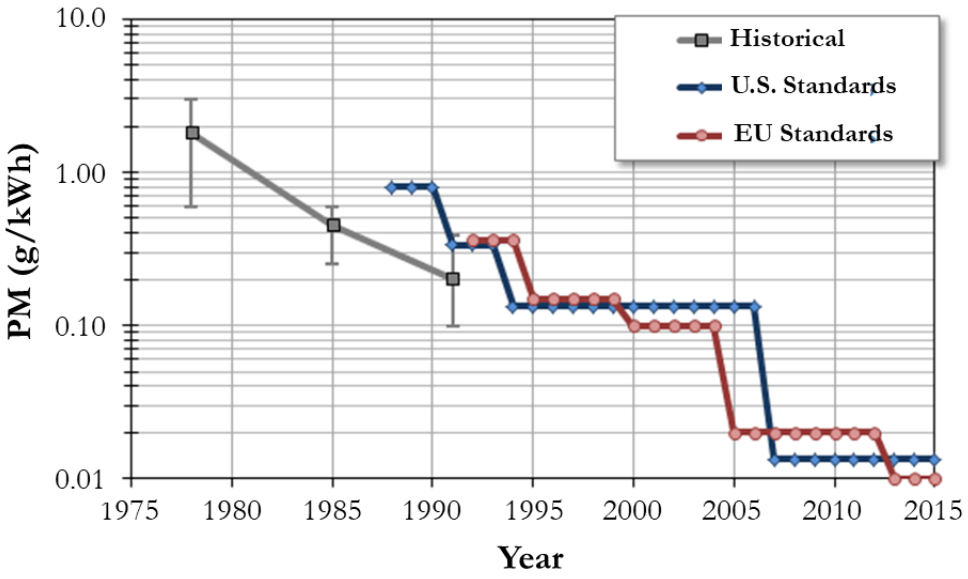

Figure 1-12: Increased stringency of PM emissions requirements as enforced by U.S. and EU regulators. Notice how the acceptable PM emissions in the U.S. as of 2007 was less than 1% that what it was just 17 years prior in 1990 [10].

There are conflicting views regarding the DPF's popularity in the coming years, though there is consensus that it will continue to play a major role in global transportation in the foreseeable future. According to one market report, the global annual growth rate of DPF sales is expected to remain strong in the foreseeable future and eclipse 8% on a compounded annual basis through 2025 [51]. However, according to a recent report on transportation published by McKinsey & Company, while the global market for gasoline particulate filters (GPFs) is expected to rise over the period 2018-2025, the market for DPFs is anticipated to decline at a 5% CAGR over the same time period [11]. McKinsey's projections—segmented into both powertrain types and global geographies—are shown in Figure 1-13 below.

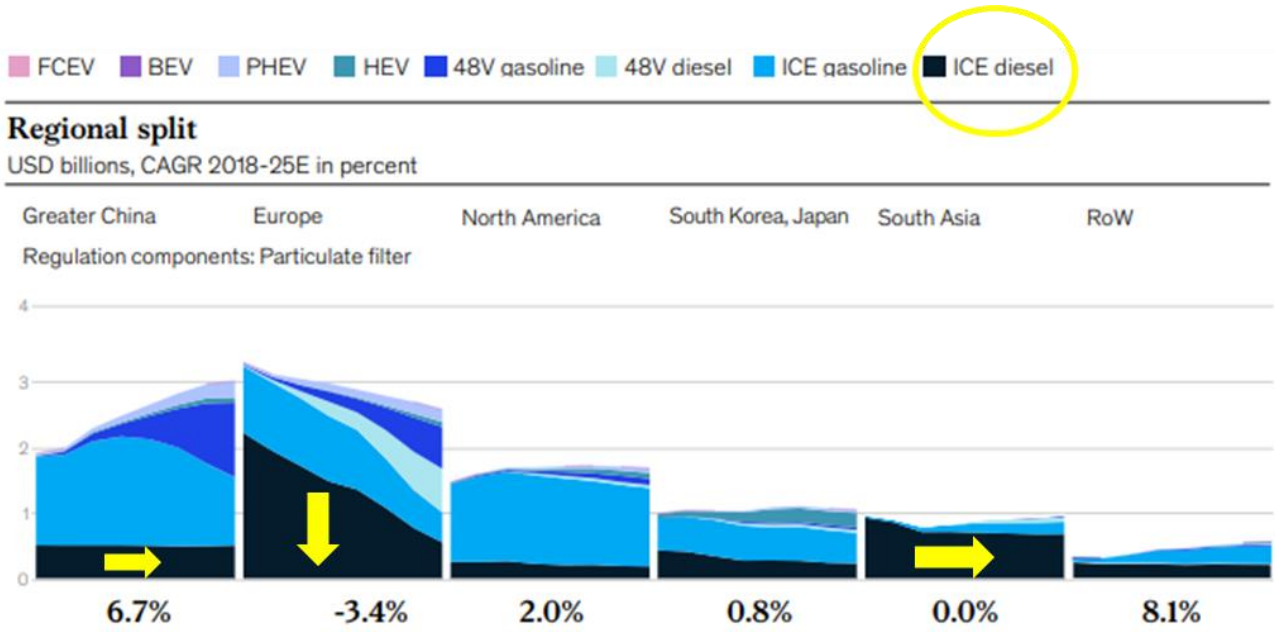

Figure 1-13: Cumulative annual growth rate (CAGR) predictions by McKinsey & Company for particulate filters, segmented by region and vehicle propulsion type. Note that the diesel internal combustion engines central to this thesis are represented by the color black [11].

It is interesting that while the use of DPFs is expected to decline precipitously in Europe over 2018-2025 and significantly in North America, South Korea, and Japan, its use is anticipated to remain flat in its greatest market China, as well as in South Asia and the rest of the world (RoW). Also notice how the market for PFs is expected to grow in every geographic region except Europe, and by over 50% in China. This seems to be largely driven by an expected substantial rise in the use of PFs on hybrid vehicles.

DPFs generally cost between $5,000 and $15,000 for passive systems, depending in size and application, and can run upwards of $50,000 for an active DPF installed in large nonroad equipment [30]. DPFs are therefore nontrivial investments for companies and individual consumers alike, with unexpected replacements potentially causing economic hardship for owners and operators. To combat reliability anxiety experienced by operators of DPFs, the California Air Resources Board (CARB) has established standards for warranty periods on CARB-certified retrofit technologies, shown in Table 1-2. Note that warrantied mileage rises as gross vehicle weight grows, corresponding to higher costs borne by DPF part manufacturers in the case of premature component failure. It is perhaps in part due to these stringent requirements—especially the case of unlimited mileage warranties in the first two years of ownership for the heaviest-duty diesel engines—that suppliers of DPFs are keenly interested in understanding the causes of, and thus providing mitigating measures for, premature congestion (and sometimes failure) of these aftertreatment devices.

Table 1-2: Required warranty periods specified by the California Air Resources Board for DPFs as a function of gross vehicle weight rating (GVWR), rated engine power, annual driving distance, and total mileage on the corresponding vehicle [30].

Category #	Classification Metric	Limit	Warranty Period
1	Gross Vehicle Weight Rating	more than 33,000 pounds	Two years and unlimited miles operated
	Horsepower	more than 100,000	
	Miles operated per year	more than 100,000	
	Total vehicle miles	less than 300,000	
2	Gross Vehicle Weight Rating	more than 33,000	Five years or 150,000 miles operated
	Horsepower	more than 250	
3	Gross Vehicle Weight Rating	between 19,500 and 33,000 pounds	Five years or 100,000 miles
4	Gross Vehicle Weight Rating	less than 19,000 pounds	Five years or 60,000 miles

As far as their efficacy is concerned, DPFs are known to reduce emissions of particulate matter by upwards of 95%, and certain DPFs can reduce emissions of hydrocarbons and carbon monoxide by 70 to 90 percent via their catalyzed substrates / washcoats [30]. The devices are, however, also known to increase NO_2 emissions and thus the proportion of NO_2 relative to total NO_x emissions, in part due to their catalytic coatings that facilitate regeneration at lower exhaust temperatures [30]. DPFs are required to be cleaned either biannually or annually, which is determined by the measured backpressure imposed by the DPF, with greater pressure corresponding to more clogging of the filter. The EPA stipulates that nominally operated DPFs should reasonably be expected to remain effective throughout the lifetime of the vehicle, which they define as 5-10 years or 10,000+ hours of operation [30].

The filters have been installed in the tailpipes of diesel-powered vehicles since the 1980s—when they were first introduced onto compact passenger vehicles in Europe—to prevent the unabated release of harmful particulate matter (PM) into the Earth's atmosphere at a time when air pollution was wreaking havoc across the globe [52]. These early filters, however, suffered from reliability issues, preventing their widespread use until more robust variants were developed in the 2000s [53].

The standard DPF is characterized by a ceramic monolithic honeycomb configuration with a grid of square channels that are plugged at alternating ends, as shown in Figure 1-14. This staggered grid plugging stands in contrast to flow-through configuration inherent in the diesel oxide catalyst device, in which all channels are open. The DPF sits downstream of the engine, where it is used to trap soot, ash, and other potentially harmful exhaust products within its channels so that those noxious products are not released into the environment. Within each channel, particulate matter

(consisting of soot and ash) accumulates either along the sides of the channel—known as the "cake layer" region—or alternatively at the far end of the channel where accumulated PM is collectively referred to as the "end plug." While end plug accumulation is not depicted on the schematic provided to the patent office by GM in 1983, it is now widely understood that end plug accumulation is very common and is the dominant mode when active regeneration is used, as subsequently discussed in this thesis.

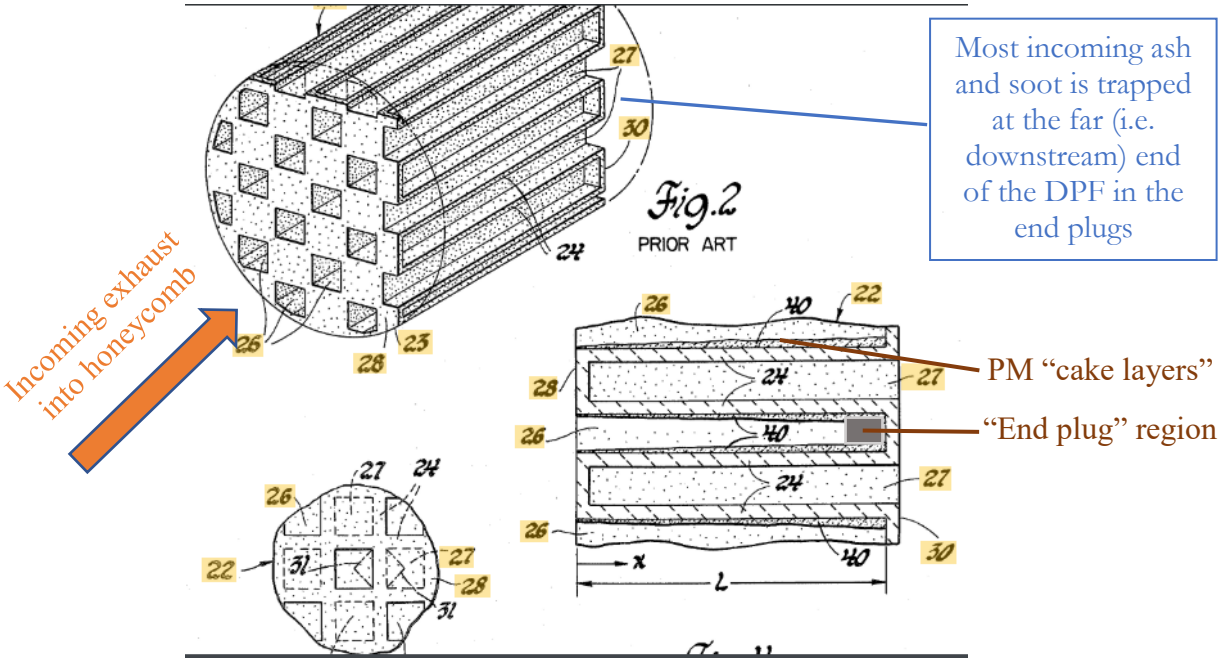

Figure 1-14: Annotated wall-flow monolith filter patent filed by General Motors in 1983 [12].

Over 99% of the particulate matter (PM) collected in the DPF is combustible soot and consists of approximately 1% highly volatile, 12% medium volatile, and 87% combustible PM that can be oxidized to CO_2 periodically or continuously via a process called regeneration [54]. The remaining incombustibles, known as ash and comprising < 1% of the PM collected in the DPF, accumulate continuously, thereby heightening flow restriction in the exhaust. The elevated exhaust backpressure causes increased engine fuel consumption and other performance problems. DPFs were more widely introduced commercially in the 2000s, which coincided with a step change in vehicular PM emissions standards in the US, Europe and Japan. Scientific study focusing on addressing the problem of adverse ash accumulation in DPFs in university settings began in the mid-2000s.

In the prevalent DPF configuration, there are hundreds of filter channels per square inch organized in a honeycomb arrangement and alternating between being plugged (i.e. closed off) at the incoming end and plugged at the downstream end where ash and soot entrained in the exhaust gases

accumulate. The channel walls are usually made of either cordierite ceramic or silicon carbide (SiC). The side walls of each channel lie tangent to the direction of the incoming exhaust stream and are porous, permitting the flow of exhaust gases through them while soot and ash are trapped inside of their pores, lodged on the outside of channel walls (i.e. on the "cake layers"), or accumulated at the far downstream end plug region of the channels. The nature of flow through a given DPF channel, along with the concepts of cake layer and end plug, are illustrated in Figure 1-15.

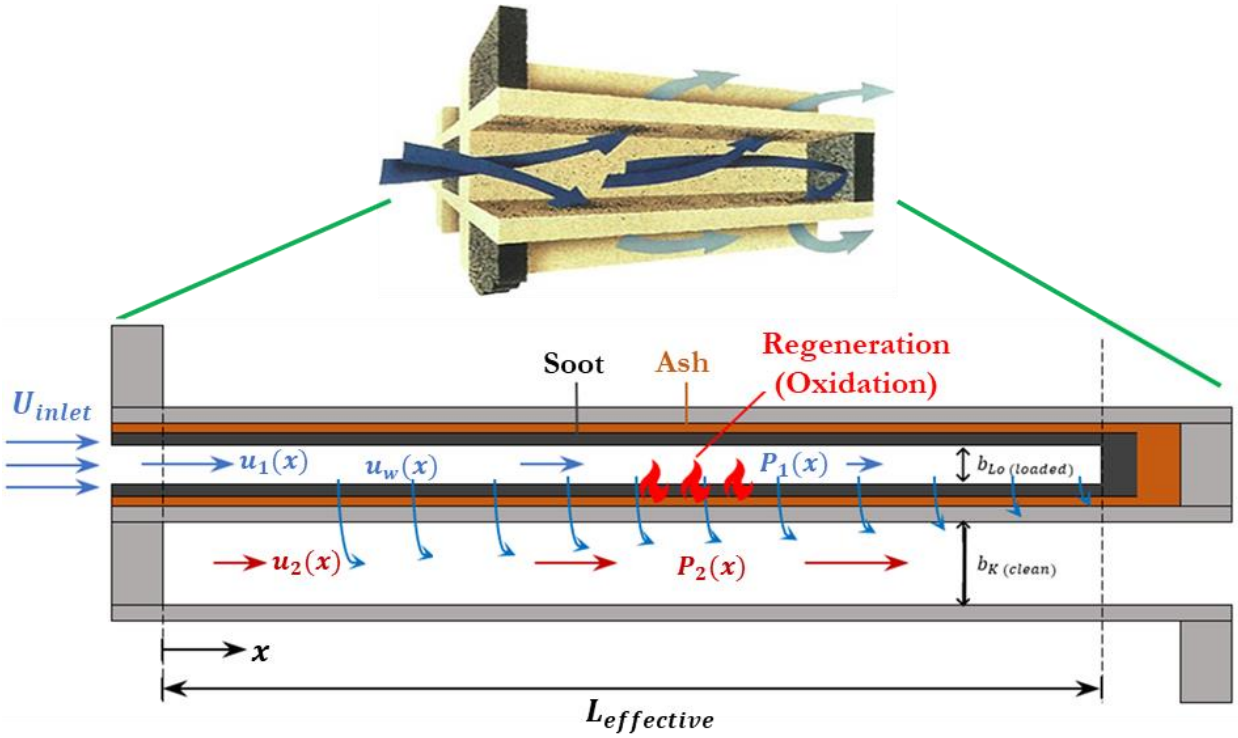

Figure 1-15: A not-to-scale depiction of exhaust flow and combustion of soot during regeneration. Characteristic length is 30cm whereas channel width is about 1mm. Note also that the magnitude of velocity through the walls is actually much smaller (on the order of 1%) than that in the channels due to continuity. However, the illustration is intended to depict the idea that flow slows in the inlet channel as exhaust is bled off into the neighboring channels and accelerates in the exit channels as more exhaust enters through the walls.

1.5.1 DPF Performance Modeling

DPF performance (i.e. efficacy) is often used to describe the backpressure that a DPF imposes onto the engine exhaust system, which requires the engine to consume more fuel in order to both deliver a given amount of power to the drivetrain (and wheels in the case of an automobile), and overcome the frictional losses required to drive the exhaust out of the tailpipe. Elevated

backpressure is therefore often correlated with increases brake-specific fuel consumption (BSFC), which is the rate of fuel consumption $\dot{m}_f$ divided by brake power P_{brake} produced [55]:

$$sfc\ \left[\frac{mg}{J}\right] = \frac{\dot{m}_f\ \left[\frac{g}{s}\right]}{P\ [kW]} \tag{1.5a}$$

$$bsfc\ \left[\frac{mg}{J}\right] = \frac{\dot{m}_f\ \left[\frac{g}{s}\right]}{P_{brake}\ [kW]} \tag{1.5b}$$

In 2020 while optimistically discussing potential improvements in aftertreatment design optimization, Viswanathan et al. provided data showing the characteristic impact of DPF and aftertreatment system (ATS) backpressure on BSFC, per Figures 1-16 and 1-17 below.

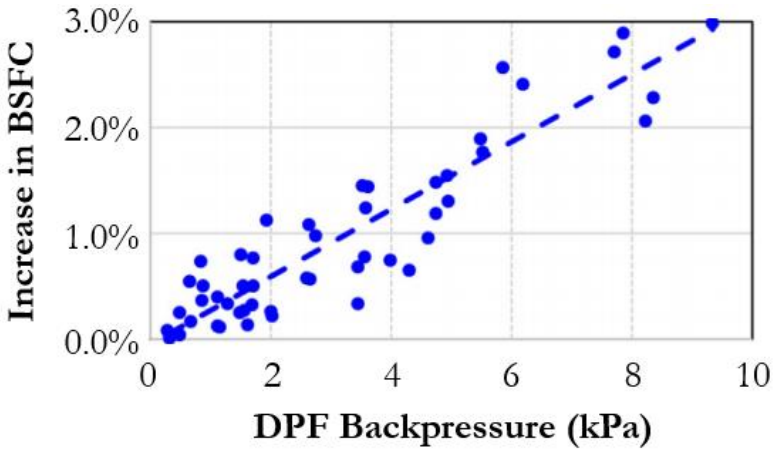

Figure 1-16: Sample data indicating the impact of DPF backpressure on increase in vehicle brake-specific fuel consumption. Adapted from [13].

The authors also provided data that compare total ATS versus distance traveled "on a line haul truck" that had accumulated PM during over 600,000 kilometers of operation [13].

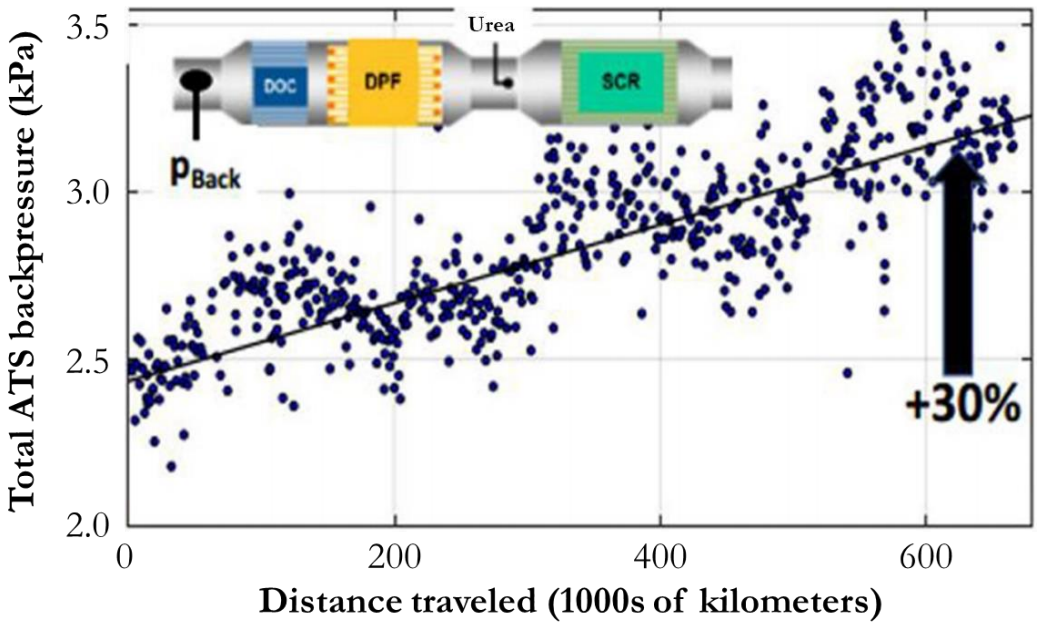

Figure 1-17: Total aftertreatment system backpressure in a tractor-trailer experiencing line haul trucking [13].

Notice that if we map the backpressure experienced by the line haul truck in Figure 1-17 to the DPF-BSFC relation shown in Figure 1-16, we can conclude that the truck experienced around a 1.0% decrease in fuel economy due to the presence of ATS, which is significant in the industry.

Analytical and numerical expressions for pressure drop experienced in both clean and PM-loaded DPFs have evolved significantly, having been presented in a variety of different forms by dozens of researchers over the past 31 years [26, 56, 57, 14, 58, 59, 60, 61, 62, 63]. The models come in one of two flavors: one involving relatively straight-forward algebraic expressions that are derived from parametric studies of empirical data, and the other involving rigorous analysis and solving of differential conservation equations originally presented by Bissett [26]. The progression of milestone models beyond Bissett's may be described as follows:

1) In 1989, Konstandopoulos et al. first presenting a Darcian closed-form analytical expression for DPF pressure drop assuming Darcian flow and a clean unloaded filter, as a function of DPF geometry and material parameters and exhaust properties [56];
2) In 1999, Konstandopoulos et al. extended their 1989 work by presenting pressure drop across the wall to consider the case in which non-Darcian flow effects are relevant—that is, when the Reynolds number of the flow through the wall is much less than unity [57, 56];

3) In 2000, Konstandopoulos et al. extended their 1989 work to include a layer of soot on the DPF substrate, assuming Darcian flow, and referred to the 1999 paper for incorporating non-Darcian effects across the wall; and
4) In 2004, Gaiser and Mucha suggest that the addition of an ash layer to the soot layer presented in 2000 presents a significant new contribution to pressure drop and consequently derived an expression for backpressure over the effective length, considering ash and soot properties independently [59].

The general consensus is that the pressure drop can be decomposed into five different components, each corresponding to different regions of the filter. These regions include the 1) inlet and 2) outlet cones that suffer respectively from compression and expansion losses, the 3) inlet and 4) outlet filter channels experiencing channel flow pressure drop, and the porous wall region—which includes the DPF substrate and PM layers—across which Darcian and non-Darcian pressure drop is experienced, such that,

$$\Delta P_{Total} = \Delta P_{inlet\ cone} + \Delta P_{inlet\ channel} + \Delta P_{wall} + \Delta P_{outlet\ channel} + \Delta P_{outlet\ cone} \qquad (1.6)$$

The middle three regions are shown in Figure 1-15 above, and one version of the inlet and outlet regions is depicted in Figure 1-11, though the inlet may also be imagined as a diverging nozzle to the left Figure 1-15 and the outlet cone a converging nozzle to the right.

Perhaps the most convincing set of simplified expressions for each pressure drop component is given by Konstandopoulos et al. in their 2000 "Fundamental Studies" article that extended the standard unladen closed-form pressure drop model by presenting an updated closed-form expression for backpressure considering PM loaded onto the DPF wall, which was validated via "presumably exact" 3-dimensional fluids simulations [14]. The constituent equations are given below, and assumes Darcian flow in the porous wall, no flow through the blocked ends of the DPF filter channels, and a uniform PM (labeled soot in the paper) layer over the wall substrate.

Note these equations extend that derived by Konstandopoulos et al. via parametric studies showing via empirical data that the total pressure drop across the DPF can be modeled as a function of just two dimensionless variables (A_1 and A_2 per page 109 of the 1989 SAE paper) [56]. That is, the more rigorous solution is simplified and can be "excellently described" by the following expressions representing a first order expansion in A_2 as $1 + \left(\frac{2}{3}\right) A_2$ [57].

The first term is essentially a scaled version of the dynamic (i.e. inertial) pressure of the fluid passing through the diverging inlet cone, and is the result of expansion flow losses in a cone with rapidly changing cross sectional area [64]:

$$\Delta P_{inlet\ cone} = \frac{\zeta_E \rho U_{inlet}^2}{2} \tag{1.7}$$

The parameter ζ_E is thought to vary from 0.2 to 0.8 depending on "area blockage ratio" and Reynolds number [14]. The factor for the inlet cone was given as 0.25 in one early study [64]. The inlet channel pressure drop is expressed as a function of exhaust stream volumetric flow rate $Q = N \cdot \rho \cdot u_1(x = 0) \cdot b_{Lo}^2$—where N is the number of open channels in the DPF, filter volume V_{Trap}, loaded filter width b_{Lo}, wall thickness s_w, PM layer thickness s_{s+a}, and flow factor $F = 28.454$ [14].

$$\Delta P_{inlet\ channel} = \frac{\mu Q}{2V_{Trap}} (b_K + s_w)^2 \left[\frac{4FL^2}{3(b_{Lo} - 2s_{s+a})^2}\right] \tag{1.9}$$

Assuming Darcian flow (i.e. viscous such that Reynolds number $\ll 1$), the pressure drop across the PM layer and DPF substrate may be expressed as follows, where k_i represents material $i's$ permeability, and D is the diameter of the DPF filter. Konstandopoulos, again, considered only soot when describing the PM atop the DPF wall substrate, which we here label as PM.

$$\Delta P_{PM\ layer} = \frac{\mu Q (b_K + s_w)^2}{L\pi D^2 k_{PM}} \cdot ln\left(\frac{b_K}{b_K - 2s_{s+a}}\right) \tag{1.10}$$

$$\Delta P_{DPF\ substrate} = \frac{\mu Q}{2V_{Trap}} (b_K + s_w)^2 \left(\frac{s_w}{k_w b_K}\right) \tag{1.11}$$

The pressure drop through the exit channel is, unsurprisingly, of the same form as that for the inlet channel, except of course the channel walls are free of any particulate matter PM deposits, yielding:

$$\Delta P_{outlet\ channel} = \frac{\mu Q}{2V_{Trap}} (b_K + s_w)^2 \left(\frac{4FL^2}{3{b_{Lo}}^2}\right) \tag{1.12}$$

Similarly, the pressure drop due to flow contraction losses through the converging outlet cone can be written is equivalent to that for the region immediately upstream of the DPF:

$$\Delta P_{outlet\ cone} = \frac{\zeta_E \rho U_{outlet}^2}{2} \tag{1.13}$$

Summing the above equations yields then the total pressure drop across the DPF, assuming Darcian flow across the wall region.

$$\Delta P_{total} = \frac{\mu Q}{2V_{Trap}}(b_K + s_w)^2 \left\{ \frac{s_w}{k_w b_K} + \frac{1}{2k_{PM}} ln\left(\frac{b_K}{b_K - 2s_{s+a}}\right) + \frac{4FL^2}{3}\left[\frac{1}{(b_K - 2s_{s+a})^4} + \frac{1}{{b_{Lo}}^4}\right]\right\} \tag{1.14}$$

It is interesting to note that many papers describing models for pressure drop across the DPF, including the this dissertation with the model presented in Chapter 4, neglect the inlet and outlet cone regions. Konstandopolous reasoned that these expansion and compression losses are negligible relative to the total pressure drop cross the loaded filter, typically by 2 to 3 orders of magnitude [14]. However, an early 1982 study by Cummins engines researchers Mogaka et al. expressed that these "end losses" due to rapid contraction and expansion of the exhaust flow in inlet and outlet cones amount to some 5% of total DPF back pressure, which is arguably not negligible [64].

The more rigorous derivation for pressure drop, yielding a relatively complicated result, was derived by Konstandopoulos et al., who applied a subset of the original set of equations proposed by Bissett [56, 26]. The model presented here reflects clean (unloaded) filters and is extended to include loaded DPFs with MCC in Chapter 4 of this dissertation. The expression for an unloaded, Darcian filter is as follows, with terms defined in the appendices:

$$\Delta \hat{P}_{total} = A_1 + A_2\left[\frac{c_1}{q_1}(e^{q_1} - 1) + \frac{c_2}{q_2}(e^{q_2} - 1) + \frac{1}{2}\right] + c_1 q_1 + c_2 q_2 \tag{1.15}$$

Considering non-Darcian flow through the wall region requires quite a bit of additional work, which is presented in detail in Chapter 4 of this dissertation and the accompanying appendix. In short, doing so involves assuming that the pressure drop through a porous medium includes inertial losses locally in the flow. The modified pressure drop may be expressed as follows, given inertial parameter β:

$$\Delta P_{wall}(x) = \frac{\mu}{k_{wall}} u_{wall}(x) \cdot s_w + \beta \cdot \rho [u_{wall}(x)]^2 \cdot s_w \tag{1.16}$$

This reduces to the solution of a differential equation representing the outlet channel velocity in non-dimensional form which can be solved numerically via the shooting methods [57]. Note that a

form of this method is invoked in Chapter 5 to solve for the temperature history of the DPF during active regeneration.

1.5.2 DPF Filtration Efficiency

While performance is often referred to in the context of DPF backpressure, the purpose of the device is of course to trap PM entrained in the exhaust flow. A critical measure of performance therefore is filtration efficiency E, or the percent of PM trapped by the DPF so that it does not continue downstream of the filter. This efficiency metric is often expressed by including either a volume or mass fraction, as follows:

$$E_m = 1 - \frac{m_{out}}{m_{in}} \tag{1.17a}$$

$$E_V = 1 - \frac{V_{out}}{V_{in}} \tag{1.17b}$$

Early reports indicated that filtration efficiency is on the order of 90%, with subsequent studies suggesting that it is even greater at over 95% across all expected particle sizes after around 5 to 10 minutes of loading for a single wall filter [64, 65].

The actual filtration scheme is often represented via a series of slabs—or layers—of unit cells, or connectors, each of which is responsible for collecting some fraction of the incoming particulate matter. Naturally, the mass flow of PM into one slab is equal to that which exits the previous slab. The general model is illustrated in Figure 1-18.

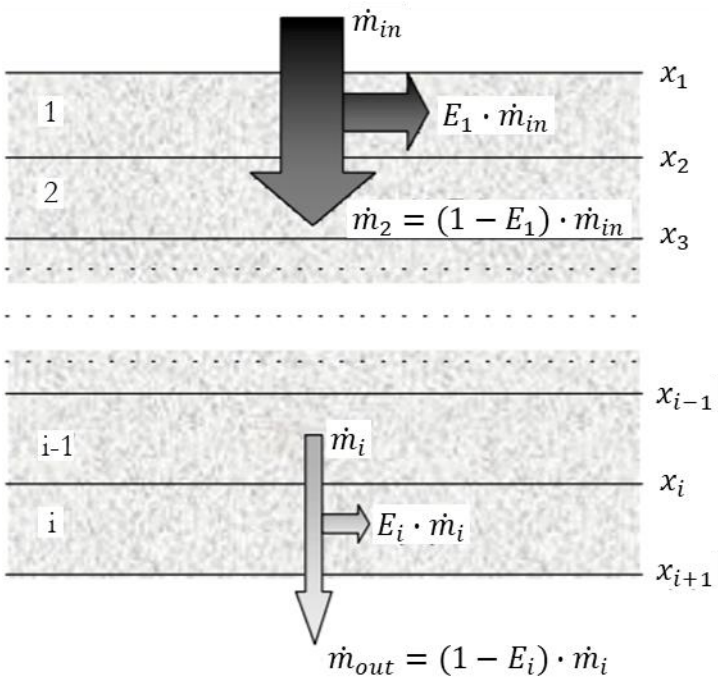

Figure 1-18: Modeling the DPF filter wall as a series of i collector layers, each with its own mass flow rate m_i and collection efficiency E_i [14].

There are four primary physical mechanisms by which aerosols may become trapped in a porous wall filter: 1) diffusion, 2) interception, 3) inertial impaction, and 4) gravity effects. Figure 1-19 illustrates the four different means of filtration. Diffusion is characterized by small particles undergoing Brownian motion, inertial impaction results from large particle mass and/or high particle speed (i.e., inertia) causing the particle to veer off its local flow streamlines, and interception falls in between by causing capture of the aerosol particle when it comes within about a particle radius of the substrate surface [66]. Capture by gravity corresponds to the weight of the particle deposited on a surface to outweigh other (e.g., flow) forces that would drive the particle through the filter wall.

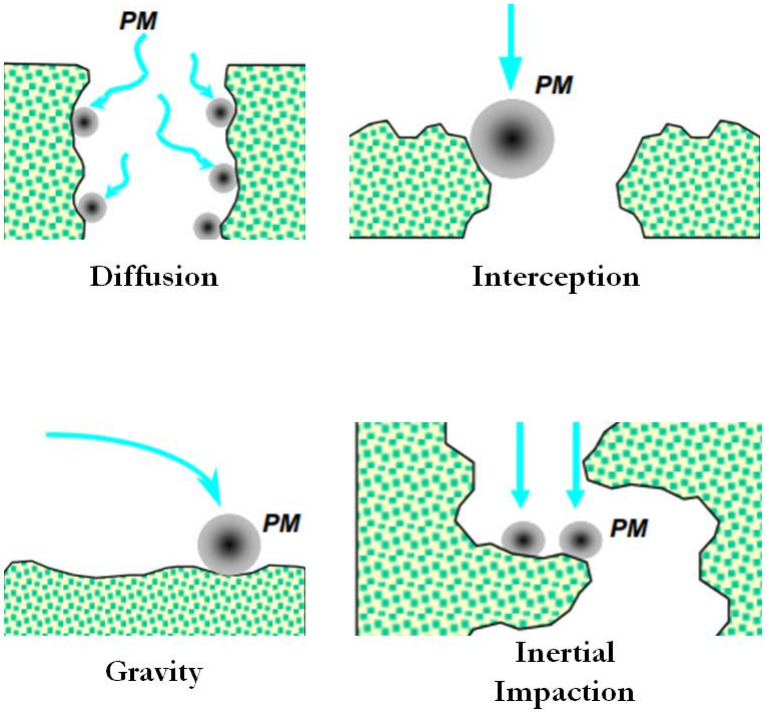

Figure 1-19: The four mechanisms of particle capture in porous fibrous filters [15].

The dominant mechanism(s) by which aerosol particles are captured within particulate filters depend on the nature of the flow and the materials present. For example, a sufficiently high Stokes number Stk will cause inertial impaction to dominate. That is, inertial impaction dominates when [56]:

$$Stk \sim \left(\frac{\rho_{exhaust} \cdot u_{particle} \cdot D_{particle}}{\mu_{exhaust}}\right)\left(\frac{D_{particle}}{D_{filter\ pore}}\right) = Re_{particle}\left(\frac{D_{particle}}{D_{filter\ pore}}\right) \gg 1 \quad (1.18)$$

Figure 1-20 provides one example of how capture mechanisms vary in magnitude with aerosolized PM particle size, at a given engine operating condition.

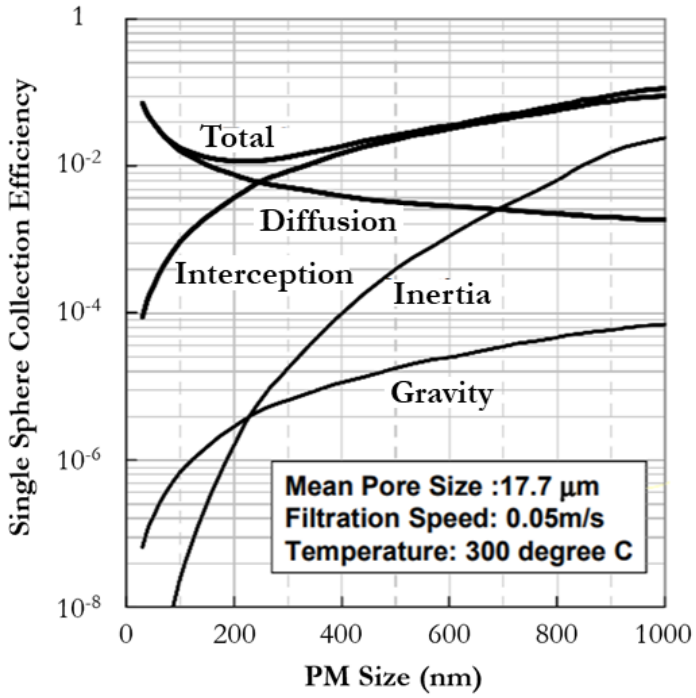

Figure 1-20: Varying collection efficiency across the four primary filtration mechanisms in the DPF channel wall as a function of PM diameter at a given engine operating condition [15].

While some vetted literature has indicated that all four (diffusion, interception, inertial impaction, and gravity) effects can be dominant contributions to PM trapping, the most prevalent literature assumes that only the first two—diffusion and interception—need to be considered, with diffusion most often dominating [67, 56, 14, 66, 68, 15, 69].

For a clean filter, the efficiency of each layer can be integrated to find the full packed bed filtration efficiency E_{filter} as a function of the local combined diffusion + interception efficiency η_{DR}, filter wall thickness s_w, wall porosity ε_0, and filter collector characteristic diameter $D_{collector}$, as follows [56, 14, 69]:

$$E_{filter} = 1 - \exp\left[-\frac{3\eta_{DR}(1-\varepsilon_0)s_w}{2\varepsilon_0 D_{collector}}\right] \tag{1.19}$$

The combined diffusion + interception diffusion efficiency term is calculated as [14]:

$$\eta_{DR} = \eta_D + \eta_R - \eta_D \cdot \eta_R \tag{1.20}$$

The (Brownian) diffusion coefficient for a single spherical collector scales as Peclet number— the ratio of advective to diffusive transport— to the minus two-thirds as follows [56]:

$$\eta_D \sim Pe^{-\frac{2}{3}} = \left[\frac{D_{collector}}{D_{particle}} \cdot \left(\frac{u_{wall}}{\varepsilon_0}\right)\right] \tag{1.21}$$

The interception mechanism efficiency scales with particle and filter collector size as [14, 16],

$$\eta_R \sim \frac{\left(\frac{D_{particle}}{D_{collector}}\right)^2}{\left(1+\frac{D_{particle}}{D_{collector}}\right)^{\frac{3-2\varepsilon_0}{3\varepsilon_0}}} \tag{1.22}$$

As the DPF is operated, the filter wall begins to accumulate soot and ash PM, ultimately forming PM plugs in the deep bed filter until the pores fill and/or are sealed by soot bridging across the gaps separating filter substrate fibers. This eventually results in PM layers accumulating atop the wall, forming what is known as the cake layer. New incoming aerosols then deposit on the cake layer and do not penetrate into the wall pores. The process of wall filling was described by Merkel et al. as occurring in progressive accumulation steps, according to Figure 1-21, in which PM is simply referred to as soot [70].

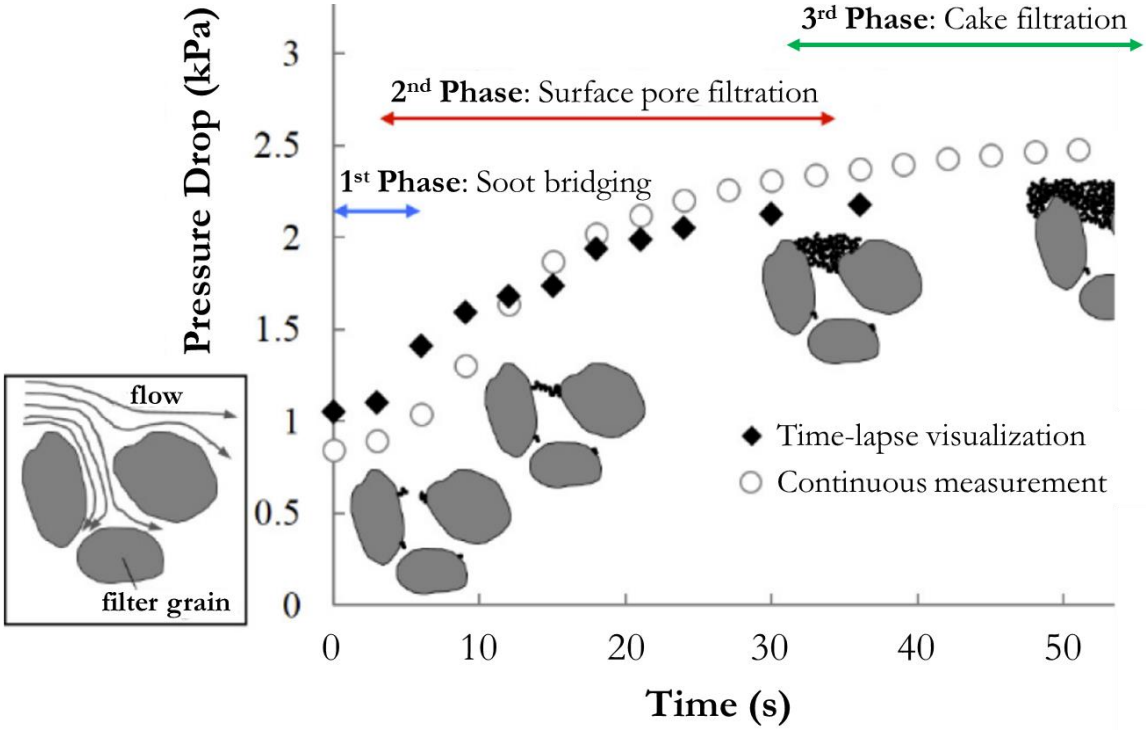

Figure 1-21. Illustrating the four-stage progression of soot/PM accumulation in the filter porous membrane [16].

As the porous membrane fills, the parameters in the collector filtration model should be updated accordingly.

1.5.3 Regeneration and Associated Performance Tradeoffs

Figure 1-22 illustrates that during typical engine operation, PM (soot) entrained in the exhaust stream is deposited on the wall region, which consists of the DPF filter substrate coated with post-regeneration ash, and pre-regeneration soot on top of the ash. The soot layer is also thought to consist of ~1% ash that fuses via high temperatures with additional ash resulting from the oxidation of soot to form ash agglomerates on the order of 5% the size of the pre-oxidized soot [54].

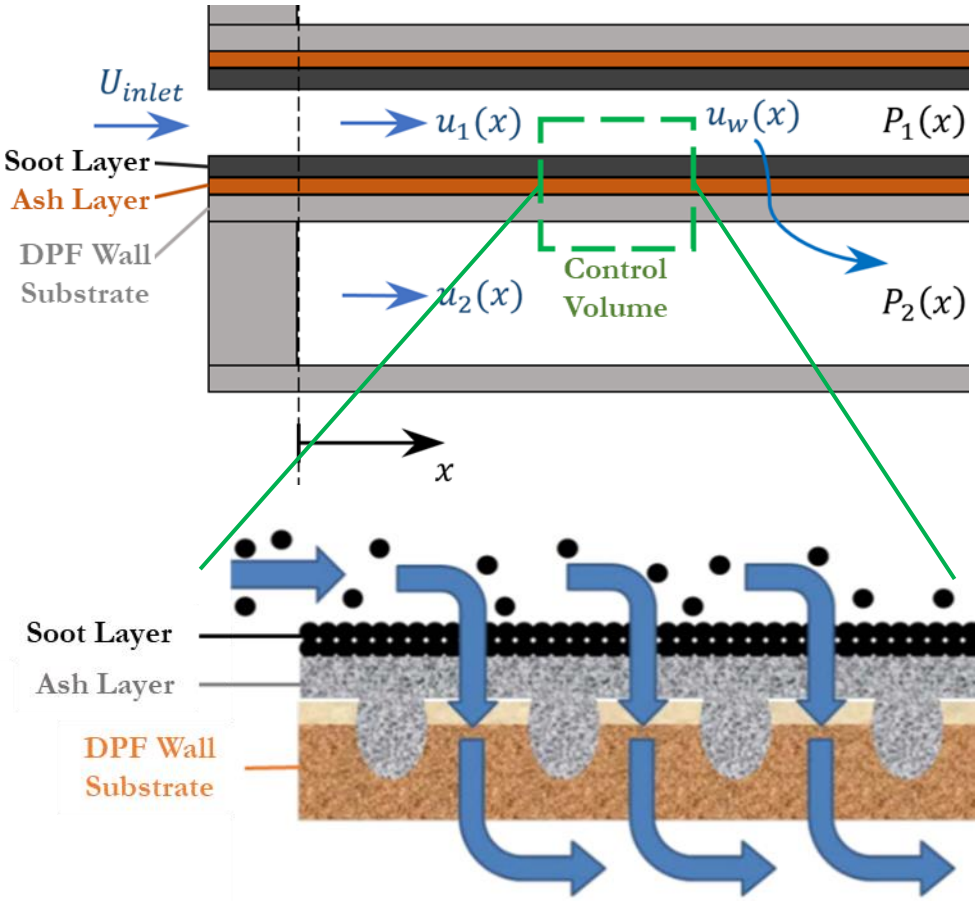

Figure 1-22: The entrance region of a DPF (top) and an illustration of the wall region, which includes soot, ash, and the underlying DPF substrate with open pores that fill with PM until they are effectively sealed shut (bottom).

Note that ash and soot are fundamentally different materials: soot forms in the engine combustion chamber because of incomplete combustion while ash is the incombustible product of complete

combustion consisting primarily of metallic compounds found in engine oil that oxidizes off the cylinder wall and/or is entrained into the exhaust flow by combustion gases.

Soot particles are periodically or continuously oxidized in an automated fashion through a process called regeneration, during which soot entrapped in the DPF is oxidized either passively via catalysts lining the DPF wall substrate or actively by raising the temperature of incoming exhaust gases, which then serve as the oxidizing agent for soot deposited on the channel walls. Passive regeneration is also known as continuous regeneration, since it occurs all through engine operation at standard exhaust temperatures, resulting in soot oxidizing along the catalyst and forming nitrogen dioxide. Ash particles, on the other hand, remain unchanged, and thus the ratio of ash to soot in the DPF increases over time during regeneration. After an ideal regeneration cycle, all soot has been burned off the cake layer, leaving behind only ash. In fact, at about 30,000 miles of engine operation, the PM deposits inside the DPF between regeneration cycles consist mostly of ash [71].

While passive regeneration is a continuous event, active regeneration takes place periodically, and usually upon exceeding some threshold value of backpressure for a given DPF sensed by vehicle electronics. The process oxidizes the soot layer, converting substantially all that soot to ash, significantly reducing the volume of PM trapped in the DPF to alleviate the backpressure. In fact, regeneration yields ash that occupies around just 5% of the original corresponding soot volume [54]. Following regeneration, soot from the incoming exhaust is then deposited on the newly formed ash layer, and the process repeats.

As the DPF fills with PM, it experiences both reduced wetted surface area in the channels and thicker PM layers on the cake layer through which exhaust must pass prior to exiting the aftertreatment system. This results in a continuous, permanent uptick in backpressure that, given a fixed backpressure threshold triggering the onset of regeneration, also results in a monotonic rise of regeneration frequency over time, as illustrated in Figure 1-23.

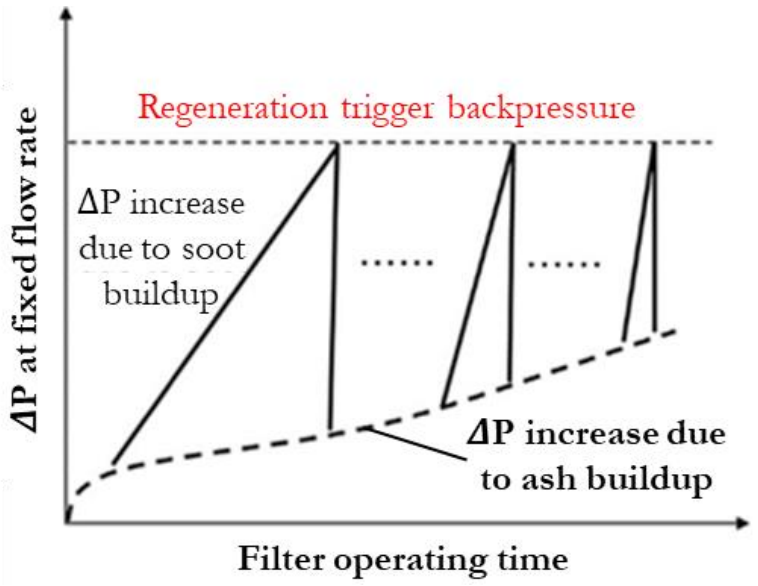

Figure 1-23: As the DPF fills with ash, regeneration frequency increases. Once the frequency becomes excessive, the filter is considered to have failed, and must be either (painstakingly) cleaned or replaced [17].

To provide some more detail on regeneration: passive regeneration, as the name suggests, relies on regular engine operation to produce exhaust with sufficiently high temperature that continuous oxidation along the catalyzed DPF channel walls may proceed, not requiring any additional external heating in order to achieve complete combustion. Since lower exhaust temperatures and catalytic oxidation are used, however, NO is converted into higher concentrations of undesirable NO_x. As only some heavy-duty diesel engines are capable of reliably, passively regenerating soot captured in the DPF, and as even those engines can suffer from incomplete combustion if they operate primarily at low load, the use of passive filters must be very carefully considered and active implementations are thus generally the default. After all, slow or inadequate passive regeneration can result in excess soot buildup in the filter, causing unacceptable levels of backpressure and potentially severely reducing filter longevity. The catalysts that promote oxidation of the soot at lower temperatures are either included in the diesel fuel and/or on the filter wall substrate surface.

Active regeneration, on the other hand, requires external energy beyond that contained in the unmodified exhaust stream to oxidize the soot layer. The most common strategy used to achieve active regeneration is that of programming the engine to burn late in the cycle so that a hotter exhaust gas is generated. Active regeneration invokes an electronic control module for continuously estimating the soot load within the DPF, and once a threshold soot loading (often prescribed in

grams soot per liter displacement of the open-inlet DPF channels) is reached by measuring backpressure as a proxy, the regeneration process is triggered and commences.

There has been relatively little research conducted to address the control of ash/soot deposit distribution within DPFs. This fact, compounded with reports of mixed performance in DPFs, has promoted further investigation into what factors drive strong variation in DPF efficacy. Performance in the present context is defined by a combination of metrics, which in relative order of importance include:

1) trapping efficiency, or fraction of exhaust PM that is trapped in the DPF;
2) fuel consumption due to regeneration and DPF backpressure;
3) and effective lifetime and maintenance interval of the DPF.

A more detailed understanding of processes within the DPF—including ash transport and inter-particle bonding—is needed to correlate device design and engine operating parameters with performance metrics.

For actively regenerated systems, a key decision variable is that of regeneration frequency. The associated tradeoff can be described as follows: a higher regeneration frequency requires more energy for external heating of the incoming engine exhaust, but also results in cleaner DPF channels that yield a lower backpressure fuel economy penalty. This tradeoff yields a performance-optimal regeneration frequency, which according to Salvat et al. is on the order of 350-400 kilometers distance traveled, with a resulting ~3.5% fuel economy penalty on the vehicle, opposed to ~7% penalty at 100 km regeneration interval and ~4% penalty at 600 km, per Figure 1-24 [18]. 2008 work from a Caterpillar and the U.S. Department of Energy cooperative instead suggests that the absolute fuel consumption penalty associated with DPF regeneration interval selection has a range on the order of 2% across viable regeneration intervals [72]. The backpressure penalty may be approximated using the pressure model presented in Chapter 4, and then dividing that by brake mean effective pressure yields the fuel economy penalty associated with backpressure [73, 74]:

$$FEP_{\Delta P} = \frac{\Delta P}{BMEP} \cdot 100\% \tag{1.23}$$

The enthalpy penalty associated with injection of additional fuel to raise the exhaust temperature so that active regeneration can be initiated and maintained is given by [74]:

$$FEP_{\Delta H} = DC \cdot (\lambda + 1) \cdot \left(\frac{C_{p,exhaust}}{\Delta H_{diesel}}\right) \cdot \Delta T_{exhaust} \tag{1.24}$$

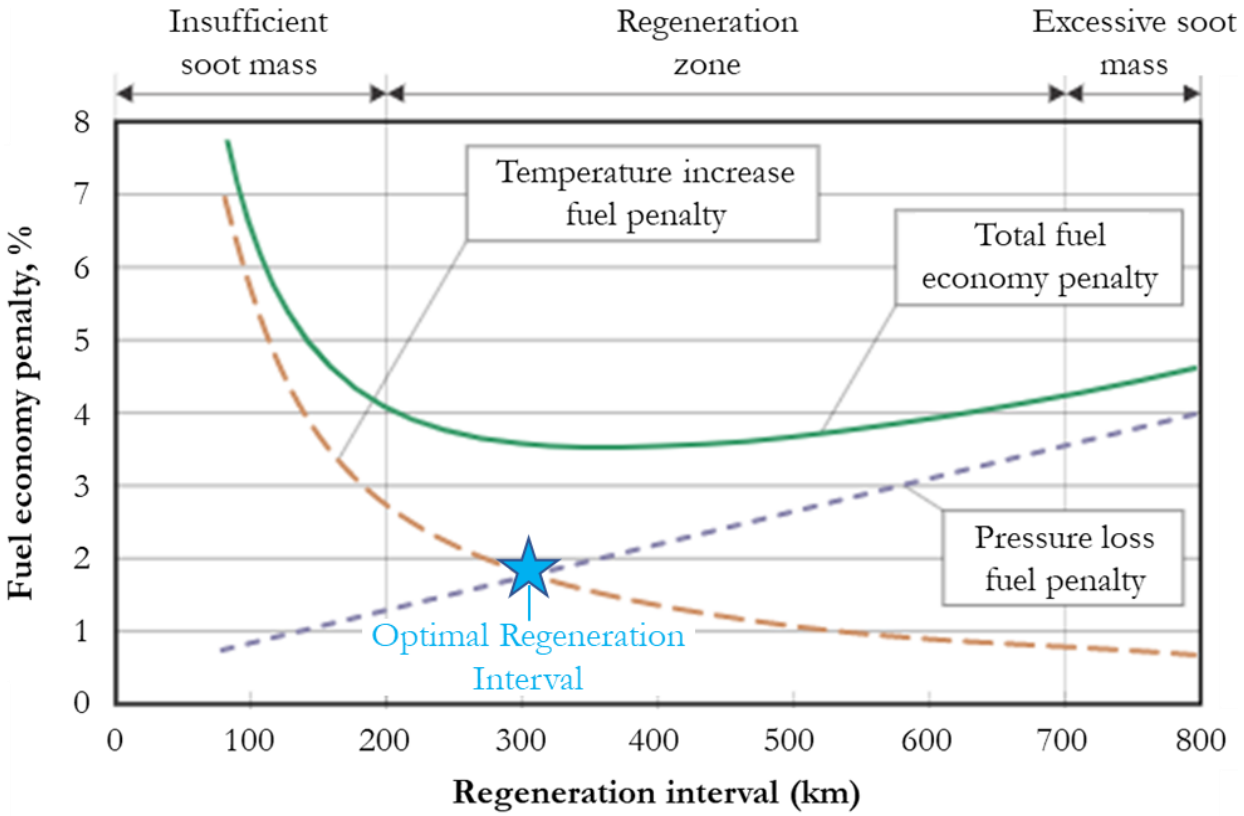

Figure 1-24: Illustrating the tradeoff between frequency of exhaust temperature increase during regeneration and pressure loss penalty due to ash accumulation central to fuel economy optimization when selecting DPF active regeneration frequency [18].

The shape of the curves in the graph suggests that one would want to bias more toward increased pressure loss fuel penalties and associated reduction in frequency of regenerations, since overall fuel economy penalty is less sensitive to regeneration interval to the right of the global minimum [18].

Most DPFs are rated to around 100,000-150,000 miles (or around 3,000-5,000 engine operating hours) before replacement or cleaning are recommended. However, unanticipated upstream as deposit formation can lead to substantial reduction of the effective lifetime of DPF systems [22]. With the cost of DPF replacement on the order of 10% of total vehicle cost, DPF replacement is an expensive proposition, highlighting the need for strong, predictable device longevity.

Two factors are particularly important to consider when addressing variable performance in current DPFs include: 1) the dynamic and variable composition/morphology of PM deposits, and 2) soot/ash transport characteristics along the DPF channel walls. It is suggested that these elements are largely affected by temperature distribution throughout the DPF over time [22, 19, 17].

1.6 Mid-Channel Congestion (MCC) in DPFs

As deposits accumulate and cake layers thicken, particles expected to be swept along by the exhaust flow to the ends of the channels, forming continuous end plugs that do not have gaps between ash agglomerates. While these nominal end plugs do occupy volume and correspondingly increase back pressure due to a subsequent reduction in surface area along the inside of DPF channels, surface area is decreased slowly and gradually. Backpressure therefore also rises slowly. Furthermore, the steady growth of agglomerates in the end plug region are accounted for in the overall design of the DPF. Figure 1-27 provides a cross-sectional view of MCC observed during engine field test operations.

Feedback from engine/vehicle manufacturers indicates that DPF backpressure in field operation sometimes rises rapidly and substantially beyond nominal values, reflected in Figure 1-25.

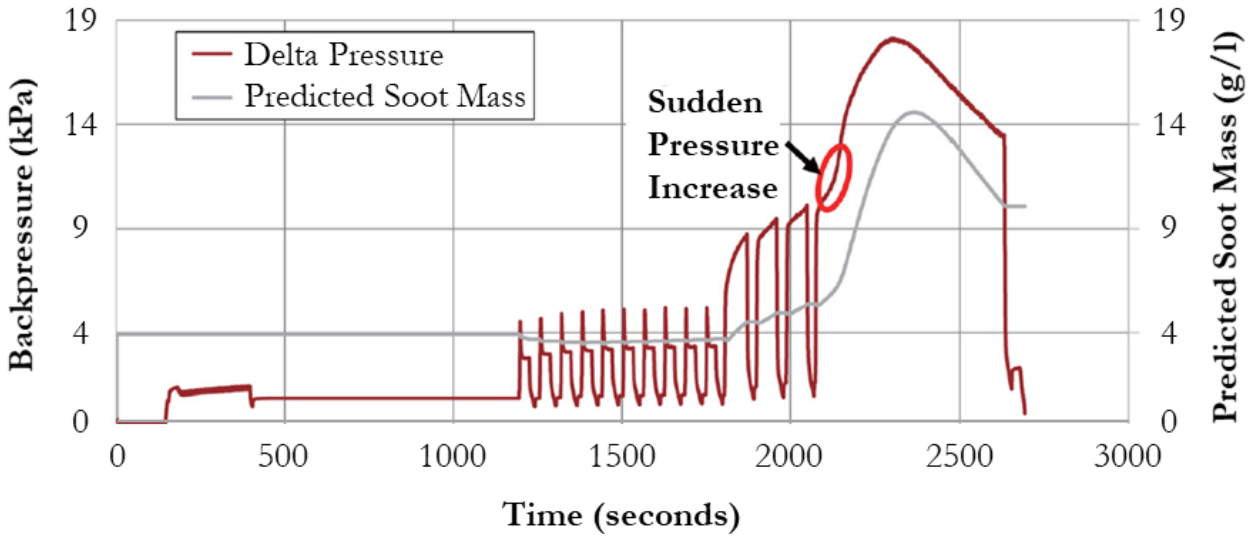

Figure 1-25: An illustration of the impact of MCC on DPF backpressure, with anomalous spikes in backpressure occurring when PM agglomerates block the channel upstream of the end plug [19].

It is suggested that the unexpected backpressure rise is due to an anomalous phenomenon characterized by PM agglomerates clogging channels of the DPF upstream of the end plug region, for reasons that remain unclear. The concept is illustrated in Figure 1-26.

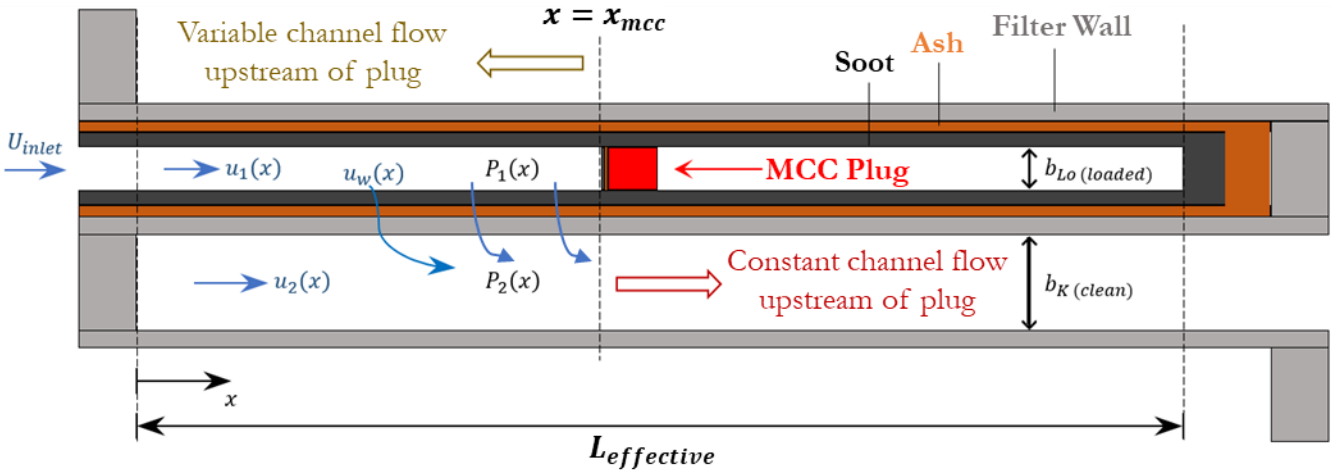

Figure 1-26: A DPF channel experiencing MCC approximately halfway down its axial length.

This premature obstruction of the filter channels can severely undermine DPF performance, requiring premature cleaning or replacement. In technical literature, it has been referred to as mid-channel congestion / clogging / collapse (MCC) and mid-channel deposits (MCD) [19, 22].

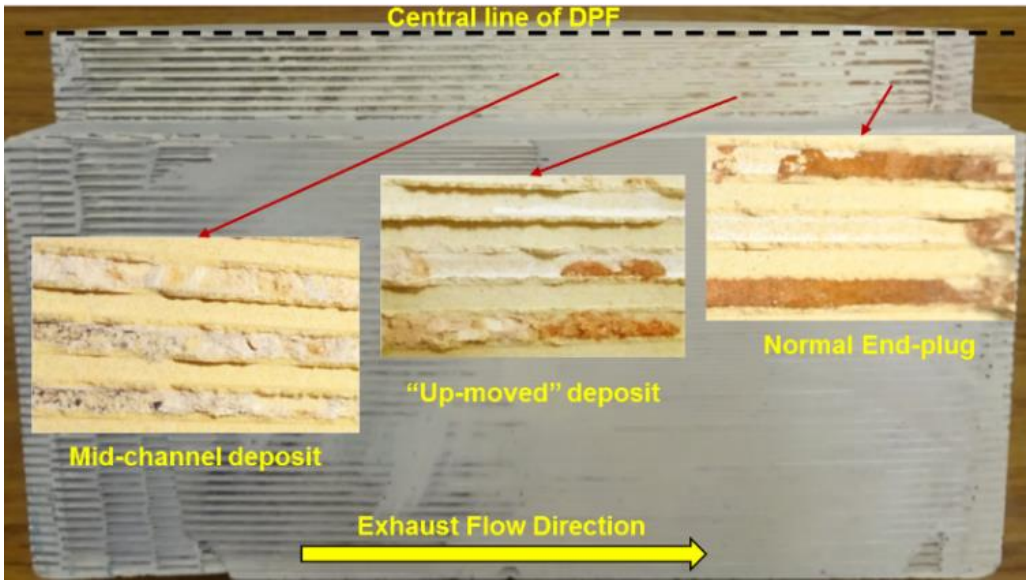

Figure 1-27: DPF sample from field testing exhibiting premature ash plugs forming in and anchoring to the mid-channel region [19].

MCC often results in a sharp increase in backpressure, which is consistent with feedback from real world diesel vehicle operators. Field data show that significant clogging of the channels does occur and likely occurs with significant prevalence. Such irregular deposits are known to lodge anywhere along the DPF channel axis, causing full or partial premature blockage, a substantial reduction in wetted channel surface area, a more rapidly rising cake layer thickness, and subsequently the significant increase in backpressure depicted in Figure 1-25. Since many of the premature

blockages have been observed to occur approximately half way along the axis of the channels, they are often referred to as mid-channel congestion, mid-channel clogging, mid-channel collapse, or simple MCC. It is presumed that these plugs result from the detachment, or collapse, of PM layers deposited along DPF channel walls, resulting in blockage of exhaust flow axially through the channels, and thus reduced channel surface area with premature lateral diversion of the incoming gases through the porous sidewalls [19]. Real world experience has shown that DPFs with a significant presence of MCC introduce so much excess backpressure to the system that the time before required DPF overhaul is reduced by as much as 50%, so from 150,000 miles (~5,000 hours) of operation to approximately 75,000 miles (~2,500 hours). Some verbal accounts from foreign DPF manufacturers indicate that frequency of replacement can be even greater.

As for the history of MCC, which is addressed in greater depth in Chapter 2, the phenomenon was first formally introduced in the literature in 2014 by a group of scientists working for GM Korea, who claimed to have witnessed an unexpected, significant rise in backpressure due to humidity-induced instances of MCC that arise under very specific use cases (to be described in greater detail in Chapter 2). In 2016, Fukui et al. from the University of Tokyo published an SAE paper corroborating GM Korea's 2014 findings related to soot layer collapse, and extended that work by providing direct optical in-situ observation, in stark contrast to the destructive and time-intensive approach applied by GM that may have artificially altered the PM deposit layer prior to imaging [20]. The study concluded that collapse of PM from the side wall caused deposit layers that resulted in a rapid, significant increase in DPF pressure drop [20].

Presented earlier in Figure 1-25 and again with more detail in Figure 1-28 below, Fukui et al. observed a Gaussian-like pressure jump above nominal values extending over an approximately 7-minute period and peaking at a backpressure of around double (18 versus 9 kPa) the pre-pressure spike value. They further noticed a series of five instances of soot collapse over four different channels during the period, with three of the collapses occurring over a ~3-minute period in the region of peak backpressure rise, per Figure 1-28.

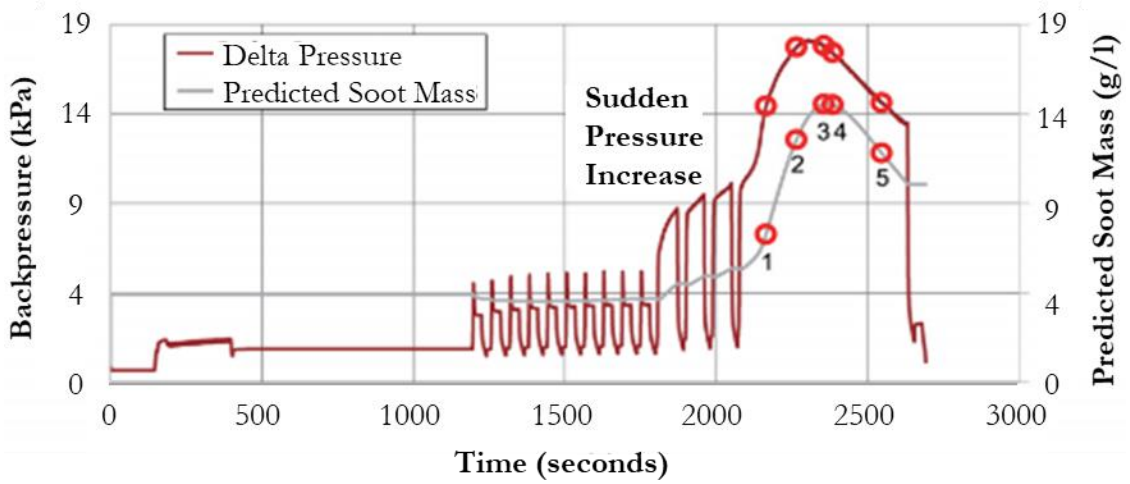

Figure 1-28: Observed anomalous DPF backpressure where small circles represent instances of observed MCC [20].

The ~30% increase in backpressure over expected values experienced by the DPF undergoing MCC is a result of the five instances of (premature) upstream channel clogging shown, which together represent upstream plugging of 4 of 10 (or 40%) of the visible channels, as shown in Figure 1-29, corresponding to Figure 8 in the source paper. Comparing this with Wang and Kamp's work, which "found that 50% mid-channel plugging can increase the DPF pressure drop about 35% and 80% mid-channel plugging can increase the pressure drop by 70% to 80%," fortunately suggests close alignment with their findings [75]. The impact of premature channel clogging in arbitrary configurations on DPF backpressure is derived and analyzed in Chapter 4 of this dissertation.

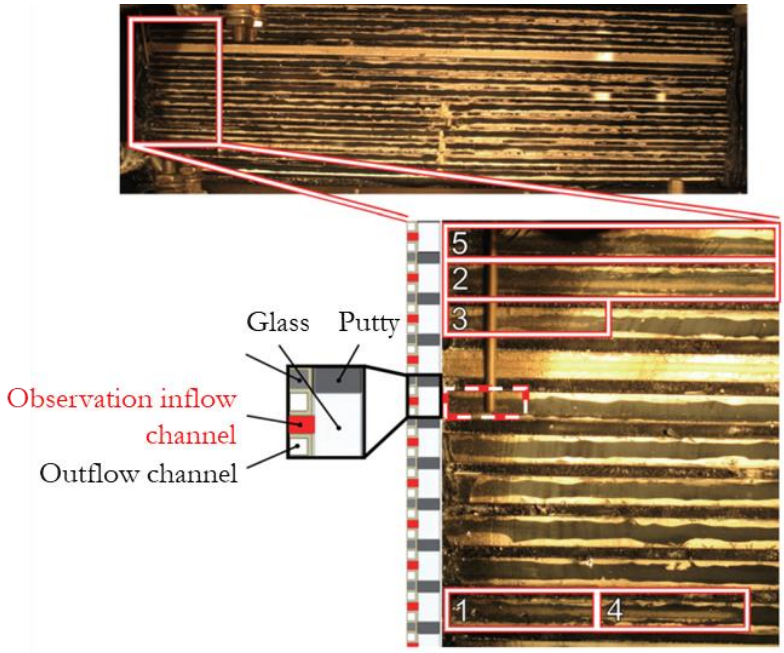

Figure 1-29: Scan of the plane of observed channels, showing locations of cake layer collapse [20].

A fascinating finding was that in both optically accessed and non-observed DPF channels, the cake layer detached from all observed surfaces at approximately the same time, suggesting that MCC is not as random or as stochastic a process as is sometimes supposed [20]. Instead, local conditions along the DPF axis arise that yield an instability in the PM layer and ultimately premature removal of that cake layer from the channel sidewalls. Alternatively, the observation hints at the idea that the sidewalls of a given axial DPF cross section are intimately connected in such a way that detachment at one point would effectively peel away the cake layer of adjacent wall faces in a given cross section. Another interesting discovery was that soot layers that collapse do not always agglomerate near the axial location of separation. They are instead sometimes transported significant axial distances and reattach to the channel walls or in the end plug region toward the far downstream end of the channel. This process of detachment, re-entrainment, and downstream transport has been observed to occur very rapidly, with part of the PM cake layer detaching and being swept downstream out of the field of view in just 0.17 seconds [20]!

1.7 Structure of Dissertation

The overall aim of this study is to improve understanding of what causes—as well as identify potential means of mitigating—the abnormal mid-channel congestion phenomenon. A combination of experimental and computer simulation approaches was conducted, with numerical simulation serving as the author's primary responsibility. Important sections for PM accumulation within the DPF include both (a) axial positions along the channel walls and (b) depth-wise penetration into (less desirable) or accumulation outside of (more desirable) the pores of the filtering medium within the channel side walls. Equally important are the processes of the initial deposition and the subsequent transport (movement) of the deposited particles from where they are initially lodged—e.g., transport due to shear, entrainment, surface stickiness/non-stickiness, etc. In recent years, research efforts have been particularly devoted to addressing the mechanisms primarily responsible for ash transport [71]. Attaining this goal will enable DPF systems to be designed with greater performance and durability, so that they can truly last the lifetime of their vehicles while minimizing energy consumed to backpressure and regeneration.

The next section will describe the progression of research that brings us to the presently prevailing hypotheses regarding how MCC develops in DPFs. Chapter 3 will describe a series of experiments conducted at MIT to generate and analyze images of MCC. Chapter 4 will describe a model for calculating backpressure (a measure of performance) in the DPF given an arbitrary ash

distribution. Chapter 5 will extend thermal models to determine the temperature history within a DPF during regeneration. Finally, Chapter 6 will conclude this work with findings and suggestions for further related research.

2 Prevailing Hypotheses for Causal Mechanisms of Mid-Channel Congestion

This section serves to provide the reader with a summary of observations and experiments conducted related to understanding the causes (and less so the consequences) of mid-channel congestion in DPFs. This is particularly important given the persistent uncertainty that prevails around what mechanisms give rise to the formation and development of anomalous plugs that form upstream of the end plug in DPFs. We review the three primary, prevailing, interrelated theories that seek to describe what causes MCC to take root and then progress into channel plugs that fully obstruct the oncoming flow. The three hypotheses are summarized in Table 2-1.

Table 2-1: A summary of the three primary causal mechanisms of MCC available in the literature as of 2020.

Hypothesis	Description
1. Humidity-induced soot cake layer separation: bulging, collapse, and re-attachment of the cake layer	A soaking of the cake layer followed by immediate application of high load yields a rapid bulge in the deposit layer that detaches as a unit, is re-attached to the wall, and clogs the channel
2. High-temperature induced shrinkage, peeling, curling, collapse, and re-attachment of the cake layer	High regeneration temperature causes fissures in the cake layer and shrinking PM (soot-ash) island sheets, peeling of those sheets into the channel exhaust flow, re-attachment of the partially-oxidized sheets to the channel, and clogging of the channel.
3. High-density ash anchors sintered to the filter substrate deep bed and subsequent growth to block the channel	High regeneration temperatures causes small, high-density ash particles embedded in the filter wall substrate pores to sinter irreversibly on the substrate, This ash ”anchor” will grow until ash “bridges” have formed to span the channel across ash anchors

These three hypotheses are based on bench and field tests of diesel engines and diesel-powered vehicles. While the theories are not mutually exclusive, they invoke different physical mechanisms as primary modes of formation for MCC. The first such mechanism was proposed by the pioneering work of GM Korea in 2014, which in fact represented the first explicit published mention of MCC.

GM Korea argued that the exposure of DPF channels to high enough levels of humidity—followed by rapid application of high load and thus sharp impulse of exhaust flow into the DPF—provides the conditions under which several large flakes of PM are prone to detaching from the filter wall and subsequently agglomerating either in the mid-channel region or downstream towards the end plug. The second mechanism was described in 2013 by MIT's Sappok et al., who supposed that for sufficiently thick soot layers, underlying PM strata coupled with increased exposure to shear stresses from the incoming exhaust flow yield instabilities in the shrinking—and subsequently outward peeling—soot layers, causing them to detach via the influence of exhaust flow, transport downstream in the exhaust flow, and reattach to the filter wall downstream of the location of detachment. Finally, the third causal phenomenon for the onset of MCC was suggested by Kamp and Bagi, who describe the irreversible bonding of high-density ash anchors to the filter substrate wall via sintering, and growth upon those anchors of additional ash also via sintering, ultimately forming bridges of ash that grow to span the channels until they are full plugged.

Note that Hypothesis #1 involves the collapse of the soot cake layer, Hypothesis #2 involves the collapse of the combined soot plus ash layer to block the channel quickly, and Hypothesis #3 involves the slow growth upon ash anchors into a larger mass of ash that blocks the channel.

It turns out that while DPFs have been in use since the 1980s, MCC is a phenomenon observed and studied only since the mid-2010s. It is unclear why MCC had not been publicly diagnosed in the interim period, though DPFs in the '80s and '90s were relatively unreliable, precluding their mass rollout until the mid-2000s and beyond. It is also feasible that operators would simply assume that afflicted DPFs are defective and require frequent cleaning, or perhaps replacement. The prevalence of MCC is still not well understood and should be further researched to help stakeholders better understand how widespread an issue MCC actually is within DPFs. MCC has been referred to as a "10% problem," which implies that it only because a notable issue in around 10% of vehicles that employ them, although this figure has not been verified and may significantly underrepresent the actual representation of MCC among DPF channels. Another credible account by researchers at MIT indicated that a major global manufacturer of DPFs in China where lubricant formulations are not well regulated requires the unexpected cleaning of the filter around 20 times over the course of the life of the device and corresponding vehicle. This frequency of cleaning, which involves physical removal of the DPF and complex treatment thereof by complex machinery, is well beyond that expected by operators of DPFs, suggesting that MCC is far widespread than a "10 percent problem would suggest" in some markets, and that changes in both lubricant formulation and fuel additive

package composition may drastically affect propensity for MCC to transpire. After all, additive packages are proprietary in nature and may vary substantially in chemistry—e.g., metals content—with some formulations thereby being more prone to sintering given metals with lower glass transition temperatures [76]. After all, different metals known to be incorporated into lubricants have sintering temperatures that vary from one another by hundreds of degrees Celsius.

A 2019 study by MIT researchers Kamp and Bagi, which described the phenomenon of MCC using the acronym MCD (for mid-channel deposits), indicated that almost every one of the field-returned (i.e. problematic and suffering from unacceptable backpressure and consequently excessive regeneration frequency) DPF specimens provided to the MIT consortium for which they researched over the past decade has exhibited at least some appreciable degree of MCC [22]. They noted that virtually all of the problematic DPFs exhibited atypical ash accumulation characterized by sizable gaps in the ash plug, significant interactions between ash and the filter substrate via sintering, and substantial variation in mechanical properties of the ash like highly variable density [22]. They further expressed that while every DPF experienced some degree of MCC, there was substantial variation in the percent of channels plugged across the collection of field samples ranging from as low as 10% to as high as 75% [75]. This suggests that not may MCC be a far more widespread issue than is generally believed, but also that the prevalence of MCC is highly variable across DPFs that may be exposed to similar operating conditions. Kamp and Bagi went on to state that MCC is a phenomenon of critical interest to the automotive (and catalysis in particular) industry, and that it is surprisingly sparingly addressed in the literature with underlying causal mechanisms still unknown [29].

2.1 Hypothesis #1: Elevated Humidity in the DPF Channels Followed by Rapid Application of High Load Causes Cake Layer Separation

MCC was first observed by a group at General Motors Korea in 2014, which hypothesized that the presence of humidity followed immediately by the application of high-load, high-pressure drive cycles causes soot layers to deform and collapse into the DPF channels. They claimed that under very specific conditions in which a vehicle is driven at a constant 100 kilometers per hour for a few hours, parked in cool ambient (~15 Celsius) temperatures with high humidity for a period of several hours such as overnight, and then driven immediately with heavy acceleration, one can observe the

sudden pressure increase associated with MMC after driving just a short distance. [77]. Kim et al. posited that a notable gaseous gap forms between the soot layer and the filter wall substrate beneath it due to passive regeneration of the soot adjacent to the catalyst, as shown in Figure 2-1.

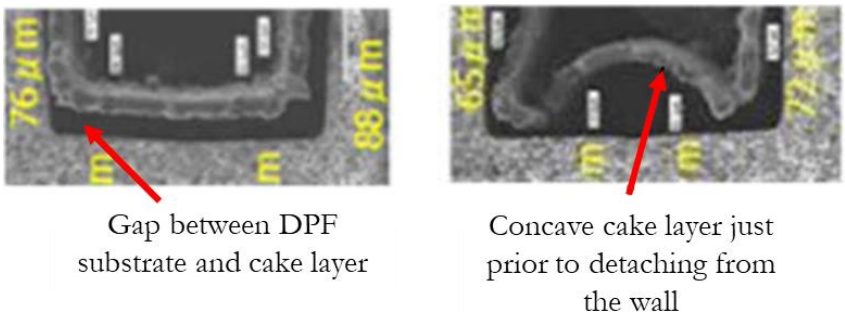

Figure 2-1: NO_x-induced gap formation before (left) and after (right) concave bulging, supposedly correlated with condensation of water onto/into the soot cake layer [19].

More specifically, the gap between the filter walls and soot (PM) layer is created by soot reacting with NO_2 that is generated when the platinum catalyst on the filter substrate washcoat oxidizes NO into NO_2 via [20]:

$$2NO + O_2 \rightarrow 2NO_2 \tag{2.1}$$

$$2NO_2 + C \rightarrow 2NO + CO_2 \tag{2.2}$$

It is supposed that the prevalence of a gap positively correlates with concentration of NO_x in the exhaust stream. In addition to a gap observed for coated (either uniformly or zonally) DPFs, the researchers observed the following contributors to the formation of MCC:

- Upon (overnight in their case) several hours of exposure by the soot in the DPF to high humidity conditions, they observed a significant concave bulge in the soot layer, which they believe is due to condensation of water onto/into the soot coupled with space constrains inherent in the fixed, rectangular DPF channel cross section design.
- The soot lump is thought to grow until it reaches a point of instability and collapses into the channel, causing several obstructions that accumulate and agglomerate into a solid plug.
- The presence of bulging was observed to be less frequent if a period of idling preceded the application of high load, perhaps due to the evaporation of water during idling that would otherwise result in the formation bulges.

Reviewing some of the images provided in [77], it seems that the expansion of humidity-induced bulges until they break away from the soot cake layer causes curved soot layer width and channel length flakes to agglomerate in the channels. Further, while it is argued that high humidity

conditions are required to accompany passive regeneration to form MCC, figure 21 in [77] shows that mid-channel plugs may form even in the absence of added water [77]. Additionally, figures 11 and 12 in Kim et al. show flatter, bulkier soot sheets bunching up in the channel, hinting that not all observed instances of MCC can be characterized by thin, curved soot flakes. Finally, the means of agglomeration and redeposition upstream of the end plug is not addressed. It is instead suggested that certain preventative measures can be taken in terms of modifying DPF hardware design and implementation, such as introducing newly sized and shaped channel structure and installing DPFs vertically—not horizontally—in order to promote a tendency for mid-channel deposits that separate from the cake layer to more readily fall into end plug and not plug the center axial region of the channels [77].

The actual mechanism(s) giving rise to PM layer detachment, the semicircular shapes exhibited by peeled PM flakes, and upstream PM flake agglomeration were not provided. For example, while Kim et al. seem to suggest that surface tension due to humidity may play a major role in the process they describe, the idea has not been verified and thus cannot be stated as fact. Additional research will be required to confirm the nuanced physics at play that give rise to forces contributing to the onset and propagation of MCC. This theme of presenting observations of physical phenomena correlated with some nontrivial degree of MCC, without explaining their fundamental causal factors, currently abounds across the relevant literature.

2.2 Hypothesis #2: Regeneration Causes Unstable Shrinkage of the Cake Layer into Soot-Ash Islands that Peel off the Cake Layer and Reenter the Exhaust Stream

Before MCC was formally observed and named, MIT published results from a comprehensive series of evaluations with optically-accessible DPF core samples showing the processes controlling the formation, transport, and interaction of the soot and ash deposits over a range of DPF regeneration conditions. Central to these findings was the conclusion that, with sufficient cake layer thickness at the beginning of regeneration, instabilities arise that cause sections of cake layer to fissure into separate islands, peel away from the channel wall and into the channel free stream until they detach from the wall altogether, become (re-)entrained in the incoming exhaust flow, and redeposit downstream either elsewhere on the channel wall or in the end plug region. Results indicate that there are strong interactions between soot and ash during regeneration, and in particular that regeneration of soot in a catalyzed DPF proceeds locally and concomitant to mobility

of the PM layer as it is oxidized. The nature of such mobility depends on the regeneration pathway at play [21]. More specifically, Sappok et al. described morphology dynamics that transpire during regeneration, which involved the detachment of partially oxidized soot layers with ash particles in tow. The report provided additional enlightening information on the constituent properties of PM that accumulates within DPFs, such as their observation that over 99% of particles by mass in untreated diesel exhaust consists of soot—or carbon sulfate—as well as other organic compounds, while the remaining 1% is ash [21].

The mechanism and nuanced dynamics at play during the PM cake layer collapse process was described in detail and represents a key hypothesis regarding how MCC transpires. It is supposed that, for a catalyzed filter, the soot layer nearest the catalyst (and thus farthest from the cake layer surface) oxidizes first, such that soot in the outermost strata of PM deposit layer are continuously moving both toward the filter wall and inward toward the center of the "island" patch to which it belongs, per Figure 2-2 below [21].

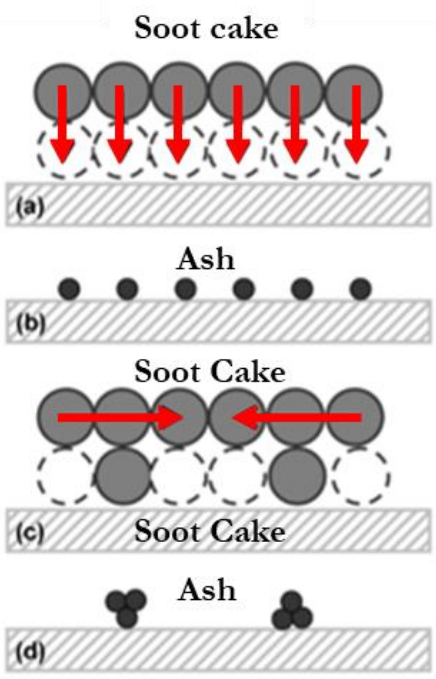

Figure 2-2: Classic (a) soot oxidation and (b) ash formation models, as well as observed (c) soot oxidation and (d) ash agglomeration phenomena [21].

Continuous motion and associated cracking of the PM deposit layer are thought to result in considerable instability along the channel walls. The cake layer islands are observed to curve away from the filter wall toward the center of the channel, thereby exposing peeling soot islands to increased exhaust flow velocities and a greater propensity to detach from their positions along the

filter wall. The peeling of partially-oxidized PM islands is illustrated in Figure 2-3, corresponding to Figure 6 from Sappok et al.

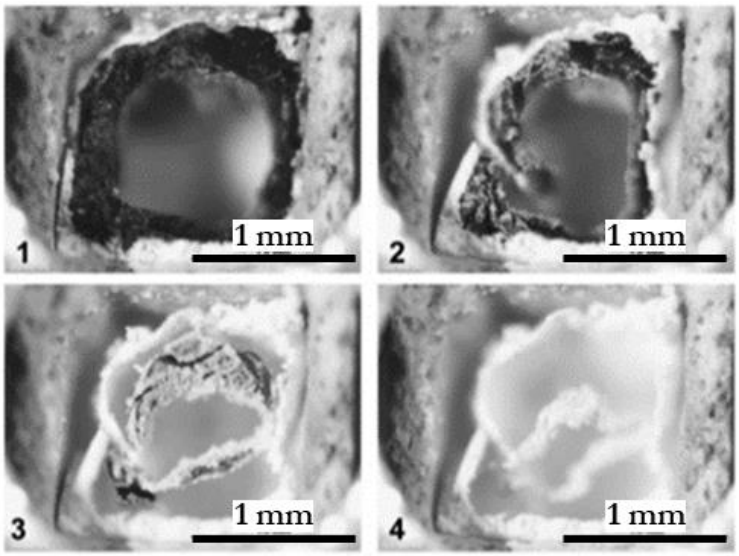

Figure 2-3: Images capturing the progression of soot cake layer oxidation in a DPF with no exhaust flow at 600 degrees Celsius, which is on the order of the exhaust temperature during regeneration. The introduction of exhaust flow would both promote detachment by serving as an axial forcing mechanism, but also provide a means of convective cooling that may slow the process of ash peeling, sintering, and agglomeration [21].

The oxidation of underlying soot is thought to loosen and shear the partially-oxidized soot cake layers and attached ash agglomerates relative to neighboring layers. Distinct islands form according to fault lines (or cracks) that result from the oxidation and shrinkage of soot into much smaller ash agglomerates during regeneration. As previously mentioned, the resulting PM layers curl into the channel and sometimes separate from the wall due to the (presumably frontal drag and/or shear) influence of the exhaust flow, becoming re-entrained into the exhaust flow and relocated downstream within the channel [21]. The curling islands consist of both partially or fully oxidized soot and attached ash particles to form thin, tubular flakes. Supposedly due to a combination of ash "stickiness" and shear stress of the incoming exhaust flow, these flakes are sometimes forced to detach from their underlying PM strata or filter substrate [21]. Several snapshot images depicting the progression of PM layer detachment, re-entrainment, and downstream transport are captured in Figure 2-4 below.

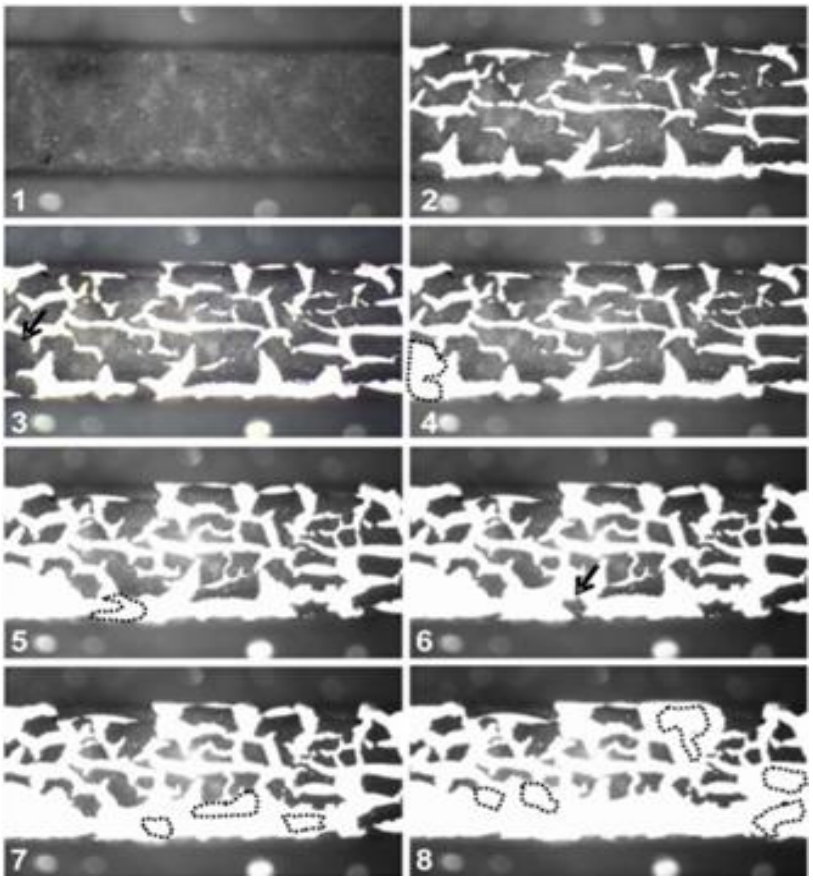

Figure 2-4: Images showing a sequential progression of regeneration at the soot cake and associated bulk transport of PM layers. Notice that dotted silhouettes indicate the entrainment and removal of PM sheets from the previous snapshot [21].

2.2.1 Impact of Soot Deposit Layer Thickness on PM Dynamics During Regeneration

Sappok et al. described the process of soot cake regeneration on a catalyzed DPF as an event dominated by local adhesion of soot and ash particles due to energy provided by oxidizing soot, which promotes agglomeration of ash and particle growth even when exposed to bulk gas temperatures considerably below the nominal ash sintering temperature. The transport of ash from the PM cake layer to the end plugs was found to be primarily a function of the soot cake layer thickness at the beginning of regeneration [21]. A thicker soot layer was both found to be less stable in terms of retaining PM on the cake layer due to nonuniform shrinkage rates in adjacent soot layer strata, and more prone to entrainment given its protrusion farther into the exhaust stream. Thicker soot layers also contain more ash precursors (assuming a uniform soot-to-ash volume ratio in the cake layer) and yield higher regeneration temperatures. Elevated temperatures in turn promote stronger adhesion of a greater number of neighboring ash particles, resulting in the formation of

larger ash agglomerates that both are more exposed to the exhaust flow prior to peeling off, and experience greater drag force when re-entrained, which increases the likelihood that larger ash agglomerates either interact with other larger agglomerates that have blocked the mid-channel region or instead become transported downstream onto the end plug [21].

Hitachi et al. supported Sappok et al.'s findings by also concluding that degree of loading prior to regeneration significantly impacts the nature of ash agglomeration and detachment from the filter sidewalls. Specifically, the experimentalists varied PM loading in three increments from 1.5 to 6.7 grams per liter at a PM regeneration temperature of 700 Celsius. While the 1.5 and 3.1 g/l regeneration cases yielded smaller, dispersed ash particles, 6.7 grams per liter loading saw PM burning in single clusters in which volume contracted during oxidation and resulted in larger ash agglomerates that were more prone to moving outside of their "confined area" [49]. That is, PM detaches more readily from the filter wall when it burns with greater loading between regenerations. Moreover, the ash agglomerates borne out of active regeneration were described as flaky, with higher permeability and a greater propensity for detaching from the cake layers, perhaps through viscous shear forces that force such flakes off the wall and into the exhaust stream. It is possible that the size and shape of the flakes increases their odds of being swept off the sidewalls, while increased porosity results in reduced resistance to income flow when such flakes themselves redeposit elsewhere on the wall and agglomerate to ultimately form instances of MCC. For example, a greater flake surface area per unit volume may expose the curling PM to heightened flow effects, including drag due to inertial forces due to larger frontal area, and/or heightened shear stress due to viscous effects in the direction of exhaust flow.

These findings thus suggest that MCC may be formed when higher regeneration temperatures couple with a larger availability of newly generated ash particles that bond to one another and form relatively large ash agglomerates that then relocate to part of the DPF at which agglomerate bonding (e.g., sintering) to the cake layer is more favorable. The experiments certainly do suggest that the temperature history of the DPF plays a critical role in determining the morphology of ash agglomerates that form during regeneration, and thereby also the nature of transport of those agglomerates within DPF channels. Thermal history of the DPF is revisited and strongly emphasized in Chapter 5 of this dissertation.

Incidentally, an MIT PhD dissertation written by Wang found that variations in the topology and surface profile of the cake layer—not the deposit layer thickness—has little influence on DPF performance. However, a 2020 publication indicates that ash plug ratio (ash cake mass divided by

total ash mass) is a parameter that can indeed be important to temperature history and DPF performance. Specifically, it was found that moving ash towards the end of the channel and thus increasing the percentage of ash in the end plug slightly decreases the pressure drop in the absence of soot, but increases the pressure drop in the presence of sufficient soot [17, 78]. Chapter 4 in this dissertation provides an extension to the conventional backpressure model for DPFs by accounting for the presence of mid-channel deposits that rapidly reduce the effective length of the channels in which they are located.

2.3 Hypothesis #3: High-Density Ash Particles Sinter to the DPF Wall and Form Irreversible Ash Anchors

A 2019 study by MIT's Kamp and Bagi (reference earlier) introduces the third and—at present—final major theory governing the formation of plugs characterizable as instances of MCC / MCD, which they suggest is an alternative "slower" phenomenon in contrast to the "fast" shearing of soot layers from the cake layer characterizing the previously described second hypothesis for MCC causality. They suggest that the adverse phenomenon is the result of high-density ash particles filling and irreversibly bonding to the filter deep bed pores, resulting in what the dubbed "ash anchors," one of which is shown in Figure 2-5 below. It is supposed that the irreversible bonding results from sintering, which suggests that high temperature effects are again critical to the formation of this mechanism of mid-channel ash agglomeration. The authors proclaimed that nearly all DPFs investigated in MIT's related consortium over the past decade that have contained instances of MCC have also exhibited the presence high-density ash anchors [22].

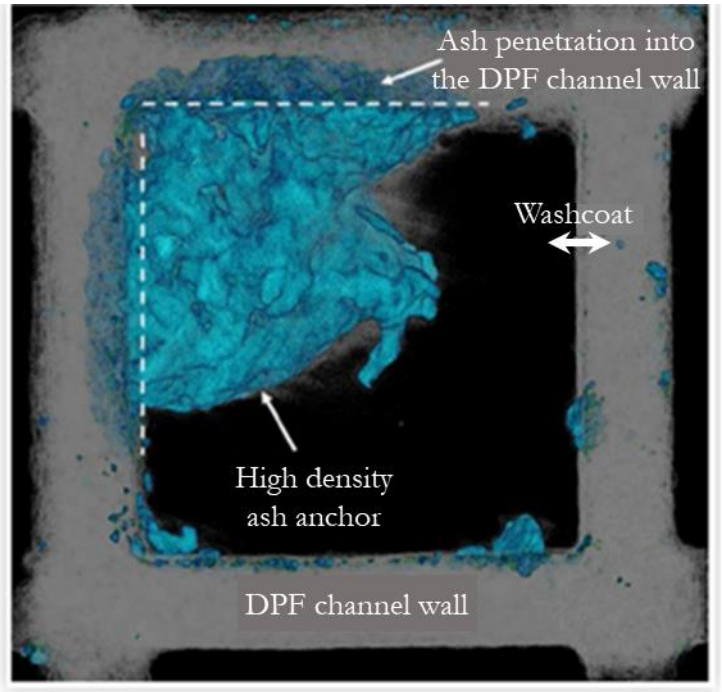

Figure 2-5: X-Ray CT image of a high-density ash anchor in the process of forming MCC / a MCD. The white dashed line represents the filter wall surface, suggesting that the ash anchor penetrates ~200 microns into the porous deep bed of the filter, effectively fixing the agglomerated ash anchor in place [22].

Ash progressively accumulates atop—and thermally bonds to—other ash layers, ultimately resulting in the formation of ash bridges that have been observed to sinter to the wall substrate at both ends and are therefore prohibitively difficult to clean and remove from the channels [22]. There does not seem to be a limit to how large the ash anchors grow, other than of course the geometric constrains imposed by the DPF channel width [22]. Additionally, abnormal agglomerations of soot upstream of a full or partial MCC formation—sometimes referred to by Kamp and Bagi as representing "extreme local soot accumulation"—is observed to produce an unusually high density of energy and thereby boost temperatures locally during regeneration, promoting strong local sintering.

Kamp and Bagi expressed that there are two complementary types of MCC: one faster mechanism associated with the collapse of PM flakes and redeposition onto the channel wall, as described in Hypothesis #2, as well as a second "slower" means characterized by bridging or spanning of ash agglomerates across a channel between fixed ash anchors [22]. A few examples of different forms of ash anchors and bridging are illustrated in Figure 2-6.

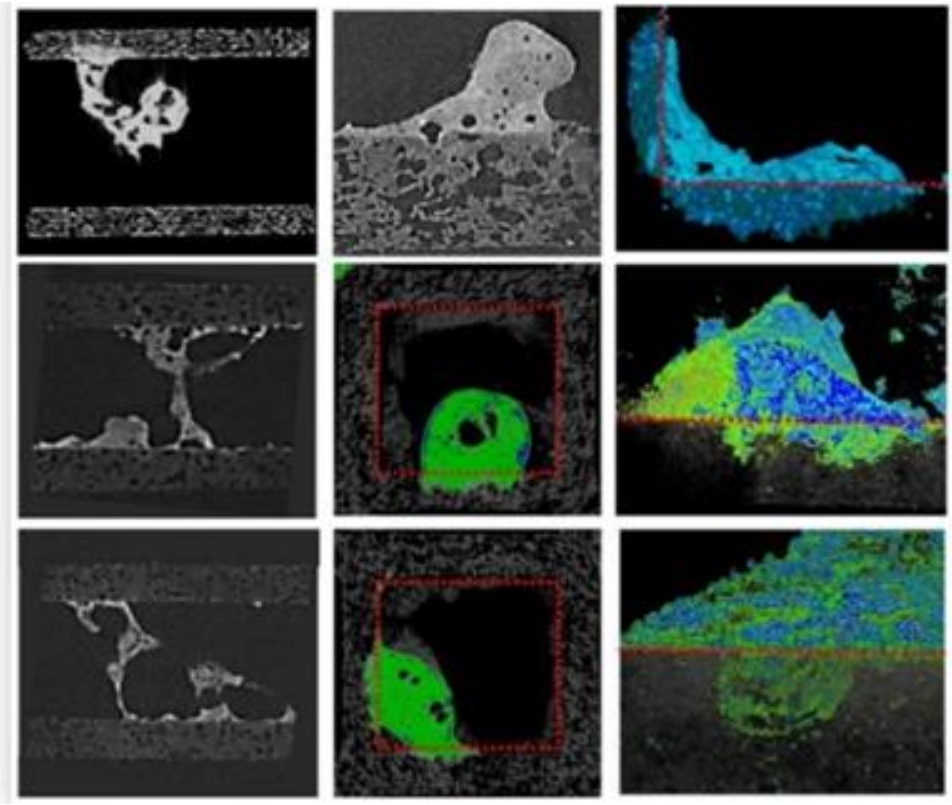

Figure 2-6: Several images taken by X-ray CT scan of "high-density ash anchors found within mid-channel ash deposits in problematic field-return DPFs." Dashed lines are provided to indicate substrate boundary [22].

Notice that not all anchors result in full channel plugging, and further that ash bridges take various forms, with an initial bridge consisting of connected ash strands with very thin widths on the order of a few layers separating upstream and downstream regions. Over time, bridges and MCC / MCD agglomerates grow in all directions. It is thought that the primary mechanism governing this "slow" means of MCC formation is highlighted above in Figure 2-2, such that shrinking and heating soot during regeneration bind ash together into sizeable agglomerates that "in some cases sinter and bridge to the washcoat" on the DPF substrate [22]. Such bridges are thought to grow upon the ash anchors shown in Figure 2-6, which illustrates that ash can penetrate deeply into the substrate wall (almost 200μm in this case) and has a higher density than even the substrate [22]. Such anchors are formed when, under certain conditions, the effects of DPF regeneration can lead to melting and wicking of ash into the DPF channel wall pores. Such "ash melt," upon forming strong bonds with the DPF deep bed substrate surface and/or neighboring ash particles, solidifies when temperatures decrease (i.e. when regeneration temperatures decline from their highest values to ~750-900 Celsius) [22].

It is important to note that the proposed mechanism of ash anchoring and bridging for MCC formation is complementary to other contributing phenomena, should they exist. It is therefore entirely feasible that MCC may occur simultaneously at different length and time scales: 1) a slow mechanism of ash sintering at the particle level, 2) a fast mechanism characterized by a relatively large soot/ash cake layer shearing off of the cake layer and redepositing elsewhere downstream, and 3) abnormal soot and ash accumulation upstream from the point of clogging [22]. Figure 2-7 shows each of these modes likely having contributed to the same instance of MCD / MCC.

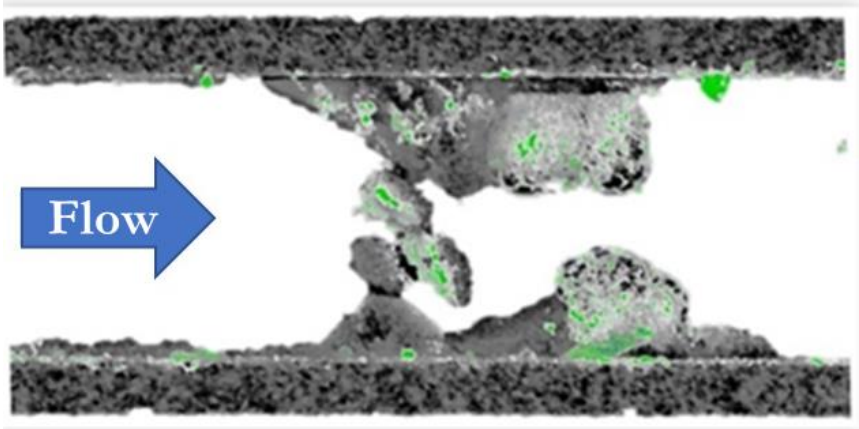

Figure 2-7: An X-Ray CT scan image showing the simultaneous presence of "fast," large agglomerates that have together sheared off the DPF cake layer during the regeneration process, smaller ash particle accumulation and sintering in the substrate walls and pores, and unexpected soot and ash accumulation upstream of instances of MCC [22].

In addition to proposing the concept of fixed ash anchors that serve as effective nucleation points for MCC development, Kamp et al. shed light on useful mechanical properties—such as chemical composition and density—of the ash precursors that ultimately combine to form full channel plugs and thus MCC.

2.3.1 Variable Material Properties around Ash Anchors

Kamp and Bagi assert that ash "sintering appears to be one of the fundamental characteristics of the mid-channel deposit phenomenon," which supports the fundamental hypothesis supported in this thesis: that high regeneration temperatures cause sintering to fuse ash agglomerates to the DPF wall and other ash agglomerates, resulting in MCC, and therefore that the temperature history of the DPF needs to be controlled in order prevent the onset and propagation of MCC. This idea will be directly addressed in Chapter 5. Sintering is defined as "a high temperature process that is accompanied with compaction and densification of solid mass of material by application of temperature, with or without the presence of pressure" [22]. It was found that density of ash is

highly variable in the region of MCC. Values in mid-channel deposits are shown to range from 60% less than to 70% greater than the average density measured throughout a given filter, with average density values found to be in the range 0.11-0.54 g/cm^3, where sintered ash found in MCC plugs are observed to exceed 1 g/cm^3 [22]. Table 2-2 provides a non-exhaustive list of SAE papers from which ash density measurements have been extracted.

Table 2-2: Key ash properties from field-aged DPFs described in six different SAE papers [23].

SAE Paper	Packing Density (g/cm^3)	Theoretical Density (g/cm^3)	Porosity (%)	Permeability (m^2)
2001-01-1016[i]	0.4 - 1.0	-	-	2.8-7.4 × 10^{-14}
2001-01-0190	0.54	3.13	83	
2004-01-0948[ii]	0.4	2.5	85	~5 × 10^{-12}
2005-01-3716[i]	-	2.85	-	
2006-01-3257[i]	0.32 - 0.52	-	-	
2008-03-0331[iii]	0.45	-	-	

i. Permeability estimated by authors in [10]
ii. Permeability listed as 10-fold that of cordierite
iii. Associated study used fuel-borne catalyst for regeneration

Figure 2-8 is a histogram of 103 data points from the literature showing ash density distribution in DPF channels.

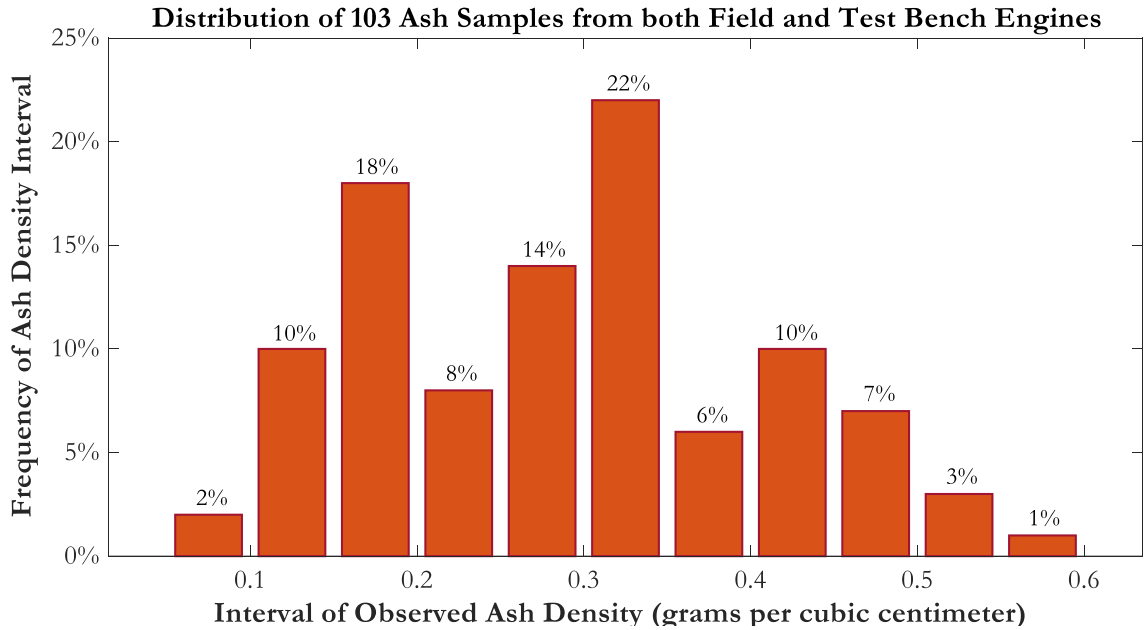

Figure 2-8: Ash density distribution from both field and accelerated engine testing across 103 data points. Mean = 0.29 g / cm^3; standard deviation = 0.11 g/cm^3 [17].

It was observed in many of MCC agglomerates that ash density is highest in the most upstream portion of the deposit, and monotonically decreases as one probes downstream. This variable density manifested itself in ash agglomerate morphology as ~1-micron densely packed primary particles upstream of MCC plugs and ~50-micron loosely packed, hollower particles downstream of instances of MCC [22]. Note that these values are considerably smaller than the larger 100- to 50-micron PM flake size characteristic of the "fast mechanism" of MCD creation previously described [22]. Ash is thought to consist of 90% material originating in metallic species from the engine lubricant and 5% from wear and corrosion byproducts, the rest comprised of fuel, coolant, and other miscellaneous contaminants [22]. These proportions align with data published in another related study by MIT in 2020, which provided the data shown in Figure 2-19 below.

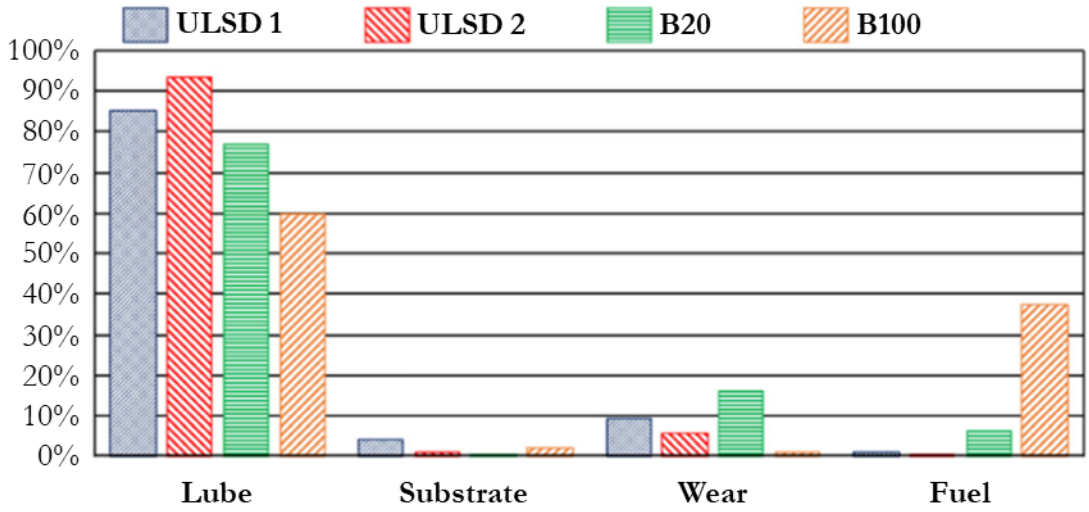

Figure 2-9: Relative distributions of sources of ash across two ultra-low sulfur diesel (ULSD) and two biodiesel fuels. Note that it is thought that the three primary mechanisms of oil consumption in an engine are droplet transport, evaporation, and blow-by [17].

2.3.2 Impact of Regeneration Type on Ash Agglomeration and Transport

Several experiments suggest that active regeneration and its corresponding higher regeneration temperatures provide conditions favorable for the development of particle-to-particle and particle-to-filter substrate sintering than does passive regeneration [21]. Additionally, as passive (or continuous) regeneration does not generally result in a substantial build-up of soot cake layer at any point, it appears that only active (or periodic) regeneration provides the unstable conditions for the cake layer that facilitate ash agglomerate growth via sintering, separation from the DPF wall surface, and subsequent reattachment to the cake wall downstream [21]. One thing to note, however, is that

passive regeneration is associated with the generation of smaller ash particles that are more prone to filling the substrate pores prior to bridging and sealing of the deep bed filtration region. More specifically, the characteristic ash particle size in passive regeneration is 10 to 100nm, whereas in the case of active regeneration, that figure jumps to over 1 micron [23].

In 2009, prior to the broad acknowledgement of MCC, Hitachi Metals Ltd. investigated the idea that ash exhibits variable morphological and transport characteristics within the DPF depending on the type of regeneration strategy applied, including regeneration type, frequency, and temperature history [49]. The researchers presented a figure that unambiguously showed mid-channel deposits forming well upstream of the end plug in DPF channels, though surprisingly made no explicit mention of the significance of those anomalously upstream deposits. Importantly, however, they did state that there is a strong correlation between DPF temperature history and behavior of ash as it passes through the filter, both in terms of ash mechanical properties and the propensity of the ash to relocate from one axial location in the DPF to another.

In one part of the study, Hitachi increased regeneration temperature from 400 to 600 Celsius in 50-degree increments and observed that ash particle size increases as temperature increases, which prompted the researchers to continue their foray into determining the impact of elevated regeneration temperatures on ash morphology and transport [49]. As temperatures were increased to 630 Celsius, it was shown that this finding held, and further it was found that even with smaller ash particles forming at elevated temperatures, repeated active regeneration yielded agglomerated particles that fix themselves to one another [49]. This hints at the notion that high temperature regeneration may cause larger ash agglomerates to sinter or otherwise bond to ash that has been embedded in or otherwise anchored to the underlying filter wall substrate. It is also perhaps noteworthy that the researchers stated that some of the entrained ash passes through the entire DPF with the exhaust stream.

Having found a strong, positive correlation between ash agglomerate size and PM regeneration temperature, Hitachi explained that 400-500 degree Celsius passive regeneration generated weaker bonding between ash agglomerates and therefore yielded smaller ash agglomerate particles that were more prone to filling the deep bed pores of the DPF wall substrate, whereas higher temperatures yielded stronger intermolecular forces between ash particles [49]. It was noted that during active regeneration, PM forms large clusters that are more likely to be swept downstream with the exhaust gas flow, as indicated in Figure 2-10, which represents the conventional view of ash transport and morphology according to regeneration type [49]. In addition to the type of regeneration employed,

increased loading prior to regeneration was also shown to yield larger, more permeable ash agglomerates as the soot layer burns in one cluster, resulting in more ash in the end plug region. It was also interesting that the group referenced thermal melting and cracking that can occur within the DPF if regeneration occurs too infrequently, which serves as one form of compromise against the fuel economy penalty accompanying excessive regeneration frequency.

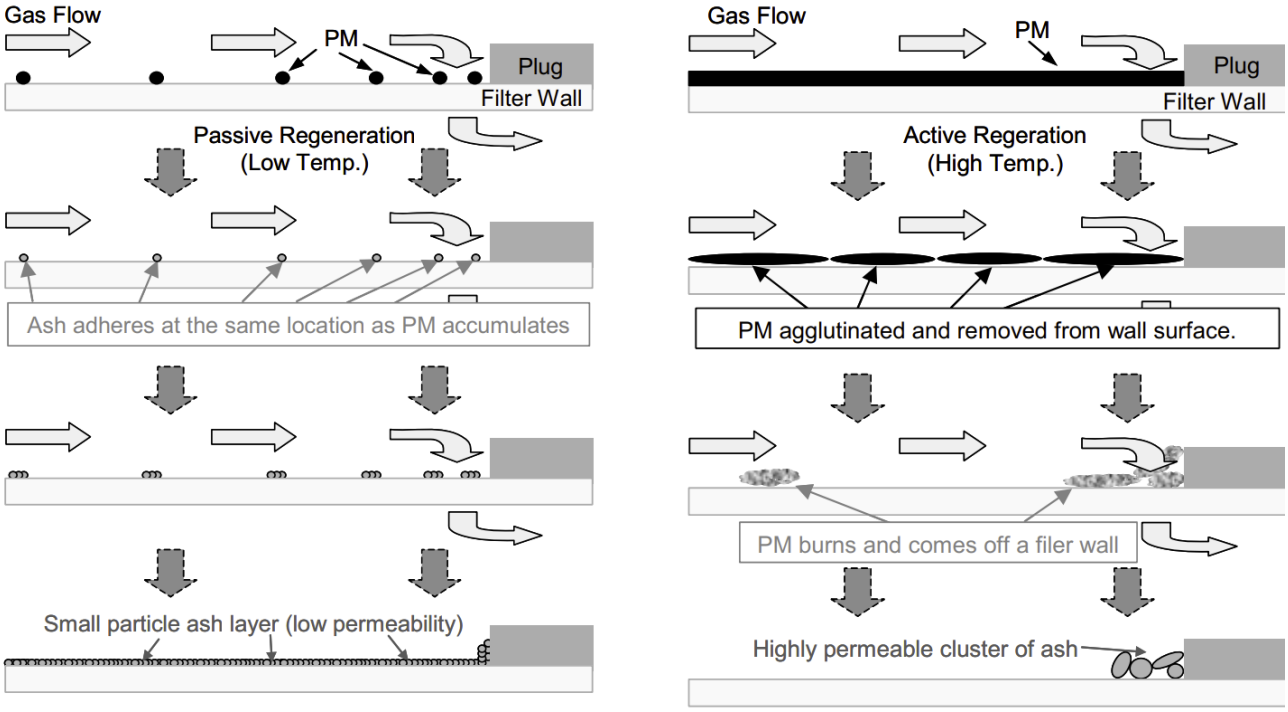

Figure 2-10: The conventional view of the mechanisms governing ash accumulation and transport in passively (left) versus actively (right) regenerated DPFs [23, 19].

On a related note, in 2019, MIT's Yuesen Wang et al. hypothesized as to the engine operating conditions and associated variables most likely to affect PM morphology, stability of deposits, and consequently also ash transport [19]. By varying soot-ash ratio and thus energy density of the PM deposit layer between regenerations for a given ash loading, one may discover a link between temperature history—primarily driven by the regeneration process—and key ash propreties. They conclude that as soot/ash ratio increases, more heating energy is available per unit volume, which promotes elevated regeneration temperatures and thus conditions more favorable for interparticle and particle-DPF sintering [19]. They show, in fact, that variable soot-ash ratio results in differing morphology of ash deposits, with lower soot/ash ratio yielding small particles that sprinkle the surface and fill smaller DPF wall pores, wheres higher soot/ash ratios exhibited larger clusters of ash deposits that reside next to the pores and are more prone to being swept downstream by the

oncoming exhaust stream [19]. These findings align with the aforementioned conventional understanding depicted above in Figure 2-10. It should be noted, however, that due to the experimental setup and a constant soot flow given a fixed engine load during testing, the proportionally higher run durations for higher soot/ash ratios and correspondingly greater volume of ash may have contributed to greater plug formation frequency and thus variable morphology as soot/ash ratio increased.

A more recent hallmark paper by Wang et al. directly relates two of the three causal mechanisms of MCC espoused in this chapter [17]. First, the probability of interparticle and particle-substrate sintering forming ash anchors is said to depend largely on the composition of ash. Second, the "fast" mechanism of PM collapse from the cake layer also results from mechanical properties of the cake layer because, specifically, the PM may have a coefficient of thermal expansion differing from that of the wall substrate material—as well as that of surrounding PM exposed to differing temperature history—leading to potential cracking/mechanical failure via thermal cycling with periodic, active regeneration [17]. That is, with sufficiently high temperatures, fissures form in the channel cake layers due to nonuniform thermal expansion of the DPF wall and strata within the cake layer, while the PM layer is simultaneously shrinking. This results in the formation of independent islands of oxidizing PM that peel off the cake layer, are subsequently re-entrained into the exhaust flow, and then deposited on the channel wall elsewhere downstream. Both channel (Figure 2-11) and pore-level (Figure 2-12) effects are illustrated below.

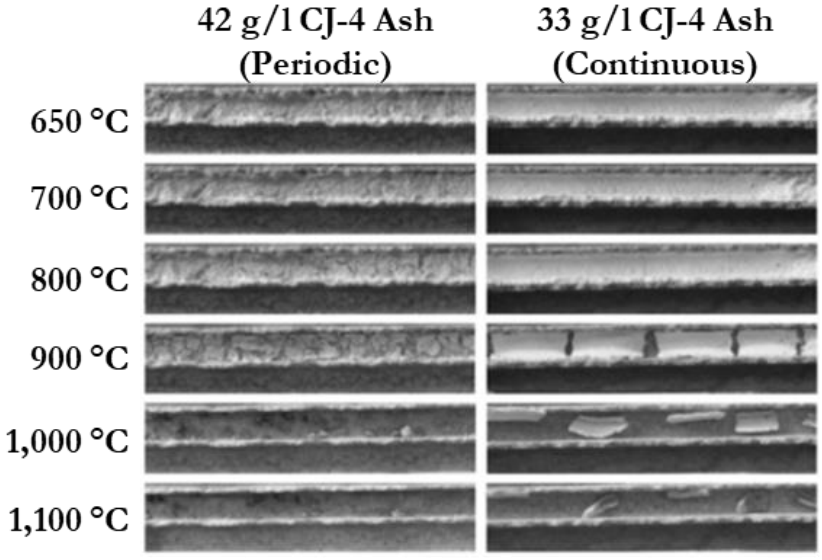

Figure 2-11: Optical microscope-rendered images showing the effects of elevated temperatures on channel ash accumulation and transport for both thicker periodic and thinner continuous regeneration cases [17, 24].

Figure 2-11 shows that beyond about 900 degrees Celsius, the PM cake layer is observed to crack, peel, and collapse off the sidewalls for both periodic and continuous regeneration cases. This clearly suggests and strong correlation between elevated DPF temperature history during regeneration and propensity for MCC to occur.

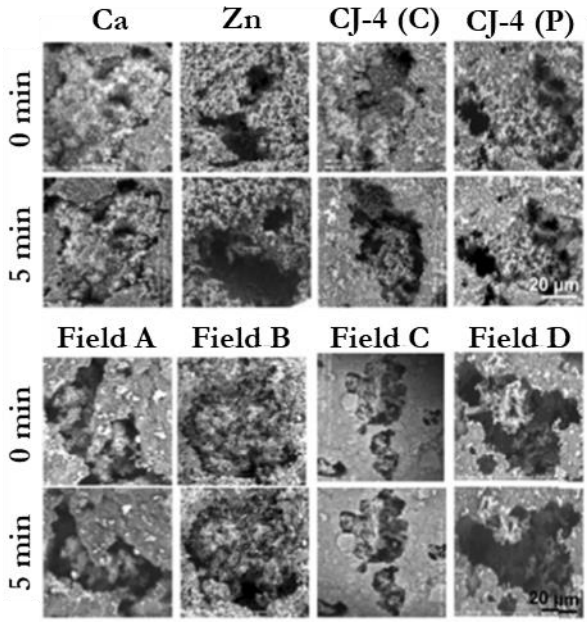

Figure 2-12: SEM showing the impact of 5 minutes of exposure to elevated (880 Celsius) temperatures on ash accumulation in DPF substrate pores [17, 24].

2.4 The Impact of Lubricant Additives on DPF Ash Morphology and Inter-Particle Fusion

Yujun Wang et al. expressed that reported ash composition varies substantially across engine platforms, fuel and lubricant formulations, duty cycles, etc., as reflected in Figure 2-12 [17, 48, 79]. Two mechanisms are described for ash particle interaction with soot agglomerates emitted from diesel engines: the first in which ash is embedded inside soot particles and the second characterized by ash nanoparticles affixed to the outside of soot particles, illustrated in Figure 2-13 [17, 80].

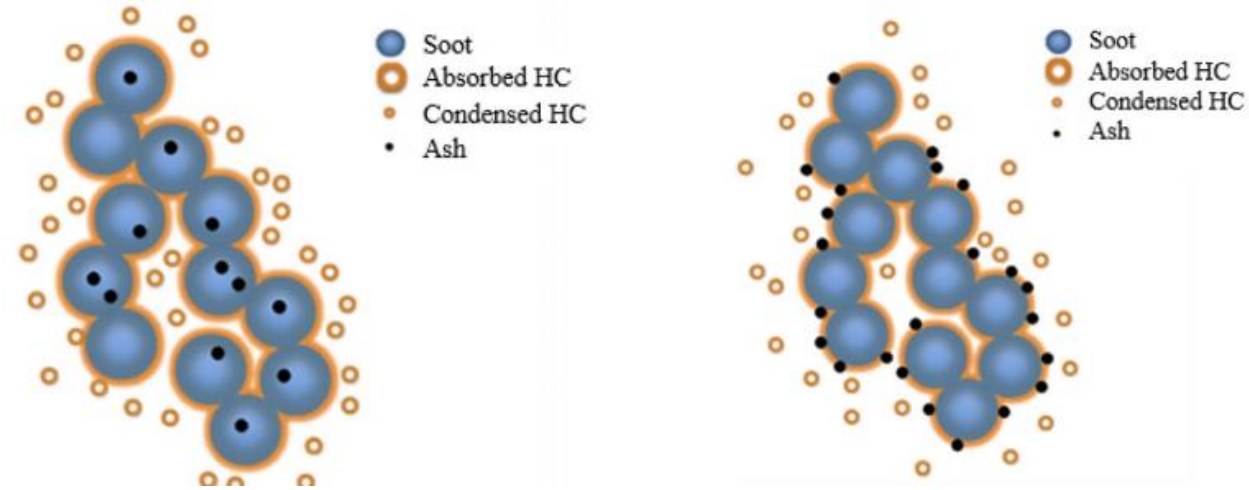

Figure 2-13: Two plausible modes of interaction between diesel exhaust soot particles and ash "nanoparticle" precursors: ash embedded into the soot particles (left) and ash nanoparticles attached to the exterior of soot (right) [17].

Generally speaking, lubricant-derived ash compounds do not exist physically separate from carbonaceous PM, suggesting that fusion among lubricant additives / ash occurs in very close proximity to the high-temperature oxidizing soot in which they are suspended, as depicted in Figure 2-2. Regarding fusion, Sappok et al. state that, because individual ash and soot particle sizes (on the order of 10 to 100nm, respectively) are much smaller than the ~1 micron characteristic ash particle sizes measured post-regeneration, ash compounds—that are at first finely distributed on the DPF wall and cake layer—fuse together and agglomerate when deposited on the cake layer [23]. Degree of fusion, according to the researchers, depends on the thermal history of the particulate matter. Figure 2-14 illustrates that density of ash can grow by ~100% with an increase in temperature from 700 C to 1100 C, which Chapter 5 will demonstrate is thought to take place locally due to variation in axial wall temperatures at a given time. The large rise in density corresponds to a shrinking of the ash, with shrinkage observed to exceed 60% as—again—temperatures increase from 750 C to 1,100 C [23].

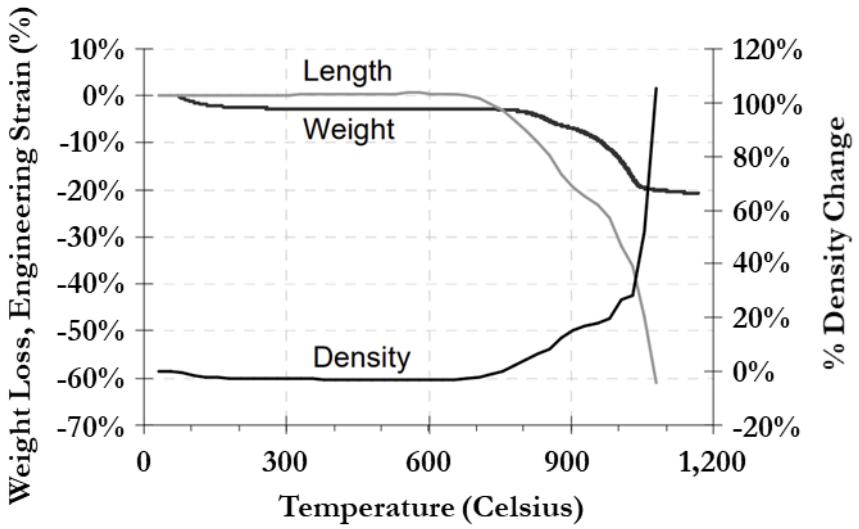

Figure 2-14: Increase in density and reduction in size of ash as a function of temperature [23].

Notable sintering begins to occur at 800 to 900 Celsius, with ash morphology changing rapidly above this temperature as "particles sinter and fuse together," as shown in Figure 2-15 [23]. This temperature threshold coincides with that for cake layer separated as depicted in Figure 2-11.

Figure 2-15: The morphology of ash samples shown at various ambient temperatures, from 25 to 1,150 Celsius. It is plainly evidence that ash sinters and shrinks into high-density agglomerates as temperature rises [23].

Ash compositional changes as a function of temperature are illustrated Figure 2-16. Note that Zinc composition changes markedly at around 800, whereas Celsius, Magnesium, Sulfur, and Phosphorus are notably altered between 850 and 1,000 Celsius [23].

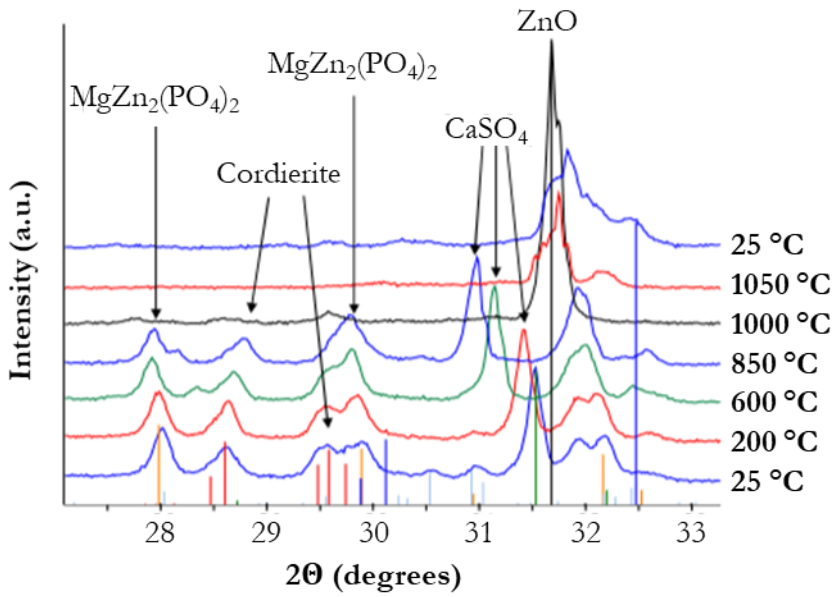

Figure 2-16: Changes in ash constituent composition (measured via X-ray powder diffraction) as a function of temperature. Major changes in mechanical properties occur between 800 and 1,000 Celsius. Note the redundant chemical compounds and 25-degree Celsius labels [23].

Wang et al. concurred with the above analysis by indicating that sintering of ash takes place beginning around 800 degrees Celsius while oxide species begin to appear around 900 °C. Further, it was found that significant ash densification was observed in the 700–880 °C range, where the extent of such volume reductions was dependent on ash chemistry and prevailing operating conditions, including flow rate, and whether regeneration was passive or active [17, 24]. Figure 2-17 provides another illustration of how ash morphology radically changes as temperature rises from 650 to 1,000 degrees Celsius.

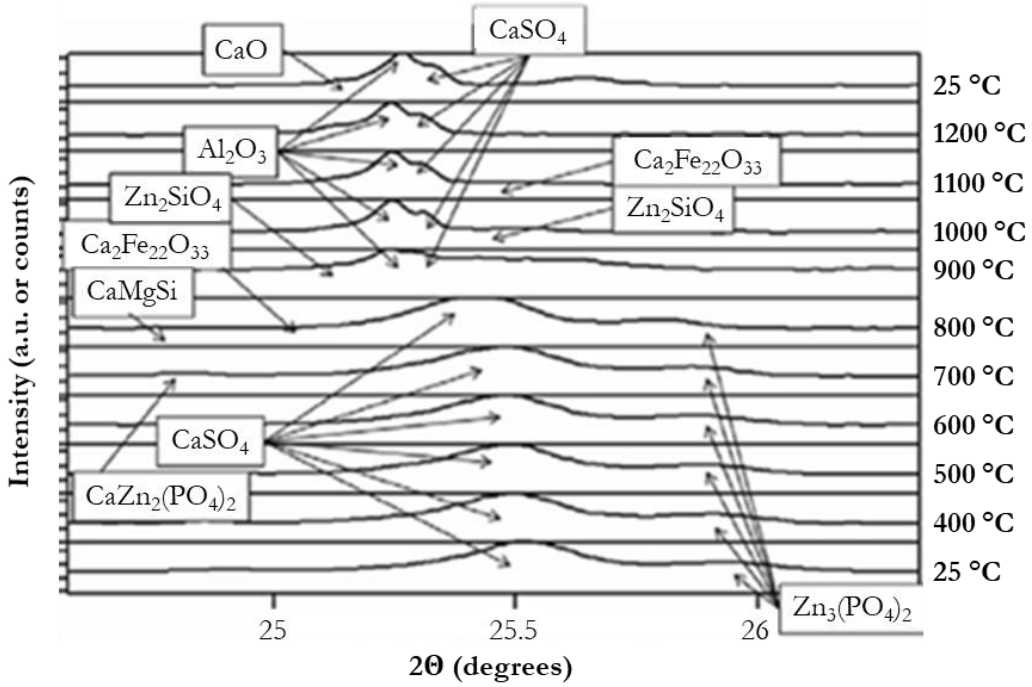

Figure 2-17: XRD scans illustrating how the chemical composition and morphology of lubricant-derived ash evolves as a function of surrounding gas temperature [17].

Zooming into ash via both transmission electron (TEM) and scanning electron microscope (SEM) technology, we may clearly observe the shrinkage and densification of ash at elevated temperatures, per Figure 2-18.

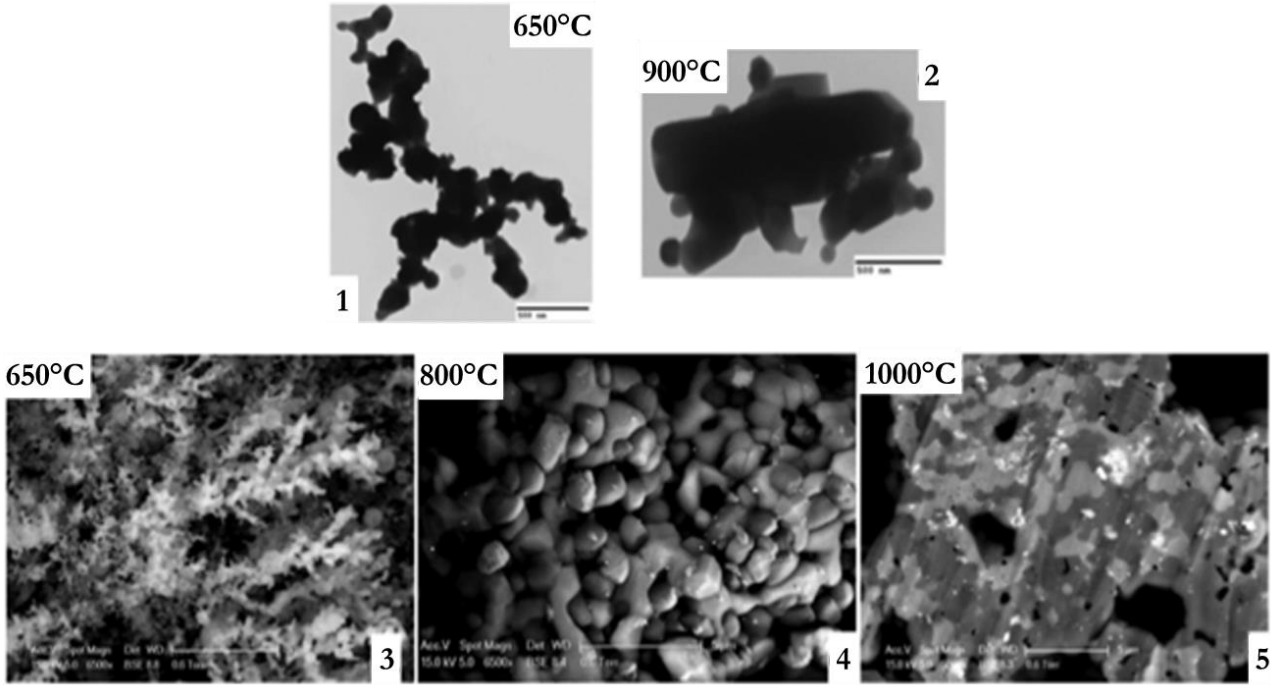

Figure 2-18: TEM and SEM scans illustrating how the chemical composition and morphology of lubricant-derived ash evolves as a function of surrounding gas temperature [17].

The lower bound for sintering of around 800 Celsius is based on the sintering temperature of Zinc, which is prevalent in lubricant additive packages (for example, as an anti-wear agent in the popular use of ZDDP). In an interesting concluding twist for this chapter, it was mentioned that for small particles, the effective melting temperature actually decreases, and can be several hundred degrees Celsius below the bulk melting temperature, as shown in Figure 2-18 [25].

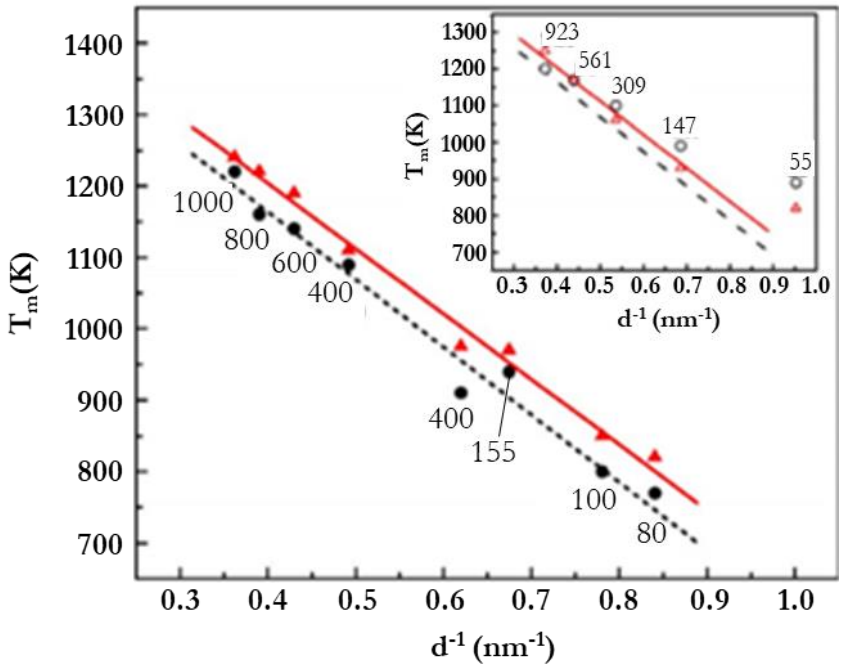

Figure 2-19: Molecular dynamics-modeled melting temperature iron nanoparticles across a range of sizes: 80 to 1000 atoms versus the inverse of particle diameter, for both free (circles) and supported (triangles) "non-magic-sizes." Both are "compared with the linear fit lines of non-magic-sizes." Note that magic sizes are given in the inset (smaller) plot at the top right corner of the figure [25].

Tying these ideas directly to the modeling presented in Chapter 5, the MIT researchers conclude that long durations of high temperature events "may cause ash and substrate sintering," as well as melting of ash adjacent to the catalyst. The locations of ash sintering could serve as ideal points for high-density ash anchors to form and subsequently serve as the basis for extensive ash bridging across the channel [17].

While this chapter has presented three compelling hypotheses regarding causality of MCC, none of the theories unfortunately describe in-depth or prove the fundamental physical mechanisms at play that give rise to the three phenomena described. The most convincing argument currently supposes that temperature history is of critical importance, and that controlling it may prevent the sintering which gives rise to irreversible ash anchors and bridges, expounded in Chapter 5. More detailed experimentation—that actually observes MCC formation in-situ and tracks sufficient

parameters and properties to definitely determine what operating conditions and material combinations are likely to promote the onset of MCC—is required.

3 Analyzing X-Ray CT Scan Images of Congested DPF Channels

This chapter describes an experimental procedure used to trap soot and ash in a cordierite DPF, in which analysis was conducted of several images showing MCC in the DPF's channels taken by an X-Ray CT scanner. Thousands of raw images were taken; subsets thereof were used depending on the number required for a particular set of analyses. Each scan provides a two-dimensional cross section of the filter, showing either the full axial "side" length of a channel at a given $\hat{z}$ value or a "front" cross-sectional view of every channel cell taken at some axial position $\hat{x}$ (reference frame illustrated in Figure 3-6 below). Characterizing these images enables us to more accurately describe the nature of prematurely clogged mid-channel deposits, examples of which are shown in Figure 3-1.

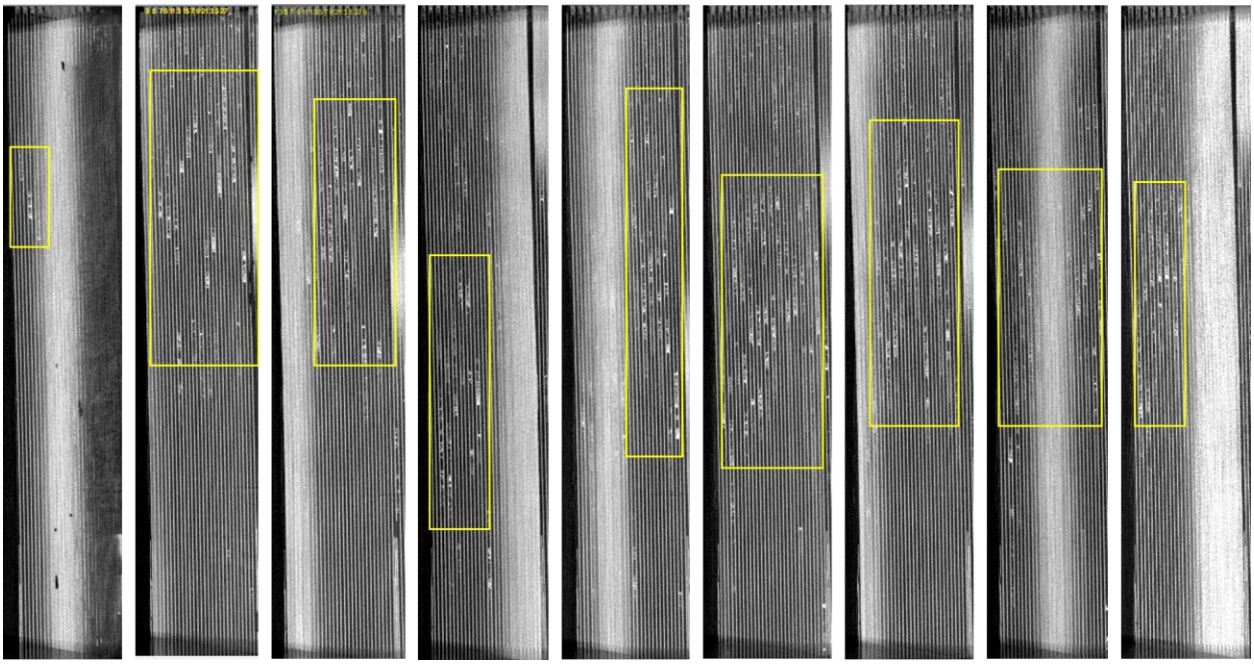

Figure 3-1: Nine DPF axial ("side") cross-sections used in analyzing the location, frequency, length, density, and spatial consistency of mid-channel deposits in a DPF after a given engine test cycle has been completed (e.g., a given soot-ash ratio applied until a threshold ash loading is achieved). The top of these images is the outlet, or downstream, region end, which is evident due to the presence of clearly discernible end plugs.

New terminology and metrics for describing MCC are proposed, and statistical testing is conducted to assess the consistency of ash distribution both axially and radially within the DPF. This is in part due to fact that gradients exist for both temperature and velocity profiles within the DPF.

3.1 Experimental Setup and Key Testing Parameters

The experimental setup included a single-cylinder diesel engine coupled with an accelerated ash loading system (e.g., commercial burner and combustion chamber). The overall system apparatus used to generate ash and soot in the quantities and conditions desired—and then filter diesel engine exhaust—is depicted in Figure 3-2. The diesel engine, whose specifications are provided in Table 3-1, was used to produce PM, some ~99% of which is soot [19].

Table 3-1: Key specifications of the diesel engine used in our series of experiments.

Parameter	Description
Model type	KD15-440
Cylinder type	Single cylinder
Bore x Stroke/mm	86 × 76
Fuel Injection/CA°	15±1° at 240 bar
PM emission/ (g/kWh)	0.6
Operating speed/rpm	3600
Rated Power/ kW	4.7 (at 3600 rpm)

A separate oil burner was used to generate ash so that a desired soot-to-ash ratio could be achieved in the bulk exhaust flow prior to entering the aftertreatment system components, by which point the flows from the engine and ash loading system had been well mixed [19]. The SAE 15W-40 CJ-4 oil was injected as a spray mist directly into the ultra-low sulfur diesel flame to yield metallic ash particles entrained in the exhaust flow nominally at 40,000 hr^{-1} space velocity and 350 degrees Celsius, which was increased to 550 Celsius during regeneration. The aftertreatment system consisted of a cooling bypass valve for regulating temperature, the diesel oxide catalyst device for converting carbon monoxide and hydrocarbons to carbon dioxide and water, the DPF just before a "sucker" vacuum pump used to drive the airflow through the system, and a parallel circuit around the DPF used to sample the constituents of the exhaust that enters the DPF.

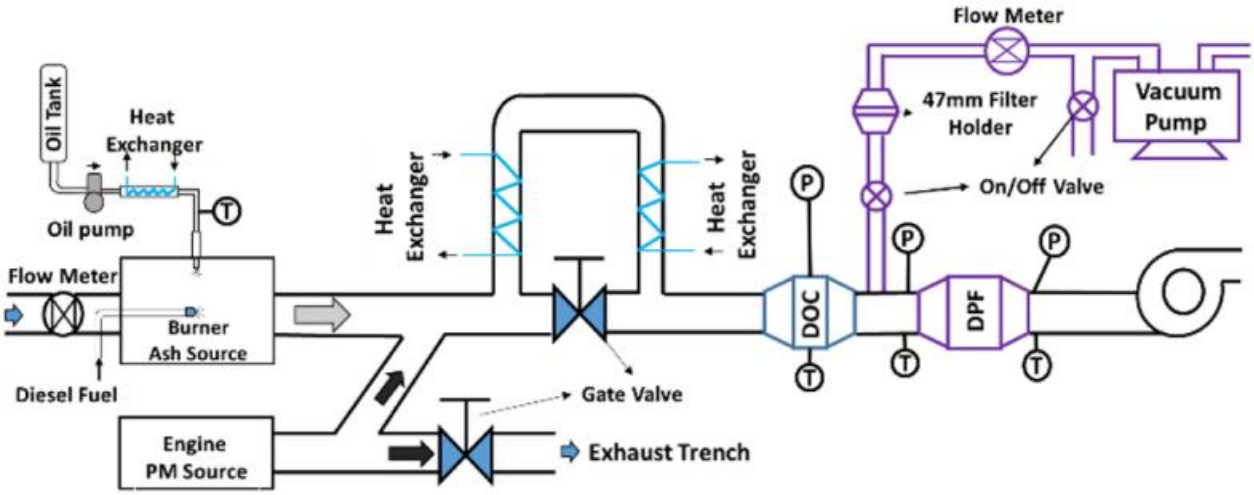

Figure 3-2: The experimental setup used to generate ash/soot that enters a DPF, described above.

A real view of the DPF holder and associated measurement probes is shown in Figure 3-3. While the probe numbers do not perfectly align with those shown in Figure 3-2 (e.g. only three of the four thermocouples are visible), the setup is reflective of the schematic and provides good visual reference regarding the assembly in which the DPF is placed during system operation.

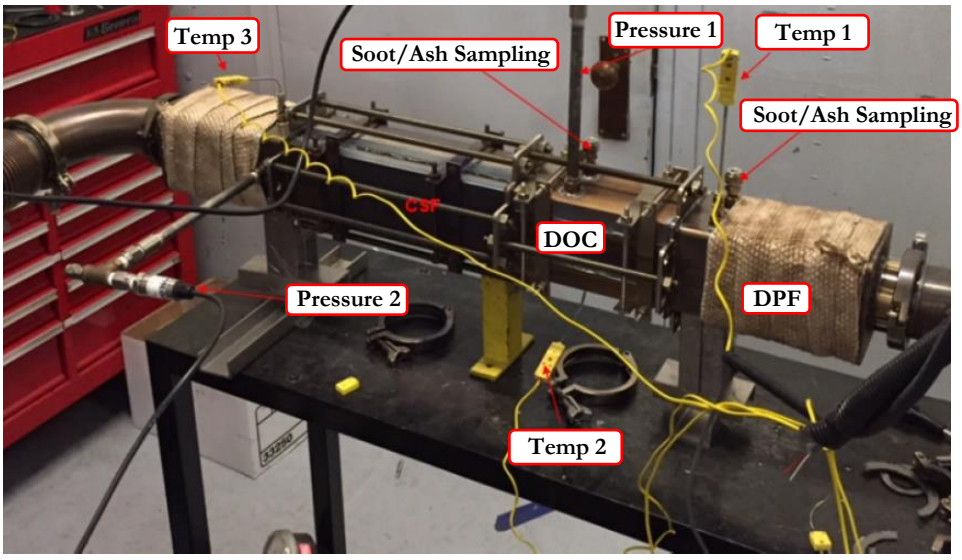

Figure 3-3: The assembly containing the DPF—and surrounding probes—used during testing. Pressure and temperature probes are used to measure corresponding flow properties before and after each major component in the aftertreatment system. One major drawback of this particular setup is the lack of ability to probe temperature within the DPF at different locations.

Temperature and pressure upstream and downstream of components were continuously monitored, and loading was calculated periodically after regeneration until desired degree of ash loading (e.g. 10 grams per liter) was achieved, after which the system was turned off and DPF

removed from its holder, transported a few miles down the road to Harvard University's materials science research facilities, and imaged using an X-Ray CT scanner. Thereafter, image analysis could commence. Regeneration exhaust temperature, flow rate, and regeneration duration were kept constant during a given test condition. Figure 3-4 provides the backpressure readings taken periodically across soot-ash ratios, after regenerations had been completed. Note that the maximum ash loading achieved was just shy of 8 grams per liter, corresponding to around 30,000 miles of vehicle operation.

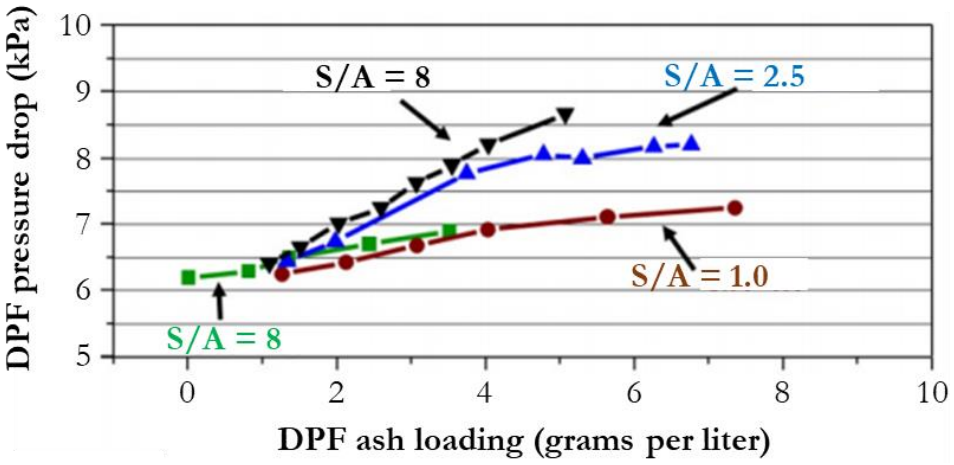

Figure 3-4: DPF Backpressure results taken across soot-ash ratios from 0.25 to 8.0.

This process was repeated for each new test iteration corresponding to a new operating point in the test matrix of metrics under investigation. Images under study all derived from a combination of four DPF blocks, each with outer dimensions of 1.65 inches wide × 1.65 inches tall × 12 inches long, illustrated in Figure 3-5 below.

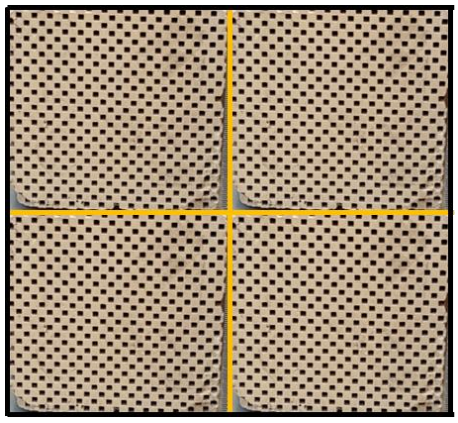

Figure 3-5: Four-block configuration of the DPF used in experimentation. Each block consists of 28-by-28 channels, half of which are inlet and the other half outlet, therefore exhibiting alternating plugging at the channel ends.

Note that this geometry differs from a standard cylindrical DPF. Key specifications are summarized in Table 3-2 below.

Table 3-2: Summary of specifications for the DPF used in our test bench apparatus.

DPF Parameter	Value
Model	Homemade
Length	12 inches
Cross-Section Dimensions	3.3-by-3.3 inches (square section)
Substrate Material	Cordierite
Cell Density	300 cells per square inch (CPSI)
Channel Wall Thickness	12 mil (0.3mm)
PM emission/ (g/kWh)	0.6

3.2 Introduction to DPF Image Analyis

Described in further detail later in this chapter, the DPF itself was analyzed by considering one of two different cross-sectional views: "front" and "side," corresponding respectively to the indicated $\hat{y} - \hat{z}$ and $\hat{y} - \hat{x}$ planes, as shown in Figure 3-6. The yellow borders in the figure were inserted for illustration purposes only. Note that only ash plugs were visible in these scans; soot was not, which significantly hampered our ability to determine whether MCC and other abnormal PM accumulation within the filter channels are mostly due to the effects of ash or soot.

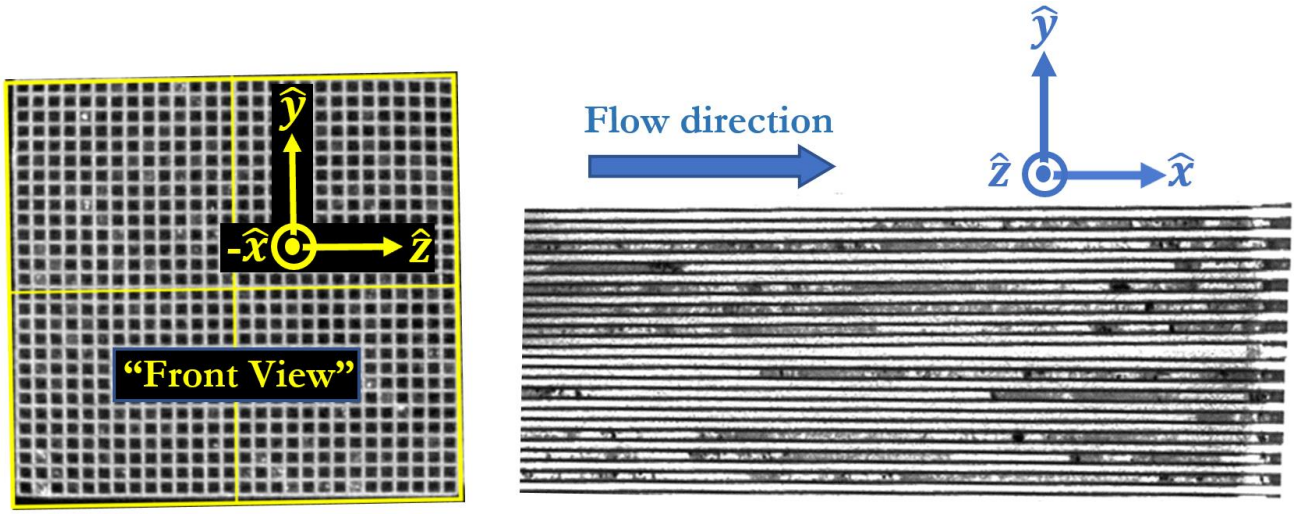

Figure 3-6: Sample image scans showing two different types of DPF cross-sections: the left represents a "front" view of the DPF, wheras the right is a "side" view showing one axial cross-sectional slice of the DPF channels. Either can be used independently to analyze the nature of ash agglomeration within the DPF; both were over the course of this study.

The left image shows a "front" cross section view for exhaust flow into the page, which provides us with a sense of radial ash / soot distribution at a given longitudinal axial position along the DPF. The right image instead provides us with a length-wise (i.e. side) perspective of the DPF, in which full channel lengths are visible and thus axial distribution of ash / soot is readily visible for a given cut.

By taking several such cross sections across the entire filter (from 0 to 1 in terms of nondimensional spatial coordinate), a full 3-D representation of the DPF can be generated. As a descriptive example, say for instance that we (statistically) requires 101 cross-sectional "front" images in order to complete our analysis. According to the conventions provided in Figure 3-6, 100 slices of equally spaced "front" cross sections would be taken from the inlet end of the DPF ($\hat{x} = \frac{x}{L} = 0$) to the outlet of the filter (at $\hat{x} = \frac{x}{L} = 1$), i.e. $\hat{y} - \hat{z}$ slices where $\hat{x} = 0, 0.01,\ 0.02\ \ldots 1.0$. The concept is depicted in Figure 3-7, which applies for a generic case in which N cross sections are taken to represent the full DPF.

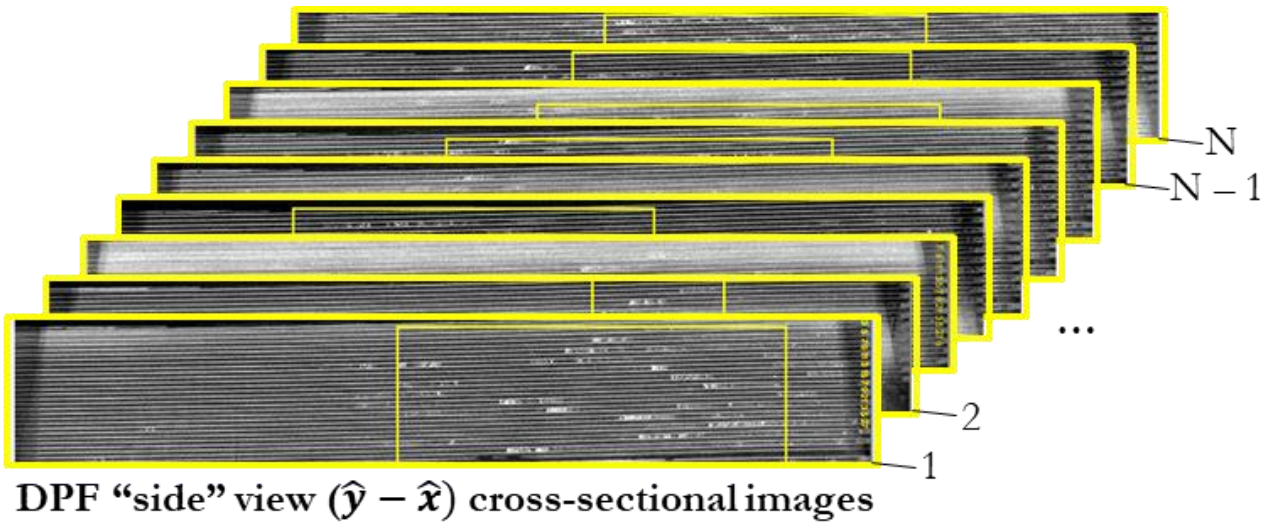

Figure 3-7: A series of N "side" view images evenly spaced in the $\hat{z}$-direction that are used to together represent the full DPF. While there are only 14 open channels in a given direction for the blocks used in our experimental setup, taking more than 14 cross sections allows us to obtain multiple snapshots per channel, accounting for intra-channel variation in PM deposit properties and accumulation intensity.

Note that for the "side" view, the DPF walls are ignored and the nondimensional $\hat{z}$ position only represents the distance traveled in the regions between the DPF channel walls. This of course prevents the use of cross sections showing just the DPF wall substrate.

Statistically sufficient quantities of images were compiled so that conclusions about prevalence and consistency of MCC formation could be drawn with statistical accuracy and significance. Key metrics used to determine degree of MCC plugging include: a) percentage of channels and cross-section plugged (i.e. plug fraction %), b) intensity of plugs within a given channel, and c) other measures of plugging prevalence and consistency within the DPF.

The front face cross section of the block, shown in Figure 3-8 shows the 28 × 28 channel configuration of one of the four blocks contained in the DPF we are analyzing. Given number of channels N and cell density σ, the expected outer dimension s of a square block is found by:

$$s = \sqrt{\frac{N}{\sigma}} \tag{3.1}$$

In our case, s is then approximately 1.62 inches in length. Figure 3-9 shows each length of the block front face to be around $1\frac{40}{64}$ =1.625 inches, which agrees with the theoretical prediction from the prescribed channel density. Figure 3-9 shows that the length of the DPF is 12 inches, as specified by the manufacturer.

Figure 3-8: A front-face view of the block under study, with a ruler for referencing size and scale.

Figure 3-9: A side-face view of the block under study, with a ruler for referencing size and scale. Note that the blocks were individually wrapped and carefully transported from the site of testing (MIT's Sloan Automotive Lab) to X-Ray CT scan facilities located a few miles down the road at Harvard University.

3.3 Test Matrix for Experimentation

The overarching goal of this research is to better understand the engine operating conditions under which premature clogging of the DPF is more likely to occur. Doing so will enable manufacturers to proactively design the system in a manner that effectively mitigates the onset of MCC in DPFs, thereby avoiding the associated increase in backpressure and reduced lifetime of the devices. Conditions that are hypothesized to give rise to premature clogging are encapsulated in a set of test metrics that are iterated in order to determine their impact on ash accumulation in the DPF. A test matrix showing proposed variation in key parameters is included in Table 3-3, and a sample schedule for iterating the different metrics in testing is given in Table 3-4.

Table 3-3: Parameters and corresponding values intended to be varied—one at a time—in order to assess each property's impact on the development of MCC in DPFs.

Parameter	Proposed Test Values
Soot-ash ratio	0.25, 1.0, 2.5, and 8.0
Filter materials	Cordierite and Silicon Carbide
Filter geometry	Symmetric and Asymmetric
Space velocity[1]	20,000, 40,000, and 60,000 hr^{-1}
Regeneration exhaust temperature	550 and 650 degrees Celsius

Table 3-4: Calendar of experimental activities to investigate the impact of several metrics on ash the behavior of ash accumulation in a DPF.

			Months				
		Month	6	7	8	9	10
Items	Experiment	1. Repeat Previous Test Conditions; Soot/Ash = 4:1(Sample2), 1:4(Sample3) and 1:1(Sample4)		-> -> ->			
		2. Try New Test Condition; Soot/Ash = 8:1(Sample5)			-> ->		
		3. Try New Filters (Asymmetric, Sic)			->	-> -> ->	-> ->
		4. Transfer the Experimental Result to Actual Engine Operation					-> ->
		5. Visualize the Mechanism of Mid-channel Ash Deposit (Flow Bench with CCD Camera)				-> -> ->	-> ->
		6. Try High SV, Pulse Flow to Move Wall Ash @ Flow Bench				-> -> ->	-> ->
		7 Find Solution to Avoid Mid-channel Ash Dep.				-> -> ->	-> ->
		8. Simulate the Mechanism of Mid-channel Ash Deposit via CFD					
	Analysis	9. Inspections (X-ray, ESEM, XRD…) of Previous Sample 1-4	-> -> ->				
		10. Inspections (X-ray, ESEM, XRD…) of Field Samples	-> -> ->	-> -> ->			
		11. Inspections (X-ray, ESEM, XRD…) of Repeated Sample 1-4			-> -> ->		
		12. Inspections (X-ray, ESEM, XRD…) of Sample 5				-> -> ->	
		13. Inspections (X-ray, ESEM, XRD…) of New Filters (Asymmetric, Sic)					-> ->

Experiments were run using the apparatus and test matrix described above. The first set of tests varied soot-ash ratio from 0.25 to 2.5, and subsequently analyzed the resulting image scans to identify patterns in ash/soot accumulation behavior. Notable differences across some test metrics

[1] Includes flow rom both the engine (producing soot) and burner (generating ash).

(such as frequency of channel plugging and spatial distribution of ash agglomerates) were observed. The results are, however, inconclusive since real-world soot-ash ratios are much larger on the order of 100-to-1, and test conditions were not necessarily directly comparable since proportionally more ash was introduced into the DPF with higher soot-to-ash ratios. Sweeping soot-ash ratios from 0.25 to 8 while maintaining constant operation of the engine (i.e. fixed soot output) not only required a correspondingly linear increase in runtime to achieve the same ash loading prior to regeneration, but also always fell well below the real-world soot : ash ≈ 100. The high proportion of ash to soot was applied in order to accentuate the effect of increasing quantity of ash.

After a given variable value is modified, X-ray CT scans were generated and analyzed to assess the corresponding metric's impact on ash accumulation (e.g., axial and radial distribution). This then yielded a set of analyses that help determine optimal values across the metrics for desired DPF performance, thereby informing a healthy compromise between backpressure and regeneration frequency for fuel economy, all while ensuring adequate filter device durability. Note that over the course of the research effort to date, only the parameters soot-ash ratio, space velocity, and temperature have been varied, and each parameter has produced inconclusive results.

3.4 Overall Process for Image Analysis

The steps involve in image analysis are as follows:

1. Select engine operating points and run the engine at conditions given by the correpsonding soot/ash ratio (e.g., soot-ash-ratio = 2.5), until a specified ash loading (e.g., 10 grams per liter) is achieved. Note that the soot flow rate was kept constant due to an unchanging engine operating point. Thus, for a higher soot-ash ratio, less ash is produced by the burner, which linearly proportionally increases the time it takes for the filter to reach a given ash loading.
2. Remove the DPF from its test apparatus encasing and transport it to an imaging center.
3. Conduct X-Ray CT scans until a desired number of cross sections have been imaged. Note that in this study, 3000 cross-sectional images were obtain in both axial and laterial directoins for every DPF imaged, and a subset was taken according to how many cross section images were statistically required for a given anaylsis.
4. Upload raw image files into software that allows for manipulation of images (e.g., changes in brightness, contrast, zoom), preferably that includes digital measurement functionality.

5. Optimize image contrast until a clear, visible continuum in shade exists to differentiate areas of dense agglomeration from regions of less plugging, with the maximim shade (of black or white) corresponding to the region of peak ash agglomerate density for a given DPF.
6. Segment images axially into thirds to enable labeling of plugs as upstream, mid-channel, or downstream. For "side" cross sections, number each channel in each cross section from 1 to 14. In the case of the "front" view ($\hat{y} - \hat{z}$) plane cross sections that show the full DPF grid pattern of 14-by-14 open channels, segment channels into equally-sized quadrants.
7. Convert image data to numeric values corresponding to metrics of interest, using built-in functions in software. This includes measuring and compiling the distribution and intensity of ash accumulation across all visibile locations and dimensions of the DPF, which may be accomplished by integrating the shade of a plug over its height and width, such that you are effectively solving the area integral:

$$Magnitude_{plugging} = \iint_A Intensity_{shade} \cdot dA \tag{3.2}$$

   Note that dA may also be expressed as $dx \cdot dy$, as one integrates the intensity of plug density first in one direction (e.g., radially across the channel width), and then in the normal direction (e.g., axially along the length of the channel for the "side" cross sections and vertically across the face of the DPF in the case of the "front" view).
8. Analyze the data and generate insightful results for metrics of interest.
9. Use statistical tools to calculate mean and standard deviation, including statistical similarity tests among data sets in order to assess consistency and significance of ash accumulation distributions.
10. Synthesize findings and generate useful characterizations of plugging behavior in the DPF across operating conditions, including % of channels plugged, distribution of plugs and their intensities axially and radially, distribution of plug lengths, etc.

This workflow is represented immediately below in Figure 3-9, where some items from the previous list have been combined into a single step.

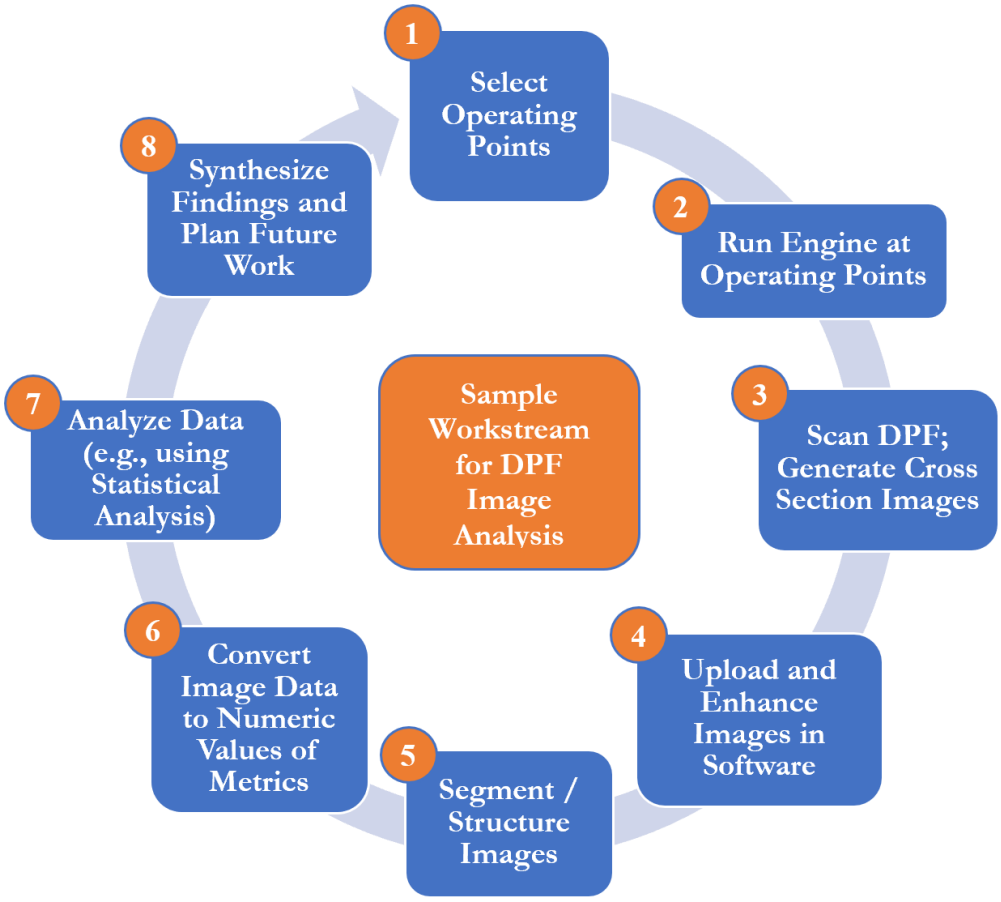

Figure 3-10: Cycle of work for conducting DPF image analysis.

Post-processing of scans was conducted by importing JPEG image files into Image-Pro Plus software, and then using the program's functions to enhance image quality until measurements can reasonably be made.

3.5 Ensuring Statistical Significance in Results

While a system was designed and implemented in order to collect data for analysis, it was important to determine how much data (i.e. how many cross-section images) needed to be collected and analyzed so that they are reasonably representative of the entire data set (i.e. full 3-dimensional volume of the DPF). Consequently, for a set of X readable images from a presumably infinite population of possible cross-sections across the DPF, we may apply probability theory in order attain 95% confidence that the sample set we analyze is representative of the entire PDF. From statistics, we find that *X* is given by the following equation, which assumes that we are dealing with measurement variables whose sample values are taken from a population of infinite size, where z-

score represents a constant corresponding to a certain level of precision (e.g. 95% or 99%), σ is the standard deviation of the data, and margin of error is set based on accuracy needs [81]:

$$X = \frac{(z - score)^2 \times \sigma^2}{(margin\ of\ error)^2} \tag{3.3}$$

We apply the standard 95%-confidence z-score of 1.96. We arbitrarily set the margin of error to ±10%, a rule of thumb common in engineering practice. However, for some metrics such as ash plug distribution, a more appropriate error margin can be applied. The standard deviation σ, however, is not known a priori and is thus estimated using the six-sigma rule for normal distributions: the standard deviation is approximately the range R of the data divided by six [81]. Considering the nature of the metrics of interest, which will be further described later in this report, enables us to calculate the number of samples needed to attain statistical significance in our results. The metrics include: variability in plugging observations, percent of channels prematurely plugged, and both radial and axial distribution of DPF plugging.

Variability testing is used to help verify that the sample we select is indeed representative of the population, and thus does not require extraordinary precision; a 10% margin of error can be retained. Hence, the total number of samples to address variability testing can be calculated as follows, where half the range $R/2$ is assumed to be the nominal mean (i.e. reference) value, for which 10% is the acceptable margin of error:

$$X = \frac{(z - score)^2 \times \sigma^2}{(margin\ of\ error)^2} = \frac{(1.96)^2 \times \left(\frac{R}{6}\right)^2}{\left[\left(\frac{1}{10}\right)\left(\frac{R}{2}\right)\right]^2} = (1.96)^2 \times \left(\frac{20}{6}\right)^2 = \mathbf{43\ required\ samples}$$

Since the percentage of channels represents an integer number divided by (in our case) 14 total channels that could be plugged, we would like to limit our margin of error to approximately 1 in 14, or 7.1%. Using the six-sigma rule, we have a range of 14 channels, which when divided by 6 yields 2.33 channels per standard deviation. Or, as a function of the range of channels R (where R = 14 in our case):

$$X = \frac{(z - score)^2 \times \sigma^2}{(margin\ of\ error)^2} = \frac{(1.96)^2 \times \left(\frac{R}{6}\right)^2}{\left(\frac{R}{14}\right)^2} = (1.96^2) \times \left(\frac{14}{6}\right)^2 = \mathbf{21\ required\ samples}$$

Radial distribution of plugging is analyzed to determine whether there is statistically significant asymmetry in plugging pattern within the DPF block. This is accomplished using t-testing for independent samples. Based on *A Power Primer* by Jacob Cohen, if we apply power statistical analysis for the t-test that assesses whether two independent means are statistically similar, while assuming 95% confidence ($\alpha = 0.05$) and a medium effect size of $d = 0.50$, then using the formula [82]:

$$n = \frac{16}{\left[\frac{\mu_0 - \mu_1}{\sigma}\right]} \tag{3.4}$$

we obtain a required **n = 64 number of samples for each group**.

Axial distribution of plugging is used to both approximate the degree of premature ash accumulation, as well as predict backpressure via the application of appropriate fluid mechanical theory. Hence, we may apply the equation to determine the number of samples from an infinite population, as before:

$$X = \frac{(z-score)^2 \times \sigma^2}{(margin\ of\ error)^2} = \frac{(1.96)^2 \times \left(\frac{R}{6}\right)^2}{\left[\left(\frac{1}{10}\right)\left(\frac{R}{2}\right)\right]^2} = (1.96)^2 \times \left(\frac{20}{6}\right)^2 = \mathbf{43\ required\ samples}$$

Note, however, that these results are borrowed from widely accepted statistical theory that is premised on the notion that data is normally distributed. While the intensity of axial distribution of ash in the channels likely resembles an exponential distribution, we assume for our purposes that a comparison across axial (e.g. exponential) distributions will result in the analysis of a normally distributed data set. Hence the standard t-test with $\alpha = 0.05$ and a specified margin of error (e.g., 10%) applies.

Reviewing these results, we find that the largest number of required samples is from the test to compare the means of two independent, normally distributed data sets. Hence, we conclude that we should take at least **64 images** (from the full set of 3,000 in each direction) for each operating condition to be used as a basis for comparison. In this report, results reflect data sets in which at least 64 image files are analyzed. Specifically, 66 cross-sectional scans were used in "front" view analysis, and between 74 and 80 images were used for "side" view images. For the latter, 70 images were initially extracted to represent an even multiple of the 14 open channels. However, due to a

significant quantity of unreadable image data resulting in "N" scores, additional data points—between 74 and 80—were instead used.

3.6 Data Set: Image Files

It was decided that a either a white or black backdrop with respectively darkened or brightened sections used to represent ash accumulation would be the most appropriate means of visual illustration given the contrast that could be derived from the approach. When an image was loaded into the program, it was manifested as a dark background without discernable channel walls and only slightly contrasting of the filled sections (e.g., ash plugs and channel walls). This is represented in the left image of Figure 3-11. Using the "Enhance → Equalize → Best Fit" function in Image-Pro Plus resulted in a transformation to the right image of Figure 3-10. Channels are clearly visible by contrasting with the backdrop, as are instances of ash accumulation.

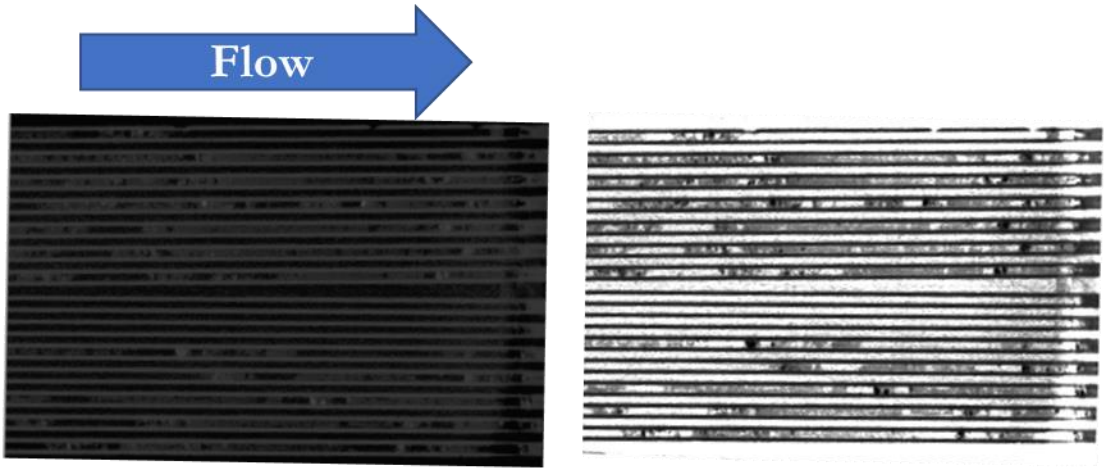

Figure 3-11: Raw image JPG file (left) enhanced by adjusting and inverting contrast (right).

This new representation scales accumulation density between pure white (no ash) to completely black (highest density, full plugging), which conveniently enables us to generate a map—for each cross section—of coordinate values that contain both location and relative intensity of accumulation. The same concept is illustrated in Figure 3-12, instead with a black backdrop and white ash agglomerates.

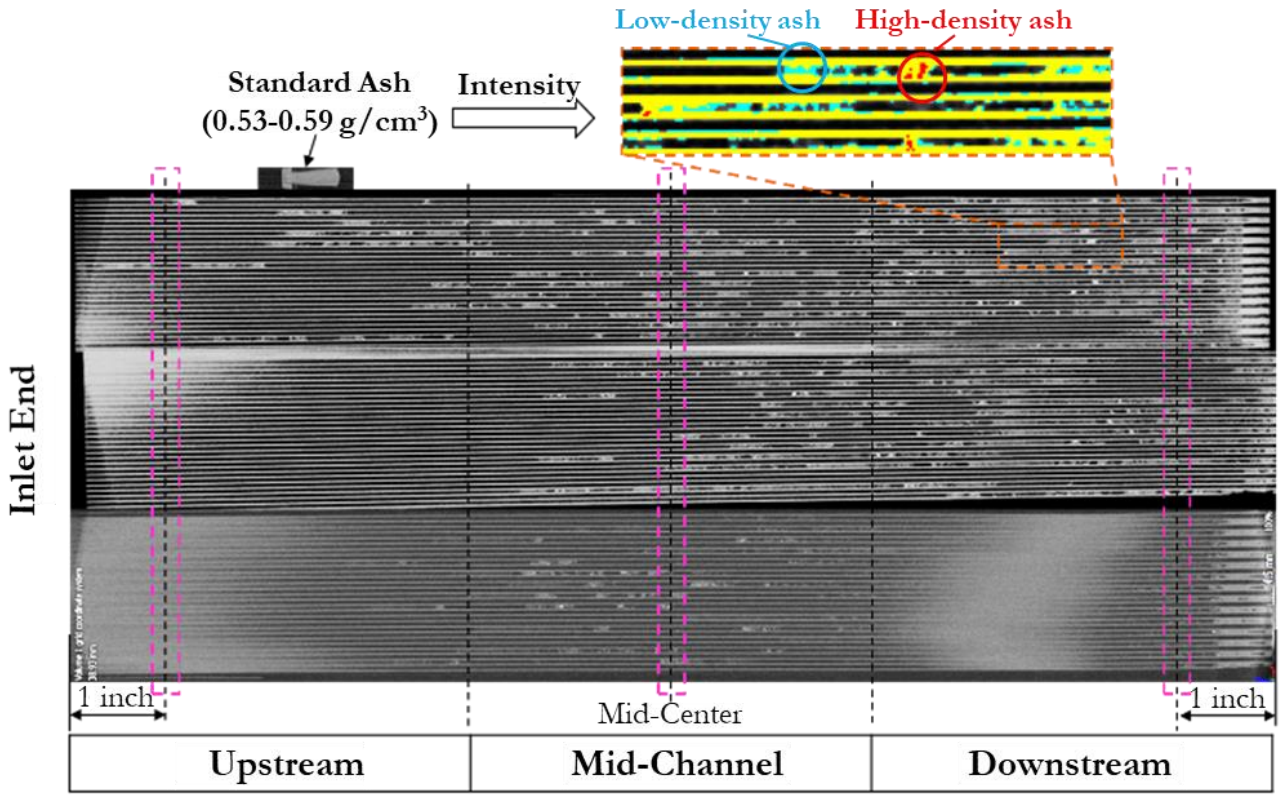

Figure 3-12: Enhanced CT X-Ray image indicating location and axial degree of plugging along the channels. Note that the densest ash plugs possessed densities ~1 g/cm^3, with most ~0.11-0.54 g/cm^3.

We notice here the presence of several ash plugs that have formed at various positions upstream of the channel ends, which we have referred to thus far interchangeably as premature plugging / clogging, MCC, and MCD.

3.7 Conversion of Image Contents to Numeric Data

In order to determine metrics of interest, raw images needed to first be processed so that a continuous numeric scheme could be developed and used to spatially map ash agglomerates of varying intensity within partially plugged channels. Once images were enhanced with the desirable contrast, numeric values for plugging intensity and geometry were assigned to each agglomerate and then analyzed accordingly. Analysis, however, required a segmentation of image components into equally spaced sections that would enable a comparison of spatial deposit distribution. For the "side" view images through which axial and radial distributions could be ascertained, full channel lengths were visible. The three axial segments were equivalent in length: inlet accumulation refers to ash in the upstream-most third section of each channel's axial direction. Similarly, the mid-channel

refers to the middle third (axially) of the DPF, and the outlet region is the aft third where the end plug region is located.

3.7.1 Image Data Generation for "Side" View Cross Sections

While each block in the DPF has 28 channels along the $\hat{y}$ and $\hat{z}$ dimensions, respectively, the alternating open and closed design of filter channels results in only half (or 14) of the channels accumulating ash deposits, with the other 14 remaining clean and conducive to unfettered flow of the exhaust gas stream that is (ideally) no longer laden with particulate matter. Figure 3-13 illustrates the axial segmentation and corresponding syntax of a single cross section in the $y - x$ plane used throughout the course of the present DPF ash accumulation analysis. Each segment (inlet, mid-channel, and outlet) and channel combination was given a separate score for degree of ash accumulation. Note that this is only one of many cross sections that were combined to represent analysis of a DPF for a given enigne operating condition and set of test parameters.

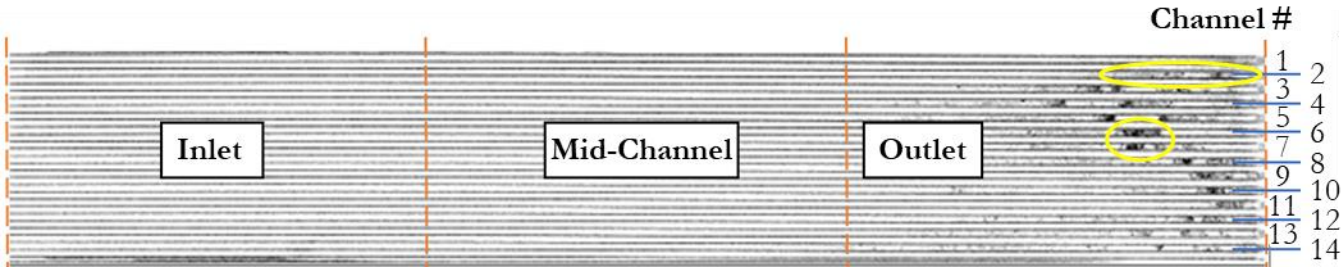

Figure 3-13: A DPF "side" ($y - x$ plane) cross section scan segmented axially into thirds, open channels numbered from 1 to 14.

The analysis was done across 64+ equally-spaced slices via both "front" ($y - z$) and "side" ($y - x$) views for each operating condition. The corresponding data for both cross-sectional plane views are provided in Appendix A. When segmentation was complete, a method of consistently tabulating ash accumulation behavior for each DPF snapshot was applied. Given the metrics of interest, a table was generated that represents the degree of ash accumulation in each section of the DPF. A snapshot of one such table is given in Table 3-5 below. Degree of ash accumulation is based on both visible ash density and accumulated plug length. The leftmost column represents the location in memory of the raw scan image.

Table 3-5: The first five data points for operating Point 2 (soot : ash = 0.25) showing ash agglomeration intensity tabulated per channel and corresponding "third" section. There are quite a few unassessable "N" values in this sample data set.

Raw Image	Image	Plug Cross Section	1	2	3	4	5	6	7	8	9	10	11	12	13	14
60	*1*	top	N	N	N	N	N	N	4		3	3	2	2	1	1
		middle	N	N	N	N	N	N	N							
		bottom	N	N	N	N	N	N	N							
		Is plugged?	N	N	N	N	N	N	N	0	1	1	1	1	0	0
70	*2*	top	3						5	4	4	3	2	2	1	1
		middle														
		bottom	3													
		Is plugged?	1	0	0	0	0	0	1	1	1	1	1	1	0	0
80	*3*	top	N	N	2						3	3	3	4	2	2
		middle														
		bottom	N	N	N	N	N	N								
		Is plugged?	N	N	N	N	N	N	0	0	1	1	1	1	1	1
90	*4*	top		3	3		1	N	N	N	N	N	N	N	N	N
		middle				N	N	N	N	N	N	N	N	N	N	N
		bottom								N	N	N	N	N	N	N
		Is plugged?	0	1	1	N	N	N	N	N	N	N	N	N	N	N
100	*5*	top	3		3	3	3		2	3	3	4	4	3	2	1
		middle														
		bottom		2												
		Is plugged?	1	1	1	1	1	0	1	1	1	1	1	1	1	0
.	.	.	.	.	.	.	.	.	.	.	.	.	.	.	.	.
.	.	.	.	.	.	.	.	.	.	.	.	.	.	.	.	.
.	.	.	.	.	.	.	.	.	.	.	.	.	.	.	.	.

The table exhibits the presence of several "N" scores. While Figure 3-13 respresents a "clean" DPF cross section in which every section of every channel is clearly visible, real-world scans sometimes produce regions that are distorted and often indecipherable due technical imperfections in the scanning process. Figure 3-14 depicts how an instance of optical distortion—sometimes referred to as optical "bleaching" due to undesirable brightness saturation—appears during image analysis. The inlet region in the figure suffers from only one instance of substantial distortion, near the top of the filter block as shown in Figure 3-14, therefore receiving a score of "0" in all channels but one, in which it is given a score of "2." That channel is considered plugged because it scored a "2" or above (rules for scoring are included in Table 3-6 below). The mid-channel region suffers from notable visual distortion near the bottom; therefore around 40% of the channels earn a score of "N." Applying the same logic, all channels in the outlet segment but one earn a score of "N."

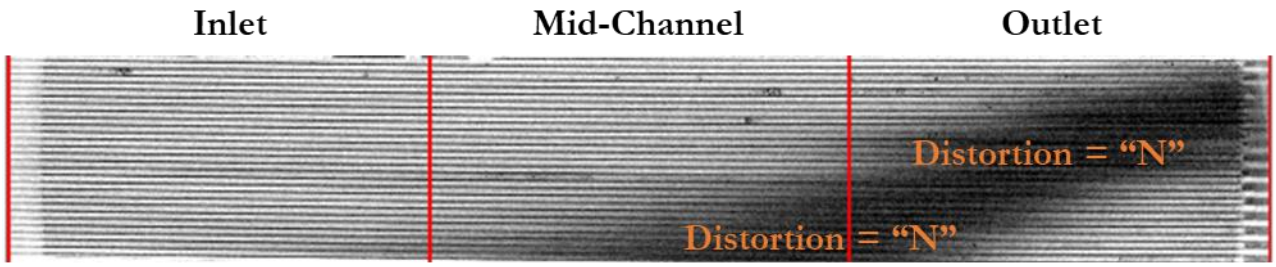

Figure 3-14: "N" scores for each channel-segment combination to indicate visually obstructed and thus unassessable channel ash accumulation.

As previously mentioned, each DPF cross section is segmented into both channel number and one of the three equal-length (inlet, mid-channel, and outlet) regions, as shown in Figures 3-12 and 3-13, and 3-14 above. Degree of plugging (between 0 and 10) is then assessed for each channel number-region combination (e.g., for Image 90, channel #2 in the outlet region scores 3), which indicates notable plugging there. Values of "N" represent channel segments with optically distorted, and therefore unusable, data that prevented us from determining whether ash agglomerates exist at those locations. Data scores of "N" were not included in the analysis, and values were normalized accordingly. The "Is plugged?" row indicates whether a given channel is plugged. "1" means that yes, the channel is plugged such that there was a score of at least "2" in any of its three regional segments. A "0" score was given if there was no meaningful optical distortion in a channel and the channel does not exhibit MCC by scoring greater than "1" in any of the channel's three axial regions, in which case it would earn the "1". A value of "N" is assigned to a channel when at least 2% of a channel is optically distorted with an "N" value and not otherwise plugged. Rules for scoring are given in Table 3-6.

The table describes the integer scale applied, with values ranging from 1 to 10. Blanks (or zeros) correspond to zero or marginal ash accumulation in that section, whereas a 10 implies the highest degree of plugging, which has defined here is the equivalent of over 32% of that channel-segment being shaded completely black. A minimum score of "2" was ascribed to any section in which the entire width of the channel has been plugged with ash, regardless of plug length. Figure 3-13 above has three ash plugs circled in yellow—one in channel #2 and the other two in channels #6 and #7. For reference, channels #2 and #7 score a "2" under our scoring scheme, whereas channel #7 scores a "3." If the plug in the "outlet" region of channel #6 were approximately 25% longer, then it would receive a score of "4." Note that a higher score is expected to increase the backpressure generated by flow through the DPF due to the presence of greater resistnace to flow, which will be described in greater detail in Chapter 4.

Table 3-6: A description of each plugging intensity score assignable to channel segments. Note that the presence of full plugging (complete ash bridging of a channel regardless of axial plug length) anywhere within the channel region fulfills the criterion for a score of "2."

"Side" View Score	Corresponding Description
Blank or 0	Traces of plugging, effective plugging < 1%
1	No full plugging, effective plugging < 2%
2	Full plugging and/or effective plugging < 4%
3	2+ isolated plugs and / or effective plugging < 8%
4	Effective plugging < 12%
5	Effective plugging < 16%
6	Effective plugging < 20%
7	Effective plugging < 24%
8	Effective plugging < 28%
9	Effective plugging < 32%
10 (never assigned)	Effective plugging > 32%

The system was designed to linearly correlate score with effective flow resistance in the channel, which would therefore yield scores that directly proportional to channel backpressure. Note that 100% effective intensity means that the channel segment is fully plugged with all either black or white shading, in contrast to the background shade. Since the maximum effective plug percent observed in a given segment was around 35%, the threshold percentages were staggered by 4 percentage points, with 32% marking the final increase in score from a 9 to 10. Effective intensities scale linearly based on both shading intensity and plug length. An equation for effective plug fraction $P_{effective}$ can then be written as follows, where σ_i is the degree of blackness of a given plug of area A_i (white = 0, black = 1), and A_{total} is the total area of the channel segment under study (i.e. the width times the length of the rectangular channel segment):

$$P_{effective} = \frac{\sum_i \sigma_i A_i}{A_{total}} \tag{3.5}$$

For rectangular plugs, A_i is given by:

$$A_i = l_i \times w_c \tag{3.6}$$

l_i is the length of plug element and w_c is the width of the channel, per counting pixels digitally.

Calculations were initially done manually with the assistance of measurement tools embedded into Image-Pro Plus software that enabled precise via pixel counts and area intensity calculaitons. Since we are interested in the fraction of the channel segment plugged, we begin by finding the length of plugs and dividing by the overall segment length. The blue font in Figure 3-14 gives both dimension numbers (D5 and D6 in this case) followed by pixels corresponding to that length measurement. As the entire channel is measured to be 2984 pixels long, which we divide by 3 in order to find the length of each channel segment. Plug lengths (e.g. D6 = 152 pixels) may then divided by the channel segment length to find the fraction of the segment that is plugged.

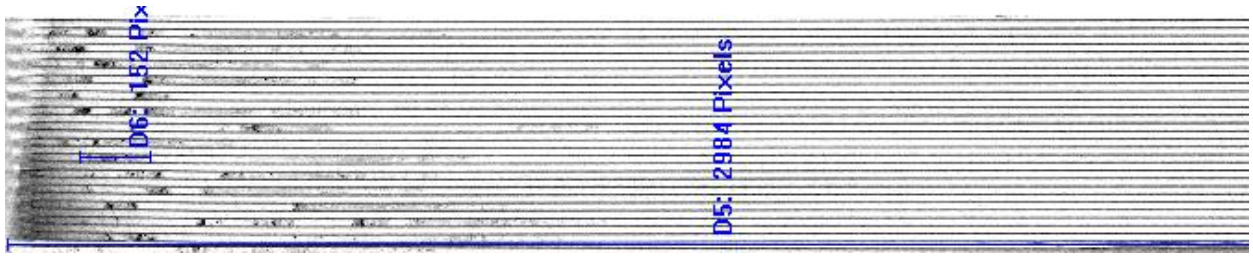

Figure 3-15: A pixel count (linear) measurement function was used to find ash plug length.

Length, however, represents only half of what is needed to find effective plugging values. The degree of either whiteness or blackness (in this case) reflects ash density at that lcation, which is the other factor that scales linearly with effective plugging, per the above equation for effective plugging intensity. Hence, we applied a different measurement tool in Image-Pro Plus that maps grayscale shading to colors given a specified number of divisions. We applied 10 color divisions so that a linearly increasing array of discrete colors scaled proportionately to density of plugs, the most dense of which earned an ash plugging density score $\sigma_i = 1$. Figure 3-16 shows the resulting channel spectrum that was used to asign plug density in each location of interest.

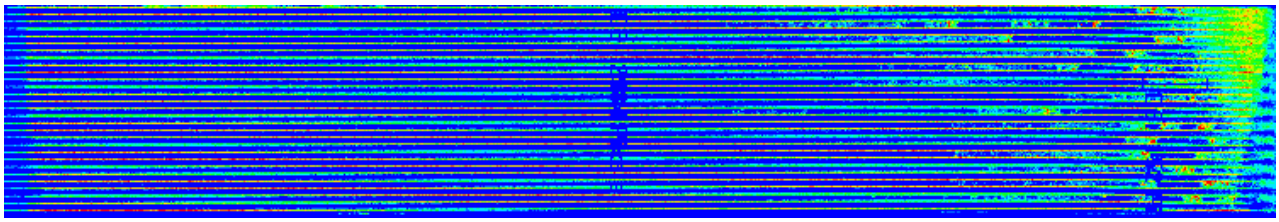

Figure 3-16: A grayscale-to-color function was used to determine relative plug density / intensity.

The effective plug fraction for a given segment and channel may then be calculated by integrating the intensity over the length of the plug for all plugs in a channel segment, and then dividing that result by the total area in that segment., as follows:

$$P_{effective,segment} = \frac{\iint_A Intensity_{shade} \cdot dA}{A_{channel,segment}} = \frac{\iint_A \sigma_i \cdot dA}{A_{channel,segment}} \tag{3.7}$$

3.7.2 Image Data Generation for "Front" View Cross Sections

Metric tabulation for "front" views of DPF cross-sections was similar in spirit, though of course the nature of the images, as well as the mapping of channel plug fraction to score, were different. Figure 3-17 shows how "front" view images were segmented into quadrants. Each quadrant was assessed for degree of total ash agglomeration on an integer scale from 1 to 10, with an empty value representing a cross section with zero or negligible plugging. A value of "10," on the other hand, indicates full plugging of a quadrant (i.e. more than 95% of the inlet channels, or 47.5% of all channels, are fully plugged and represented by white squares). Both size (percent of channel shaded white in the case of Figure 3-17 below) and intensity (magnitude of brightness / whiteness) were considered in scoring channels and quadrants. In Figure 3-17, the top left and bottom right quadrants earn a score of "2," whereas the bottom left quadrant scores a "1" and the top right receives a blank score for virtually no ash accumulation based on image cell shading.

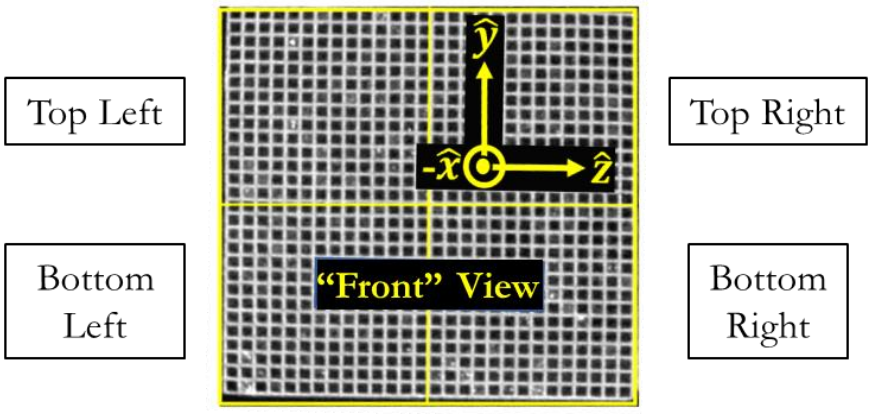

Figure 3-17: "Front" view cross section segmentation for evaluating ash accumulation. Note that the shading has been inverted from the "side" view such that white ash plugs are visible on a black background.

This exercise was completed several times across each of the three operating points (S/A ratios of 0.25, 1.0, and 2.5) under study. 66 data points were acquired for operating Point 1 (S : A = 1),

Point 2 (S : A = 0.25), and Point 3 (S : A = 2.5). There was interesingly no discernible visual distortion in any of the "front" view images studied. The data points were collected in evenly spaced increments from the inlet end to the outlet end, i.e. in the $\hat{x}$-direction. Even spacing was enforced so that a reasonably accurate representation of DPF ash accumulation can be generated, which precludes data sets with large gaps between cross section without apriori knowledge of expected ash distribution. Table 3-7 depicts data generated for the first 15 snapshots collected from the DPF representing Point 1 operation. The full data sets across each operating point are included in Appendix A for both "front" and "side" views.

Table 3-7: Ash accumulation data representing "front" view cross sections for the first 15 snapshots of Point 1 (S : A = 1) operation. The data represents the percent of inlet channels plugged, where 0 corresponds to negligble or ~0%, 5 to 50% plugging, and 10 to 100% plugging, rounded to the nearest 10% increment.

Point 1 (S : A = 1.0)					
Data #	Raw Image #	Top-left	Top-right	Bottom-left	Bottom-right
1	60	3	4	2	4
2	90	3	4	2	4
3	120	2	2	3	3
4	150	3	3	2	3
5	180	4	2	2	3
6	210	4	4	2	4
7	240	4	4	5	4
8	270	6	4	4	4
9	300	5	5	5	6
10	300	4	2	3	5
11	330	4	2	3	2
12	360	5	2	3	2
13	390	5	2	5	3
14	420	6	2	4	3
15	450	4	3	5	2
.	.	.	.	.	.
.	.	.	.	.	.
.	.	.	.	.	.

3.8 Evaluating Metrics of Interest

After images were segmented, labeled, and structured in a manner amenable to efficient data collection, image data were tabulated and stored per the manner indicated in Tables 3-5 and 3-6

above. After data were collected, metrics of interest could be determined. Metrics evaluated in the present analyses are provided in Table 3-8 below.

Table 3-8: Key metrics of interest, evaluated using image analysis.

Metric #	Metric Name	Metric Description
1	Variability of plugging observations for offset channels	Used to ensure statistical similarity of ash agglomerate results across image batches differing by a small offset based on the initial image selected and maintaining constant spacing between images
2	Percent of channels prematurely plugged	Indicates the degree of undesirable ash agglomeration in a section of the DPF that does not include the end plug where ash accumulation is expected and therefore does not represent an instance of MCC accumulation
3	Consistency of axial and radial distribution of plugging	Determines whether there is statistically asymmetric ash accumulation in the DPF

These metrics enable us to ascertain the general spatial agglomeration tendencies of ash in the DPF, and furthermore provides a means of predicting DPF backpressure through the application of fluid mechanics theory to a specified distribution of ash accumulation in DPF channels. This modeled backpressure can then be compared with empirically measured backpressure in order to improve existing predictive models for backpressure. Metrics 1 and 2 were determined via "side" view data, whereas Metric 3 reflects a combination of "side" and "front" view image analysis.

3.9 Testing Local Variation in Plugging Observations Between Two Offset X-Ray CT Cross-Section Image Batches ("Side" View)

As mentioned above, two offset data sets representing the numerically tabulated representation of ash accumulation in the DPF were compared to ensure that the choice of initial image versus its neighbors does not materially affect the resulting ash distribution. Variability testing for two offset data sets consisting of images from the same scanned DPF was conducted by implementing a two-tailed Welch's *t*-test for 80 unpaired data points representing the 80 cross-sectional cuts generated for "side" view analyses. The images were divided into two offset batches of 40 cross-sectional images, such that they stagger one another and share the same spacing in the $\hat{z}$-direction [83]. The null hypothesis H_0 is that the means between the two offset data sets are statistically the same, or in

other words that their difference is not statistically significant. An unpaired *t*-test was used since there were varying numbers of non-"N" valued data points, and thus a one-to-one pairing of data values between sets was not possible. The data itself, presented in Table 3-9, reflect ash accumulation intensity, as defined in Table 3-6. Six different combinations of left and right sides of the DPF and axial inlet, mid-channel, and outlet DPF regions served to segment the data. Right and left correspond to two halves of the DPF blocks as labeled above in the "front" cross section schematic, Figure 3-17.

Table 3-9: Plugging intensity values across six segments for two batches from the same data set.

Batch 1	**Top Left**	**Top Right**	**Middle Left**	**Middle Right**	**Bottom Left**	**Bottom Right**
# Channels	40	40	40	40	40	40
# Channels not "N"	30	28	29	29	29	26
Effective Plugging	**3.27**	**2.77**	**0.43**	**1.26**	**0.14**	**0.58**
Standard Deviation	2.35	1.63	0.77	1.17	0.35	0.91
Batch 2 (Offset)	**Top Left**	**Top Right**	**Middle Left**	**Middle Right**	**Bottom Left**	**Bottom Right**
# Channels	40	40	40	40	40	40
# Channels not "N"	30	28	29	29	29	26
Effective Plugging	5.27	4.96	2.84	3.54	2.64	3.22
Standard Deviation	8.04	8.09	8.51	8.35	8.69	8.69

We notice that the higher average effective plugging value between batches 1 and 2 alternates across the six segments. Furthermore, it seems that the average values are fairly similar, especially considering how much larger the standard deviations are from the difference of means. However—again—in order to make this a more rigorous comparison of means, we will apply an unpaired, two-tailed Welch's *t*-test. The general equations to be applied follow—the first yielding the statistic *t* and the second calculating the number of degrees of freedom df. The variable $\bar{x}$ represents a sample mean, *N* is the number of samples, and $s^2$is the sample variance (i.e. the square of the sample standard deviation). The equation for the statistic t is given by Welch's *t*-test designed for unequal variances, while maintaining the assumption of normality. This test is an approximate solution to the Behrens-Fisher problem.

$$t = \frac{\bar{x}_1 - \bar{x}_2}{\sqrt{\frac{s_1^2}{N_1} + \frac{s_2^2}{N_2}}} \tag{3.8}$$

We notice that the denominator is not based on a pooled variance estimate. The number of degrees of freedom df associated with this variance estimate can be approximated using the Welch-Satterthwaite equation, as follows.

$$df \approx \frac{\left(\frac{s_1^2}{N_1} + \frac{s_2^2}{N_2}\right)^2}{\frac{s_1^4}{N_1^2(N_1 - 1)} + \frac{s_2^4}{N_2^2(N_2 - 1)}} \tag{3.9}$$

Both t and df then readily follow from Table 3-6

Results are expressed in Tables 3-10 to 3-12 below for three different segmentations of the DPF, which indicate that the null hypothesis holds and the mean plugging values between the offset batches are statistically similar. Recall that our null hypothesis is that the difference of means between the two unpaired data sets of different variance is statistically not different (i.e. negligible). Thus, assuming $\alpha = 0.05$ and a two-tailed normal distribution, if our p-value is < 0.05 then we reject the hypothesis, which implies that there is a statistically significant difference between the means of the offset data sets. Otherwise, when p > 0.05, we fail fail to reject the null hypothesis and conclude statistically equal sample means.

Table 3-10: Two-tailed Welch's *t*-test for Point 1 with the DPF segmented into six regions.

	Outlet Left	**Outlet Right**	**Mid-Channel Left**	**Mid-Channel Right**	**Inlet Left**	**Inlet Right**
t score	0.41	0.70	-0.48	-1.15	2.11	0.73
df	62.96	53.97	62.77	59.99	28.00	44.74
p-value	0.69	0.49	0.63	0.26	0.05	0.47
Means equal?	**Yes**	**Yes**	**Yes**	**Yes**	**Borderline**	**Yes**

Table 3-11: Two-tailed Welch's *t*-test for Point 1 with the DPF segmented into three regions.

	Outlet	**Mid-Channel**	**Inlet**
t score	0.66	-1.02	1.14
df	118.93	124.99	98.26
p-value	0.51	0.31	0.28
Means equal?	**Yes**	**Yes**	**Yes**

Table 3-12: Two-tailed Welch's *t*-test for Point 1 with the DPF segmented into two regions.

	Left	Right
t score	0.35	0.49
df	186.05	170.35
p-value	0.77	0.63
Means equal?	**Yes**	**Yes**

We observe that in each case, means of offset data sets were statistically equivalent, and we therefore confidently retain our null hypothesis that offset points from the same data set are statistically equal. This verifies that results are consistent and repeatable for a given operating point regardless of the choice of initial image (i.e. offset / phase).

3.10 Percent of Channels Prematurely Plugged ("Side" View)

Based on Table 3-6, and as previously stated, a channel visible in "side" view image analysis is considered plugged if at least one of the segments achieves a score of at least "2." Conversely, a channel is considered not plugged if none of its segments scores "N" (i.e. optically distorted beyond what may be confidently inferred by visual inspection), and if none of its segments achieve a score of "2" or greater. Thus, each segment in an unplugged channel must score either values "0" or "1." The percentage of channels plugged is calculated as the number of channels plugged divided by the number of channels that do not earn a mark of "N" in any of their segments. That is, only channel segments whose plugging distribution can be completely discerned are considered in the the analysis.

Table 3-13 summarizes premature plugging percent for each operating point. Note that the number of samples that have no segments with score "N" is less than the 64 mentioned before. This is the case because although over 64 images were used in the analysis, several of them had some level of visual distortion that necessitated the removal of those distorted channels from the calculation used to determine the percent of channels that are prematurely plugged. Tables 3-14, 3-15, and 3-16 provide detailed statistical accounts of the percent of each specific channel plugged across the three operating points, and are summarized in Table 3-13. Again, note that the number of channels for each operating point in which no segment is illegible is notably less than the total number of channels investigated for a given operating point, due to optical distortion / imperfect images yielded by the X-Ray CT scanning equipment used to generate visual cross sections of the DPF. The 14 channels displayed in the first row of Tables 3-14 to 3-16 correspond to those representing the x-axis of Figure 3-18. "Average value" represents the mean percentage of channels

plugged across all visually discernible snapshots of a given channel # that corresponds to a specific operating point.

Table 3-13: Summary of premature plugging prevalence for all channels across specified operating points.

Operating Point	Number of Samples	Number of non-"N" Samples	Average % Channels with Premature Plugging	Standard Deviation of % Channels Plugged
Point 1 (S : A = 1.0)	80	35-51	49.6%	50.0%
Point 2 (S : A = 0.25)	74	40-44	73.6%	44.1%
Point 3 (S : A = 2.5)	80	46-52	72.2%	44.8%

Table 3-14: Summary statistics for percent of channels plugged for operating Point 1 (S : A = 1.0).

Point 1 (Soot : Ash = 1.0)														
Channel #	**1**	**2**	**3**	**4**	**5**	**6**	**7**	**8**	**9**	**10**	**11**	**12**	**13**	**14**
# Channels not "N"	51	50	49	43	41	41	39	40	41	41	38	36	35	38
Average % MCC for a given Channel	**49%**	**44%**	**55%**	**63%**	**51%**	**56%**	**51%**	**35%**	**41%**	**37%**	**39%**	**61%**	**77%**	**37%**
Standard Deviation	50%	50%	50%	49%	51%	50%	51%	48%	50%	49%	50%	49%	43%	49%

Table 3-15: Summary statistics for percent of channels plugged for operating Point 2 (S : A = 0.25).

Point 2 (Soot : Ash = 0.25)														
Channel #	**1**	**2**	**3**	**4**	**5**	**6**	**7**	**8**	**9**	**10**	**11**	**12**	**13**	**14**
# Channels not "N"	42	44	44	43	41	40	41	42	42	42	42	43	43	43
Average % MCC for a given Channel	**52%**	**84%**	**91%**	**91%**	**88%**	**80%**	**80%**	**76%**	**79%**	**88%**	**86%**	**77%**	**35%**	**26%**
Standard Deviation	51%	39%	32%	32%	35%	42%	42%	44%	43%	35%	37%	44%	48%	44%

Table 3-16: Summary statistics for percent of channels plugged for operating Point 3 (S : A = 2.5).

Point 3 (Soot : Ash = 2.5)														
Channel #	**1**	**2**	**3**	**4**	**5**	**6**	**7**	**8**	**9**	**10**	**11**	**12**	**13**	**14**
# Channels not "N"	47	46	47	51	49	49	50	52	49	51	52	52	51	48
Average % MCC for a given Channel	**43%**	**76%**	**81%**	**75%**	**73%**	**71%**	**72%**	**69%**	**84%**	**78%**	**81%**	**81%**	**67%**	**58%**
Standard Deviation	50%	43%	40%	44%	45%	46%	45%	47%	37%	42%	40%	40%	48%	50%

From the data, we see that around 50% of the time at one of the three prescribed operating points, a given channel in the DPF exhibits MCC somewhere upstream of the end plug. Furthermore, the

middle soot-ash-ratio of unity (Point 1) yielded significantly less premature plugging than Points 2 and 3 did. In fact, Figure 3-18 below plots the above data and shows that there is a notable drop in plugging frequency for Point 1. It also indicates that there may be a tendency for ash to accumulate less on the outer channels (1 and 14) of a given block than near the block's radial center.

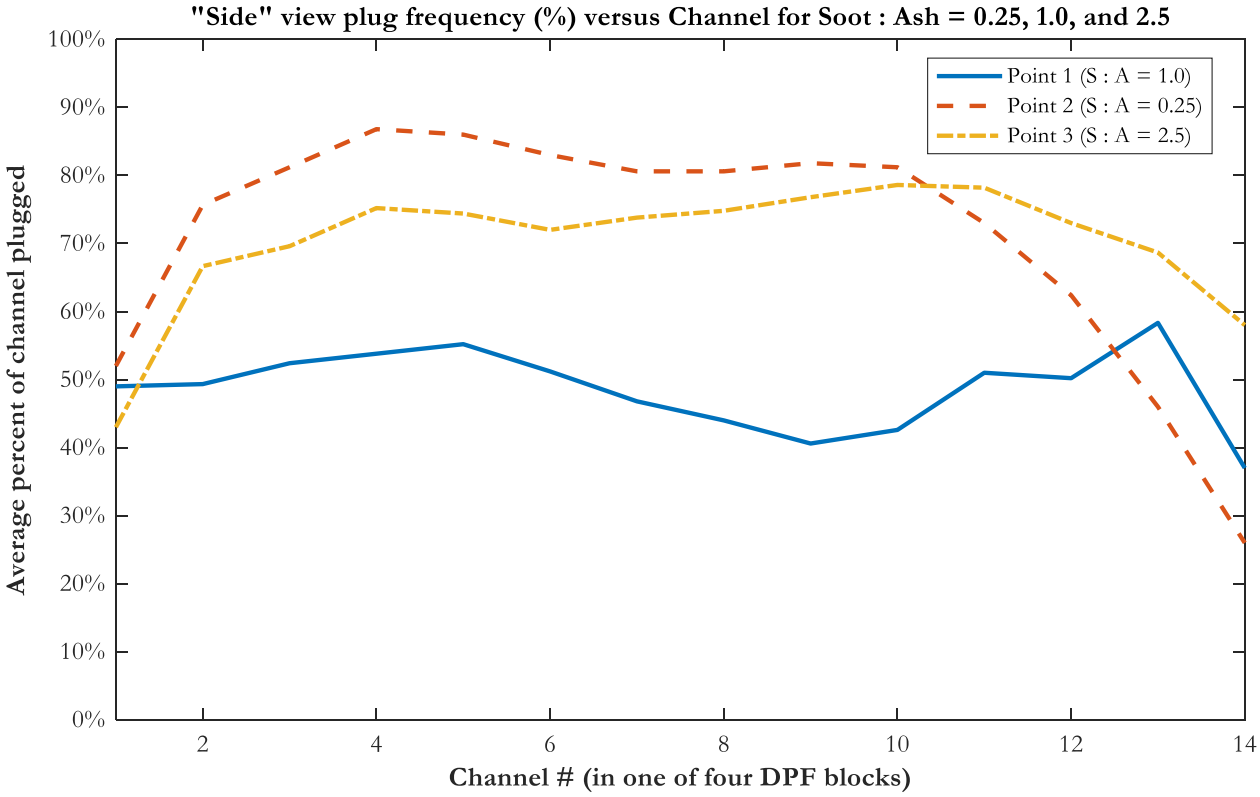

Figure 3-18: Percent of channels plugged across operating Points 1-3. Premature plugging is less prevalent for Point 1, as well as in a given block's outer channels.

The process of determining percentage of channels plugged was eventually automated using an in-house MATLAB script written by Yuesen Wang, a postdoc in the automotive lab during the period over which these experiments were taken [84, 19]. His script generated a 3-dimensional depiction of variable-density ash plugs from the thousands of cross-sectional snapshots taken throughout the DPF, illustrated in Figure 3-19 below. Variants of such a representation were used to assess ash plug distribution across the particulate filter.

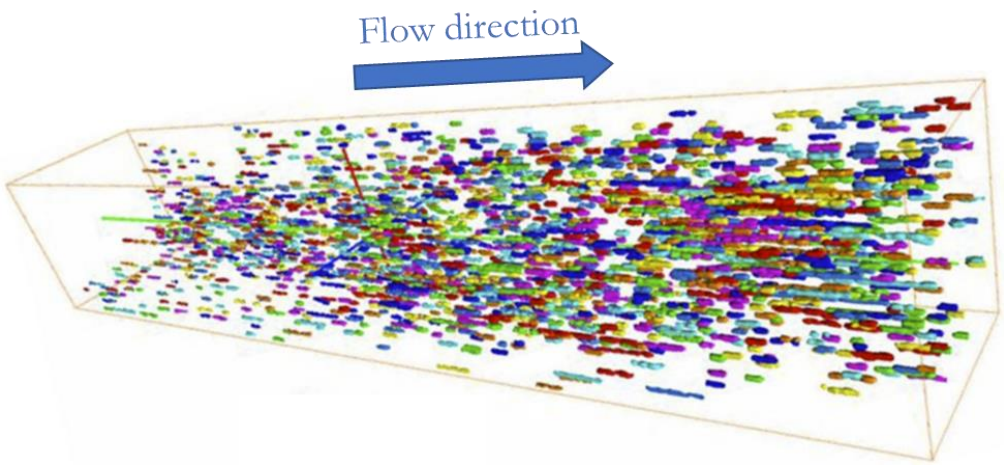

Figure 3-19: A 3-dimensional rendering of all ash plugs observed in a DPF via X-Ray CT scans, consolidated using MATLAB code [84].

These 3-dimensional representations of ash agglomerates in the DPF were used to calculate the pressure drop across the filter in the next chapter of this dissertation, Chapter 4.

3.11 Variation in Distribution of Plugging ("Side" and "Front" Views)

Of interest is whether ash agglomerates plug the DPF symmetrically, both axially and radially. Beginning with the axial distribution, we are interested in both the change in degree of premature plugging in different axial locations, as well as expected location of initial plugging in each channel. Beginning with general axial plugging, Tables 3-17, 3-18, and 3-19 summarize plugging intensity in the three different axial channel segments (inlet, mid-channel, and outlet) across Points 1, 2, and 3. These data represent a synthesis of "side" view cross sections across the DPF. Each table displays the total number of cross sections considered, average "side" view effective plugging score in each "third" segment—according to Table 3-6—and standard deviation of the corresponding data.

Table 3-17: Effective plug intensity for Point 1 (S : A = 1.0) across axial "third" regions.

Point 1	**Outlet**	**Mid-Channel**	**Inlet**
# Data Points not "N"	121	127	121
Average "Side" View Effective Plugging Intensity Value	**2.9**	**1.0**	**0.3**
Standard Deviation	2.2	1.2	0.6

Table 3-18: Effective plug intensity for Point 2 (S : A = 0.25) across axial "third" regions.

Point 2	Outlet	Mid-Channel	Inlet
# Data Points not "N"	117	121	121
Average "Side" View Effective Plugging Intensity Value	**5.4**	**0.3**	**0.4**
Standard Deviation	2.2	1.0	1.6

Table 3-19: Effective plug intensity for Point 3 (S : A = 2.5) across axial "third" regions.

Point 3	Outlet	Mid-Channel	Inlet
# Data Points not "N"	125	136	135
Average "Side" View Effective Plugging Intensity Value	**7.0**	**3.4**	**0.3**
Standard Deviation	6.4	4.6	1.9

Clearly, there is far more premature plugging in the outlet region than in either the mid-channel and inlet regions, and there is hardly any ash agglomeration in the "inlet" region for the three operating points tested here. In fact, effective ash accumulation in the inlet "third" region accounts for less than 3% of ash agglomerates in the DPF.

Figures 3-20 through 3-22 were instead generated via "front" image cross section analysis, and more graphically illustrate the axial distribution of premature plugs. Note that segmentation was done by dividing the cross section into quadrants, per Figure 3-17. As expected, "side" and "front" image analysis express the same results, both in terms of overall plugging and axial distribution. They are, after all, merely different representations of the same data. For example, for both analyses, Point 1 (S : A = 1) yields the least absolute degree of plugging, and Point 2 (S : A = 0.25) exhibits the least prevalence of premature plugging in the inlet and mid-channel regions. Additionally, the "front" image results seem to indicate that the axial distribution of ash can be modeled as an exponential distribution with a lambda parameter value of less than unity.

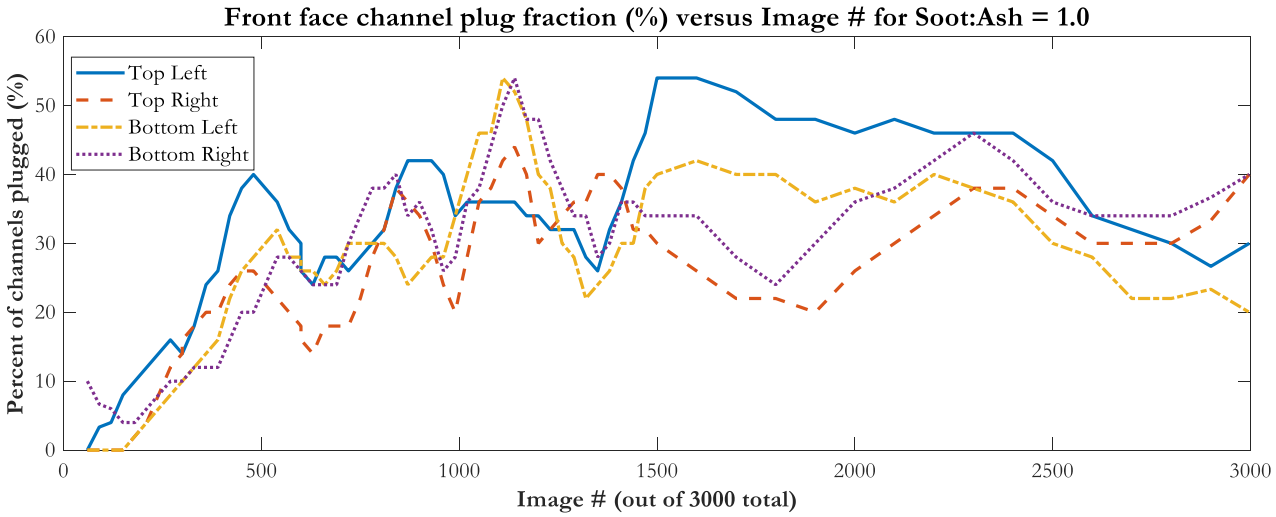

Figure 3-20: Point 1 degree of plugging along the DPF axis according to "front" image analysis.

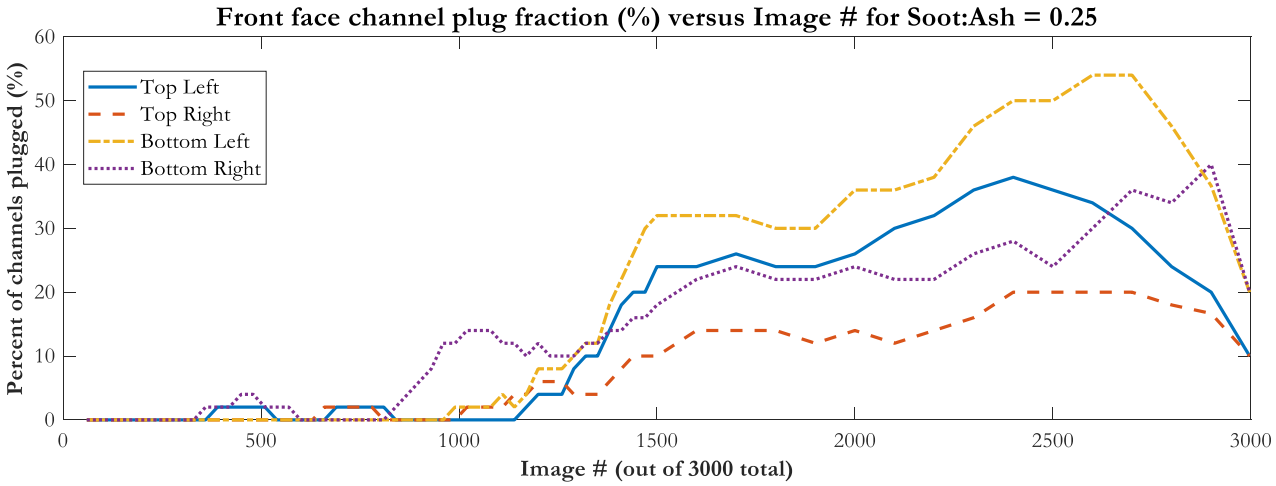

Figure 3-21: Point 2 degree of plugging along the DPF axis according to "front" image analysis.

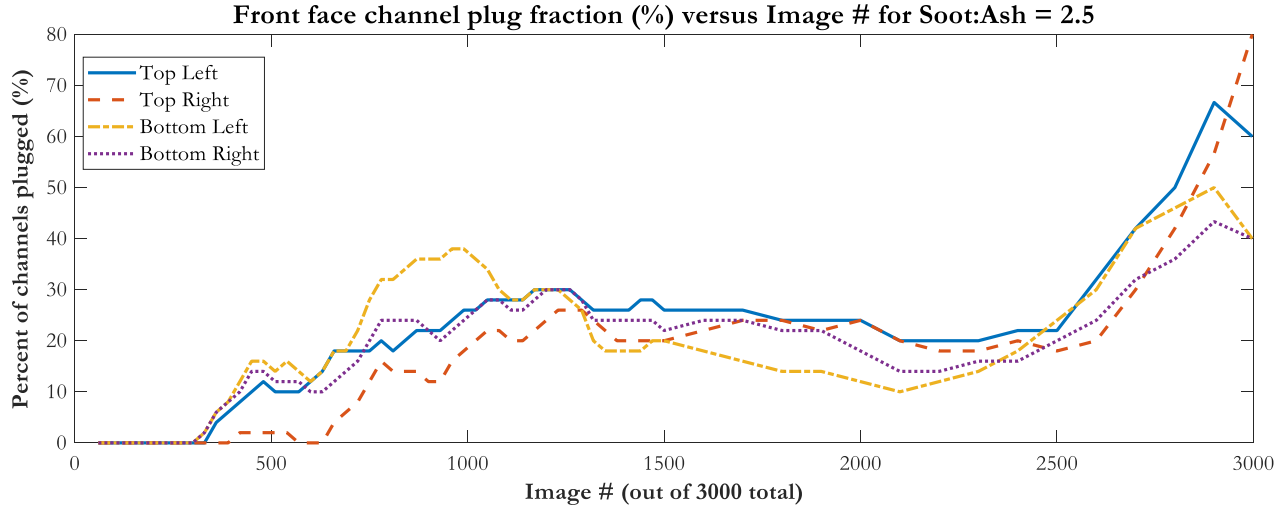

Figure 3-22: Point 3 degree of plugging along the DPF axis according to "front" image analysis.

These semi-manually generated figures were ultimately automated and used to generate summary Figures 3-23, 3-24, and 3-25 below. An additional soot : ash ratio of 8 was included in these later analyses.

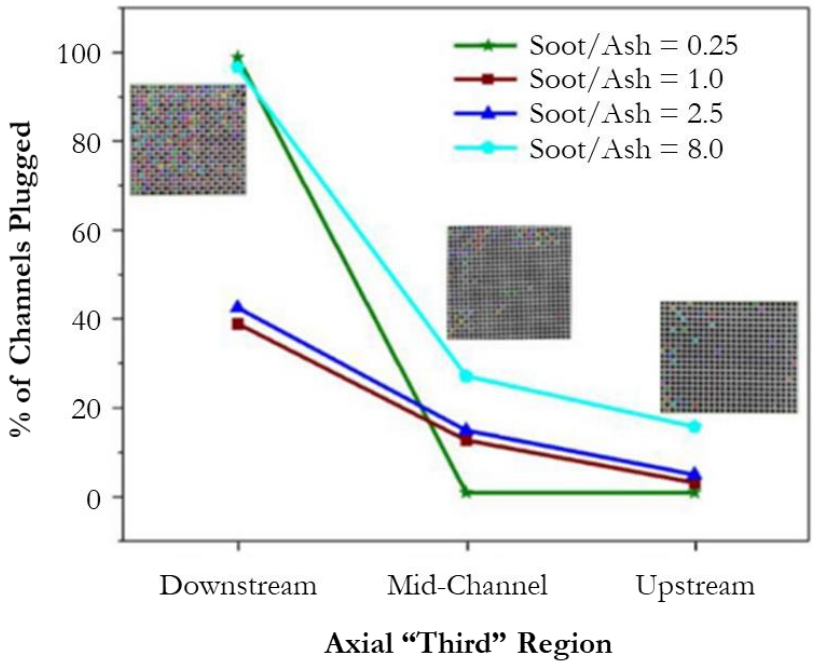

Figure 3-23: Average percentage of channels plugged as a function of axial "third" region and soot-to-ash ratio. Note that these data align with previous sentiments that there is relatively far more plugging in the downstream end of the DPF [19].

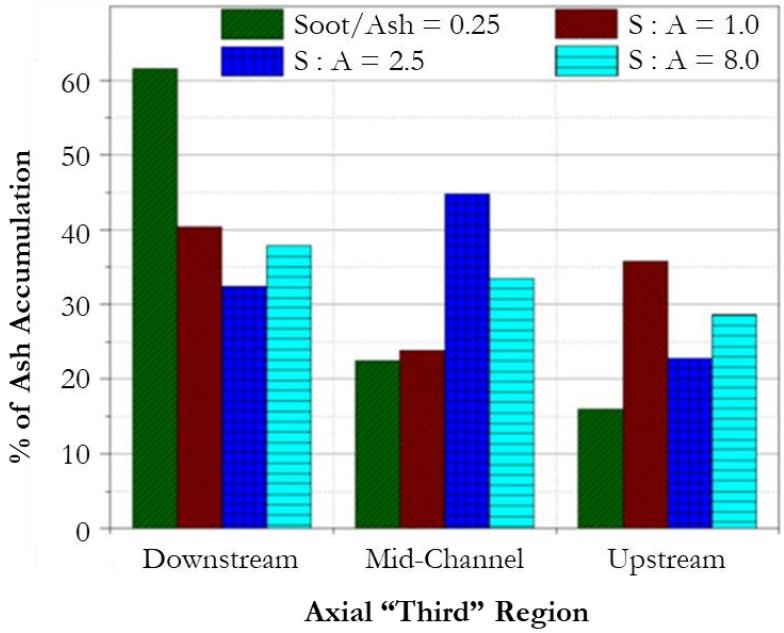

Figure 3-24: Axial distribution of ash agglomerates while varying soot-ash ratio from 0.25 to 8.0 [19].

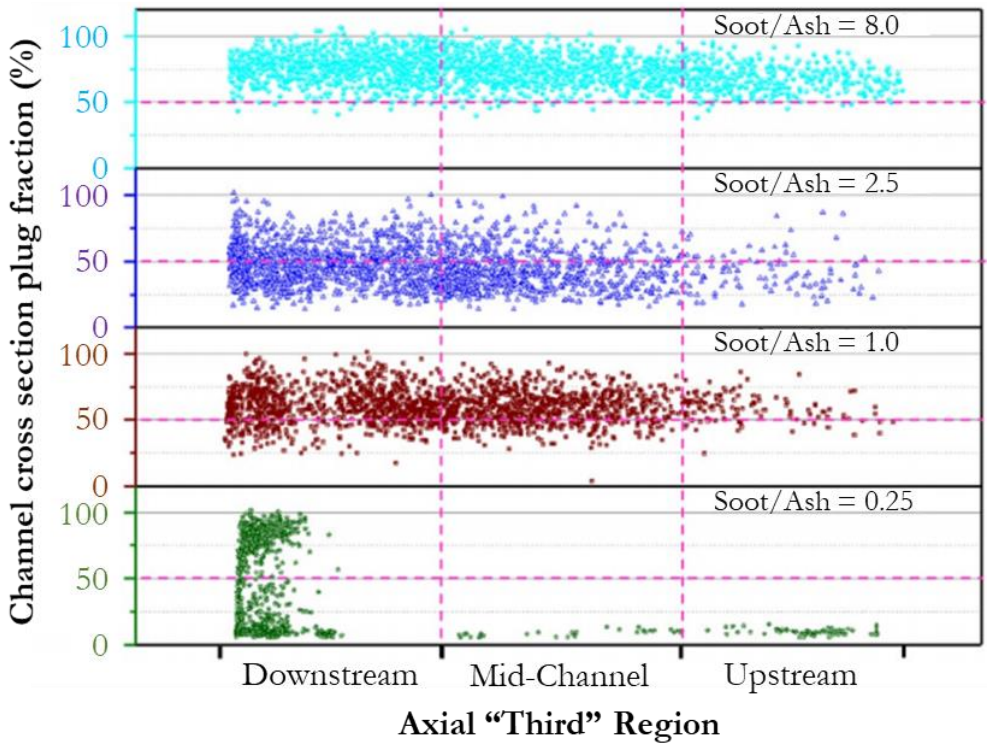

Figure 3-25: A high-resolution image indicating cross-section plug fraction for individual channels over the full axial length of the DPF while varying soot-ash ratio [19].

To study radial distribution systematically, we consolidate effective plugging values for left and right halves of the "side" view images separately, and then compare the means of the inner versus outer halves of the blocks via unpaired, two-tailed t-testing (as was done before for difference of means between the batches of data representing offset initial choice of cross section images). Inner here is defined as the half of each block closest to the centerline of the DPF "front" face along the $\hat{z}$ axis. If means are statistically different, then we can claim statistical variation in plugging intensity with radial position (or at least laterally along the $\hat{z}$-direction). Left and right segments were selected because the DPF block under study here was situated in a quadrant of the overall DPF. Thus, its entire width-wise span in the $\hat{z}$-direction reflects radial distribution of ash within the overall DPF system. Tables 3-20, 3-21, and 3-22 synthesize effective plugging data for inboard versus outboard halves of the full DPF under study.

Table 3-20: Radial effective plug intensity for Point 1 (S : A = 1.0) comparing radially inner versus radially outer portions of a block (each block comprising ¼ of the DPF).

Point 1	Inner	Outer
# Data Points not "N"	191	178
Average "Side" View Effective Plugging Intensity Value	**1.3**	**1.5**
Standard Deviation	2.1	1.5

Table 3-21: Radial effective plug intensity for Point 2 (S : A = 0.25) comparing radially inner versus radially outer portions of a block (each block comprising ¼ of the DPF).

Point 2	Inner	Outer
# Data Points not "N"	183	176
Average "Side" View Effective Plugging Intensity Value	**2.4**	**1.5**
Standard Deviation	3.3	2.3

Table 3-22: Radial effective plug intensity for Point 3 (S : A = 2.5) comparing radially inner versus radially outer portions of a block (each block comprising ¼ of the DPF).

Point 3	Inner	Outer
# Data Points not "N"	199	197
Average "Side" View Effective Plugging Intensity Value	**3.8**	**3.2**
Standard Deviation	5.8	4.9

Again, we apply the t-test approximate solution to the Behrens-Fisher problem as well as an estimate of variance using the Welch-Satterthwaite equation. Assuming $\alpha = 0.05$, we arrive at the statistical results exhibit in Table 3-23. What is striking is that, for Point 2, inboard and outboard plugging are statistically different from one another, which implies a dependence on radial position.

Table 3-23: Statistical testing shows that Point 2 exhibits radially varying ash accumulation behavior.

Left v. Right Pluggin Intensity	Point 1	Point 2	Point 3
t score	-1.30	3.01	1.05
df term 1	*1.2E-03*	*8.1E-03*	*8.4E-02*
df term 2	*2.6E-06*	*1.9E-05*	*1.4E-04*
df term 3	*9.6E-07*	*5.4E-06*	*7.4E-05*
df	349	329	384
p-value	0.19	0.00	0.29
Means equal?	**Yes**	**No**	**Yes**

Analysis of radial dependence on ash accumulation may be extended by considering the "front" view of the channel and comparing plugging intensity across the four quadrants of a DPF to one another. This effectively serves as another means of assessing radial variation in ash plugging since, recall, the DPF is comprised of four equal rectangular blocks arranged into a larger rectangular block. Taking Point 1 as an example with the top-left quadrant as reference, we may use two-tailed t-testing to determine whether there is statistically significant variation in degree of ash plugging across the four different "front-facing" quadrants of the DPF. Results are displayed below in Table 3-24.

Table 3-24: Statistical testing to determine whether there is a difference in degree of ash plugging across the four different "front-facing" quadrants of the DPF.

Paired Two-Sample t-Test for Means	Top-left	Top-right	Bottom-left	Bottom-right
Mean	3.20	2.55	2.71	2.88
Variance	2.22	2.13	2.36	2.57
Observations	66	66	66	66
Pearson Correlation	0.59			
Hypothesized Mean Difference	0			
df	65			
t Stat		3.95	2.89	1.64
P(T<=t) one-tail		0.0001	0.0026	0.0534
t Critical one-tail		1.67	1.67	1.67
P(T<=t) two-tail		0.0002	0.0052	0.1067
t Critical two-tail		2.00	2.00	2.00

We find, interestingly, that since t-stat > t-critical for both top-right and bottom-left quadrants, there is a significant difference in effective degree of plugging exhibited by those two quadrants when

compared to the top-left. The bottom-right quadrant, however, has statistically similar plugging behavior to the top-left quadrant across the axial length of the channel.

4 Extending the Backpressure Model for DPFs to Include MCC

This chapter is virtually identical to the corresponding sections of SAE 2019-01-0972 [19]. The purpose of channel flow modeling is to be able to quantitatively evaluate the effects of various parameters, such as MCC plugging axial location, radial distribution, and plugging severity (partial or complete blockage) on DPF performance—namely, backpressure. As mentioned in the introductory Chapter 1 of this dissertation, an accurate analytical, closed-form solution for modeling backpressure in a loaded DPF was developed in 1989 by Konstandopoulos et al. and confirmed by the same author via comparison to 3-D CFD solutions in 2001 [48, 80]. More importantly, the models can help interpret the experimental results—shown previously in Figure with sound analytical basis. The current simulations extend the fundamental flow equations of Konstandopoulos et al., which were subsequently modified to include soot and ash wall layers and soot/ash end plugs by Gaiser and Mucha [52, 48, 49], to cases where deposit plugs or restrictions occur somewhere upstream of the end plug region, referred to here generally as the "mid-channel" region.

4.1 Mid-Channel Congestion (MCC) Models

In addition to the impermeable ceramic end-plugs alternately placed at the front and rear of the inlet and exit channels, this MCC model accounts for deposits that can form anywhere part way along the inlet channels. In one extreme, these mid-channel deposits could be solid impermeable plugs that fully plug channels upstream of the end plug. In other cases, the plugs or congestions could be permeable by the nature of the deposits or by their not occupying the entire width of the channels, causing only partial blockage. The former case is called the Mid-Channel Solid-Plug Model, which will be described first and the latter the Mid-Channel Partial-Plug Model. The reason for breaking the presentation into two sections is that the solid plug model allows for a closed-form solution as well as a numerical solution, while the general partial-plug case can best be solved numerically using the "shooting" method. Solutions of the partial-plug model converge to that of the solid-plug model when the flow restriction in the partial blockage case becomes very large such that the partial plug effectively becomes solid and impermeable.

To account for the radially non-uniform distribution of MCC deposits, a two-step process was applied for both the axial distribution effect plus the non-uniform radial distribution effect. The first step is to determine the flow resistance of the MCC-plugged channels, i.e. the pressure-drop versus

flow relationship, for the axially plugged channels assuming uniform radial deposit distribution. This step will establish the pressure drop dependence on flow for each channel. The second step calculates the flow-rate distribution among the channels for non-uniform radial deposit distribution. Using the results from the first step and the variation in flow rates in the second step, the overall effect on the total pressure drop for the filter will be determined.

The modeling described immediately below pertains to the first step, where uniform distribution of deposits among the channels is assumed, so that the analysis can be performed on one pair of inlet and exit channels and extended to the entire filter by symmetry. This approach has largely been used across previous studies [57, 85, 59].

4.2 Impermeable Solid-Plug Mid-Channel Congestion (MCC) Model

Figure 4-1, a copy of Figure 1-26, shows a simple schematic of the mid-channel (MCC) solid-plug scenario for the simulation. From X-Ray CT imagery data, we noticed that there could be multiple plugs (congestions) along the same channel, of various lengths. However, for a solid plug, the location of the edge of the first (most-upstream) plug matters most. The length of the plug or the presence of subsequent plugs will have negligible impact, as there is no flow behind the first solid plug. In Figure 4-1, since the MCC plugs are impermeable, they act like regular ceramic plugs at the ends of the inlet channels. Upstream of the MCC plugs, the same flow equations as in [57] apply to both the inlet and exit channels. However, the boundary conditions are different from the classical analyses, e.g. [56, 57]. Accordingly, the restrictions, flows, and pressure drops are different. The results are presented below and the details in Appendix B. Downstream of the MCC plugs, there is essentially pipe flow in the exit channels, at a constant (steady, incompressible) exit velocity.

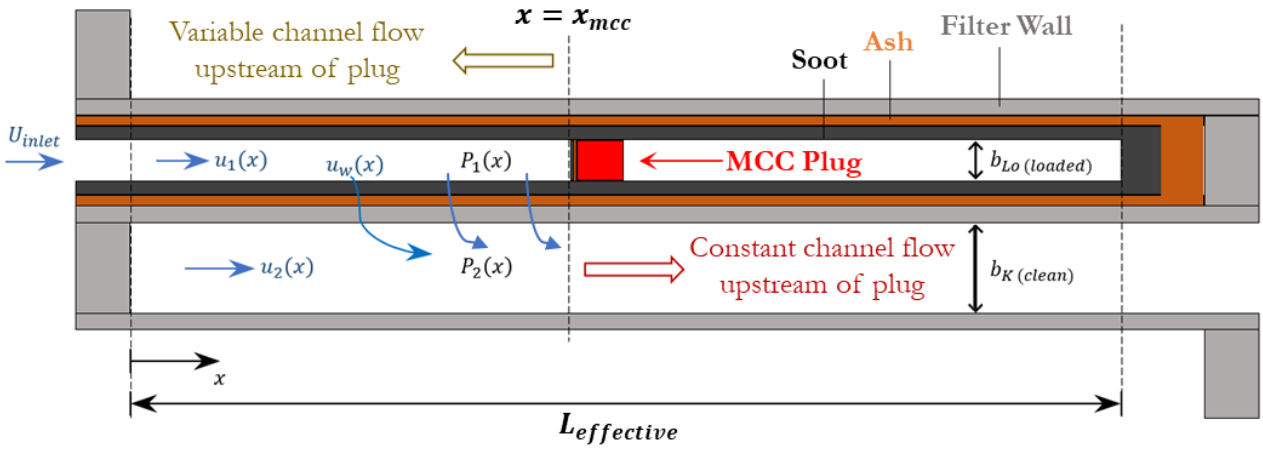

Figure 4-1: Schematic of the MCC Solid-Plug Model, as per Figure 1-26.

Following traditional analyses, we define the following five variables as functions of the axial location, x, along the channels, as shown in Figure 4-1:

- the one-dimensional flow velocities $u_1(x)$, $u_2(x)$ in the inlet and exit channels respectively;
- the pressures $p_1(x)$, $p_2(x)$ in the inlet and exit channels respectively; and
- $u_w(x)$ as the wall velocity of the flow through the substrate wall, ash and soot layers.

The next question is to determine which type of model we seek to develop: one based on parametric studies to determine the coefficients of dominant dimensionless terms, or instead apply a more rigorous approach involving solving a nontrivial set of conservation equations that, given their nonlinear nature, may result in a solution that requires numerical analysis via—for example—the shooting method for solving implicit differential equations. The option involving straightforward nondimensional terms requires using ample empirical data to validate the values of coefficients. In the absence of such data, we opt for the more arduous approach, and thereby default to our conservation equations, whose simultaneous solution is now modified by virtue of new boundary conditions imposed on the problem by the presence of unplanned, upstream channel congestion.

We thus correspondingly apply five equations, consisting of mass and momentum balances in the inlet and outlet channels, and the flow equation across the filtration layers (wall, soot and ash layers). The five equations—which were introduced by Konstandopoulos who in turn drew his inspiration from Bissett—are non-dimensionalized and simplified in Appendix B. Reworking the usual fundamental equations, as discussed in detail in the appendix, and dropping a non-linear term involving $\hat{u}_2 \frac{d\hat{u}_2}{d\hat{x}}$ in equation B.16, we arrive at, for the case of purely Darcian flow through the substrate wall and deposit layers (i.e. no Forchheimers nonlinear term in wall velocity), the following

basic equation for the exit channel, upstream of the MCC plug, which is a single differential equation in the dimensionless outlet channel velocity $\hat{u}_2$:

$$\frac{d^2\hat{u}_2}{d\hat{x}^2} - 2\frac{A_1}{B_1}\frac{b_K^2}{b_{Lo}^2}\frac{d\hat{u}_2}{d\hat{x}} - \left(1 + \frac{b_K^4}{b_{Lo}^4}\right)\frac{A_2}{B_1}\hat{u}_2 + \frac{b_K^2}{b_{Lo}^2}\frac{A_2}{B_1} = 0 \tag{4.1}$$

Where A_1, A_2, and B_1 are constants involving geometric, flow, soot, ash and filter substrate material parameters. A more detailed derivation is provided in Appendix B.

4.3 Derivation of the Closed-Form Solution for the Mid-Channel Collapse (MCC) Pressure Drop Model for Solid Plugs

The major difference between the MCC model and the traditional honeycomb filter simulations, such as those in Konstandopoulos et al. [56, 57] and Gaiser et al. [59], lies in the fact that in the MCC situation there is mid-channel clogging, in contrast to just ash and soot accumulation as end-plugs and uniform cake layers in earlier simulations. With mid-channel plugging, the channel flows and the wall flow through the honeycomb wall equations are only applicable in a portion of the filter (up to 50% or more and in some cases less). The boundary conditions are therefore different from traditional analyses. Although the derivation is straightforward, for the convenience of future users, the new formulation and solution for the MCC case are presented below:

The basic mass and momentum balance equations and the flow-across-channel-wall equation (total of five) for the applicable region still remain applicable in the current analysis. The key is that they are applicable in the filtration region only up to the location where the MCC plug begins. Due to the different boundary conditions, the final solution takes a different form, which converges to the conventional expressions [1,2] when the mid-channel plug is located at the end of the channel.
For easy reference and completeness, the five aforementioned mass, momentum balance and the flow-across-wall equations are summarized in Appendix B, up to the axial location of the occurrence of the MCC plug, per Figure 4-1 at:

$$x = x_{mcc} = m$$

Equation B.40 reduces to the special case of an unloaded clean filter with no mid-channel congestion (MCC), as originally derived by Konstandopoulos et al. in [56]. B.39 should be used for a loaded filter with mid-channel congestion.

Velocities are normalized by the inlet velocity, U, for example,

$$\hat{u}_2 = \frac{u_2}{U}$$

Equation (4.1) is of the form (see Appendix equation B.17 as well):

$$\frac{d^2\hat{u}_2}{d\hat{x}^2} - 2A_{1L}\frac{d\hat{u}_2}{d\hat{x}} - 2A_{2L}\hat{u}_2 + A_{3L} = 0 \tag{4.2}$$

Where,

$$A_{1L} = \frac{A_1}{B_1}\frac{b_K^2}{b_{Lo}^2}A_{2L} = \left(1 + \frac{b_K^4}{b_{Lo}^4}\right)\frac{A_2}{2B_1} \quad A_{3L} = \frac{b_K^2}{b_{Lo}^2}\frac{A_2}{B_1} \tag{4.3}$$

The boundary conditions are as follows, using the non-dimensionalization in the appendix. For simplicity, the flow changes in the short distance of the ceramic plug length at the inlet of the channel are not considered for simplicity.

For an MCC plug located at $x = x_{mcc}$, $m = \frac{x_{mcc}}{L}$ (non-dimensional MCC plug location),

$$\hat{u}_2(0) = 0, \tag{4.4a}$$

$$\hat{P}_2(1) = 0 \tag{4.4b}$$

at the MCC plug location in the outlet channel and constant thereafter, and $\hat{u}_1(m) = 0$, which via continuity is equivalent to:

$$\hat{u}_2(m) = \frac{b_{Lo}^2}{b_K^2} \tag{4.4c}$$

For the exit pressure in the outlet channel up to the start of the pipe flow,

$$\hat{P}_2(\hat{x} = m) = A_{2L}(1 - m) \tag{4.4d}$$

Boundary conditions are the above collective equations (4.4a, 4.4b, 4.4c, and 4.4d). A closed-form solution to equation (4.2) exists in which the exit velocity is given by:

$$\hat{u}_2(\hat{x}) = c_1 e^{q_1 \hat{x}} + c_2 e^{q_2 \hat{x}} + c_3 \tag{4.5}$$

for the proper choice of the characteristic values of $c_1, c_2, \ and \ c_3$, which are all functions of material and geometric parameters. Their values are solved and given in Appendix B.

$$\hat{u}_1(\hat{x}) = 1 - \hat{u}_2(\hat{x}) \frac{b_K^2}{b_{Lo}^2} \tag{4.6}$$

for $\hat{x}$ from 0 to m in the filtering section upstream of the MCC plug. Likewise, the pressures in the inlet and exit channels can be evaluated once the velocities are known (per Appendix B). The pressure drop across the entire filter is then given by:

$$\Delta \hat{P}_{total} = A_{1L} \frac{b_{Lo}^4}{b_K^4} + A_{2L} \left[\frac{c_1}{q_1} (e^{q_1 m} - 1) + \frac{c_2}{q_2} (e^{q_2 m} - 1) + c_3 m + 1 - m \right] + \\ + B_1 (c_1 q_1 + c_2 q_2) \tag{4.7}$$

Using the solid-plug model above, the effects of MCC plug axial location can be quantitatively evaluated.

4.4 Impact of MCC Axial Plug Location, Timing of MCC Formation, and Ash Loading Level

The severity of the MCC problem, as shown by the increase in DPF backpressure compared to the absence of mid-channel congestion, is illustrated in Figure 4-2. We observe the following from the results depicted in the figure:

1. The MCC problem can easily increase the filter pressure drop by a factor of two and for many conditions by several times the normal pressure drop compared to when orderly loading of deposits towards the back of the channel occurs. Since the pressure-drop-rise factor around the major service interval is about two or less, the MCC occurrence depicted dictates that the DPF requires premature major service.

2. The severity of the MCC problem increases when the MCC clogging occurs closer to the entrance of the filter. The restriction increases sharply towards the entrance direction.

3. At higher loading levels, say at 20 g/L of nominal filter volume or higher, the problem is quite acute due to the smaller available volume left for ash and soot accumulation.

4. The timing of formation of MCC plugs has a significant impact on subsequent performance of the DPF. Early formation of MCC is worse than late formation. There is a factor of two difference in pressure drop levels comparing the case where the MCC plug is formed early (at time = 0) against the other extreme case of the MCC plug forming late. The reason is that when MCC is formed early, subsequent ash and soot will pile on in front of the MCC plug in a much-shortened inlet channel operating length.

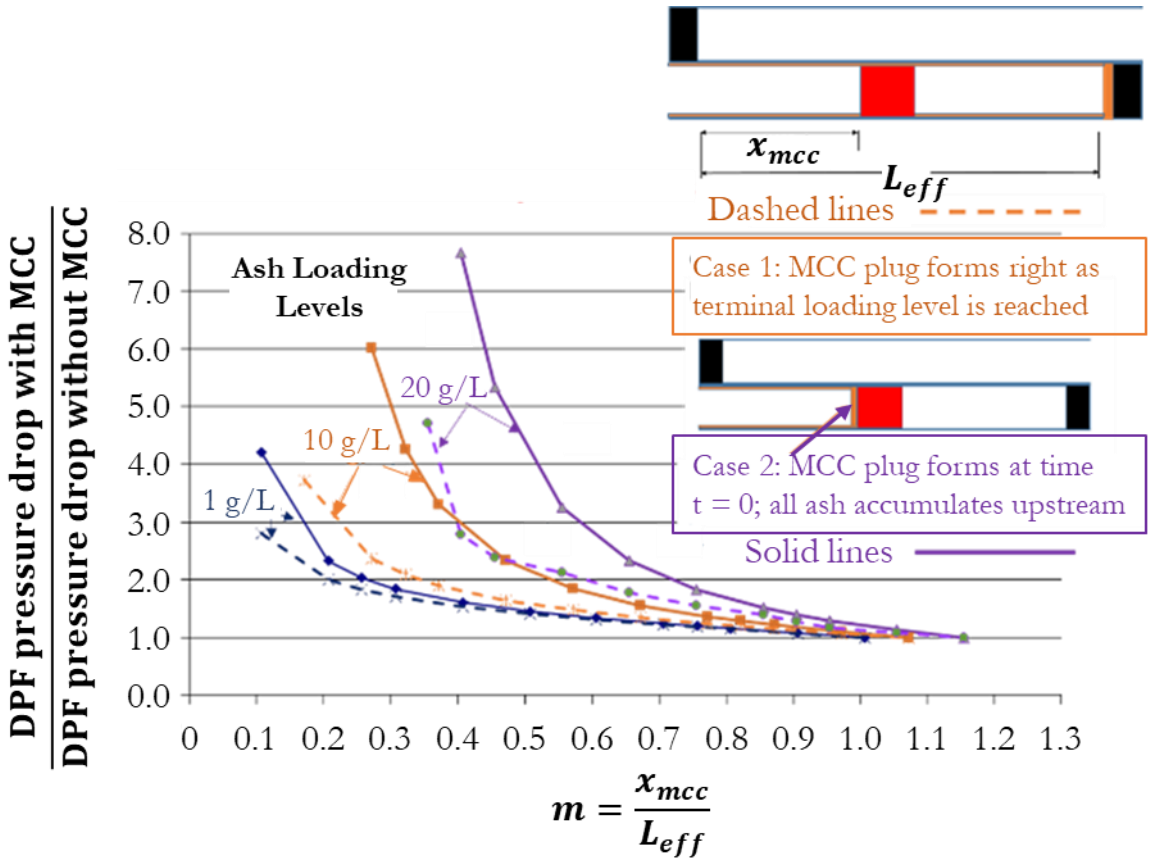

Figure 4-2: Impact of MCC location $m = \frac{x_{mcc}}{L_{eff}}$, ash loading level, and timing of MCC formation on severity of the MCC Problem (e.g., very early versus very late during loading). The plots are based on numerical simulation of ash-only loaded DPFs with uniform channel agglomerates. Ash loading therefore reflects the thickness of the ash layer above the DPF wall interface.

DPF geometric and engine operating parameters corresponding to results presented in Figure 4-2 are given in Table 4-1.

Table 4-1. Simulation DPF geometric and engine operating input parameter values.

DPF Operating Parameter	Applied Value
Cells Per Square Inch (CPSI)	300
Length (cm)	30.48
Space Velocity (1/hr)	40,000
Exhaust Temperature (°C)	350

4.5 Effects of Non-Uniform Radial Distribution of MCC Deposits on Fraction of All Channels plugged

When not all the channels are plugged, the flows in the individual channels redistribute themselves such that the pressure drop from the inlet to the outlet of the DPF maintains a common pressure difference across each of the channels, much like a parallel circuit that enforces a uniform voltage drop between any two prescribed nodes. The fluid mechanics of the flow distribution is analogous to the electrical network model, and is illustrated in Figure 4-3, where the electric currents are replaced by exhaust volumetric flows and the voltage difference corresponds to the pressure drop.

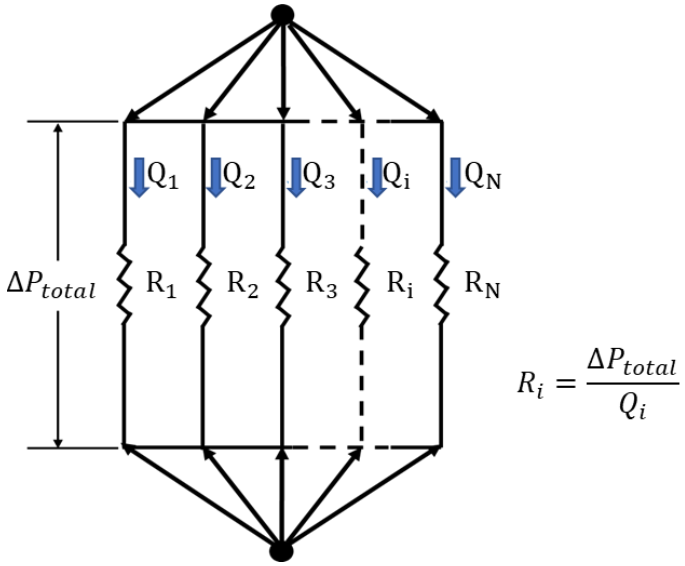

Figure 4-3: Resistance network reflecting axially non-uniform ash agglomeration in channels exhibiting MCC.

Let x be the fraction of channels that are plugged with flow resistance R_{mcc}, and $(1-x)$ the fraction of channels with resistance R_{nmcc}. The subscripts designate mid-channel clogging (MCC)

and no mid-channel clogging (n_{mcc}). The overall resistance (defined as $\frac{pressure\ drop}{flow\ rate}$) of the set of parallel channels is given by:

$$\frac{1}{R_{total}} = \frac{x}{R_{mcc}} + \frac{(1-x)}{R_{nmcc}} \tag{4.8}$$

Letting $r = \frac{R_{mcc}}{R_{nmcc}}$, it can easily be shown that

$$\frac{R_{total}}{R_{nmcc}} = \frac{r}{[r - x(r-1)]} \tag{4.9}$$

Performance results for some insightful examples of non-uniform radial plugging of the filter are shown in Figure 4-4. Plugging is varied by axial location of solid, impermeable agglomerates and the fraction of inlet channels actually plugged. Note how the availability of unplugged channels limits the severity of the MCC problem. Regardless of the degree to which the clogged channels are restricted, the open channels will still allow flow to pass through for significantly lower resistance. It turns out that the fraction of open channels determines to a great extent the overall pressure-drop across the overall filter. Conversely, the MCC problem becomes very acute when all the channels become plugged in the upstream region.

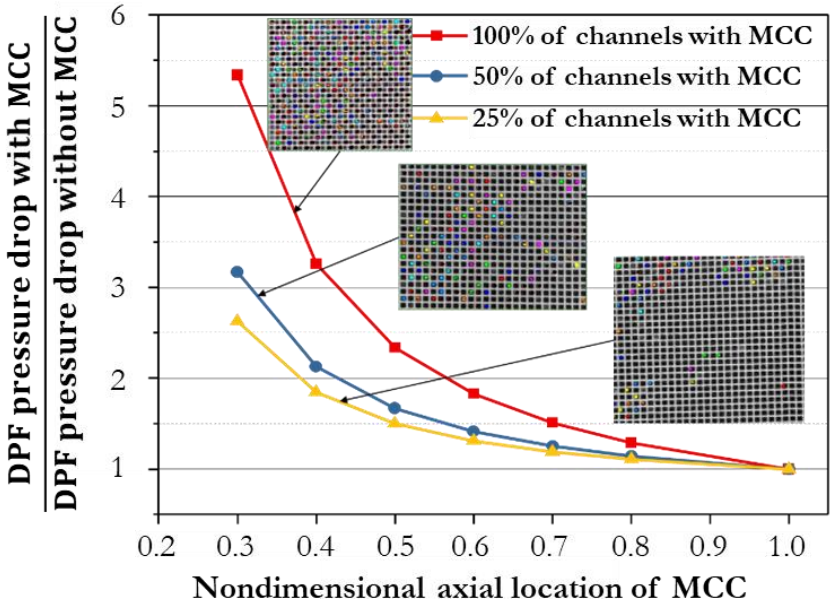

Figure 4-4: Effects of non-uniform and fractional plugging of all channels in a filter. Data is based on numerical simulation, with corresponding frontal cross-sectional plugging illustrated by sample scan images.

4.6 Permeable or Porous Mid-Channel Congestion (MCC) Model

When MCC plugs are not solid but instead permeable, or when they do not occupy the entire channel flow area, some exhaust flow is able to pass through the MCC plugs. In this case, the closed form solution as presented in the previous section does not apply, especially when the restriction varies along the channel, i.e. variable restriction as a function of axial distance. In such a case, a numerical solution to the original flow equations in the inlet and outlet channels is required and was used. For porous plug media, we can model the flow that corresponds to laminar flow, i.e.,

$$Pressure\ Drop \propto\ flow\ velocity$$

After all, Darcy's law for flow through a porous medium (i.e. "medium") is given by [86]:

$$\Delta P_{Drop,Darcy} = \frac{Q \cdot \mu \cdot L}{k \cdot A}$$

Q is the volumetric flow rate, μ the dynamic viscosity of the fluid passing through the medium, L the length of the medium in the flow direction, k the permeability of the medium, and A the cross-sectional area of the flow. In such a case, the composite friction factor (regular channel friction plus permeable plug restriction) becomes:

$$F = \frac{K}{Re} \tag{4.10}$$

with some proportionality constant, K. In such a case, the same form of the momentum equation applies to the channels with modified effective friction. Given this form of flow restriction for the MCC deposits, we can model the additional restriction due to the MCC plug(s) by applying an amplification factor (which varies with axial distance) as shown in Figure 4-5.

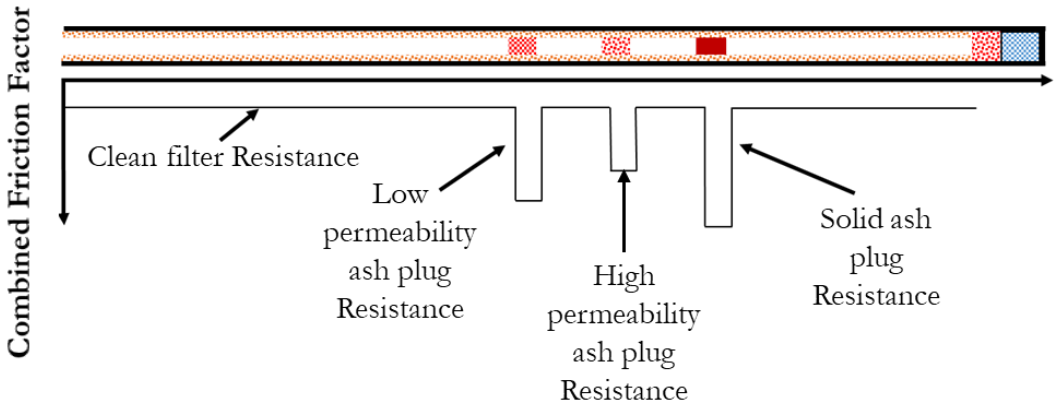

Figure 4-5: Combined MCC restriction indicated via combined friction factor versus axial distance for permeable ash agglomerates.

Notice in Figure 4-5 that there can be multiple MCC plugs in a channel that impose variable flow restrictions. The numerical model was solved using the usual "shooting method" [56, 57]. Results of the effects of the plugging intensity (degree to which the plug is permeable to flow) are shown in Figure 4-6, where "overall resistance" is simply the amplification factor described immediately above. Notice that in the extreme case the partial flow/plug model asymptotically converges to the solid plug model when the degree of plugging becomes very large (i.e. in the limit as the plug becomes fully solid and thus impermeable). The solid plug model results are provided at the far right of the permeable plug simulation predictions in Figure 4-6 below.

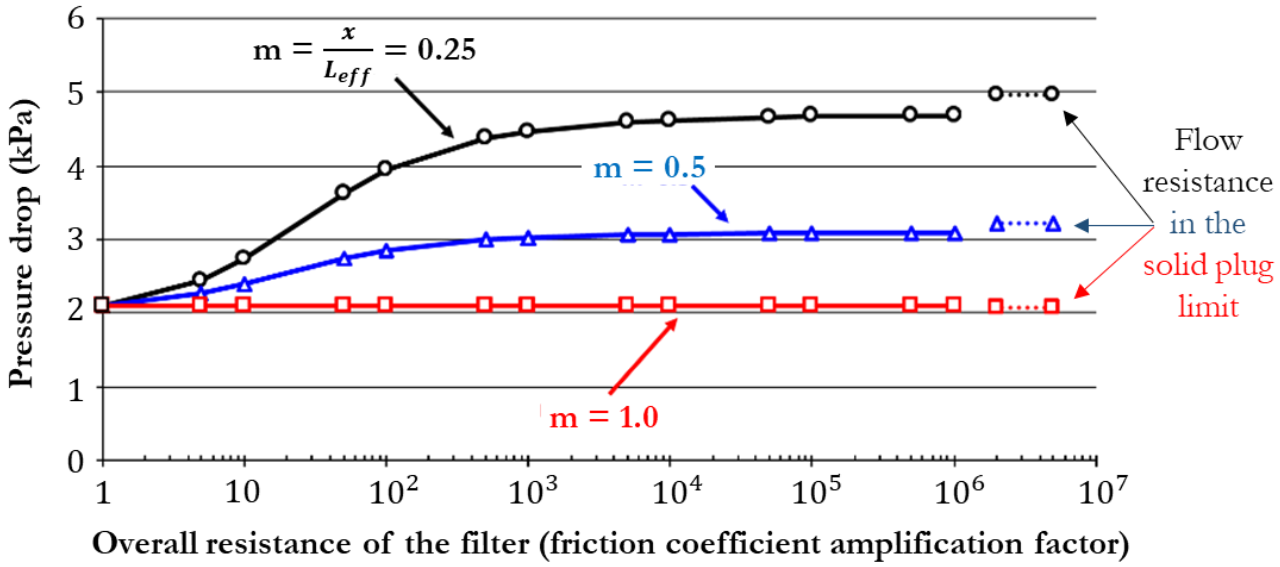

Figure 4-6: Effects of the degree of permeability (and thus resistance) of the MCC plugs on pressure drop. The data points offset to the right indicate converged pressure drop as overall resistance approaches ∞ and are thus reflective of the solid plug model.

Effects of the various types of MCC plugging are shown in Figure 4-7. In Figure 4-7, we consider several plugs along the same channel at various levels of restrictions.

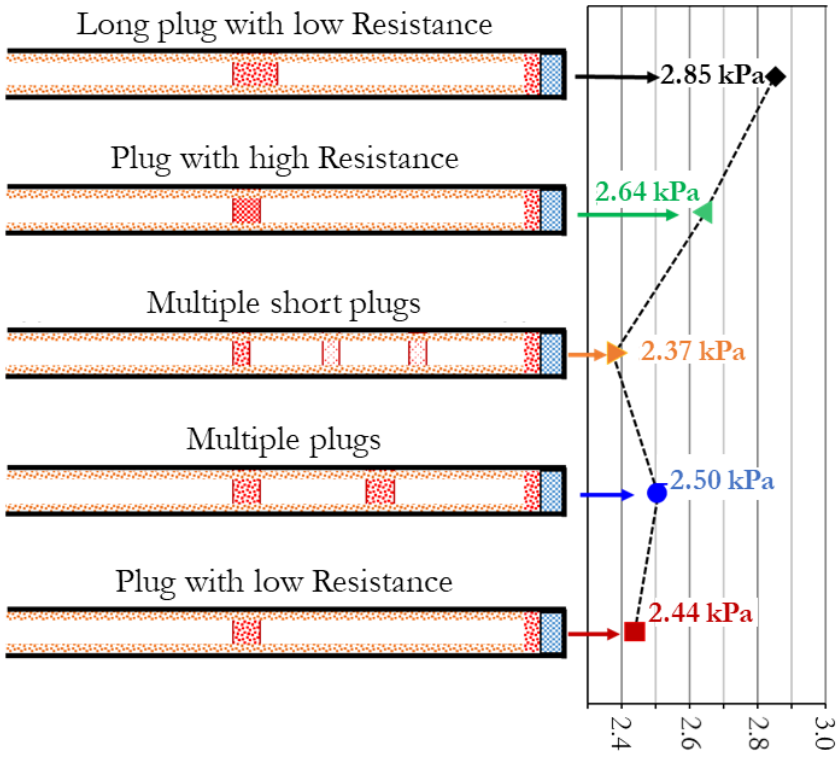

Figure 4-7: Effects of MCC plug position and effective resistance on channel backpressure. Assume nominal values for properties that are not included in a given MCC instance's description.

The results show that the position and level of plugging of the foremost MCC plug are the most important. Subsequent plugs behind the first plug exposed to the full flow have lowered effects. The implication is that the position of the first plug is most important.

4.7 Comparison Between Simulations and Experimental Data

Using the following input information from the image measurements, we exercised the computer simulations and checked against the experimental observations of the pressure drop:

(a) axial locations of MCC plugs in each case; and

(b) fraction of channels in the radial cross section that contain mcc plugs (none of the cross sections experience 100% of channels plugged).

Since the permeability of the ash deposits has a large effect on channel pressure drop, we selected the appropriate value by calibrating against one set of data (the soot/ash ratio = 0.25 case). The same permeability was maintained for all the other cases calculated. The results of the comparisons are shown in Figure Table 4-2.

Table 4-2: Comparison between MCC simulation against experimental pressure drop data.

Soot-Ash Ratio	Loading Level (g/L)	Experimental Pressure Drop (kPa)	Simulated Pressure Drop (kPa)	% Difference
0.25	3.5	6.9	6.9	0%
1	8.7	7.7	7.7	0%
2.5	6.5	8.2	7.3	-11%
8	5.1	8.7	8.2	-6%

Notice in Table that there is very good agreement between theory and experiments. The simulations are based on the physical effects due to flow restrictions only and therefore are not perfect. No account is made yet as of this manuscript (but will be) of the effects of soot/ash ratio on ash layer temperature and thus the possibility of partial sintering affecting the ash layer permeability, which was kept constant, though the model presented in Chapter 5 may be used to do so. Another limitation is that the simulation results from the fraction of channels plugged and the observed plugging locations are only as good as the quality of the input data. This may be compromised in the case of low-quality image data, e.g., significant "N" scores per the convention used in Chapter 3. In the case of S/A = 2.5, the discrepancy could be due to one or both of the following:

(1) if partial sintering occurs in the ash layer, the permeability of the ash layer may decrease resulting in a higher pressure drop; and
(2) if the fraction of channels plugged is higher than what is optically observable, the predicted pressure drop should correspondingly be increased.

In any case, the discrepancy between the predicted results and the measured data varied by about only 10%, which could be further improved by accounting for more effects and influences on ash-layer permeability, for example. In the absence of any 'adjustable parameters', the simulation is remarkably good, which suggests that the conceptual model accounts for the major mechanisms driving backpressure in plugged DPF channels.

4.8 Additional Sensitive Analysis for Select Mechanical Properties on DPF Performance

We may conduct sensitivity analyses showing the impact of varying ash mechanical properties on backpressure in a given channel. Two key parameters include ash permeability and density. As expected and as illustrated in Figure 4-8 below, significantly reduced ash permeability will give rise to a substantial pressure rise since the exhaust must pass through the ash layer as it exits the deposit-laden channels, though as ash permeability increases, the resistance associated with ash tapers off, yielding very strongly diminishing returns after reaching around 10^{-13} m^2.

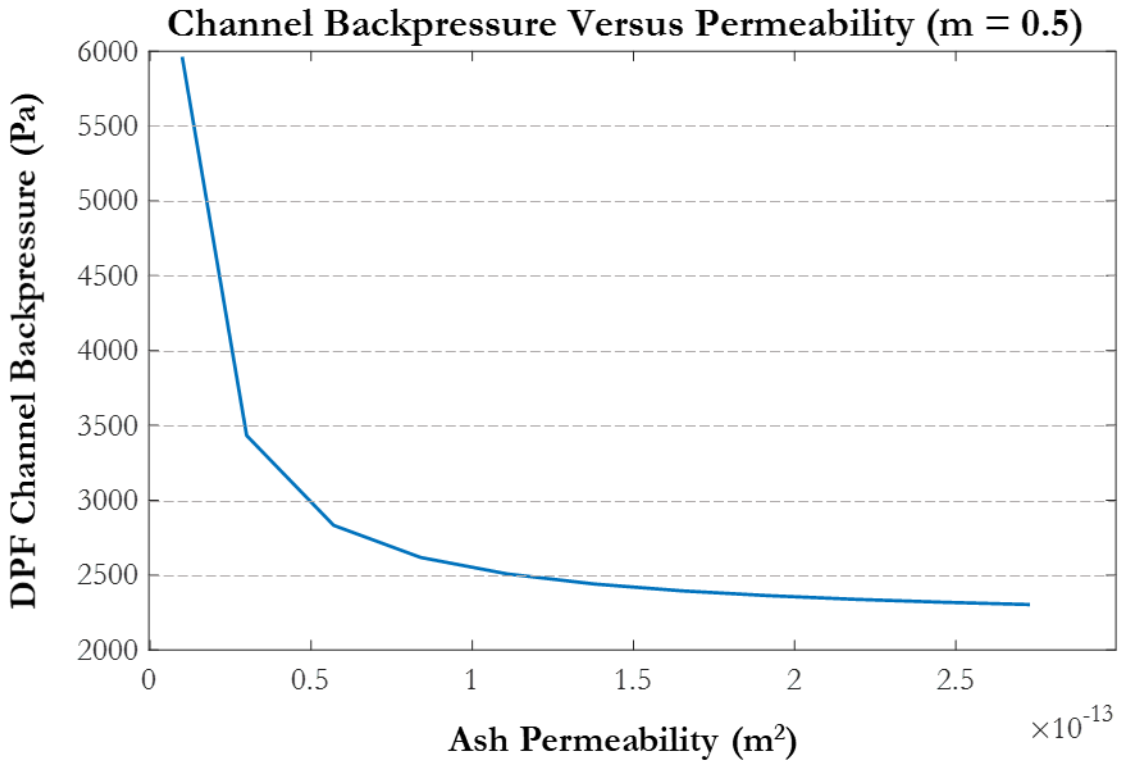

Figure 4-8: Impact of ash permeability on DPF backpressure, assuming the presence of a solid ash plug at mid-channel (i.e. $m = \frac{x_{mcc}}{L_{eff}} = 0.5$).

In a similar vein—shown in Figure 4-9—as ash density decreases for a given amount of deposited ash, we experience significant volume growth, which restricts flow through both the channels and porous sidewalls. Diminishing returns are similarly seen as density increases, effectively reducing the relevance of ash resistance on overall DPF pressure drop compared to other contributing factors, such as channel losses and flow through the ostensibly fixed DPF wall substrate.

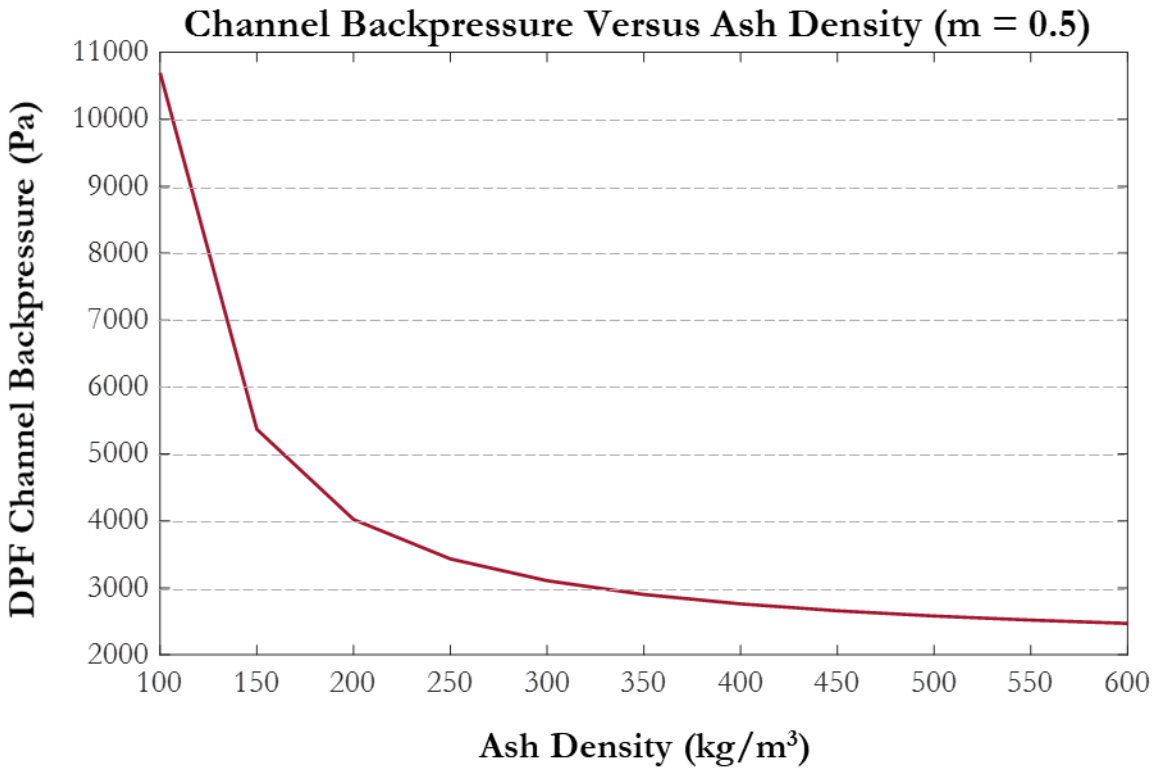

Figure 4-9: Impact of ash density on DPF backpressure, assuming the presence of a solid ash plug at mid-channel (i.e. $m = \frac{x_{mcc}}{L_{eff}} = 0.5$).

5 Extending the Thermal Regeneration Model to Investigate MCC

Arguably the most important item in this thesis involves understanding the temperature history of the particulate matter as it enters the DPF, oxidizes from soot into ash, and subsequently undergoes a transport process. During the transport process, PM either remains in place on the cake layer or in the end plug throughout regeneration, or instead separates from the cake layer and is relocated to another axial location within the DPF channel, which may give rise to undesirable MCC. Chapter 2 contains very strong arguments suggesting that sintering plays a pivotal role in the onset of MCC, such as the direct illustration of cake layer collapse presented in Figure 2-11.

This section presents the industry standard thermal regeneration model—written by Bissett of General Motors in 1983—in a new, arguably more streamlined way [26]. After all, key players in this field have explicitly called out Bissett's model as "nontrivial," which have resulted in the development of "fast[er] and [more] reliable algorithms for this task" [87]. The present work also extends the analysis to include simulations of DPF channels that are experiencing the onset of MCC—that is, channels in which soot agglomerations have formed along the otherwise smooth, uniform cake layers. The intent is to determine whether regeneration produces conditions conducive to fusion of relocated deposit layers to the cake layer, and whether the presence of additional PM on the surface of the channel walls promotes the adhesion (e.g., via sintering) of that PM to the wall.

Note that while in his Ph.D. dissertation, MIT's Yujun Wang concluded that distribution of the deposit / cake layer surface (e.g., flat versus wavy versus jagged) had an insignificant impact on DPF performance in terms of backpressure, he did not extend his analysis to considering the impact of various cake layer geometry on local or global temperature history [78]. We therefore provide here an investigation into changes to ash morphology and transport behavior that may result from variations in PM layer distribution, such as that of newly introduced PM onto the cake layer prior to regeneration. Doing so is, of course, important given a prevailing theory that collapse of PM from one location of the cake layer followed by deposition onto and bonding to another location is a primary mechanism for the onset of MCC.

What we will uncover in this chapter is twofold:

1. The temperature history of the DPF substrate and attached PM layer exceeds the sintering temperature of common metals included in diesel engine lubricants (e.g., zinc).

2. While the introduction of new PM material onto the cake layer does affect local temperatures during regeneration, those effects seem to be small and inconsequential in terms of having an effect on ash morphology (e.g., propensity for sintering at that location).

5.1 Regeneration System of Interest with Key Assumptions and Parameters

The system of equations models the flow in the DPF as a laminar flow in a square channel with nonporous walls, together with a much smaller transverse velocity component representing flow through the wall system (i.e. through the deposit layer and porous side walls) resulting in a model with a single spatial variable, x (given as z in [26]). A schematic showing one pair of inlet and outlet channels, with corresponding variables of interesting, is given in Figure 5-1.

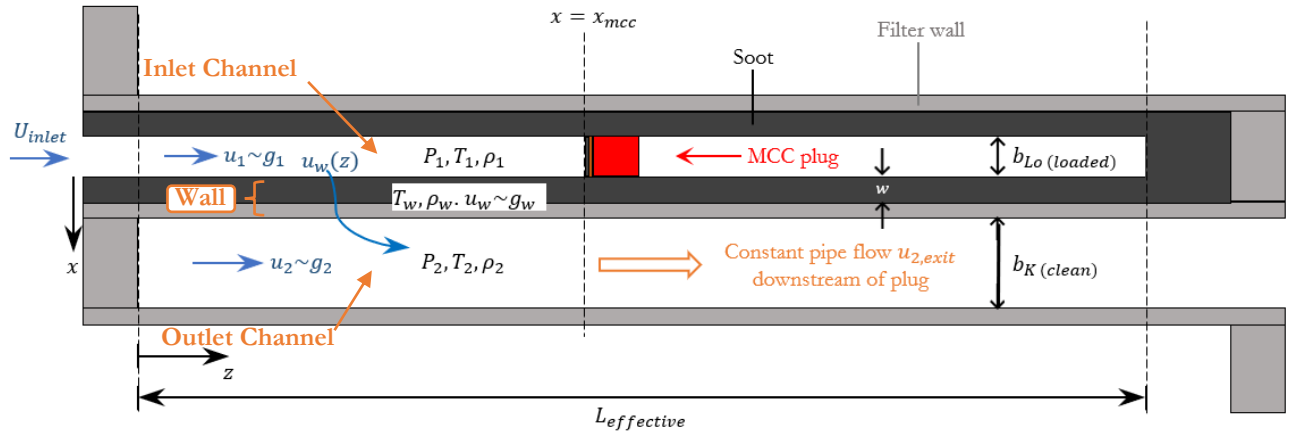

Figure 5-1: A schematic of the system of interest tailored to illustrating key parameters of interest in the thermal regeneration model.

Much of this setup—including governing equations, as we will see—is identical to that applied in the performance backpressure model above, though we notice that an underlying ash layer is neglected and that the wall region consists of a combustible deposit layer sitting atop the filter wall substrate (e.g., cordierite or silicon carbide).

5.1.1. Key Assumptions for Thermal Regeneration Model

1) Gas entering the monolith is spatially uniform (but possibly time-dependent) and the outer walls of the monolith are assumed to be perfectly insulated, which are both reasonable.
2) The inlet oxygen mass fraction is constant.
3) The inlet mass flow rate is constant.

4) Initial deposit layer thickness may be arbitrarily specified at the walls.
5) Conduction through the wall is so dominant that the temperature through of the wall region T_w may be taken as independent of x, such that T_w is also the temperature of the channel gas inside and "just outside the wall system [26]". Hence, the substrate, ash, and deposit layer are all lumped into a single thermal entity.
    a) Thus, the transverse temperature profile in a channel cross section is determined by wall temperature T_w and average cross section temperature T_i.

Model parameters are provided in Appendix B. Notes on these parameters include:

1) Since there is considerable radial variation in density, velocity, and temperature, the variables $\rho_i, u_i,$ and T_i represent average quantities over a channel cross section, typical for 1D channel flow modeling.
2) The variable i takes on one of two values: 1 for the inlet channel and 2 for the outlet channel.
3) The term $\bar{u}_i$ was not explicitly defined in Bissett's paper and is not included in the final system of equations, so is not yet expressed here.

5.2 System of Equations to be Solved with Boundary Conditions

Our system of differential equations is as follows. The ideal gas law stipulates that:

$$1 = \bar{\rho}_1 \cdot \bar{T}_1 \rightarrow \bar{\rho}_1 = \frac{1}{\bar{T}_1} \tag{5.1}$$

$$1 = \bar{\rho}_2 \cdot \bar{T}_2 \rightarrow \bar{\rho}_2 = \frac{1}{\bar{T}_2} \tag{5.2}$$

$$1 = \bar{\rho}_w \cdot \bar{T}_w \rightarrow \bar{\rho}_w = \frac{1}{\bar{T}_w} \tag{5.3}$$

Applying Darcy's law for flow through porous media yields:

$$\bar{P}_1 - \bar{P}_2 = \left(\bar{\mu}(T_w) \cdot \bar{u}_w + B_7 \overline{\rho_w u_w}^2\right)\left(B_8 + \bar{\phi}(\bar{w})\right) \tag{5.4}$$

Conservation of mass dictates that:

$$\frac{\partial}{\partial \bar{z}} \bar{G}_1 = -\overline{\rho_w u_w} \tag{5.5}$$

$$\bar{G}_2 = \bar{G}_f - \bar{G}_1 \tag{5.6}$$

Conservation of momentum for the channel gas provides:

$$\frac{\partial}{\partial \bar{z}} \left(\bar{P}_1 + \frac{B_1 \bar{G}_1^2}{\bar{\rho}_1} \right) = \frac{-B_2 \bar{\mu}(\bar{T}_1) \cdot \bar{G}_1}{\bar{\rho}_1} \tag{5.7}$$

$$\frac{\partial}{\partial \bar{z}} \left(\bar{P}_2 + \frac{B_1 \bar{G}_2^2}{\bar{\rho}_2} \right) = \frac{-B_2 \bar{\mu}(\bar{T}_2) \cdot \bar{G}_2}{\bar{\rho}_2} \tag{5.8}$$

Note that to facilitate integration efforts, we may recast part of these equations as follows:

$$\frac{\partial}{\partial \bar{z}} \left(\frac{\bar{G}_i^2}{\bar{\rho}_i} \right) = \bar{G}_i^2 \frac{\partial}{\partial \bar{z}} \left(\frac{1}{\bar{\rho}_i} \right) + \frac{2\bar{G}_i}{\bar{\rho}_i} \frac{\partial \bar{G}_i}{\partial \bar{z}}$$

Conservation of energy for the channel gas gives:

$$\bar{G}_1 \frac{\partial \bar{T}_1}{\partial \bar{z}} = \left(-\overline{\rho_w u_w} + B_3 \bar{\mu}(\bar{T}_1) \right) (\bar{T}_w - \bar{T}_1) \tag{5.9}$$

$$\bar{G}_2 \frac{\partial \bar{T}_2}{\partial \bar{z}} = \left(\overline{\rho_w u_w} + B_3 \bar{\mu}(\bar{T}_2) \right) (\bar{T}_w - \bar{T}_2) \tag{5.10}$$

Then we may also specify a set of "burn" equations for soot oxidation and heat transfer during regeneration:

$$\frac{\partial \bar{w}}{\partial \bar{t}} = -\bar{Y}_f \overline{\rho_w u_w} \left(1 - e^{-\frac{\bar{k}(\bar{T}_w)\bar{w}}{\bar{u}_w}} \right) \tag{5.11}$$

$$\overline{C_p}(\bar{w}, \bar{T}_w) = \left(1 + \bar{T}_w \frac{\partial}{\partial \bar{z}} \right) \cdot \left(\overline{C_{ps}}(\bar{T}_w) + \bar{w} \cdot \overline{C_{pp}}(\bar{T}_w) \right) \tag{5.12}$$

$$\overline{C_p}(\bar{w},\bar{T}_w)\cdot\frac{\partial\bar{T}_w}{\partial\bar{t}}=B_4\left[\frac{\partial^2\bar{T}_w}{\partial\bar{z}^2}+B_5\frac{\partial}{\partial\bar{z}}\left(\bar{w}\frac{\partial\bar{T}_w}{\partial\bar{z}}\right)\right]-B_3[\bar{\mu}(\bar{T}_1)\cdot(\bar{T}_w-\bar{T}_1)+$$
$$\bar{\mu}(\bar{T}_2)\cdot(\bar{T}_w-\bar{T}_2)+\left[B_6+\overline{C_{pp}}(\bar{T}_w)\cdot\bar{T}_w\right]\cdot\bar{Y}_f\overline{\rho_w u_w}\cdot\left(1-e^{\frac{\bar{k}(T_w)\bar{w}}{\bar{u}_w}}\right)\qquad(5.13)$$

Rearranging (4), or Bisset (48), into a quadratic equation dependent on $\bar{u}_w$ yields:

$$\left(B_8+\bar{\phi}(\bar{w})\right)\cdot B_7\bar{\rho}_w\cdot{\bar{u}_w}^2+\bar{\mu}(\bar{T}_w)\cdot\left(B_8+\bar{\phi}(\bar{w})\right)\cdot\bar{u}_w+\bar{P}_2-\bar{P}_1=0$$

This equation can be solved and the positive root used to substitute for $\bar{u}_w$ as a function of $(\bar{T}_w,\bar{w},\bar{P}_1,\bar{P}_2)$ in our system of equations:

$$\bar{u}_w=-\bar{\mu}(\bar{T}_w)\cdot\left(B_8+\bar{\phi}(\bar{w})\right)\pm\frac{\sqrt{\bar{\mu}(\bar{T}_w)^2\cdot\left(B_8+\bar{\phi}(\bar{w})\right)^2-4\cdot\left(B_8+\bar{\phi}(\bar{w})\right)\cdot\frac{B_7}{\bar{T}_w}\cdot(\bar{P}_2-\bar{P}_1)}}{2\cdot\left(B_8+\bar{\phi}(\bar{w})\right)\cdot\frac{B_7}{\bar{T}_w}}$$

Alternatively, since the quadratic term is generally small, we may (and in this case do) simplify by neglecting that term:

$$\frac{\partial}{\partial\bar{t}}\left[\left(\overline{C_{pp}}(\bar{T}_w)\bar{w}+\overline{C_{ps}}(\bar{T}_w)\right)\bar{T}_w\right]$$
$$=B_4\left[\frac{\partial^2\bar{T}_w}{\partial\bar{z}^2}+B_5\frac{\partial}{\partial\bar{z}}\left(\bar{w}\frac{\partial\bar{T}_w}{\partial\bar{z}}\right)\right]-B_3[\bar{\mu}(\bar{T}_1)(\bar{T}_w-\bar{T}_1+\bar{\mu}(\bar{T}_2)(\bar{T}_w-\bar{T}_2)]$$
$$+B_6\bar{Y}_f\overline{\rho_w u_w}\left(1-e^{-\frac{\bar{k}(T_w)\bar{w}}{\bar{u}_w}}\right)\qquad(5.14)$$

Furthermore, we may replace equations (5.12) and (5.13) above with Bissett (53) if desired to avoid the temperature time derivative term on the left-hand side of (5.13).

Initial and Boundary Conditions

Boundary conditions are provided at both $\bar{z}=0$ at the inlet of the channel at $\bar{z}=1$ at the channel's far end.

At axial position $\bar{z} = 0$:

$$\bar{T}_1|_{\bar{z}=0} = \bar{T}_f$$

$$\bar{G}_1|_{\bar{z}=0} = \bar{G}_f$$

$$\bar{G}_2|_{\bar{z}=0} = 0$$

$$\bar{T}_2|_{\bar{z}=0} = \bar{T}_w$$

$$\left.\frac{\partial \bar{T}_w}{\partial \bar{z}}\right|_{\bar{z}=0} = 0$$

At axial position $\bar{z} = 1$:

$$\bar{G}_1|_{\bar{z}=1} = 0$$

$$\bar{P}_2|_{\bar{z}=1} = 0$$

$$\left.\frac{\partial \bar{T}_w}{\partial \bar{z}}\right|_{\bar{z}=1} = 0$$

At time $\bar{t} = 0$:

$$\bar{T}_w = 1$$

$$\bar{w} = \bar{w}_b = 1$$

5.3 Solution Method

While Bissett solved the nonlinear, coupled, mixed algebraic and ordinary differential equations using LSODI, an extension of GEARIB that solves equations of the form $C\frac{d\bar{y}}{dt} = f(\bar{y})$, we instead make use of MATLAB's fully implicit differential equation solver ode15i together with its built-in $fsolve()$ and decic functions, as described further below.

Equations (5-5), (5-7), (5-8), (5-9), and (5-10) represents the "flow equations" in our system, while (5-11) and (5-13) make up the "burn equations," for a total of seven equations and seven

unknowns. The five "flow" equations are 1st-order ordinary differential equations that are solved via MATLAB solver. The two "burn" equations are solved via direct time integration (i.e. explicit integration following the establishment of prescribed initial conditions), as follows:

$$\bar{w}(t+\Delta t) = \left(\frac{\partial \bar{w}}{\partial \bar{t}}\right)\Delta t + \bar{w}(t) \tag{5.15}$$

$$\bar{T}_w(t+\Delta t) = \frac{\partial \bar{T}_w}{\partial \bar{t}}\Delta t + \bar{T}_w(t) \tag{5.16}$$

The $\frac{\partial}{\partial \bar{z}}$ terms were evaluated using center differencing, as follows, where subscript "i" denotes the x-coordinate index on the discretized grid:

$$\frac{\partial^2 \bar{T}_w}{\partial \bar{z}^2} = \frac{\bar{T}_{w,i+1} + \bar{T}_{w,i-1} - 2\bar{T}_{w,i}}{\Delta \bar{z}^2} \tag{5.17}$$

$$\frac{\partial}{\partial \bar{z}}\left(\bar{w}\frac{\partial \bar{T}_w}{\partial \bar{z}}\right) = \left(\bar{w}\frac{\partial \bar{T}_w}{\partial \bar{z}}\right)_{i+\frac{1}{2}} - \left(\bar{w}\frac{\partial \bar{T}_w}{\partial \bar{z}}\right)_{i-\frac{1}{2}} =$$

$$= \left(\frac{\bar{w}_i + \bar{w}_{i+1}}{2}\right)\left(\frac{\bar{T}_{w,i+1} - \bar{T}_{w,i}}{\Delta \bar{z}^2}\right) - \left(\frac{\bar{w}_i + \bar{w}_{i-1}}{2}\right)\left(\frac{\bar{T}_{w,i} - \bar{T}_{w,i-1}}{\Delta \bar{z}^2}\right) \tag{5.18}$$

The procedure for solving for DPF pressures, temperatures, deposit layer thickness, and velocities over time includes:

1. Establish a discretized, one-dimensional grid of equally spaced nodes that represent different axial locations along the DPF;
2. Specify the initial conditions corresponding to the "burn equations": soot thickness $\bar{w}(\bar{z})$ and wall temperature $\bar{T}_w(\bar{z})$ in the form of two row vectors with length equal to the grid size;
3. Find solutions to the "flow" equations:
   3a) guess values for $\bar{P}_1(\bar{z}=0)$ and $\bar{P}_2(\bar{z}=0)$, and then use MATLAB's $ode15i$ to integrate the system of five flow equations to find $\bar{P}_2(\bar{z}=1)$ and $\bar{G}_1(\bar{z}=1)$
   3b) use the built-in MATLAB function $fsolve()$ to find the correct $\bar{P}_1(\bar{z}=0)$ and $\bar{P}_2(\bar{z}=0)$ such that the boundary conditions $\bar{P}_2(\bar{z}=1)=1$ and $\bar{G}_1(\bar{z}=1)=0$ are met;

3c) repeat procedure 3a) with the converged values of $\bar{P}_1(\bar{z}=0)$ and $\bar{P}_2(\bar{z}=0)$ in order to yield the correct solution matrix containing $\bar{P}_1$, $\bar{P}_2$, $\bar{T}_1$, $\bar{T}_2$, and $\bar{G}_1$, each expressed as a row vector of length equal to that of the mesh.

4. Repeat from Step 2 for the next time step, using the newest values continued in the solution matrix, noting that auxiliary variables are solved for as a function of those in the solution matrix (e.g., $\bar{G}_2$ from equation (5-6) and $\bar{u}_w$ from equation (5-4). The implicit scheme is used because of the exponential dependence on $\bar{T}_w$ in (5-11).

$Ode15i$ is applied using the form:

$$[x, y] = ode15i\big(odefun, xspan, y_0, y_{0p}\big)$$

$Odefun$ is function of the form $f = (x, y, y_p)$ in which, for solution matrix y and lowercase indicating nondimensionalization:

$$\begin{aligned} p_1 &= y(1) & dp_1 &= y_p(1) \\ p_2 &= y(2) & dp_2 &= y_p(2) \\ t_1 &= y(3) & dt_1 &= y_p(3) \\ t_2 &= y(4) & dt_2 &= y_p(4) \\ g_1 &= y(5) & dg_1 &= y_p(5) \end{aligned}$$

The "flow" equations are then correspondingly written as, for example, with constants B_i imported via a global statement:

$$f(1) = dp1 + B_1\left(g_1^2 dt_1 + \frac{2g_1 dg_1}{\rho_1}\right) + B_2\mu(t_1)g_1 t_1 \ldots \tag{5.19}$$

After the five parameters addressed using ode15i are found, $\bar{u}_w$, $\bar{w}$, and $\bar{T}_w$ are evaluated explicitly, using the boundary conditions at the ends of the DPF to evaluate $\bar{T}_w$ there.

In terms of special and temporal tolerances, it was found that a mesh length of $N = 201$ represented an approximate upper bound for generating stable (i.e. non-oscillatory) solutions for a nondimensional time interval of $dt = 0.5$. If a finer spatial mesh is desired, maintaining stability will require a smaller time step. With these program parameters in plus executed on modern computer hardware, the time required for each time step to be computed was on the order of 10 seconds.

5.4 Review of Temperature History with an Initially Flat Soot Profile

We begin by presenting results that are identical to those found in Bissett's original work on a regeneration model, as a means of validating our approach and algorithm for implementation and informing the reader as to the general nature of how key parameters (e.g., temperatures, pressures, flow velocities, and soot layer thickness) evolve over time. Figure 5-2 is a reproduction of DPF wall temperature versus time results, directly from Bissett. Note that regeneration temperature is stepped up from 600 K at $t = 0$ to 950 K at $t > 1$, which explains why wall temperature begins at around 600 K and eventually rises to above the incoming exhaust stream temperature (950 K in Bissett's case).

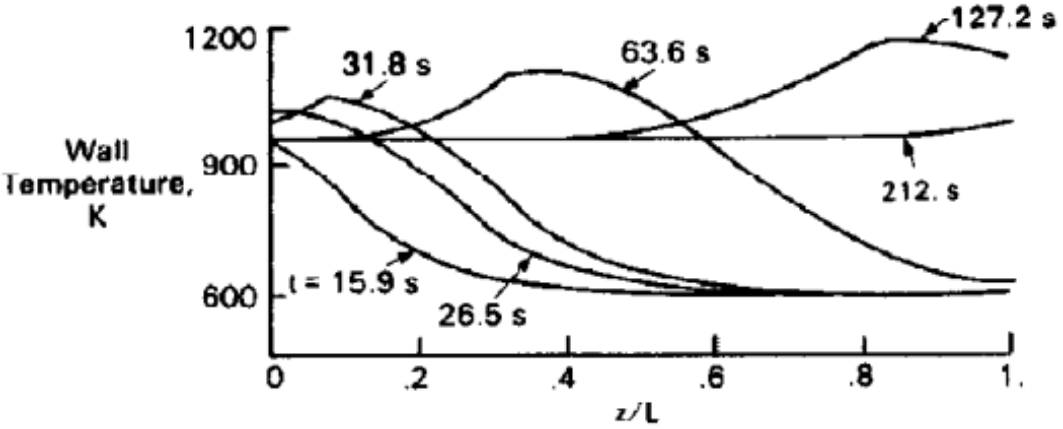

Figure 5-2: Wall temperature as a function of both nondimensional axial distance from the inlet to outlet end of the DPF, as well as time, according to Bissett. Notice that peak temperature at mid-channel occurs somewhere between 60 and 100 seconds after the beginning of regeneration, with global peak temperatures increasing monotonically in time until they reach a maximum when the peak of the temperature "wave" reaches the end plug region [26].

Applying our algorithm invoking MATLAB's built-in functions and (apparently inconsequentially) relaxing default tolerances for implicit solution convergence in order to boost throughput yielded an indistinguishable set of results representing temperature history of the DPF wall, as shown in Figure 5-3.

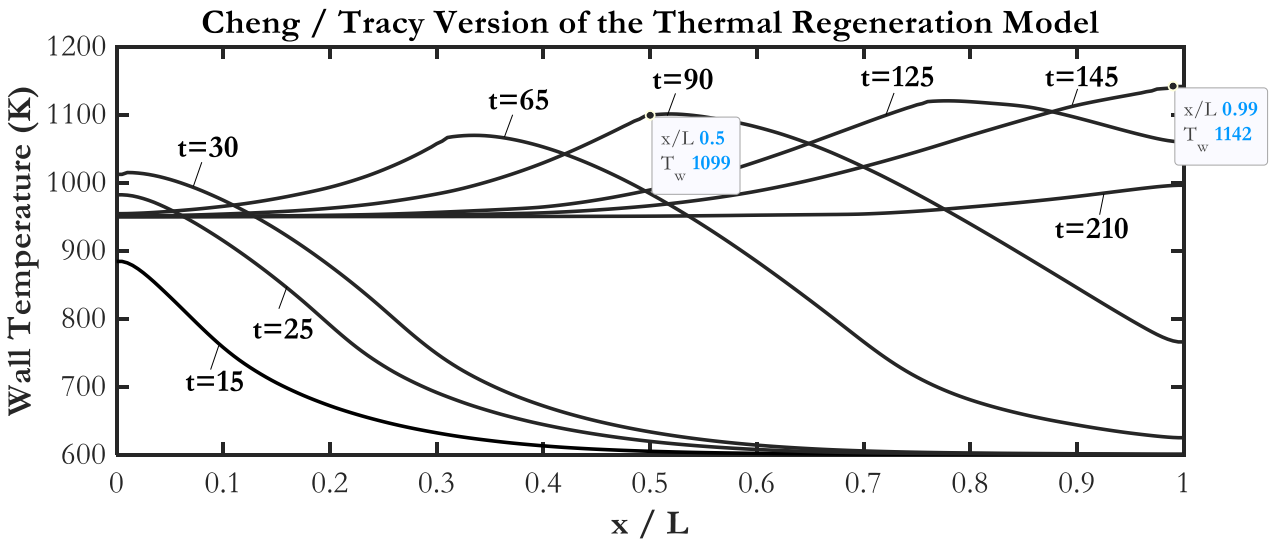

Figure 5-3: Wall temperature as a function of both nondimensional axial distance from the inlet to outlet end of the DPF, as well as time, according to Wai Cheng and Ian Tracy's model. Specific wall temperatures are given at mid-channel $\left(\frac{x}{L} = 0.5\right)$ and the location of peak temperature $\left(\frac{x}{L} = 0.99\right)$. Notice the striking similarity to results generated by Bissett in 1983, which validates the equivalence of our arguably more intuitive and efficient approach.

Notice as well that the threshold for sintering of ~800 degrees Celsius ≈ 1075 Kelvin is breached for several seconds at every axial location in the downstream half of the DPF, suggesting that conditions are ripe for irreversible ash-to-ash and ash-to-substrate bonding in the mid-channel region.

The solution method expressed previously of course provides solutions for additional nondimensional (and those lowercase) parameters as well, including inflow and outflow channel pressures p_1 and p_2, inflow and outflow temperatures t_1 and t_2, wall velocity v_w, deposit thickness w, and flow rate through the inlet channel g_1 (recall is equal to 1 minus the outlet channel flow rate g_2). Snapshot of these values along the axial length of the DPF are provided in Figures 5-4, 5-5, and 5-6 below, which correspond to the times around which peak wall temperatures are achieved at mid-channel ($t \approx 90$). Additional results for a lower exhaust regeneration temperature of 850K are provided in Appendix C.

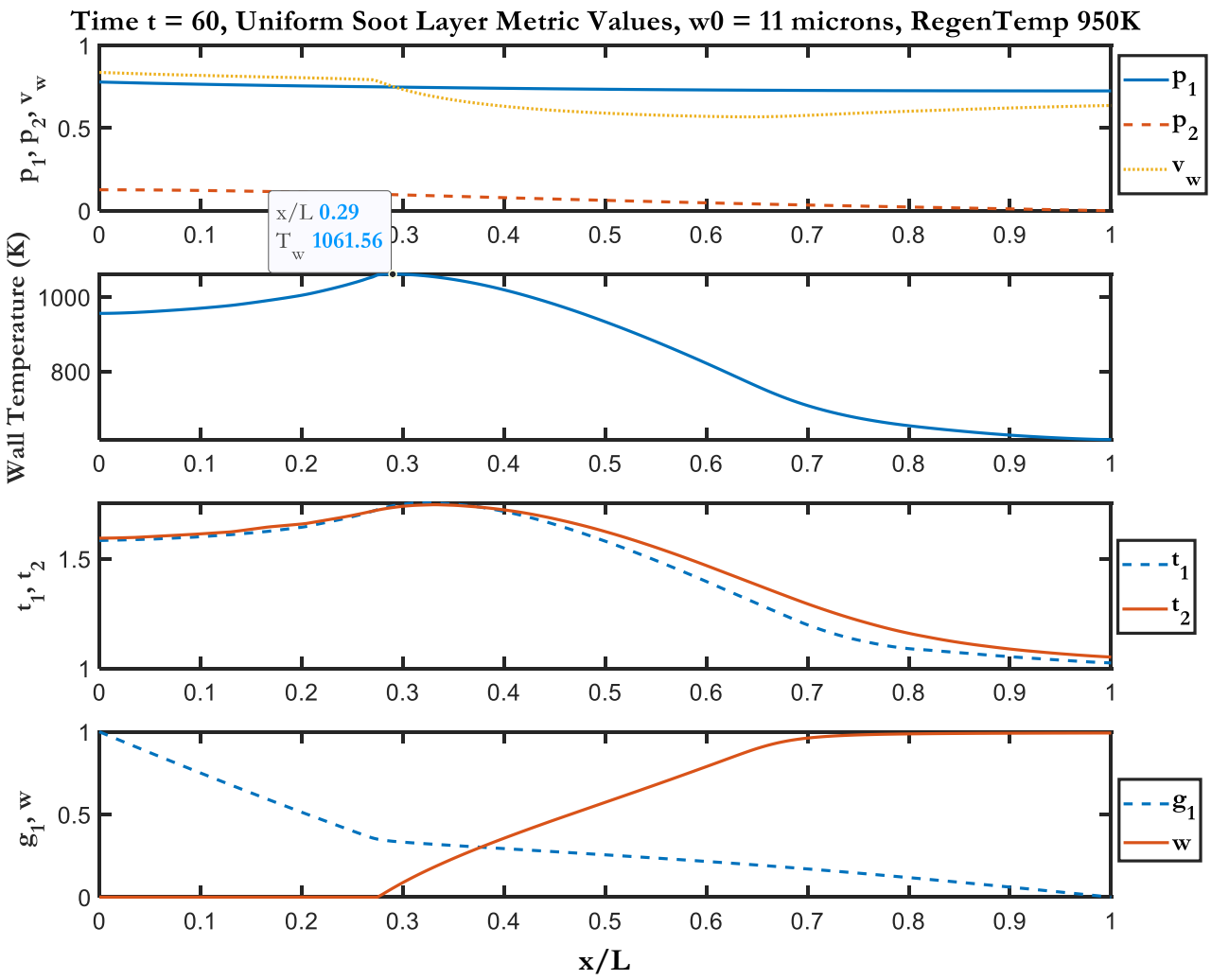

Figure 5-4: Regeneration model results across several mechanical properties for a uniform soot layer with initial height 11 microns and inlet exhaust temperature of 950 K at time t = 60, prior to the mid-channel region reaching its peak temperature during the regeneration period. Notice how the peak temperature at x/L = 0.29 has almost achieved the characteristic sintering temperature of 800 degrees Celsius = 1073 Kelvin.

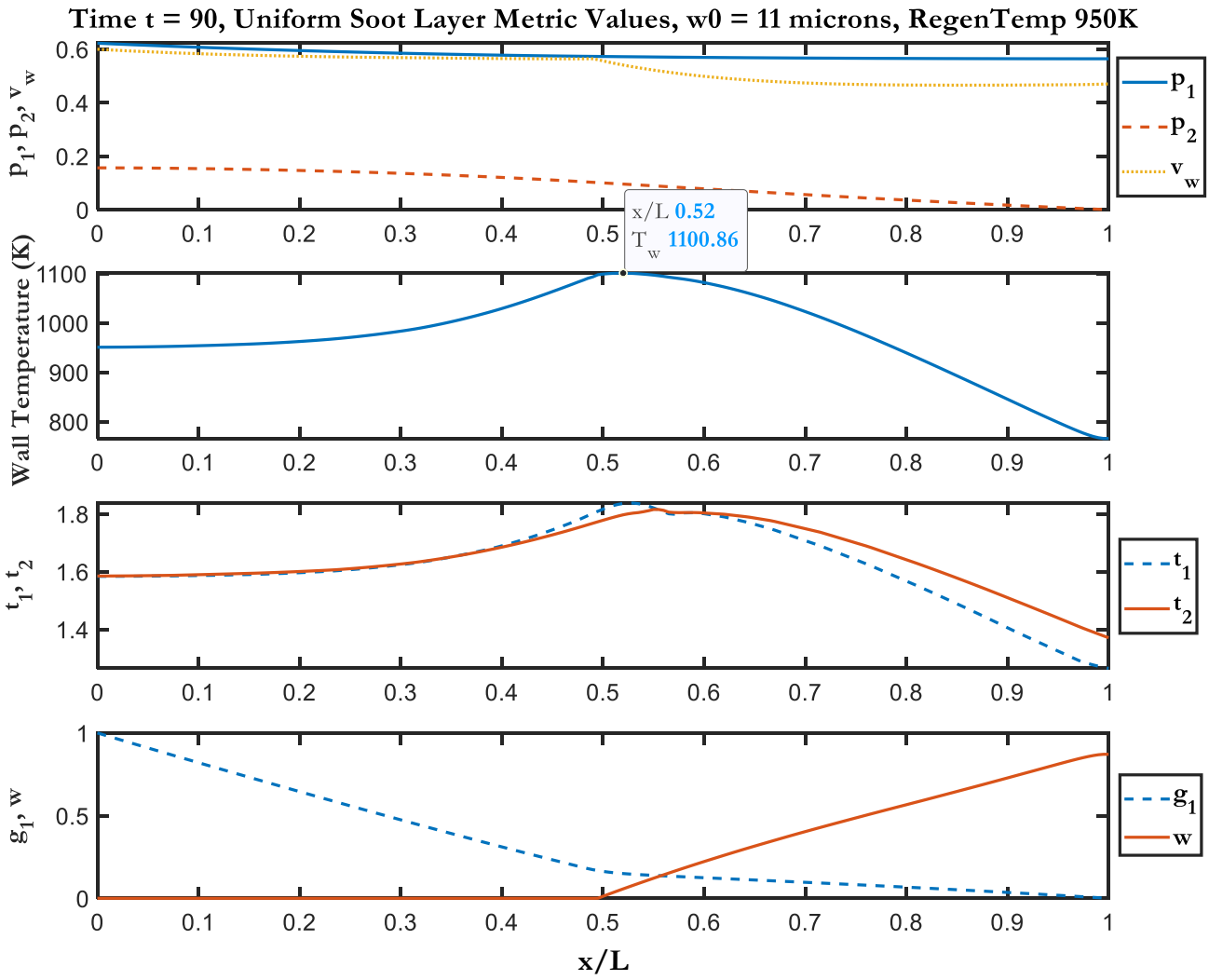

Figure 5-5: Regeneration model results across several mechanical properties for a uniform soot layer with initial height 11 microns and inlet exhaust temperature of 950 K at time t = 90 when the mid-channel region has reached approximately its peak temperature for the entire regeneration period. Notice how the peak wall temperature ~1100 K has exceeded the 1073 Kelvin threshold for sintering of some lubricant-derived ash (e.g., zinc-based).

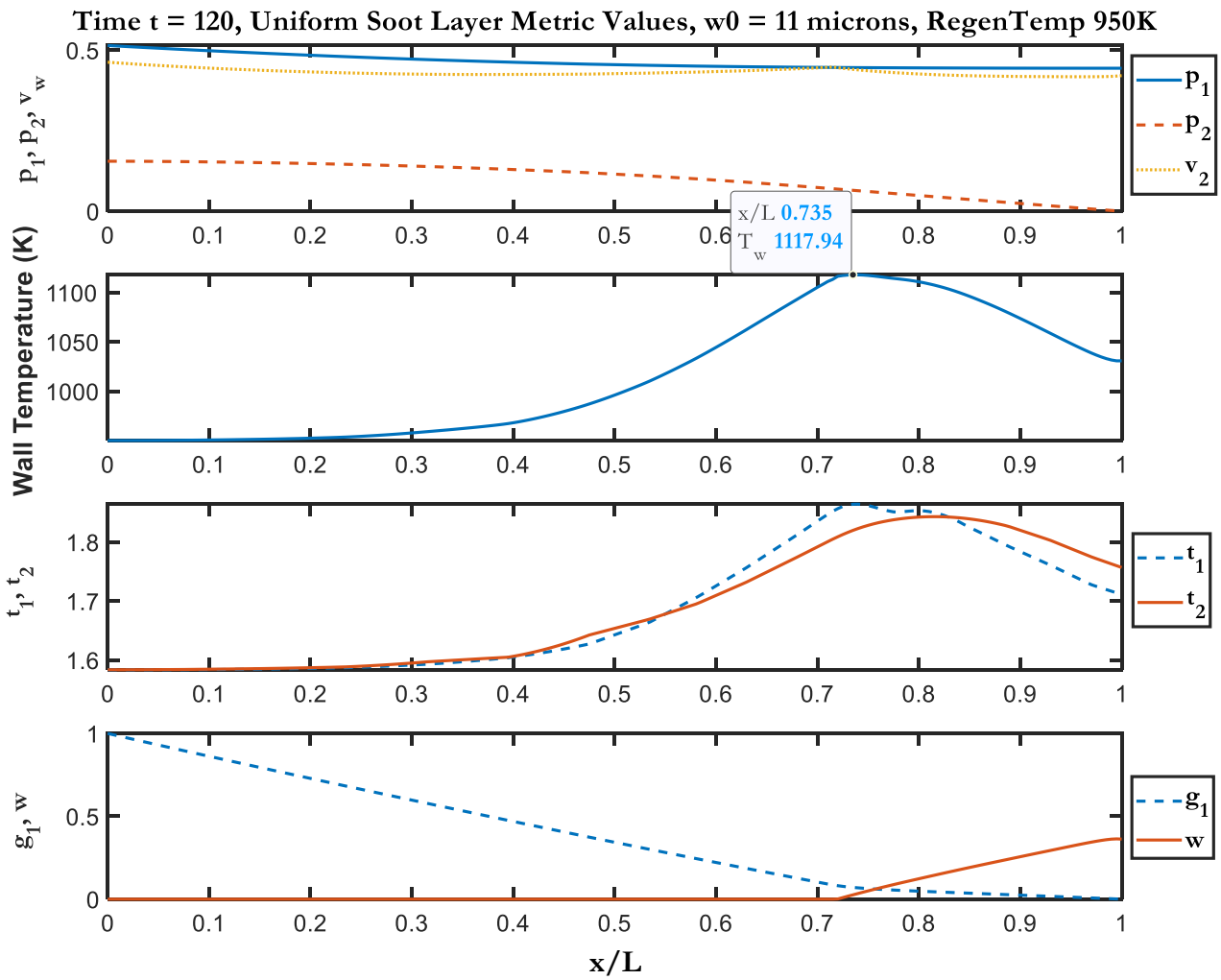

Figure 5-6: Regeneration model results across several mechanical properties for a uniform soot layer with initial height 11 microns and inlet exhaust temperature of 950 K at time t = 120, after the mid-channel region has reached its peak temperature during the regeneration period. Notice how the peak temperature of 1118 K has exceeded characteristic sintering temperature of 1073 Kelvin by 4-5%.

Note that the pressure differential between inlet and outlet channels is substantially reduced during the regeneration event, resulting in a corresponding reduction in flow velocity axial gradient through the DPF filter walls, such that the velocity profile flattens out, though for a constant incoming exhaust flow rate with fixed density, the area under the wall velocity curves should be unchanging. A standard test for testing the compressibility of an ideal gas is to calculate the Mach number M as a function of freestream velocity u; if $M < 0.3$, the fluid may be considered incompressible:

$$M = \frac{u}{\sqrt{\gamma RT}} \tag{5.20}$$

γ is the (nondimensional) ratio of specific heat of gas at a constant pressure to that at a constant volume, and may be approximated as 1.4 for air. R is the ideal gas constant for the fluid = $287 \frac{J}{kg \cdot K}$, and T is the fluid temperature. We may determine a characteristic gas velocity u_0 using either the value specified in Bissett's model or, instead, by inferring from empirically set space velocity. Beginning with the latter, given a space velocity of 40,000 hr^{-1}, we may find the characteristic velocity (for a 12-inch long DPF) as:

$$u_0 = 40{,}000\ hr^{-1} \times \frac{1}{3600} \frac{s^{-1}}{hr^{-1}} \times 12\ in \times \frac{1m}{39.37\ in} = 3.39 \frac{m}{s}$$

Taking the characteristic velocity from Appendix B:

$$u_0 = \frac{G_f(t=0)}{\rho_0} = \frac{0.272 \frac{g}{cm^2 \cdot s}}{\left(\frac{p_{atm}}{RT_b}\right)} = \frac{2.72 \frac{kg}{m^2 \cdot s}}{\left(\frac{1.013 \times 10^5 \frac{kg}{m \cdot s^2}}{287 \frac{m^2}{s^2 \cdot K} \cdot 600\ K}\right)} = 4.62 \frac{m}{s}$$

While these values are similar, we will take the most conservative value 4.62 m/s, just as we will take the lowest temperature the fluid is likely to experience (i.e. ambient temperature ~300 K) as the temperature term in the denominator for determining characteristic Mach number. A conservative estimate for Mach number is therefore given as:

$$M_0 = \frac{u_0}{\sqrt{\gamma RT}} = \frac{4.62 \frac{m}{s}}{\sqrt{1.4 \cdot 287 \frac{m^2}{s^2 \cdot K} \cdot 300\ K}} = 0.0133 \ll 0.3$$

We may thus safely assume that the flow is incompressible.

Further note that, interestingly, the location of the peak of the wall temperature "wave" that moves downstream axially over time is consistently about 5-10% the DPF length downstream of the axial location at which soot is being consumed to completion, which is the result of a reduction in thermal energy emitted by the combusting soot layer as it completes burning at a given axial location

along the channel wall. It also hints that downstream axial locations experiencing incremental heating due to upstream increase in enthalpy / temperature.

5.5 Control of Peak DPF Wall Temperature and Propensity for Ash-to-Ash and Ash-to-Substrate Sintering

Note that given a reference temperature of $T_0 = 600\ K$ and regeneration exhaust flow temperature $T_0 = 950\ K$, peak DPF wall temperatures—which are used as a proxy for deposit layer temperature—rise to nearly 1150K (over 850 Celsius), which exceeds the sintering temperature for many types of lubricant-derived ash, supporting the notion that conditions are ripe for ash anchors to form and propagate across the channel to result in MCC. It may therefore reasonably be concluded that an engineering constraint on setting regeneration frequency would be to ensure that global DPF temperatures do not exceed to the ~800 Celsius or ~1075 K threshold. The most direct way to accomplish this is to regulate the soot layer thickness that is achieved prior to triggering regeneration. Naturally, a thicker combustible deposit layer will burn longer, elevate the baseline exhaust temperature (e.g., 600 K) to a higher global peak level, and increase the probability of irreversible thermal bonding among particles.

It is therefore also important to choose an incoming exhaust flow temperature that one actually expects to see in field operation. While the 950 K value was chosen by Bissett, both field and test bench operations conducted at MIT have instead opted for lower regeneration temperatures of approximately 550-600 Celsius, or around 850 K. It is foreseeable that use of advanced catalysts would enable active regeneration to be conducted at even lower exhaust temperatures. Simulations were therefore run in order to determine the sensitivity of engine exhaust temperature on peak regeneration temperatures. Figure 5-7 provides such an illustration for the time at which peak temperatures are reached at approximately the mid-channel location.

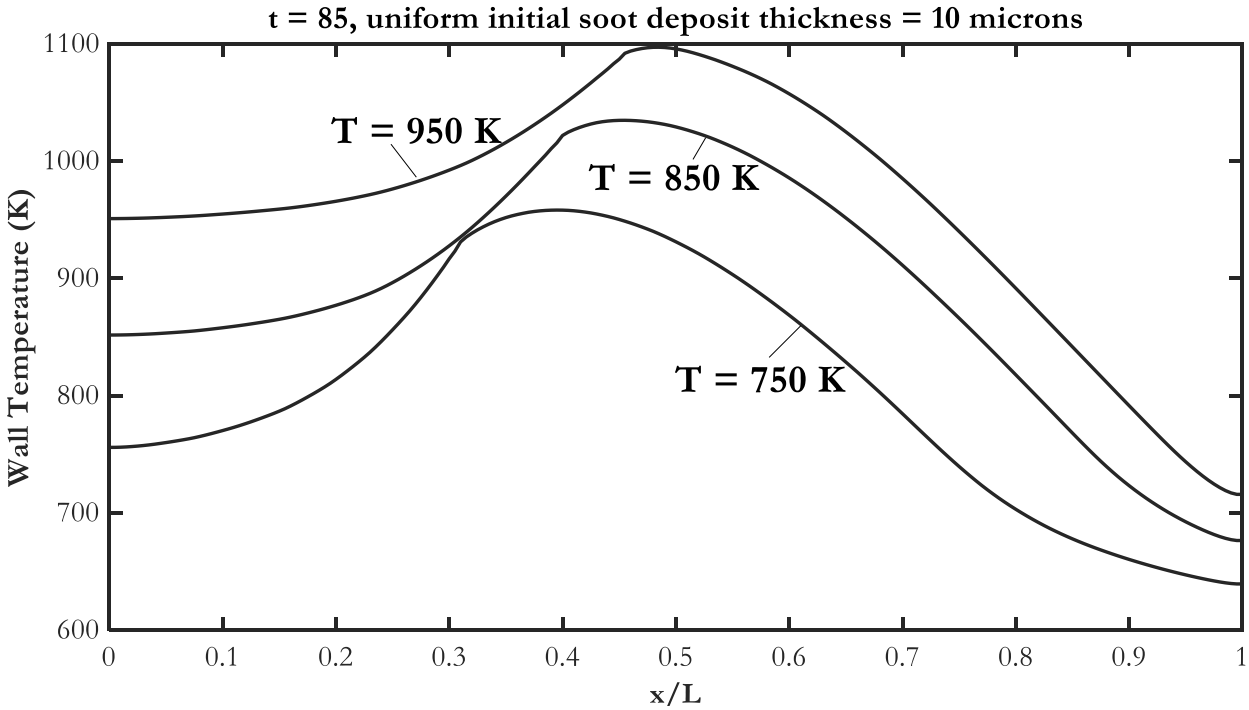

Figure 5-7: Simulating wall temperature while varying incoming exhaust temperature at time t = 85, when peak temperatures have been achieved at around the mid-channel (x/L = 0.5) axial location.

The figure shows that peak temperatures vary on a nearly per-degree basis with incoming exhaust temperature such that a 100-degree Celsius in exhaust temperature results in approximately a 100-degree Celsius increase in peak mid-channel wall temperature. Hence, reducing exhaust temperature during regeneration may play a pivotal role in mitigating the onset of sintering, and thus may aid in preventing an unacceptable degree of MCC formation. It is also interesting to note that as exhaust temperature rises, the peak of the temperature "wave" shifts farther downstream, which reflects the fact that the soot layer is being burned faster and the axial location at which the last amount of soot is being combusted is farther downstream.

We now seek the maximum initial loading permissible by iterating initial soot thickness until the peak filter temperature reaches 1075 K, assuming constant incoming exhaust temperature of 850 K and constant income exhaust (space) velocity. It is sensible to apply the temperature threshold for sintering as far downstream as is permissible for MCC to form from a performance perspective, though a conservative approach is of course to do so at the end plug region, i.e. at $\frac{x}{L} = 1$. For sake of our exercise, we will use that conservative axial location of the outlet as our reference, as well as an elevated sintering temperature of 900 Celsius. Figure 5-8 provides peak wall temperature as initial deposit (soot) thickness varies from 5 to 25 microns in increments of 5 or 10 microns.

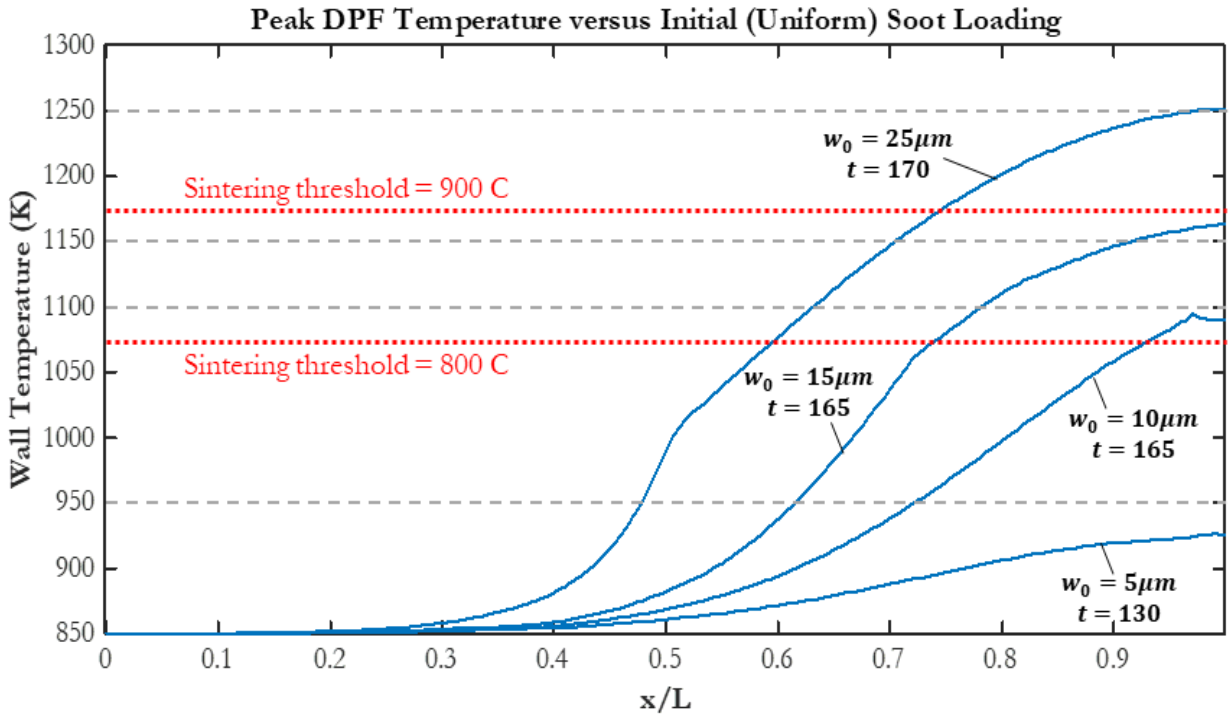

Figure 5-8: Axial wall temperature curves at the time of peak global wall temperature for differing initial deposit (soot) layer thicknesses, varied from 5 to 25 microns. Note that for a sintering threshold temperature of 800 Celsius, the maximum permissible initial deposit layer thickness less just under 10 μm; when that wall temperature bound increases to 900 degrees C, an initial soot thickness prior to regeneration of over 15 microns then becomes acceptable.

It is interesting that an over 50% difference in permissible initial soot layer thickness is observed when threshold sintering temperature is moved 100 Celsius from 800 to 900 degrees C, which makes that bound quite important to get right from a performance versus efficiency perspective.

It also necessitates a more precise correlation of sintering temperature to allowable deposit layer thickness; such a plot has therefore been provided in Figure 5-9, where the red star corresponds to the maximum permitted soot loading in the case of 900 degrees Celsius being taken as the max allowable (i.e. sintering threshold) wall temperature. Three abscissas (i.e. horizontal axes) are included to reflect the tradeoff between backpressure and enthalpy related fuel economy penalties presented previously in Figure 1-24.

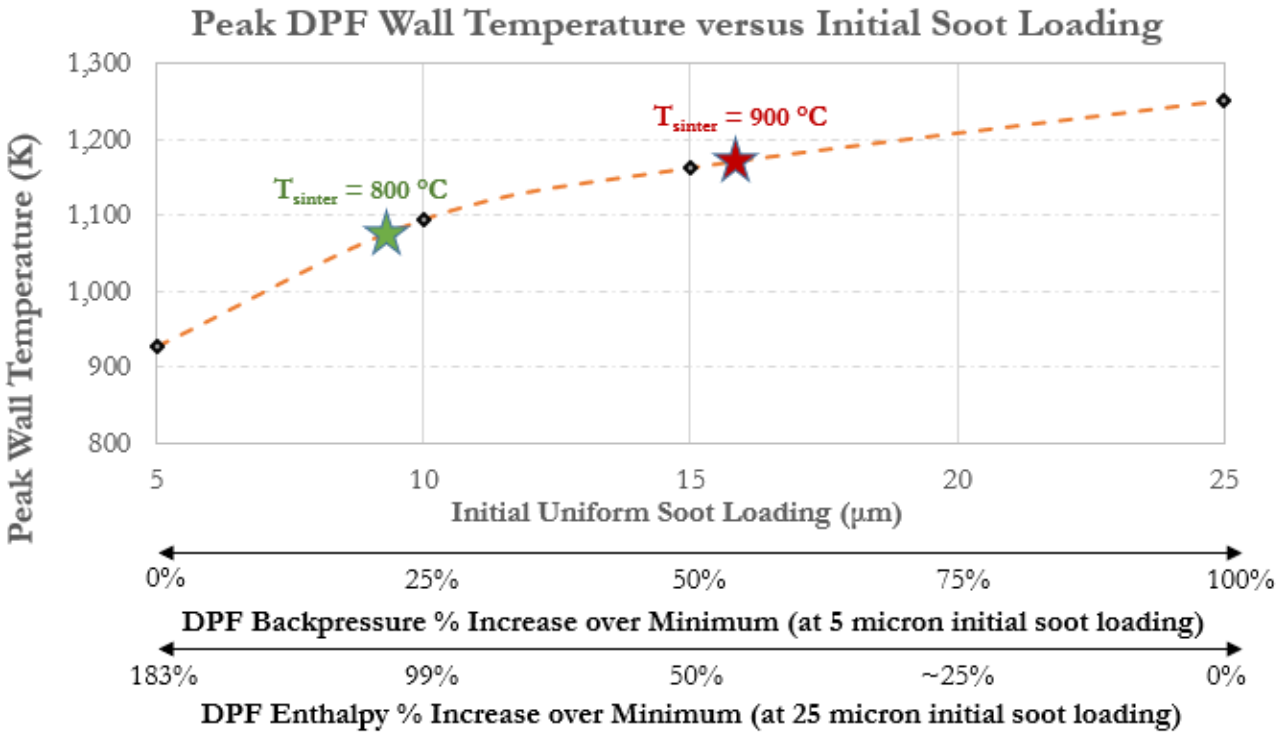

Figure 5-9: Peak DPF wall temperature versus initial (uniform) soot loading prior regeneration, assuming 950 K exhaust flow and constant space velocity of 40,000 hr^{-1}. We have included two additional axes to indicate the degrees of (countervailing) backpressure fuel economy penalty and enthalpy fuel economy penalty that results from excess fuel burn to induce elevated temperature of the exhaust gas. Note that the backpressure fuel economy penalty scales approximately linearly with initial uniform soot loading, while enthalpy losses exhibit an exponential dependency, which aligns with those dependencies depicted in Figure 1-24.

Values as provided in Figure 5-9 were tabulated as depicted in Table 5-1. Note that given a characteristic regeneration time of 5-10 minutes, and multiple hours between regeneration, the regeneration time was deemed negligible compared to that of the full cycle.

Table 5-1: An accounting for backpressure and enthalpy fuel economy penalty as a function of initial soot load during active regeneration.

Initial Soot Loading (µm)	Peak Temp (K)	g/L Ash	Pressure Drop (kPa)	Nondimensional Time (approx. in seconds)	Regen Fraction of Cycle % of Max	Regen Time % of Max	Peak Temp % of Max	Backpressure Increase % from Min	Enthalpy Increase % from Min
5	926	1.0	2.6	130	100%	76%	74%	0%	183%
10	1,095	2.1	3.2	155	50%	91%	87%	24%	99%
15	1,163	3.0	3.8	165	33%	97%	93%	49%	50%
25	1,252	4.9	5.3	170	20%	100%	100%	105%	0%

We may also determine initial allowable soot loading in the case for which sintering is viewed as a time-dependent process such that a minimum duration is required above the sintering temperature

in order for thermal effects to contribute to the onset of MCC. Figure 5-10 illustrates the determination of maximum soot loading in the mid-channel region under the assumption that a sintering temperature of 800 Celsius may not be exceeded for over 30 seconds.

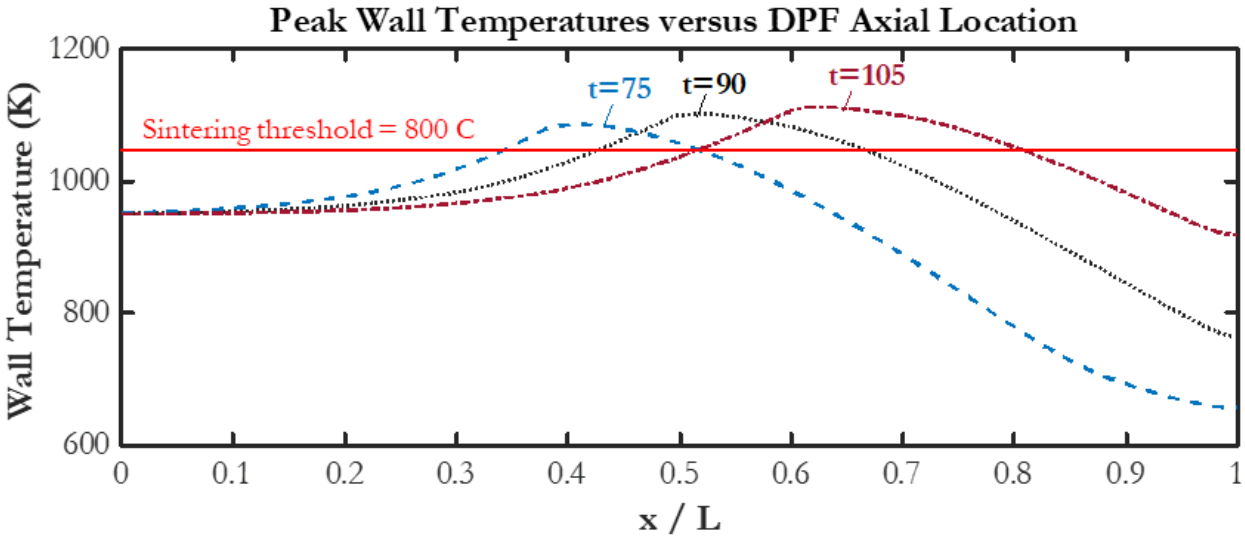

Figure 5-10: Determining maximum soot loading prior to regeneration under the assumption that sintering temperature 800 Celsius may not be exceeded for more than 30 seconds.

One additional avenue of comparison worth pursuing is that of varying incoming exhaust (i.e. space) velocities. Wang et al. explicitly mentioned that high flow velocities are preferred during active regeneration, both because they provide a cooling effect to reduce peak wall temperatures, and also to induce greater downstream transport of PM particles that may otherwise become fixed to the cake layer [17]. This may, in fact, prove to significantly mitigate the prevalence of MCC in DPFs, and will be further addressed in Chapter 6, which largely emphasis the forcing mechanisms responsible for PM transport within the DPF channels. As an initial foray into this question, we varied space velocity from a default 40,000 hr^{-1} to 80,000 and then up to 160,000 hr^{-1} to test the impact of varying exhaust flow rate on both peak regeneration temperature and duration of the regeneration process. Results varied monotonically, and data for the extreme 40,000 and 160,000 hr^{-1} are included in Figure 5-11, which plots wall temperature over time versus space velocity.

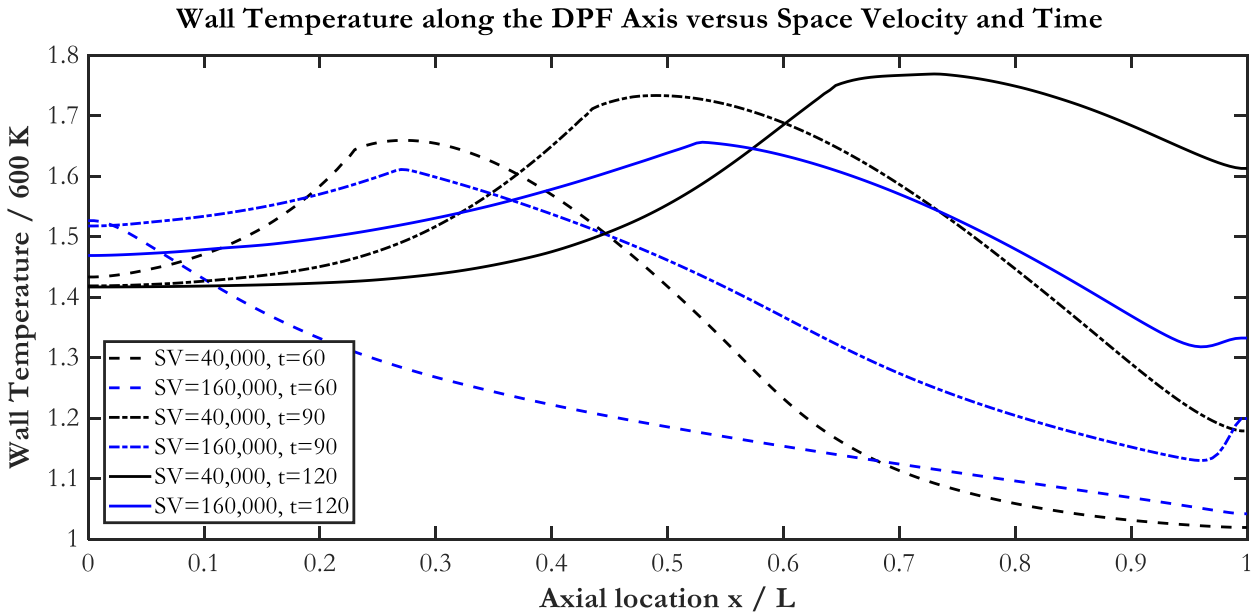

Figure 5-11: Wall temperature as a function of space velocity and time, all else held constant. A given color corresponds to a given time. There is a clear reduction in peak wall temperature with increased space velocity during regeneration due to convective cooling, suggesting that increasing exhaust speed may help reduce peak temperature. However, doing so requires more energy and prolongs the regeneration period.

5.6 Temperature History with the Introduction of Cake Layer Protrusions

Another purpose for reproducing a more efficient version of Bissett's thermal regeneration model was to enable the investigation of temperature history of a DPF in the case in which MCC-like PM deposits accumulate on the cake layer, thereby introducing protrusions to the cake layer surface. While Wang demonstrated little sensitivity of deposit layer shape on backpressure, we are not now interested in the thermal effects of an additional volume of soot deposited on the cake layer, to simulate the impact of a partially combusted soot layer peeling off of the cake layer and being redeposited elsewhere on the channel wall. The program was run in an iterative fashion, varying key relevant parameters (e.g., soot protrusion shape and thickness, initial substrate thickness, etc.) to use as bases for comparison and subjects of a sensitivity study that expresses the relative impact of variables on the temperature history of the DPF. The cases run include:

1. A uniform soot layer with thickness as prescribed originally by Bissett and previously described in this chapter, with inlet exhaust temperature stepping up from 600 K to 850 K at dimensionless time t = 2.
2. A uniform soot layer with an increased regeneration temperature of 950K.

3. 15 Gaussian bump distributions consisting of combinations of five variable heights (ranging from 20 to 500 microns above the DPF wall substrate surface) and width (3mm to 9mm per minimum bounds prescribed by the mesh sparsity resulting from an axial node count of 201) at a regeneration temperature of 850 K. Note that attempts to incorporate variable mesh size in the region around the introduced bump yielded unacceptable instabilities in computation. One possibility here, as previously mentioned, is to simultaneously reduce the time increment while increasing mesh size, though an exponential relationship between mesh size and number of time steps required may result in unsustainable computation time.
4. 15 flat sheet distributions consisting of variable height (20 to 500 microns) and width (3mm, 6mm, and 9mm), again with regeneration temperature 850 K.
5. 15 Gaussian bump distributions with the same height and width combinations specified above in item 3 but with a uniform soot layer on the DPF whose thickness has been doubled.

What we see is that such protrusions result in a reduction in local temperature upstream of the peak of the temperature "wave" reaching a given axial location along the DPF, but that this effect flips and results in a positive jump in local wall temperature at the protrusion location after the temperature wave peak has passed. This, in effect, may prolong the duration over which high temperatures are retained at that location, and may promote longer-duration and more adhesive sintering of a given PM agglomerate to the local underlying substrate + anchored ash at that location. Note, however, that difference in temperature experienced between the default (non-protruded) cake layer and those with various additions of soot layers is small, is only on the order of a few (single-digit) percent. Figures 5-12 (t = 95 when the uniform profile exhibits higher peak temperature) and 5-14 (t = 130 when the uniform profile instead exhibits a lower peak temperature) show both a macro (full DPF length displayed) and zoomed-in views (around the point of peak temperature). The results for different times are included in Appendix D.

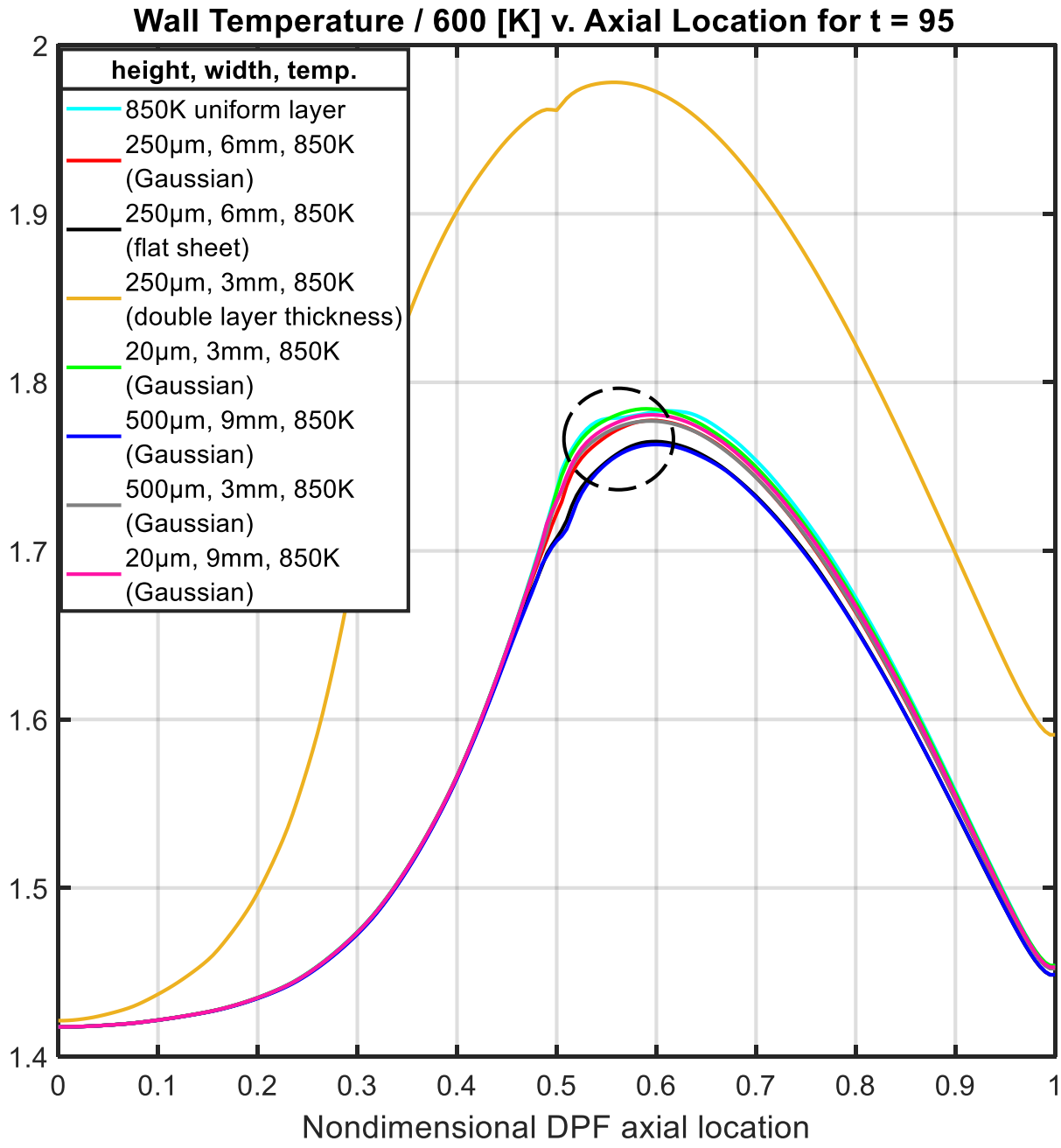

Figure 5-12: Zoomed out peak DPF wall temperature at t = 85 across several initial soot deposit profiles. At x/L = 0.5, the temperature for the uniform soot layer case is $600\ K\ \times 1.736 = 1042\ K$, whereas at that for a 500 micron (~half the channel width) soot flake of length 9mm deposited locally on the cake layer at x/L = 0.5 is $600\ K\ \times 1.706 = 1024\ K$, which represents about a 1.7% reduction in temperature at that axial location.

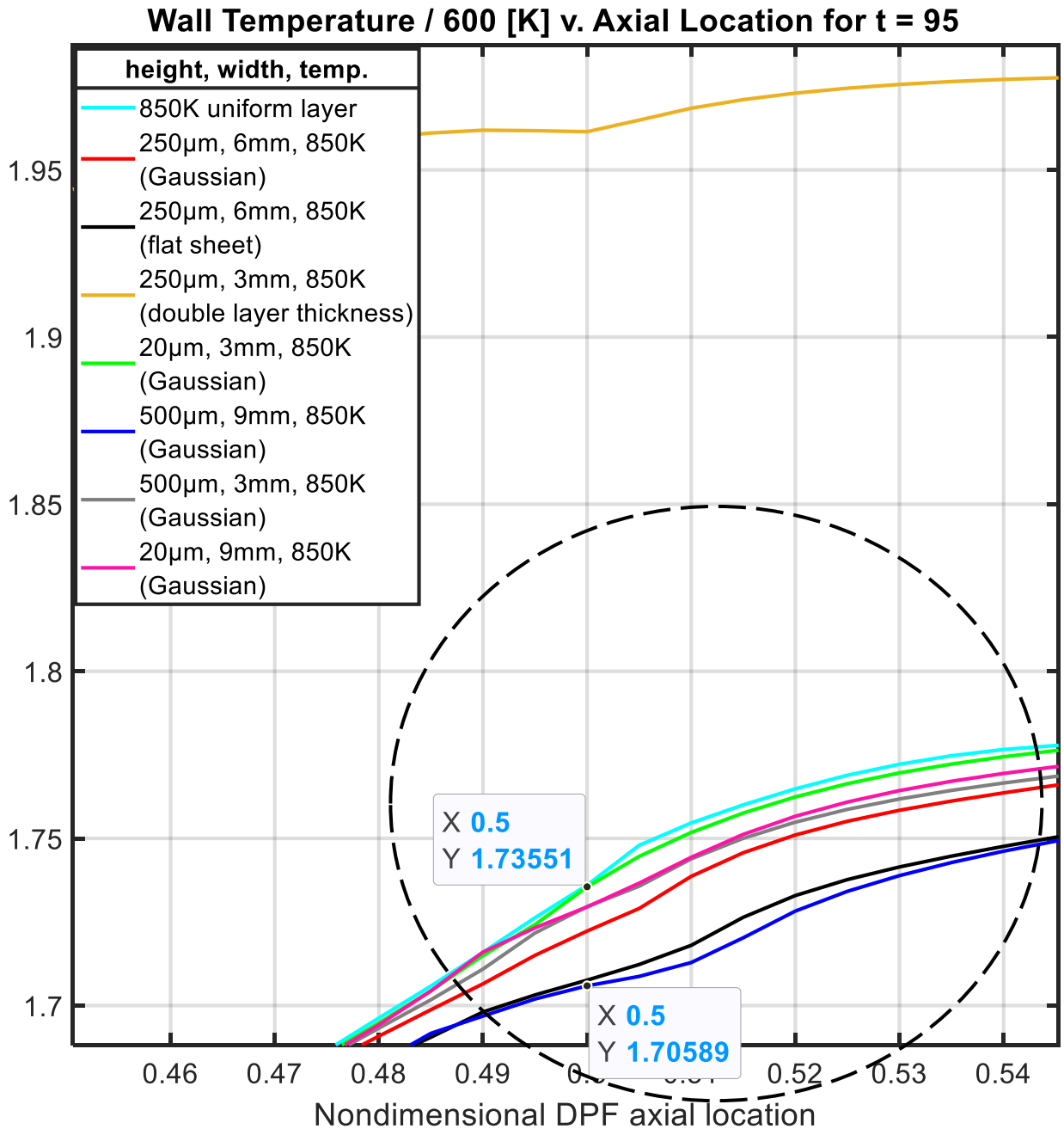

Figure 5-13: Zoomed in peak DPF wall temperature at t = 85 across several initial soot deposit profiles. At x/L = 0.5, the temperature for the uniform soot layer case is $600\ K\ \times 1.736 = 1042\ K$, whereas at that for a 500 micron (~half the channel width) soot flake of length 9mm deposited locally on the cake layer at x/L = 0.5 is $600\ K\ \times 1.706 = 1024\ K$, which represents about a 1.7% reduction in temperature at that axial location.

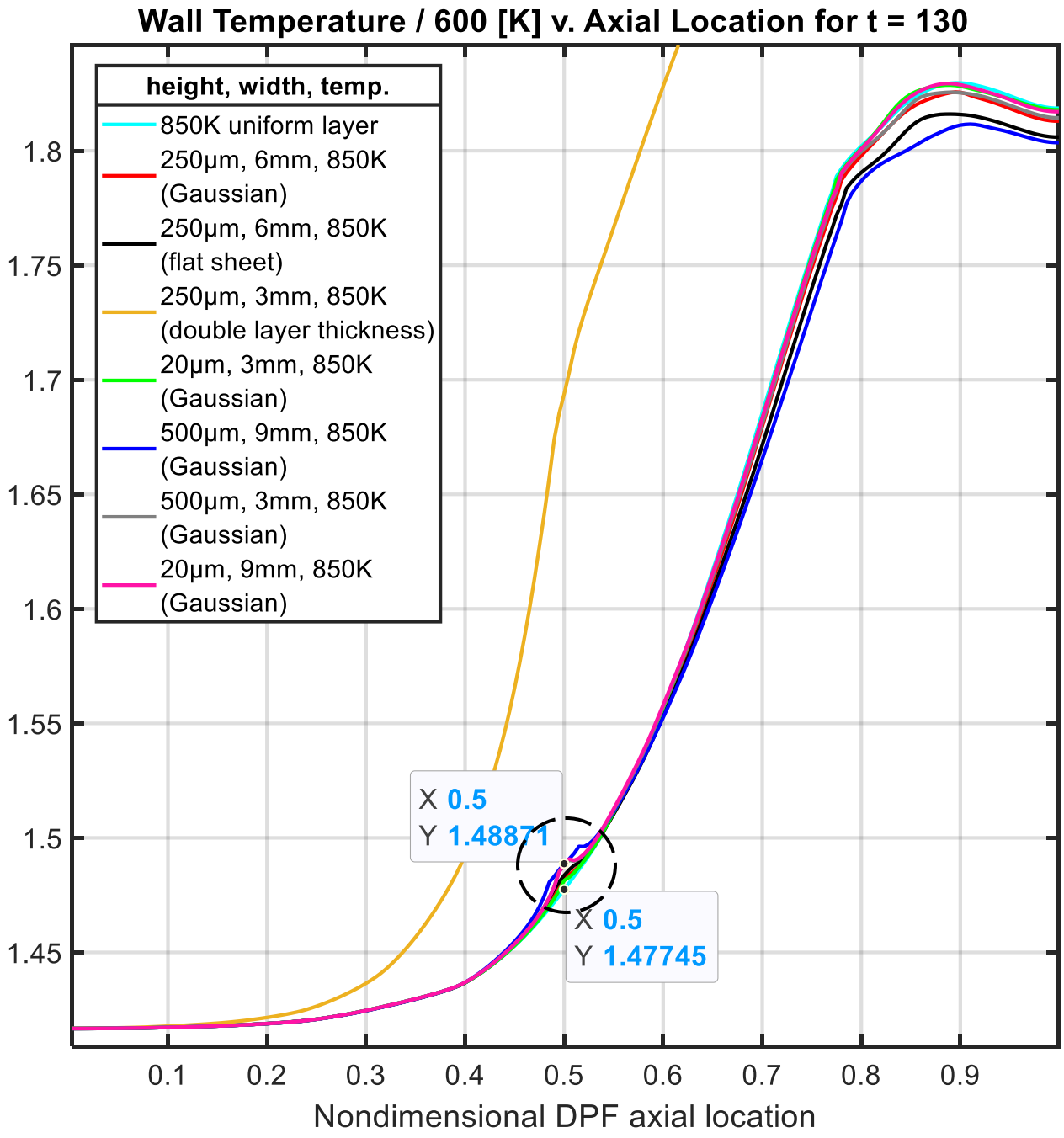

Figure 5-14: Zoomed out peak DPF wall temperature at t = 130 across several initial soot deposit profiles. At x/L = 0.5, the temperature fort the uniform soot layer case is $600\ K\ \times 1.477 = 886\ K$, whereas at that for a 500 micron (~half the channel width) soot flake of length 9mm deposited locally on the cake layer at x/L = 0.5 is $600\ K\ \times 1.489 = 893\ K$, which represents about a 0.8% increase in temperature at that axial location.

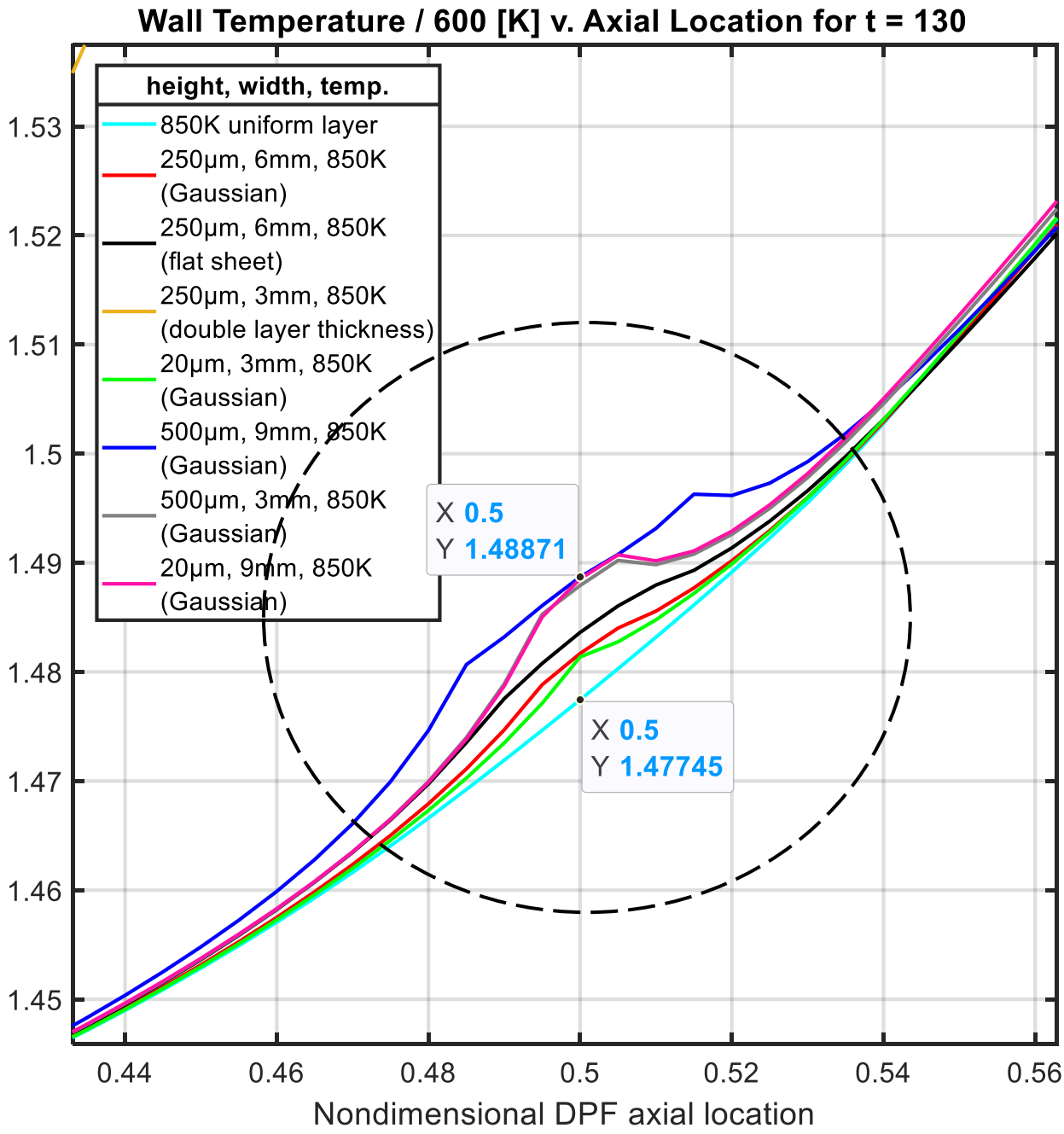

Figure 5-15: Zoomed in peak DPF wall temperature at t = 130 across several initial soot deposit profiles. At x/L = 0.5, the temperature fort the uniform soot layer case is $600\ K\ \times 1.477 = 886\ K$, whereas at that for a 500 micron (~half the channel width) soot flake of length 9mm deposited locally on the cake layer at x/L = 0.5 is $600\ K\ \times 1.489 = 893\ K$, which represents about a 0.8% increase in temperature at that axial location.

6 Concluding Remarks and Recommendations for Further Related Research

6.1 Contributions

The contributions made in the contents of this thesis included:

1) Synthesizing and rationalizing the growing body of literature that directly relates to explaining the causal mechanisms and performance effects of mid-channel clogging in DPFs;
2) Introducing a protocol for analyzing image scan cross sections of the DPF that depict instances of MCC, including defining key metrics to address the magnitude and consistency of MCC formation;
3) Extending the industry performance (backpressure) model to accurately simulate the effects of arbitrary distributions of MCC within DPF channels;
4) Reformulating Bissett's DPF regeneration model to simulate additional cases in order to determine whether DPF wall temperatures exceed sintering threshold temperatures for an appreciable amount of time;
5) Suggest a starting point for identifying and evaluating different forces that act on PM agglomerates and drive their transport through the filter channels; and
6) Identify tangible approaches for mitigating the onset and development of MCC: maximum permissible soot loading prior to regeneration, flow velocities, exhaust humidity, lubricant additive package chemical composition, etc.

6.2 General Recommendations for Further Research

As has been mentioned throughout this dissertation, there remains considerable mystery surrounding the prevalence and causal mechanisms of MCC. There are consequently several avenues of additional research that can prove fruitful in helping address these two high-level outstanding issues. Here we describe both numerical and empirical studies, as well as relations with companies that specialize in the manufacture, testing, and operation of DPFs and associated products.

In order to better understand the prevalence of MCC in DPFs, it is suggested that researchers gather additional data from major DPF manufacturers and operators across the globe, as they are likely to have the reach and resources available to assess how frequently MCC arises in consequential

form across markets. Such data includes nature of reported issues regarding DPF performance including logs operating performance and access to the associated DPFs so that additional scans of channel ash accumulation can be obtained. The global aspect is important because, as mentioned in in Chapter 2, there is strong reason to believe that the details of lubricant, engine, and even coolant formulation are relevant for determining the composition of ash formed in the DPF. The composition of ash is important, again, because different metallic species begin to sinter at different temperatures, with hundreds of degrees Celsius separating sintering thresholds among metals commonly found in lubricant chemistry.

Causal mechanisms can first be investigated via conversations with DPF manufacturers, testers, suppliers, operators, and other researchers in the field. In addition to nominal and DPF samples, they can provide accounts of distances vehicles have traveled prior to the onset of anomalous behavior in the aftertreatment system, the nature of cleaning and what more specifically the very difficult cleaning process of MCC-afflicted DPFs is like, and whether—either through formal reporting or less formal interviews—MCC accompanied any other discernable behavior/activity in the operated vehicle or platform.

Additional experimental studies can serve to gain a more detailed, real-time understanding of the mechanical properties of the DPF before, during, and after MCC forms. This can be accomplished by using advanced sensors to monitor temperature and pressure within the filter, and advanced optical and scanning methods to noninvasively track ash and soot agglomerates within DPF channels. One such attempt was made by Srilomsak et al., who provided direct visual temporal data regarding the separation of the PM cake layer from the DPF substrate wall, shown in Figure 6-1 below.

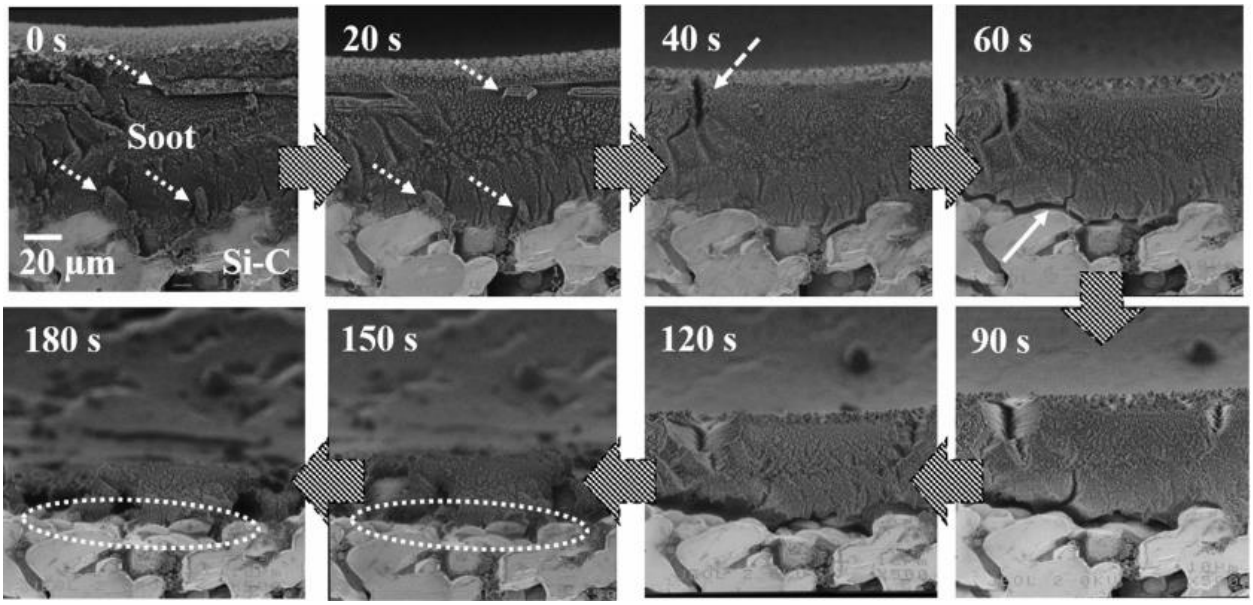

Figure 6-1: FE-SEM images showing a cross-sectional view of DPF during regeneration over time at 250x magnification clearly illustrating separation between the PM cake layer and underlying Si-C substrate after around 60 seconds of active regeneration [27].

Such investigations can ideally shed more light on the relative impact of and relationship between high-density ash anchor formation and separation of PM layers from the channel walls, as well as definitively determine what combinations of operating conditions and PM properties yield substantial prevalence of MCC. DPF manufacturers and operators will then be able to effectively operate so as to mitigate the onset of problematic premature clogging of filter channels.

Assuming temperature history does play the predominant role suggested in this dissertation, further research probing temperature effects are in order. Such investigations may include the study of variations in:

- Flow rate during regeneration, as higher space velocities provide more convective cooling and thus should yield lower peak wall temperatures. This study should also assess the corresponding impact on fuel economy and any other metrics of interest.
- Soot loading prior to regeneration, as more loading yields higher peak temperatures. Note that additional considerations could be made regarding thermal stresses and cracking of the DPF, which Bissett mentioned are key considerations underlying the heuristics used to determine conventional sizing of DPFs [26].
- Variation in exhaust temperatures which will naturally increase peak DPF temperatures during regeneration. Note that applying this approach will require additional energy

expenditure upstream; a corresponding understanding of fuel economy penalty should be included.

- A better understand of relevant properties of PM and the DPF substrate under various operating and loading conditions in order to shed light on the nature of PM transport within the DPF. Since ash transport is intimately related to MCC, a model that reasonably simulates the motion of PM in the DPF channels would be helpful in understanding what types of forces are likely conducive to the ash accumulation patterns reflective of MCC. Such mechanical properties including the following, which should be specified for ash / PM agglomerates over appropriate temperatures and pressures, as well as other key mechanical properties such as density and permeability:
    - viscosity;
    - surface tension;
    - roughness and characteristic separation distance between our specific PM molecules;
    - charge density and distribution in particles; and
    - particle-to-particle and particle-to-DPF "stickiness."

6.3 Modeling Ash Morphology and Transport

Of particular interest to researchers who study DPFs and MCC is the development of a model that accurately simulates the motion of PM within DPF channels. One approach to developing such a model involves updating the instantaneous force balance on a given particle/agglomerate every sufficiently small time increment dt. Doing so of course requires accurately representing all relevant (i.e. dominant) forces at play at a given time and location within the DPF. While various studies have at least speculated as to relevant forces at play and have even provided empirical data regarding relative forces experienced between objects within DPF channels (per Figures 6-2 through 6-4), there have been to date no fully comprehensive ash transport models developed. Figure 6-2, for example, is very general and does not suggest either the relative magnitude or even types of major forces at play.

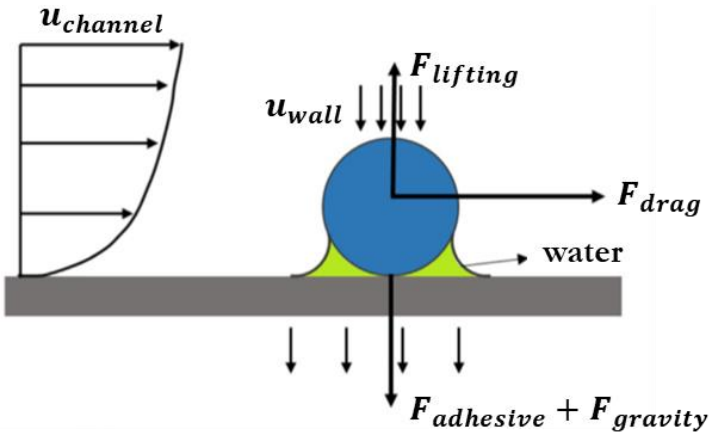

Figure 6-2: An illustration of high-level forces at play: lifting, drag, adhesive, and gravitational. Lifting and drag forces can merely be viewed as orthogonal forces due to the effects of flow and corresponding to two normal axes along the channel wall. Note the parallel axial flow $u_{channel}$ and perpendicular wall flow u_{wall} [17].

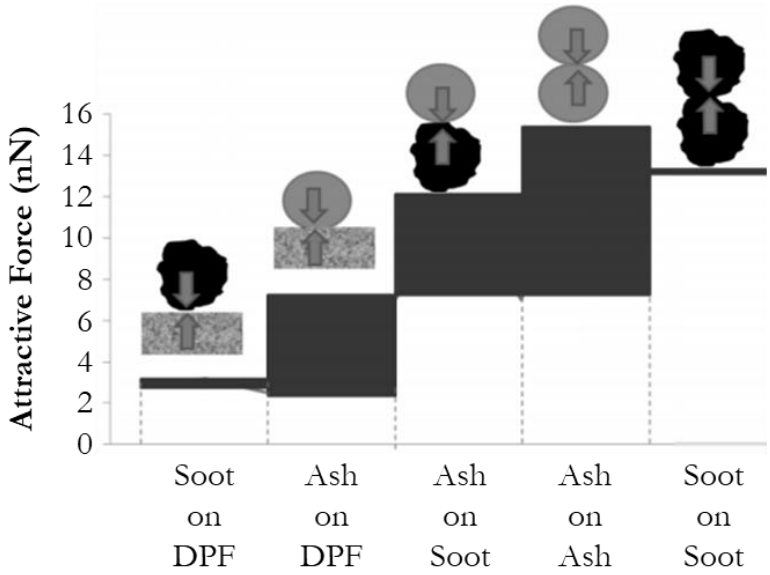

Figure 6-3: Atomic force microscope measurements of adhesive force across different pairs of combinations of ash, soot, and substrate materials comprising the DPF wall region [28].

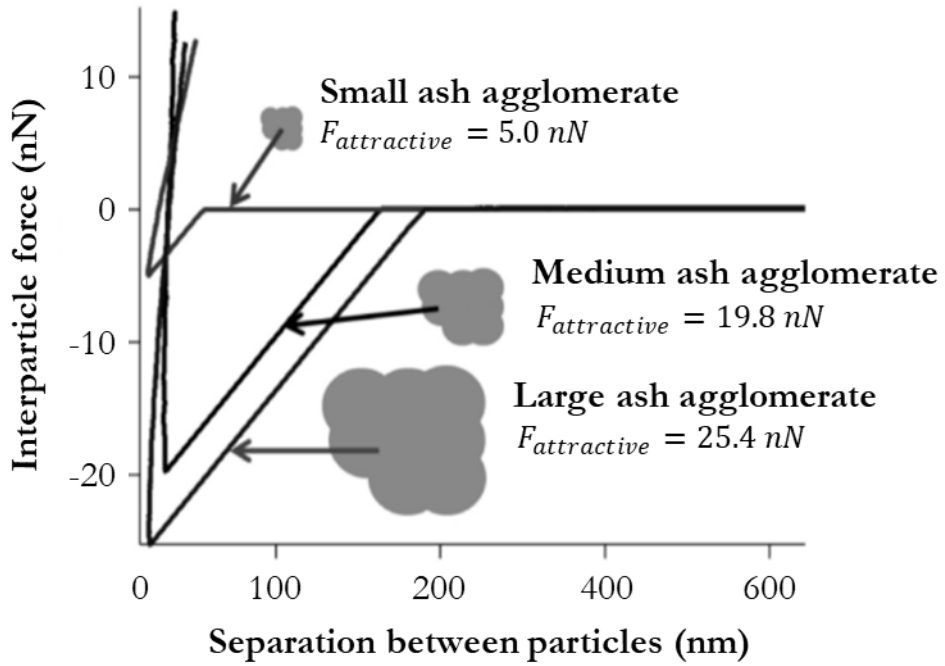

Figure 6-4: Attractive force versus particle separation distance for agglomerates of varying size. It seems that the more neighboring particles one has, the more reinforcing attractive force one should expect to experience [28].

Figure 6-4 may be rationalized by considering the Lennard-Jones potential commonly used to model forces between two interacting molecules—for example, particles i and j—and is particularly notable because it reflects the strong repulsion experienced between molecules at close range [88]:

$$V_{LJ,ij} = 4\varepsilon\left[\left(\frac{\sigma}{r_{ij}}\right)^{12} - \left(\frac{\sigma}{r_{ij}}\right)^{6}\right]$$

The separation distance at which the potential is zero (i.e. there is neither repulsion nor attraction) is given by σ, and the minimum potential energy is $V_{LJ,ij,min} = -\varepsilon$, which occurs at $r_{min} = 2^{1/6}\sigma$. Note that both σ and ε depend on the specific atomic structure in the $i - j$ molecular pair. This equation serves as the basis for many molecular dynamics simulations and can be used to approximate intermolecular forces for a wide variety of interacting compounds.

Returning to our discussion on DPFs and forces experienced by PM agglomerates therein, researchers have identified characteristic particle sizes amenable to re-entrainment of particles that reside in or on the cake layer. Table 6-1 illustrates summarizes the results. We observe that both relatively very large (> 500-micron) and very small (< 10-mircon) particles are not likely to be swept away by the income exhaust stream. Small particles, due to their low surface areas, are unlikely to

gain exposure to significant shear or lifting force from the incoming flow, whereas large particles are held in place due to magnitude of their own weight.

Table 6-1: Particle size categorized into transport regimes of re-entrainable into the exhaust freestream versus not re-entrainable, with associated transport mechanism descriptions [21].

Particle Size (μm)	Transport Mechanism	Re-Entrainable
< 10	Not re-entrainable	Single particle re-entrainment is "impossible." Agglomerates may be re-entrained.
10 - 100	Re-entrainment by flow	Yes - re-impaction possible
100 - 500	Re-entrainment by flow	Yes - via pneumatic conveyance
> 500	Rolling, creeping, slipping	No

There have similarly been studies seeking the minimum flow velocity required to dislodge particles from substrate surfaces. Figure 6-5 presents the results of such work generated by four different experimentalists.

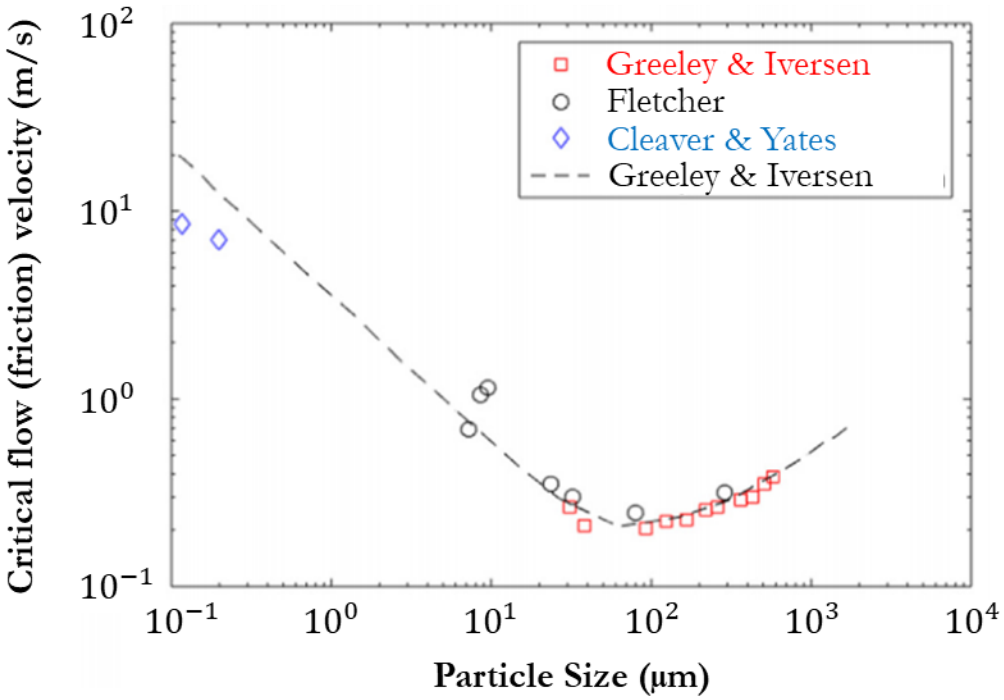

Figure 6-5: Critical flow velocity required to remove a dust particle from a substrate versus particle size [17, 29].

We here, in Tables 6-2 and 6-3 propose the following list of forces that, while not necessarily relevant nor exhaust, is intended to provide a starting point for one who seeks to develop such an all-encompassing transport model. For example, while inertial forces may exist, for very low Reynolds numbers, they are often deemed negligible and ignored. Additionally, electrostatic (Coulombic) forces imply the presence of charged PM, which is by no means clear and—in fact—sometimes refuted as not the case with particles generally considered neutrally charged [17]. Several related citations that may well serve as useful starting points for researchers endeavoring to develop such a transport model are included in references [88] to [139].

Table 6-2: Sample summary of potential major forces at play on cake layer PM, with characteristic values based on relevant literature.

Force	Description
Sheet-level Capillarity	Surface tension supporting a pressure difference across the PM cake layer sheet according to the Young-Laplace equation
Shear Forces from Exhaust Flow at the Wall	Shear stress in the axial direction on the surfaces of the deposit wetted by the exhaust flow
Wall Pressure Forces from Exhaust Flow	Inertial forces (i.e. pressure drag) in the axial direction due to the exhaust flow
Stokes Drag Normal to Wall	Stokes drag in the direction normal to the channel due to low speed creeping flow through the porous wall
Particle-Wall Van der Waals	Dipole-dipole interactions dominated by London Dispersion forces between a particle and wall
Brownian Motion	Random diffusive fluid interactions
Gravitational Force	Force due to the Earth's gravitational field
Thermal Forces / Thermophoresis	Force from pressure imbalance due to a temperature gradient around particles
Particle-Wall Electrostatic Forces	Attractive force between charged particle and wall
Sintering Force	Cohesion due to softening, shrinking, and agglomeration of diesel particulate matter

Table 6-3: Sample summary of potential major forces at play on PM entrained within the channel exhaust play, with characteristic values based on relevant literature.

Force	Description
Particle-level Capillary	Surface tension affecting the motion of a single PM particle / agglomerate
Channel Drag for $Re >> 1$	Pressure drag for inertial >> viscous forces, i.e. for around 100-micron size agglomerates and larger
Stokes Drag in Channel for Re<<1	Stokes' Drag on a < 1-micron sphere, of which 1/3 is pressure and 2/3 is skin friction drag [89]
Particle-Particle Van der Waals	Dipole-dipole interactions dominated by London Dispersion forces between particles
Brownian Motion	Random diffusive fluid interactions
Gravitational Force	Force due to the Earth's gravitational field
Thermal Forces / Thermophoresis	Force from pressure imbalance due to a temperature gradient around the particle
Particle-Particle Electrostatic (Coulombic) Forces	Attractive force due to charged diesel particles in proximity to one another
Sintering Force	Cohesion due to softening, shrinking, and agglomeration of diesel particulate matter

Once equations for each force contribution have been developed as a function of ambient conditions, engine operating parameters, agglomerate / particle size, and agglomerate / particle properties, all dominant force contributions can be plotted as a function of, say, characteristic particle size. An example of such a plot, which in this case contains both dominant and weak forces, is provided in Figure 6-6.

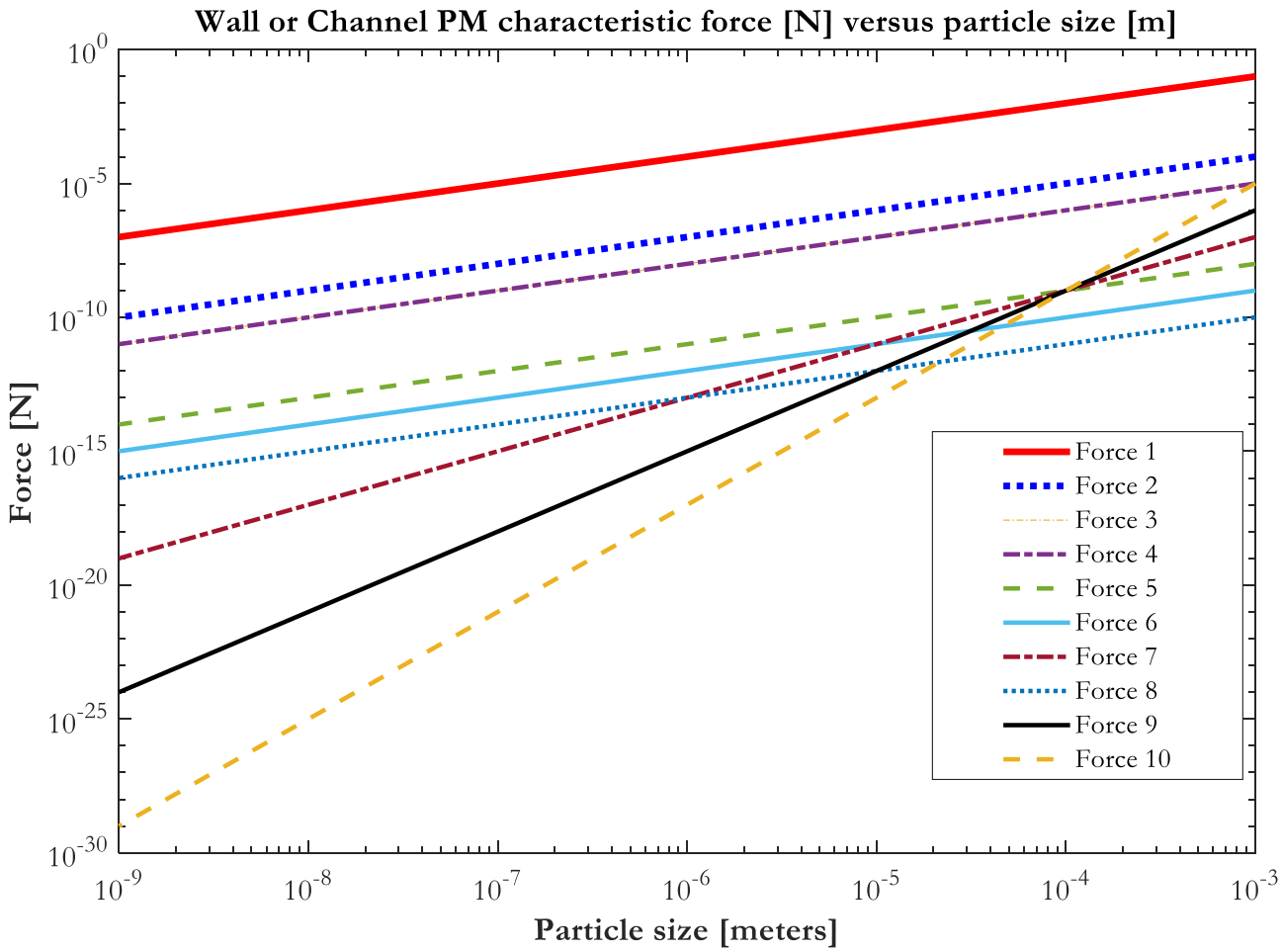

Figure 6-6: A sample depiction of characteristic force on a given PM agglomerate / particle as a function of agglomerate / particle characteristic size (e.g., diameter). Note that all other properties of interest (e.g., viscosity) must be properly accounted for as ambient conditions such as temperature and pressure change.

Appendix A. Full "Front" and "Side" Cross Section Image Data Sets for Operating Points 1, 2, and 3

"Front" view, Point 1 (soot : ash = 1.0) data:

Point 1 (S : A = 1.0)					
Data #	Raw Image #	Top-left	Top-right	Bottom-left	Bottom-right
1	60	3	4	2	4
2	90	3	4	2	4
3	120	2	2	3	3
4	150	3	3	2	3
5	180	4	2	2	3
6	210	4	4	2	4
7	240	4	4	5	4
8	270	6	4	4	4
9	300	5	5	5	6
10	300	4	2	3	5
11	330	4	2	3	2
12	360	5	2	3	2
13	390	5	2	5	3
14	420	6	2	4	3
15	450	4	3	5	2
16	480	6	2	3	4
17	510	6	4	4	5
18	540	5	4	4	3
19	570	2	3	3	3
20	600	2	3	1	3
21	600	3	5	3	4
22	630	4	5	2	2
23	660	2	4	3	2
24	690	3	1	2	6
25	720	4	3	4	3
26	750	3	4	4	6
27	780	4	4	6	4
28	810	3	3	4	5
29	840	3	6	6	6
30	870	5	5	6	6
31	900	3	3	5	4
32	930	4	2	2	1
33	960	3	2	4	2
34	990	3	2	3	5
35	1020	4	1	3	2

“Front” view Point 1 (soot : ash = 1.0) image data continued…

36	1050	6	5	2	3
37	1080	5	5	2	4
38	1110	3	4	3	4
39	1140	3	3	2	4
40	1170	2	2	5	5
41	1200	3	2	3	2
42	1230	4	3	2	4
43	1260	2	1	3	2
44	1290	2	1	2	2
45	1320	3	2	3	2
46	1350	3	2	2	2
47	1380	2	1	3	4
48	1410	3	2	3	3
49	1440	4	2	3	2
50	1470	4	3	3	3
51	1500	5	3	4	2
52	1600	3	2	2	2
53	1700	4	3	2	1
54	1800	3	2	2	2
55	1900	2	2	1	1
56	2000	1	1	1	0
57	2100	2	2	1	2
58	2200	1	2	1	1
59	2300	1	1	1	1
60	2400	2	1	1	1
61	2500	2	0	0	0
62	2600	1	0	0	1
63	2700	0	0	0	0
64	2800	0	0	0	0
65	2900	1	0	0	1
66	2997	0	0	0	1

"Front" view Point 2 (soot : ash = 0.25) data:

Point 2 (S : A = 0.25)					
Data #	Raw Image #	Top-left	Top-right	Bottom-left	Bottom-right
1	60	1	1	2	2
2	90	2	2	4	5
3	120	3	2	5	5
4	150	3	2	6	2
5	180	3	2	6	3
6	210	4	2	6	3
7	240	4	2	4	2
8	270	4	2	3	2
9	300	4	2	6	4
10	300	2	0	4	2
11	330	2	1	2	1
12	360	3	1	3	2
13	390	2	3	3	3
14	420	3	1	3	3
15	450	2	1	4	2
16	480	3	1	3	2
17	510	2	1	3	1
18	540	2	1	3	1
19	570	1	1	2	2
20	600	2	1	2	2
21	600	2	0	1	1
22	630	0	0	1	1
23	660	0	0	0	0
24	690	1	1	2	2
25	720	1	1	1	1
26	750	0	1	0	1
27	780	0	0	1	1
28	810	0	0	0	1
29	840	0	0	0	1
30	870	0	1	0	2
31	900	0	0	1	1
32	930	0	0	0	2
33	960	0	0	0	1
34	990	0	0	0	1
35	1020	0	0	0	1

“Front” view Point 2 (soot : ash = 0.25) image data continued…

36	1050	0	0	0	1
37	1080	0	0	0	0
38	1110	0	0	0	0
39	1140	0	0	0	0
40	1170	0	0	0	0
41	1200	1	0	0	0
42	1230	0	1	0	0
43	1260	0	0	0	0
44	1290	0	0	0	0
45	1320	0	0	0	0
46	1350	0	0	0	0
47	1380	0	0	0	0
48	1410	0	0	0	0
49	1440	0	0	0	1
50	1470	0	0	0	0
51	1500	1	0	0	0
52	1600	0	0	0	1
53	1700	0	0	0	0
54	1800	0	0	0	0
55	1900	0	0	0	0
56	2000	0	0	0	0
57	2100	0	0	0	0
58	2200	0	0	0	0
59	2300	0	0	0	0
60	2400	0	0	0	0
61	2500	0	0	0	0
62	2600	0	0	0	0
63	2700	0	0	0	0
64	2800	0	0	0	0
65	2900	0	0	0	0
66	2997	0	0	0	0

"Front" view Point 3 (soot : ash = 2.5) data:

Point 3 (S : A = 2.5)					
Data #	Raw Image #	Top-left	Top-right	Bottom-left	Bottom-right
1	60	6	8	4	4
2	90	8	7	8	6
3	120	6	2	3	3
4	150	2	2	4	3
5	180	3	2	4	2
6	210	2	2	2	2
7	240	3	2	2	2
8	270	1	1	0	1
9	300	2	3	1	1
10	300	2	1	2	2
11	330	2	2	1	1
12	360	3	3	1	2
13	390	3	3	1	3
14	420	2	2	2	3
15	450	2	2	2	2
16	480	3	2	2	2
17	510	3	2	2	2
18	540	3	2	2	2
19	570	3	2	2	4
20	600	2	2	1	2
21	600	2	2	2	2
22	630	3	2	2	2
23	660	3	3	2	2
24	690	3	3	3	4
25	720	3	3	4	4
26	750	3	2	3	3
27	780	3	2	3	2
28	810	3	2	2	2
29	840	3	2	3	3
30	870	2	2	3	3
31	900	3	2	3	3
32	930	3	3	4	3
33	960	3	2	4	2
34	990	2	1	4	2
35	1020	2	1	4	2

“Front” view Point 3 (soot : ash = 2.5) image data continued…

36	1050	2	1	3	2
37	1080	2	1	3	2
38	1110	3	2	4	3
39	1140	2	2	4	3
40	1170	1	1	3	2
41	1200	1	1	2	2
42	1230	3	2	3	2
43	1260	2	0	2	1
44	1290	2	0	1	1
45	1320	1	0	1	1
46	1350	1	0	2	1
47	1380	1	0	1	1
48	1410	1	0	1	1
49	1440	1	0	2	2
50	1470	1	1	2	1
51	1500	1	0	1	1
52	1600	2	0	2	2
53	1700	0	0	1	1
54	1800	0	0	0	0
55	1900	0	0	0	0
56	2000	0	0	0	0
57	2100	0	0	0	0
58	2200	0	0	0	0
59	2300	0	0	0	0
60	2400	0	0	0	0
61	2500	0	0	0	0
62	2600	0	0	0	0
63	2700	0	0	0	0
64	2800	0	0	0	0
65	2900	0	0	0	0
66	2997	0	0	0	0

“Side” view Point 1 (soot : ash = 1.0) image data

Image #	Raw Image #	Plug Cross Section	1	2	3	4	5	6	7	8	9	10	11	12	13	14
1	*100*	top	2	2		2	1	2	2	2	2	2	1	1		
		middle													2	3
		bottom														
		Is Plugged?	1	1	0	1	0	1	1	1	1	1	0	0	1	1
2	*110*	top	1	2		N	N	N	N	N	N	N	N	N	N	N
		middle	1					2	2							3
		bottom														
		Is Plugged?	0	1	0	N	N	N	N	N	N	N	N	N	N	N
3	*120*	top				2	2	2	2	2	1	2				
		middle	N	N	N	N	N	N	N							
		bottom	N	N	N	N	N	N	N	N	N	N	N	N	N	N
		Is Plugged?	N	N	N	N	N	N	N	N	N	N	N	N	N	N
4	*130*	top	2													
		middle	2		1		2	1	1	2	1	2			2	
		bottom														
		Is Plugged?	1	0	0	0	1	0	0	1	0	1	0	0	1	0
5	*140*	top	N	N	N	N	N	N	N	N	N	N		2		1
		middle	N	N	N	N	N	N	N	N	N	N	N	N	N	N
		bottom						N	N	N	N	N	N	N	N	N
		Is Plugged?	N	N	N	N	N	N	N	N	N	N	N	N	N	N
6	*150*	top				2										2
		middle												2		2
		bottom														
		Is Plugged?	0	0	0	1	0	0	0	0	0	0	0	1	0	1
7	*160*	top	N	N	N	N	N	N	N	N	N	N	N	N	N	N
		middle			3		2				N	N	N	N	N	N
		bottom		3												
		Is Plugged?	N	N	N	N	N	N	N	N	N	N	N	N	N	N
8	*170*	top			3	3	3	3	1			2	2	3	2	3
		middle	N	N	N											
		bottom	N	N	N	N	N	N	N	N	N					
		Is Plugged?	N	N	N	N	N	N	N	N	N	1	1	1	1	1
9	*180*	top	N	N	N	N	N	N	N	N	N	N	N	N	N	N
		middle	N	N	N	N	N	N	N	N	N	N	N	N	N	N
		bottom	N	N	N	N	N	N	N	N	N	N	N	N	N	N
		Is Plugged?	N	N	N	N	N	N	N	N	N	N	N	N	N	N
10	*190*	top	N	N	N	N	N	N	N	N	N	N	N	N	N	N
		middle	N	N	N	N	N	N	N	N	N	N	N	N	N	N
		bottom	N	N	N	N	N	N	N	N	N	N	N	N	N	N
		Is Plugged?	N	N	N	N	N	N	N	N	N	N	N	N	N	N
11	*200*	top	N			1	1	3	2	2	1	1				3
		middle	N	N	N	N	N									1
		bottom	N	N	N	N	N	N	N	N	N	N	N	N	N	N
		Is Plugged?	N	N	N	N	N	N	N	N	N	N	N	N	N	N
12	*210*	top	2	2	2	3	3	3				N	N	N	N	3
		middle														
		bottom														
		Is Plugged?	1	1	1	1	1	1	0	0	0	N	N	N	N	1
13	*220*	top	N	N	N	N	N	N	N							3
		middle	N	N	N	N	N	N	N	N	N	N	N	N	N	N
		bottom							N	N	N	N	N	N	N	N
		Is Plugged?	N	N	N	N	N	N	N	N	N	N	N	N	N	N
14	*230*	top	1	2	2	1	3	2	3	2		1				2
		middle														4
		bottom														
		Is Plugged?	0	1	1	0	1	1	1	1	0	0	0	0	0	1
15	*240*	top			N	N	N	N	N	N	N	N	N	N	N	N
		middle													N	N
		bottom	1	1											2	2
		Is Plugged?	0	0	N	N	N	N	N	N	N	N	N	N	N	N
16	*250*	top					1	1	3	3	2	2		1		3
		middle														1
		bottom														1
		Is Plugged?	0	0	0	0	0	0	1	1	1	1	0	0	0	1

"Side" view Point 1 (soot : ash = 1.0) image data continued…

17	*260*	top	2	1	2	2	3	3	N	N	N	N	N	N	N	N
		middle														
		bottom														
		Is Plugged?	1	0	1	1	1	1	N	N	N	N	N	N	N	N
18	*270*	top	2	2		3	3	2	2		1			N	N	N
		middle													3	2
		bottom														
		Is Plugged?	1	1	0	1	1	1	1	0	0	0	0	N	N	N
19	*280*	top	N	N	N	N	N				2	1		2		3
		middle	N	N	N	N	N	N	N	N	N	N	N	N	N	N
		bottom	N	N	N	N	N	N	N	N	N	N	N	N	N	N
		Is Plugged?	N	N	N	N	N	N	N	N	N	N	N	N	N	N
20	*290*	top	N	N	N	N	N	N	N	N	N	N	N	N	N	N
		middle						N	N	N	N	N	N	N	N	N
		bottom													N	N
		Is Plugged?	N	N	N	N	N	N	N	N	N	N	N	N	N	N
21	*300*	top	N	N	N	N	N	N	N	N	N	N	N			3
		middle	N	N	N	N	N	N	N	N	N	N	N	N	N	N
		bottom	N	N	N	N	N	N	N	N	N	N	N	N	N	N
		Is Plugged?	N	N	N	N	N	N	N	N	N	N	N	N	N	N
22	*310*	top	2	2	3	3	3	3	2	1				2	2	2
		middle											1		3	4
		bottom													2	2
		Is Plugged?	1	1	1	1	1	1	1	0	0	0	0	1	1	1
23	*320*	top		2	2	2	N	N	N	N	N	N	N	N	N	N
		middle											N	N	N	N
		bottom										5			N	N
		Is Plugged?	0	1	1	1	N	N	N	N	N	N	N	N	N	N
24	*330*	top					2	2	1							4
		middle	N	N											1	
		bottom	N	N	N	N	N	N	N	N	N			1		
		Is Plugged?	N	N	N	N	N	N	N	N	N	0	0	0	0	1
25	*340*	top	2	1	2	2	2	2	1	1	N	N	N	N	N	N
		middle	2				2								3	3
		bottom														
		Is Plugged?	1	0	1	1	1	1	0	0	N	N	N	N	N	N
26	*350*	top	N	N	N	N	N	N	N	N		2				2
		middle		2		1		2						2	3	4
		bottom													2	3
		Is Plugged?	N	N	N	N	N	N	N	N	0	1	0	1	1	1
27	*360*	top			2	3	3	1	2	2	1	1		N	N	N
		middle						2							2	2
		bottom														
		Is Plugged?	0	0	1	1	1	1	1	1	0	0	0	N	N	N
28	*370*	top		N	N	N	N	N	N	N	N	N	N	N	N	N
		middle	2		N	N	N	N	N	N	N	N	N	N	N	N
		bottom											N	N	N	N
		Is Plugged?	1	N	N	N	N	N	N	N	N	N	N	N	N	N
29	*380*	top		2	2	2	2	2	2	2	2				2	2
		middle											1	2	3	
		bottom	N	N	N	N										
		Is Plugged?	N	N	N	N	1	1	1	1	1	0	0	1	1	1
30	*390*	top	3	2	3	2	N	N	N	N	N	N	N	N	N	N
		middle	2						2		1	2			N	N
		bottom													2	2
		Is Plugged?	1	1	1	1	N	N	N	N	N	N	N	N	N	N
31	*400*	top					N	N	N	N	N	N	N	N	N	N
		middle													N	N
		bottom													2	2
		Is Plugged?	0	0	0	0	N	N	N	N	N	N	N	N	N	N
32	*410*	top			1						2			2	2	
		middle												1	2	5
		bottom	N	N	N	N	N	N	N	N					1	1
		Is Plugged?	N	N	N	N	N	N	N	N	1	0	0	1	1	1

"Side" view Point 1 (soot : ash = 1.0) image data continued…

33	*420*	top	2	2	2	2	2	1	2	2	2	2	N	N	N	N
		middle		1							2			1		
		bottom		2												
		Is Plugged?	1	1	1	1	1	0	1	1	1	1	N	N	N	N
34	*430*	top											2	1	2	2
		middle	N	N	N	N	N	N	N	N	N	N	N			
		bottom	N	N	N	N	N	N	N	N	N	N	N	N	N	N
		Is Plugged?	N	N	N	N	N	N	N	N	N	N	N	N	N	N
35	*440*	top	2	1	2	2	2	2	2		1	1	1	2	2	3
		middle											2			2
		bottom														
		Is Plugged?	1	0	1	1	1	1	1	0	0	0	1	1	1	1
36	*450*	top	2	2	2	N	N	N	N	N	N	N	N	N	N	N
		middle					N	N	N	N	N	N	N	N	N	N
		bottom											N	N	N	N
		Is Plugged?	1	1	1	N	N	N	N	N	N	N	N	N	N	N
37	*460*	top			2	2	1	2	2		2	1		2	3	4
		middle										1			1	3
		bottom													1	3
		Is Plugged?	0	0	1	1	0	1	1	0	1	0	0	1	1	1
38	*470*	top	2	1	3	3	3		N	N	N	N	N	N	N	N
		middle											2			3
		bottom														
		Is Plugged?	1	0	1	1	1	0	N	N	N	N	N	N	N	N
39	*480*	top	N	N	N	N	N	N	1	2	2	2	1	2		3
		middle	N	N	N	N	N	N	N	N	N	N	N	N	N	N
		bottom	N	N	N	N	N	N	N	N	N	N	N	N	N	N
		Is Plugged?	N	N	N	N	N	N	N	N	N	N	N	N	N	N
40	*490*	top	2	2	2	2	2	2	3	1	1	1		2	N	N
		middle													3	3
		bottom													1	
		Is Plugged?	1	1	1	1	1	1	1	0	0	0	0	1	N	N
41	*500*	top						1		3		4	4			
		middle				2	1	3				1	1			
		bottom						2								
		Is Plugged?	0	0	0	1	0	1	0	1	0	1	1	0	0	0
42	*510*	top	N	N	N	N	N			1		2	3	2	1	
		middle	N	N	N	N	N	N	N	N	N	N	N			
		bottom	N	N	N	N	N	N	N	N	N	N	N	N	N	N
		Is Plugged?	N	N	N	N	N	N	N	N	N	N	N	N	N	N
43	*520*	top			1		3		2			2		2	2	
		middle		2							2			3	2	
		bottom												2		
		Is Plugged?	0	1	0	0	1	0	1	0	1	1	0	1	1	0
44	*530*	top				N	N	N	N	N	N	N	N	N	N	N
		middle		1		1		1	N	N	N	N	N	N	N	N
		bottom											N	N	N	N
		Is Plugged?	0	0	0	N	N	N	N	N	N	N	N	N	N	N
45	*540*	top					1		1		2		3	2	1	
		middle											2	2	4	
		bottom										1	2	2		
		Is Plugged?	0	0	0	0	0	0	0	0	1	0	1	1	1	0
46	*550*	top								1	2	N	N	N	N	
		middle				2										
		bottom											2			
		Is Plugged?	0	0	0	1	0	0	0	0	1	N	N	N	N	0
47	*560*	top	N	N	N								2	2		
		middle	N	N	N	N	N	N	N							
		bottom	N	N	N	N	N	N	N	N	N	N	3			
		Is Plugged?	N	N	N	N	N	N	N	N	N	N	1	1	0	0
48	*570*	top			2	2								2	4	
		middle		2		1		1				1	2	2	2	
		bottom											1		4	
		Is Plugged?	0	1	1	1	0	0	0	0	0	0	1	1	1	0

"Side" view Point 1 (soot : ash = 1.0) image data continued…

49	*580*	top	N	N	N	N	N	N	N	N	N	N	N		3	
		middle	N	N	N	N	N	N	N	N	N	N	N	N	N	N
		bottom							N	N	N	N	N	N	N	N
		Is Plugged?	N	N	N	N	N	N	N	N	N	N	N	N	N	N
50	*590*	top			1	2	2	2	2			2	1	2	3	
		middle														
		bottom														
		Is Plugged?	0	0	0	1	1	1	1	0	0	1	0	1	1	0
51	*600*	top	N	N	N	N	N	N	N	N	N	N	N	N	N	N
		middle	N	N	N	N	N	N	N	N	N	N	N	N	N	N
		bottom	N	N	N	N	N	N	N	N	N	N	N	N	N	N
		Is Plugged?	N	N	N	N	N	N	N	N	N	N	N	N	N	N
52	*610*	top														
		middle											2	1		
		bottom														
		Is Plugged?	0	0	0	0	0	0	0	0	0	0	1	0	0	0
53	*620*	top									N	N	N	N	N	N
		middle								N	N	N	N	N	N	N
		bottom										N	N	N	N	N
		Is Plugged?	0	0	0	0	0	0	0	N	N	N	N	N	N	N
54	*630*	top	2	2					2	1				1	2	
		middle											1	2	4	
		bottom													2	
		Is Plugged?	1	1	0	0	0	0	1	0	0	0	0	1	1	0
55	*640*	top	N	N	N	N	N	N	N	N	N	N	N	N	N	N
		middle	N	N	N	N	N	N	N	N						
		bottom	N	N	N	N	N	N	N	N						
		Is Plugged?	N	N	N	N	N	N	N	N	N	N	N	N	N	N
56	*650*	top													2	
		middle														
		bottom														
		Is Plugged?	0	0	0	0	0	0	0	0	0	0	0	0	1	0
57	*660*	top	N	N	N	N	N	N	N							
		middle	N	N	N								2	2	4	
		bottom	N	N	N											
			N	N	N	N	N	N	N	0	0	0	1	1	1	0
58	*670*	top											N	N	N	N
		middle											N	N	N	N
		bottom												N	N	N
		Is Plugged?	0	0	0	0	0	0	0	0	0	0	N	N	N	N
59	*680*	top								1	2				1	
		middle													2	
		bottom														
		Is Plugged?	0	0	0	0	0	0	0	0	1	0	0	0	1	0
60	*690*	top				N	N	N	N	N	N	N	N	N	N	N
		middle				N	N	N	N	N	N	N	N	N	N	N
		bottom							N	N	N	N	N	N	N	N
		Is Plugged?	0	0	0	N	N	N	N	N	N	N	N	N	N	N
61	*700*	top				2		2	2							
		middle		2					2					2	2	
		bottom														
		Is Plugged?	0	1	0	1	0	1	1	0	0	0	0	1	1	0
62	*710*	top	N	N	N	N	N	N	N	N	N	N	N	N	N	N
		middle	N	N	N	N							1	2	2	
		bottom	N	N	N	N	N	N								
		Is Plugged?	N	N	N	N	N	N	N	N	N	N	N	N	N	N
63	*720*	top		2	2	2										
		middle											N	N	N	
		bottom														
		Is Plugged?	0	1	1	1	0	0	0	0	0	0	N	N	N	0
64	*730*	top						2	2	3	1	2	2		4	
		middle									2	2	1	2	4	
		bottom														
		Is Plugged?	0	0	0	0	0	1	1	1	1	1	1	1	1	0

"Side" view Point 1 (soot : ash = 1.0) image data continued…

65	*740*	top	2	2	2		N	N	N	N	N	N	N	N	N	N
		middle				1		N	N	N	N	N	N	N	N	N
		bottom								N	N	N	N	N	N	N
		Is Plugged?	1	1	1	0	N	N	N	N	N	N	N	N	N	N
66	*750*	top	2		2	2	2	2	1	2	2	2	1			
		middle													2	
		bottom													3	
		Is Plugged?	1	0	1	1	1	1	0	1	1	1	0	0	1	0
67	*760*	top	N	N	N	N	N	N	N	N	N	N	N	N	N	N
		middle	N	N	N	N	N	N					1		2	
		bottom	N	N	N	N	N	N	N	N	N	N	N	N	N	N
		Is Plugged?	N	N	N	N	N	N	N	N	N	N	N	N	N	N
68	*770*	top	2	1	2	1		2	1			2	2		2	
		middle						2							3	
		bottom													3	
		Is Plugged?	1	0	1	0	0	1	0	0	0	1	1	0	1	0
69	*780*	top	N	N	N	N				2	2	2	2			
		middle										1	2	2	2	
		bottom													2	
		Is Plugged?	N	N	N	N	0	0	0	1	1	1	1	1	1	0
70	*790*	top	2		2	2		2								
		middle		1												
		bottom														
		Is Plugged?	1	0	1	1	0	1	0	0	0	0	0	0	0	0
71	*800*	top	2		2	2	2	2	2			1	2			
		middle													4	
		bottom													2	
		Is Plugged?	1	0	1	1	1	1	1	0	0	0	1	0	1	0
72	*810*	top	N	N	N	N	N	N	N	N	N	N	N	N	N	N
		middle	N	N	N	N	N	N	N	N	N	2		1	2	
		bottom	N	N	N	N	N	N	N	N	N	N	N	N	N	N
		Is Plugged?	N	N	N	N	N	N	N	N	N	N	N	N	N	N
73	*820*	top	2	2	2	3	2	2	2	2	2	2	2	1	2	
		middle												2	2	
		bottom														
		Is Plugged?	1	1	1	1	1	1	1	1	1	1	1	1	1	0
74	*830*	top	N	N	N	N	N							1	3	
		middle	N	N	N									2	3	
		bottom	N	N	N	N	N	N	N							
		Is Plugged?	N	N	N	N	N	N	N	0	0	0	0	1	1	0
75	*840*	top	2	2	2	3	2	2	2		2	1			3	
		middle	2	2									N	N	N	N
		bottom														
		Is Plugged?	1	1	1	1	1	1	1	0	1	0	N	N	N	N
76	*850*	top		2	2	2	2	2	2	2	2		3	1	2	
		middle								2	1			1	2	
		bottom														
		Is Plugged?	0	1	1	1	1	1	1	1	1	0	1	0	1	0
77	*860*	top	2	1	2	N	N	N	N	N	N	N	N	N	N	N
		middle				N	N	N	N	N	N	N	N	N	N	N
		bottom								N	N	N	N	N	N	N
		Is Plugged?	1	0	1	N	N	N	N	N	N	N	N	N	N	N
78	*870*	top	2	2	2	N	N	N	N	N	N	N	N	N	N	N
		middle	1			N	N	N	N	N	N	N	N	N	N	N
		bottom								N	N	N	N	N	N	N
		Is Plugged?	1	1	1	N	N	N	N	N	N	N	N	N	N	N
79	*880*	top	N	N	N	N	N	N	2	N	N	N	N	N	N	N
		middle	N	N	N	N	N								2	
		bottom	N	N	N	N	N	N	N	N	N	N	N	N	N	N
		Is Plugged?	N	N	N	N	N	N	N	N	N	N	N	N	N	N
80	*890*	top	3	2	2	1	3	1	1	2	2	2	2	2		2
		middle		2											2	2
		bottom														
		Is Plugged?	1	1	1	0	1	0	0	1	1	1	1	1	1	1

“Side” view Point 2 (soot : ash = 0.25) image data

Image #	Raw Image #	Plug Cross Section	1	2	3	4	5	6	7	8	9	10	11	12	13	14
1	*60*	top	N	N	N	N	N	N	4		3	3	2	2	1	1
		middle	N	N	N	N	N	N	N							
		bottom	N	N	N	N	N	N	N							
		Is plugged?	N	N	N	N	N	N	N	0	1	1	1	1	0	0
2	*70*	top	3						5	4	4	3	2	2	1	1
		middle														
		bottom	3													
		Is plugged?	1	0	0	0	0	0	1	1	1	1	1	1	0	0
3	*80*	top	N	N	2						3	3	3	4	2	2
		middle														
		bottom	N	N	N	N	N	N								
		Is plugged?	N	N	N	N	N	N	0	0	1	1	1	1	1	1
4	*90*	top		3	3		1	N	N	N	N	N	N	N	N	N
		middle				N	N	N	N	N	N	N	N	N	N	N
		bottom								N	N	N	N	N	N	N
		Is plugged?	0	1	1	N	N	N	N	N	N	N	N	N	N	N
5	*100*	top	3		3	3	3		2	3	3	4	4	3	2	1
		middle														
		bottom		2												
		Is plugged?	1	1	1	1	1	0	1	1	1	1	1	1	1	0
6	*110*	top	3	N	N	N	N	N	N	N	N	N	N	N	2	2
		middle	N	N	N	N	N	N	N	N	N	N	N			
		bottom	N	4	N	N	N	N	N	N	N	N	N	N	N	N
		Is plugged?	N	N	N	N	N	N	N	N	N	N	N	N	N	N
7	*120*	top	4				3				4	3	3	3		2
		middle	2	4												
		bottom			3		4			N	N	N	N	N	N	N
		Is plugged?	1	1	1	0	1	0	0	N	N	N	N	N	N	N
8	*130*	top				4			4	2	2	3	3		3	
		middle			2		2					3				
		bottom	N	N	4	4	4	N	N							
		Is plugged?	N	N	1	1	1	N	N	1	1	1	1	0	1	0
9	*140*	top	4	3	2				1	N	2	2	2		2	
		middle	2		4			N	N				2			
		bottom			2		5			N	N	N	N	N	N	N
		Is plugged?	1	1	1	0	1	N	N	N	N	N	N	N	N	N
10	*150*	top	3	2	1	3		2		2	3	3	3	3	3	
		middle					4									
		bottom				2										
		Is plugged?	1	1	0	1	1	1	0	1	1	1	1	1	1	0
11	*160*	top	4	2	N	N	N	N	N	N	N	N	N	N	N	N
		middle	N	N	N	N	N	N	N	N	N	N	N	N	N	N
		bottom		3	3			N	N							
		Is plugged?	N	N	N	N	N	N	N	N	N	N	N	N	N	N
12	*170*	top	4		3	3	3	2	3	2	2	3	3	2	1	
		middle						3								
		bottom		2												
		Is plugged?	1	1	1	1	1	1	1	1	1	1	1	1	0	0
13	*180*	top	N	N	N	2	4	2			1	2	2	3	2	1
		middle	N	N	N		3									
		bottom	N	N	N	N	N	N	N							
		Is plugged?	N	N	N	N	N	N	N	0	0	1	1	1	1	0
14	*190*	top	3	4	3	2	3	2					2	2		
		middle					2									
		bottom									3			2	N	N
		Is plugged?	1	1	1	1	1	1	0	0	1	0	1	1	N	N
15	*200*	top	3		3	3	2		2	2	2	3	2	2		
		middle	2					3								
		bottom					N	N	N							
		Is plugged?	1	0	1	1	N	N	N	1	1	1	1	1	0	0
16	*210*	top	2	3	3	3	N	N	N	N	N	N	N	N	N	N
		middle			N	N	N	N	N	N	N	N	N	N	N	N
		bottom														
		Is plugged?	1	1	N	N	N	N	N	N	N	N	N	N	N	N

"Side" view Point 2 (soot : ash = 0.25) image data continued…

17	*220*	top	2		2	3	2			2	2	2	2	3	2	
		middle					1									
		bottom						3								
		Is plugged?	1	0	1	1	1	1	0	1	1	1	1	1	1	0
18	*230*	top	N	N	N	N	N					2	2	3	1	
		middle	N	N	N	N	N									
		bottom			N	N	N	N	N							
		Is plugged?	N	N	N	N	N	N	N	0	0	1	1	1	0	0
19	*240*	top	2	3	2	3	2	1	2	1	1	2	1	2	2	
		middle														
		bottom								N	N	N	N	N	N	N
		Is plugged?	1	1	1	1	1	0	1	N	N	N	N	N	N	N
20	*250*	top	N		2		2	2	2	1				3	2	2
		middle														
		bottom	N	N	N	N	N									
		Is plugged?	N	N	N	N	N	1	1	0	0	0	0	1	1	1
21	*260*	top	3	3	3	3		N	N	N	N	N	N	N	N	N
		middle					N	N	N						N	N
		bottom								N	N	N	N	N		
		Is plugged?	1	1	1	1	N	N	N	N	N	N	N	N	N	N
22	*270*	top			2	3	2	3	2		1	2	2	1	1	2
		middle														
		bottom	N	N												
		Is plugged?	N	N	1	1	1	1	1	0	0	1	1	0	0	1
23	*280*	top	N	N	N	N	N	N	N	N	N	N	N	N	N	N
		middle	N	N	N	N	N	N	N	N	N	N	N	N	N	N
		bottom						N	N							
		Is plugged?	N	N	N	N	N	N	N	N	N	N	N	N	N	N
24	*290*	top	N	N	N	N	N	N	N	N	N	N	N	N	N	N
		middle	N	N	N	N	N	N	N	N	N	N	N	N	N	N
		bottom	N	N	N	N	N	N	N	N	N	N	N	N	N	N
		Is plugged?	N	N	N	N	N	N	N	N	N	N	N	N	N	N
25	*300*	top				3	3	3	2		2		2			
		middle														
		bottom			2	2	2				2				2	
		Is plugged?	0	0	1	1	1	1	1	0	1	0	1	0	1	0
26	*310*	top							2	2	1	2	2	3	2	2
		middle										2				
		bottom														
		Is plugged?	0	0	0	0	0	0	1	1	0	1	1	1	1	1
27	*320*	top		2	2	3	2	3	4	3		2			2	2
		middle					2							1		
		bottom														
		Is plugged?	0	1	1	1	1	1	1	1	0	1	0	0	1	1
28	*330*	top	N	N	N	N	N	N	N	N	N	N	N	N	N	N
		middle	N	N	N	N	N	N	N					3		
		bottom														
		Is plugged?	N	N	N	N	N	N	N	N	N	N	N	N	N	N
29	*340*	top		2	3	2	3	3	3	2	2	2	2	2	2	2
		middle														
		bottom														
		Is plugged?	0	1	1	1	1	1	1	1	1	1	1	1	1	1
30	*350*	top		2	2	2	2	2	2	2	2	2			N	N
		middle								N	N	N	N	N	N	N
		bottom	N	N	N	N	N	N	N	N	N	N				
		Is plugged?	N	N	N	N	N	N	N	N	N	N	N	N	N	N
31	*360*	top		2	3	2	3	3	3	3	3	2	2	2		
		middle														
		bottom														
		Is plugged?	0	1	1	1	1	1	1	1	1	1	1	1	0	0
32	*370*	top	1	2	3	3	3	4	3	3	3	2	1	2		
		middle														
		bottom														
		Is plugged?	0	1	1	1	1	1	1	1	1	1	0	1	0	0

"Side" view Point 2 (soot : ash = 0.25) image data continued…

33	*380*	top	N	N	N	N	N	N	N	N	N	N	N	N		
		middle														
		bottom														
		Is plugged?	N	N	N	N	N	N	N	N	N	N	N	N	0	0
34	*390*	top		2	2	2	2	3	3	2	2	2	2	2		
		middle														
		bottom														
		Is plugged?	0	1	1	1	1	1	1	1	1	1	1	1	0	0
35	*400*	top		2	3	3	1		2	N	N	N	N	N	N	N
		middle														
		bottom														
		Is plugged?	0	1	1	1	0	0	1	N	N	N	N	N	N	N
36	*410*	top		2	3	3	2	3	3	3	2	3	2	1		
		middle														
		bottom														
		Is plugged?	0	1	1	1	1	1	1	1	1	1	1	0	0	0
37	*420*	top		2	2	3	2	3	3	3	3	2		2		
		middle														
		bottom														
		Is plugged?	0	1	1	1	1	1	1	1	1	1	0	1	0	0
38	*430*	top	2	2	3	3	2	3		3	3	2	2	2		
		middle														
		bottom														
		Is plugged?	1	1	1	1	1	1	0	1	1	1	1	1	0	0
39	*440*	top		3	2	2	2	3	2	3	2	3	2	2		
		middle														
		bottom														
		Is plugged?	0	1	1	1	1	1	1	1	1	1	1	1	0	0
40	*450*	top	N	N	N	N	N	N	N	N	N	N	N	N	N	N
		middle	N	N	N	N	N									
		bottom														
		Is plugged?	N	N	N	N	N	N	N	N	N	N	N	N	N	N
41	*460*	top		2	3	3	2	3	2	3	2	2	2	2		
		middle														
		bottom														
		Is plugged?	0	1	1	1	1	1	1	1	1	1	1	1	0	0
42	*470*	top		3	2	2	2	3	2	2	2	2	1			
		middle									N	N	N	N	N	N
		bottom	N	N	N	N	N	N	N	N	N	N	N	N	N	N
		Is plugged?	N	N	N	N	N	N	N	N	N	N	N	N	N	N
43	480	top		3	3	3	3	3	2	2	2	2	2	2		
		middle														
		bottom														
		Is plugged?	0	1	1	1	1	1	1	1	1	1	1	1	0	0
44	*490*	top		2	3	3	3	3	2	2	2	2	2	2		2
		middle														
		bottom														
		Is plugged?	0	1	1	1	1	1	1	1	1	1	1	1	0	1
45	*500*	top	N	N	N	N	N	N	N	N	N	N	N	N	N	N
		middle		3	3	3	2	3	2	2	2	2	2	2		2
		bottom														
		Is plugged?	N	N	N	N	N	N	N	N	N	N	N	N	N	N
46	*510*	top		3	3	3	2	3	2	2	2	2	2	2		2
		middle					2									
		bottom														
		Is plugged?	0	1	1	1	1	1	1	1	1	1	1	1	0	1
47	*520*	top		2	2	2	3	3	3	3	2	2	N	N	N	N
		middle	N	N	N	N	N	N	N	N	N	N	N	N	N	N
		bottom	N	N	N	N	N									
		Is plugged?	N	N	N	N	N	N	N	N	N	N	N	N	N	N
48	*530*	top		2	3	3	3	3	3	3	2	2	2	3		
		middle														
		bottom														
		Is plugged?	0	1	1	1	1	1	1	1	1	1	1	1	0	0

"Side" view Point 2 (soot : ash = 0.25) image data continued…

49	*540*	top		2	3	2		2	2	2	1	2				
		middle														
		bottom								N	N	N	N	N	N	N
		Is plugged?	0	1	1	1	0	1	1	N	N	N	N	N	N	N
50	*550*	top	N	N	N	N	N	N	N	N	N	N	N			
		middle														
		bottom														
		Is plugged?	N	N	N	N	N	N	N	N	N	N	N	0	0	0
51	*560*	top	1	1	3	3	3	3	2	3	2	2	3	3		
		middle														
		bottom														
		Is plugged?	0	0	1	1	1	1	1	1	1	1	1	1	0	0
52	*570*	top	N	N	N	N	N	N	N	N	N	N	N	N	N	N
		middle	N	N	N	N	N	N	N	N	N					
		bottom														
		Is plugged?	N	N	N	N	N	N	N	N	N	N	N	N	N	N
53	*580*	top	2	3	3	3	3	2	2	3		2	3	2		
		middle														
		bottom														
		Is plugged?	1	1	1	1	1	1	1	1	0	1	1	1	0	0
54	*590*	top	3	3	3	3	2	2	2	2	2	2	3	2		
		middle												N	N	N
		bottom	N	N	N	N	N	N	N	N	N	N	N	N	N	N
		Is plugged?	N	N	N	N	N	N	N	N	N	N	N	N	N	N
55	*600*	top	N	4	3	2	2	2	2	2	2	2	2	1		
		middle														
		bottom														
		Is plugged?	N	1	1	1	1	1	1	1	1	1	1	0	0	0
56	*610*	top	2	3	3	3	3	2	3	3	2	3				
		middle														
		bottom														
		Is plugged?	1	1	1	1	1	1	1	1	1	1	0	0	0	0
57	*620*	top	N	N	N	N	N	N	N	N	N	N	N	N	N	N
		middle														
		bottom														
		Is plugged?	N	N	N	N	N	N	N	N	N	N	N	N	N	N
58	*630*	top	2	3	3	3	3	2	3	2	2	2	2	3		2
		middle														
		bottom														
		Is plugged?	1	1	1	1	1	1	1	1	1	1	1	1	0	1
59	*640*	top	2	2	2	3	3	2	2	2					2	
		middle	N	N	N	N	N	N	N	N	N	N	N	N	N	N
		bottom	N	N	N	N	N	N	N	N	N	N	N	N	N	N
		Is plugged?	N	N	N	N	N	N	N	N	N	N	N	N	N	N
60	*650*	top	3	3	2	3	3	3	3	2	2	2	2	2	2	
		middle														
		bottom														
		Is plugged?	1	1	1	1	1	1	1	1	1	1	1	1	1	0
61	*660*	top	2	3	3	3	2	3	3	3	3	2	4			2
		middle														
		bottom														
		Is plugged?	1	1	1	1	1	1	1	1	1	1	1	0	0	1
62	*670*	top	N	N	N	N	N	N	N	N	N	N	N	N	N	N
		middle														
		bottom											1			
		Is plugged?	N	N	N	N	N	N	N	N	N	N	N	N	N	N
63	*680*	top	3	3	3	3	3	3	3	3	3	3	2	1		
		middle														
		bottom														
		Is plugged?	1	1	1	1	1	1	1	1	1	1	1	0	0	0
64	*690*	top	2	2	3	3	3	3	3	N	N	N	N	N	N	N
		middle	N	N	N	N	N	N	N	N	N	N	N	N	N	N
		bottom	N	N	N	N	N	N	N	N	N	N	N	N	N	N
		Is plugged?	N	N	N	N	N	N	N	N	N	N	N	N	N	N

"Side" view Point 2 (soot : ash = 0.25) image data continued…

65	*700*	top	2	3	3	3	3	3	3	3	3	2	2	2	1	
		middle			1			2								
		bottom														
		Is plugged?	1	1	1	1	1	1	1	1	1	1	1	1	0	0
66	*710*	top	3	3	3	3	3				2	1	2	2	1	1
		middle														
		bottom	N	N	N	N	N	N	N	N	N	N	N	N	N	N
		Is plugged?	N	N	N	N	N	N	N	N	N	N	N	N	N	N
67	*720*	top	N	3	N	N	N	N	N	N	N	N	N	N	N	N
		middle	2													
		bottom														
		Is plugged?	N	1	N	N	N	N	N	N	N	N	N	N	N	N
68	*730*	top	2	4	4	2	2					3	2	3	3	
		middle														
		bottom											1			
		Is plugged?	1	1	1	1	1	0	0	0	0	1	1	1	1	0
69	*740*	top	N	N	N	N	N	N	N	N	N	N	N	N	N	N
		middle	N	N	N	N	N	N	N	N	N	N	N	N	N	N
		bottom										2				
		Is plugged?	N	N	N	N	N	N	N	N	N	N	N	N	N	N
70	*750*	top	2	3	2	2	2	2	2	3	2		2	2	2	2
		middle														
		bottom														
		Is plugged?	1	1	1	1	1	1	1	1	1	0	1	1	1	1
71	*760*	top			2	2										
		middle	N	N	N	N	N	N	N	N	N	N	N	N	N	N
		bottom	N	N	N	N	N	N	N	N	N	N	N	N	N	N
		Is plugged?	N	N	N	N	N	N	N	N	N	N	N	N	N	N
72	*770*	top				3								2	2	
		middle														
		bottom														
		Is plugged?	0	0	0	1	0	0	0	0	0	0	0	1	1	0
73	*780*	top	N	N	N	N	N	N	N	N	N	N	N	N	N	N
		middle	N	N	N	N	N	N	N	N	N	N	N	N	N	N
		bottom	N	N	N	N	N	N	N	N	N	N	N	N	N	N
		Is plugged?	N	N	N	N	N	N	N	N	N	N	N	N	N	N
74	*790*	top	N	N	N	N	N	N	N	N	N	N	N	N	N	N
		middle	N	N	N	N	N	N	N	N	N	N	N	N	N	N
		bottom	N	N	N	N	N	N	N	N	N	N	N	N	N	N
		Is plugged?	N	N	N	N	N	N	N	N	N	N	N	N	N	N

“Side” view Point 3 (soot : ash = 2.5) image data

Image #	Raw Image #	Plug Cross Section	1	2	3	4	5	6	7	8	9	10	11	12	13	14
1	front208	top		5	5		N	N	N	N	N	N	N	N	N	N
		middle				5	N	N	N	N	N	N	N	N	N	N
		bottom					N	N	N	N	N	N	N	N	N	N
		Is plugged?	0	1	1	1	N	N	N	N	N	N	N	N	N	N
2	front218	top			5	5			5	5		5	10	10	10	
		middle				10	15				10	5				5
		bottom														
		Is plugged?	0	0	1	1	1	0	1	1	1	1	1	1	1	1
3	front228	top	N	N	5	5		3	5	3		3	5	10		
		middle	N	N		5	10		3		5	3			8	7
		bottom	N	N												
		Is plugged?	N	N	1	1	1	1	1	1	1	1	1	1	1	1
4	front238	top	N	N	N			4	9	8	5	5	5		8	8
		middle	N	N	N	9	5	5			5		5		3	
		bottom	N	N	N											
		Is plugged?	N	N	N	1	1	1	1	1	1	1	1	0	1	1
5	front298	top			13	13	13		5		N	N	N	N	N	N
		middle	10	8				10		5	N	N	N	N	N	N
		bottom									N	N	N	N	N	N
		Is plugged?	1	1	1	1	1	1	1	1	N	N	N	N	N	N
6	front288	top		N	N	5	0	0	10	10	5	0	10	10	5	10
		middle		N	N	0	5	5	0	0	0	10	0	0	5	0
		bottom		N	N											
		Is plugged?	0	N	N	1	1	1	1	1	1	1	1	1	1	1
7	front278	top				5			N	N	N			5	5	
		middle			10	5	10	20	N	N	N	3	5			10
		bottom		3					N	N	N					
		Is plugged?	0	1	1	1	1	1	N	N	N	1	1	1	1	1
8	front268	top			5											
		middle	5	5	5	5	5	5	5	5		5	5			10
		bottom		5												
		Is plugged?	1	1	1	1	1	1	1	1	0	1	1	0	0	1
9	front258	top			N	N	N	N		5		5	5			
		middle	3	5	N	N	N	N		5	5	5	5	5		
		bottom	5	10	N	N	N	N	5							
		Is plugged?	1	1	N	N	N	N	1	1	1	1	1	1	0	0
10	front248	top											N	N	N	N
		middle						5	5		5	5	N	N	N	N
		bottom		5	5	5							N	N	N	N
		Is plugged?	0	1	1	1	0	1	1	0	1	1	N	N	N	N
11	front398	top			5	10	5	N	N	N	N	N	N			
		middle	5	5	5			N	N	N	N	N	N			
		bottom						N	N	N	N	N	N			
		Is plugged?	1	1	1	1	1	N	N	N	N	N	N	0	0	0
12	front388	top						5	5	5	5	3	3			
		middle		3	5	5	5							5	3	
		bottom														
		Is plugged?	0	1	1	1	1	1	1	1	1	1	1	1	1	0
13	front378	top			N	N	N	N	N		5			3		5
		middle			N	N	N	N	N						5	
		bottom			N	N	N	N	N							
		Is plugged?	0	0	N	N	N	N	N	0	1	0	0	1	1	1
14	front368	top		5	10	10	10	10	15	5	5	5	N	N	N	N
		middle	5	5			5						N	N	N	N
		bottom											N	N	N	N
		Is plugged?	1	1	1	1	1	1	1	1	1	1	N	N	N	N
15	front358	top	N	N	N	N	10	5	5	5	10	5	5	5	5	
		middle	N	N	N	N						10	10	10	10	
		bottom	N	N	N	N										
		Is plugged?	N	N	N	N	1	1	1	1	1	1	1	1	1	0
16	front348	top				10	20	5								
		middle	5	10	10	10	5									
		bottom		5												
		Is plugged?	1	1	1	1	1	1	0	0	0	0	0	0	0	0

“Side” view Point 3 (soot : ash = 2.5) image data continued…

17	front338	top	N	N		5	10	10	15	15		10	10	10	10	5
		middle	N	N	5						10			3	3	3
		bottom	N	N												
		Is plugged?	N	N	1	1	1	1	1	1	1	1	1	1	1	1
18	front328	top				5	N	N	N	N	3	3	5	5	10	
		middle		3	5	5	N	N	N	N						
		bottom					N	N	N	N						
		Is plugged?	0	1	1	1	N	N	N	N	1	1	1	1	1	0
19	front318	top					5	10	5	5	5	0	5			N
		middle		5	5	5	5	5	10							N
		bottom														N
		Is plugged?	0	1	1	1	1	1	1	1	1	0	1	0	0	N
20	front308	top	N	N	N	N	N	N	5	5	5	5		10		10
		middle	N	N	N	N	N	N					10		10	
		bottom	N	N	N	N	N	N								
		Is plugged?	N	N	N	N	N	N	1	1	1	1	1	1	1	1
21	front498	top				N	N	N	N	N		3	3	3	3	
		middle				N	N	N	N	N						
		bottom				N	N	N	N	N						
		Is plugged?	0	0	0	N	N	N	N	N	0	1	1	1	1	0
22	front488	top			15	10	10	10	10	5	5	0	0	3	N	N
		middle		8	3	3									N	N
		bottom													N	N
		Is plugged?	0	1	1	1	1	1	1	1	1	0	0	1	N	N
23	front478	top	N	N	N	N	N	5	5	5	5	5	5	3	3	3
		middle	N	N	N	N	N									
		bottom	N	N	N	N	N									
		Is plugged?	N	N	N	N	N	1	1	1	1	1	1	1	1	1
24	front468	top			5	5	5	5	N	N	N	N	N	N	N	N
		middle	5	5	5	3			N	N	N	N	N	N	N	N
		bottom							N	N	N	N	N	N	N	N
		Is plugged?	1	1	1	1	1	1	N	N	N	N	N	N	N	N
25	front458	top	N	N	5	0	5	10	10	5	5	5	10	10	0	0
		middle	N	N												
		bottom	N	N												
		Is plugged?	N	N	1	0	1	1	1	1	1	1	1	1	0	0
26	front448	top				3		N	N	N	N	N	3	3	3	3
		middle						N	N	N	N	N				
		bottom						N	N	N	N	N				
		Is plugged?	0	0	0	1	0	N	N	N	N	N	1	1	1	1
27	front438	top	5	5	5	10	15	15	10	10	10	5	5	0	0	0
		middle			5	3										
		bottom														
		Is plugged?	1	1	1	1	1	1	1	1	1	1	1	0	0	0
28	front428	top	N	N	N	N	N	N		3	5	3	3	3	3	0
		middle	N	N	N	N	N	N								
		bottom	N	N	N	N	N	N								
		Is plugged?	N	N	N	N	N	N	0	1	1	1	1	1	1	0
29	front418	top														
		middle		3	3	5	10	5	3		N	N	N	N	N	N
		bottom			3	5					N	N	N	N	N	N
		Is plugged?	0	1	1	1	1	1	1	0	N	N	N	N	N	N
30	front408	top	N	N	N	3	3	3	3	5	5	5	3	3	3	3
		middle	N	N	N											
		bottom	N	N	N		5									
		Is plugged?	N	N	N	1	1	1	1	1	1	1	1	1	1	1
31	front598	top	N	N	N	N	N	N	3		3	3	3	3	3	3
		middle	N	N	N	N	N	N								
		bottom	N	N	N	N	N	N								
		Is plugged?	N	N	N	N	N	N	1	0	1	1	1	1	1	1
32	front588	top				5	3	3	3		N	N	N	N	N	N
		middle			5						N	N	N	N	N	N
		bottom									N	N	N	N	N	N
		Is plugged?	0	0	1	1	1	1	1	0	N	N	N	N	N	N

"Side" view Point 3 (soot : ash = 2.5) image data continued…

33	front578	top	N	N	N					3	3	5	3	3		
		middle	N	N	N											
		bottom	N	N	N											
		Is plugged?	N	N	N	0	0	0	0	1	1	1	1	1	0	0
34	front568	top		3				N	N	N	N	N				
		middle		3			N	N	N	N	N	N				
		bottom					N	N	N	N	N	N				
		Is plugged?	0	1	0	0	N	N	N	N	N	N	0	0	0	0
35	front558	top	0	3	0	5	5	5	5	5	5	5	5	3	0	0
		middle			5											
		bottom														
		Is plugged?	0	1	1	1	1	1	1	1	1	1	1	1	0	0
36	front548	top	N	N	N	N	N	N	N	3	3	3	3	3		
		middle	N	N	N	N	N	N								
		bottom	N	N	N	N	N	N								
		Is plugged?	N	N	N	N	N	N	N	1	1	1	1	1	0	0
37	front538	top			3	5	3	3	3	3		N	N	N	N	N
		middle									N	N	N	N	N	N
		bottom									N	N	N	N	N	N
		Is plugged?	0	0	1	1	1	1	1	1	N	N	N	N	N	N
38	front528	top	N	N	N	N				3	3	3	3	3		
		middle	N	N	N	N										
		bottom	N	N	N	N										
		Is plugged?	N	N	N	N	0	0	0	1	1	1	1	1	0	0
39	front518	top		5	3	3	3	3	N	N	N	N	N	N	N	N
		middle		5	3				N	N	N	N	N	N	N	N
		bottom							N	N	N	N	N	N	N	N
		Is plugged?	0	1	1	1	1	1	N	N	N	N	N	N	N	N
40	front508	top				3	5	5	5	3	3	3	5	5	3	3
		middle		3	3	3										
		bottom														
		Is plugged?	0	1	1	1	1	1	1	1	1	1	1	1	1	1
41	front698	top	N	N	N	N	N	N	N	N	N	N	N	N	N	N
		middle	N	N	N	N	N	N	N	N	N	N	N	N	N	N
		bottom	N	N	N	N	N	N	N	N	N	N	N	N	N	N
		Is plugged?	N	N	N	N	N	N	N	N	N	N	N	N	N	N
42	front688	top	N	N	N	N	N	N	N	N	N	N	N	N	N	N
		middle	N	N	N	N	N	N	N	N	N	N	N	N	N	N
		bottom	N	N	N	N	N	N	N	N	N	N	N	N	N	N
		Is plugged?	N	N	N	N	N	N	N	N	N	N	N	N	N	N
43	front678	top						3			3			3	N	N
		middle												N	N	N
		bottom												N	N	N
		Is plugged?	0	0	0	0	0	1	0	0	1	0	0	N	N	N
44	front668	top	N	N	N	N	N	N	N	N	N				3	N
		middle	N	N	N	N	N	N	N				3	3		N
		bottom	N	N	N	N	N	N	N							N
		Is plugged?	N	N	N	N	N	N	N	N	N	0	1	1	1	N
45	front658	top					5		3	3	4		N	N	N	N
		middle	3	4							N	N	N	N	N	N
		bottom									N	N	N	N	N	N
		Is plugged?	1	1	0	0	1	0	1	1	N	N	N	N	N	N
46	front648	top	N	N	N	N	N				3	4	3	3		3
		middle	N	N	N	N	N					3	3	3	3	3
		bottom	N	N	N	N	N									
		Is plugged?	N	N	N	N	N	0	0	0	1	1	1	1	1	1
47	front638	top					2	2		N	N	N	N	N	N	N
		middle	5	3	2					N	N	N	N			
		bottom								N	N	N	N			
		Is plugged?	1	1	1	0	1	1	0	N	N	N	N	N	N	N
48	front628	top	N	N	N	5	3	5	5	5	5	5	10		5	5
		middle		4	4	2								5	3	N
		bottom														N
		Is plugged?	N	N	N	1	1	1	1	1	1	1	1	1	1	N

“Side” view Point 3 (soot : ash = 2.5) image data continued…

49	front618	top				N	N	N	N	N	N	N	3	3		3
		middle	N	N	N	N	N	N	N					3		
		bottom	N	N	N	N	N	N	N							
		Is plugged?	N	N	N	N	N	N	N	N	N	N	1	1	0	1
50	front608	top			3	3		3	3	3	3					
		middle	3	5			3									
		bottom														
		Is plugged?	1	1	1	1	1	1	1	1	1	0	0	0	0	0
51	front798	top	2		2	2	2						2			
		middle		4	3	3					3	3	3	2	3	3
		bottom														
		Is plugged?	1	1	1	1	1	0	0	0	1	1	1	1	1	1
52	front788	top									2	3	3	2	2	
		middle										2	2	3	2	2
		bottom														
		Is plugged?	0	0	0	0	0	0	0	0	1	1	1	1	1	1
53	front778	top	N	N	N	N	N	N	N	N	N	N	N	N	N	N
		middle	2		3							2	2	3		
		bottom														
		Is plugged?	N	N	N	N	N	N	N	N	N	N	N	N	N	N
54	front768	top										3	3	2	2	
		middle	2	2	3	3				3	3	3	3		3	
		bottom														
		Is plugged?	1	1	1	1	0	0	0	1	1	1	1	1	1	0
55	front758	top	N	N	N	N	N	N	N	N	N	N	N	N	N	N
		middle	N	N	N	N	N	N	N	N	N	N	N	N	N	N
		bottom	N	N	N	N	N	N	N	N	N	N	N	N	N	N
		Is plugged?	N	N	N	N	N	N	N	N	N	N	N	N	N	N
56	front748	top	3											7		2
		middle	2	2	2							3	4		2	
		bottom														
		Is plugged?	1	1	1	0	0	0	0	0	0	1	1	1	1	1
57	front738	top												2		
		middle		2								2			3	2
		bottom	N	N	N	N	N	N	N							
		Is plugged?	N	N	N	N	N	N	N	0	0	1	0	1	1	1
58	front728	top					N	N	N	N	N	N	N	N	N	N
		middle	1	5	3								3		3	2
		bottom														
		Is plugged?	0	1	1	0	N	N	N	N	N	N	N	N	N	N
59	front718	top	N	N	N	N	N	N	N	N	N	N	N	N	N	N
		middle	N	N	N	N	N	N	N	N	N	N	N	N	N	N
		bottom	N	N	N	N	N	N	N	N	N	N	N	N	N	N
		Is plugged?	N	N	N	N	N	N	N	N	N	N	N	N	N	N
60	front708	top	N	N	N	N	N	N	N	N	N	N	N	N	N	N
		middle	N	N	N	N	N	N	N	N	N	N	N	N	N	N
		bottom	N	N	N	N	N	N	N	N	N	N	N	N	N	N
		Is plugged?	N	N	N	N	N	N	N	N	N	N	N	N	N	N
61	front898	top	N	N	N	N	N	N	N	N	N	N	N	N	N	N
		middle														
		bottom														
		Is plugged?	N	N	N	N	N	N	N	N	N	N	N	N	N	N
62	front888	top	2	2	2	2	2	2	2	2	3	3	2	3	3	3
		middle											3			
		bottom														
		Is plugged?	1	1	1	1	1	1	1	1	1	1	1	1	1	1
63	front878	top	N	N	N	N	N	N	N	N	N	N	N	N	N	N
		middle	N	N	N	N	N	N	N	N	N	N	N	N	N	N
		bottom	N	N	N	N	N	N	N	N	N	N	N	N	N	N
		Is plugged?	N	N	N	N	N	N	N	N	N	N	N	N	N	N
64	front868	top		2		3	3				3	4	3	3		3
		middle												2	2	
		bottom														
		Is plugged?	0	1	0	1	1	0	0	0	1	1	1	1	1	1

"Side" view Point 3 (soot : ash = 2.5) image data continued…

65	front858	top	N	N	N	N	N	3	3	3		2				
		middle														2
		bottom														
		Is plugged?	N	N	N	N	N	1	1	1	0	1	0	0	0	1
66	front848	top	2	2	2	2	1	N	N	N	N	N	N	N	N	N
		middle											3	1	2	
		bottom														
		Is plugged?	1	1	1	1	0	N	N	N	N	N	N	N	N	N
67	front838	top	3				3	3	3		3		3			2
		middle	2												3	2
		bottom														
		Is plugged?	1	0	0	0	1	1	1	0	1	0	1	0	1	1
68	front828	top	N	N	N	N	N	N	N	N	N	N	N	N	N	N
		middle	4										N	N	N	N
		bottom												N	N	N
		Is plugged?	N	N	N	N	N	N	N	N	N	N	N	N	N	N
69	front818	top	3	5	5	5	5	5	3	3	5	3	3	4		3
		middle		2	2	3						3	3	3	5	5
		bottom														
		Is plugged?	1	1	1	1	1	1	1	1	1	1	1	1	1	1
70	front808	top	N	N	N	N	N	N	N	N	N	N				2
		middle	N	N	N	N	N	N	N	N	N	N	N	N	N	N
		bottom	N	N	N	N	N	N	N	N	N	N	N	N	N	N
		Is plugged?	N	N	N	N	N	N	N	N	N	N	N	N	N	N
71	front998	top	N	N	N	N	N	N	N	N	N	N	N	N	N	N
		middle	N	N	N	N	N	N	N	N	N	N	N	N	N	N
		bottom	N	N	N	N	N	N	N	N	N	N	N	N	N	N
		Is plugged?	N	N	N	N	N	N	N	N	N	N	N	N	N	N
72	front988	top		2	3	2	2	3	2	3	3	2	2	2		1
		middle														
		bottom														
		Is plugged?	0	1	1	1	1	1	1	1	1	1	1	1	0	0
73	front978	top	N	N	N	N	N	N	N			1		2	1	1
		middle	N	N	N	N	N	N	N							
		bottom	N	N	N	N	N	N	N							
		Is plugged?	N	N	N	N	N	N	N	0	0	0	0	1	0	0
74	front968	top					1	2	1	N	N	N	N	N	N	N
		middle				1										
		bottom														
		Is plugged?	0	0	0	0	0	1	0	N	N	N	N	N	N	N
75	front958	top		2	3	3			3	3	2	3	2		3	2
		middle	2											3		3
		bottom														
		Is plugged?	1	1	1	1	0	0	1	1	1	1	1	1	1	1
76	front948	top	N	N	N	N	N	N	N	N	N	N	N	N	N	N
		middle	2									N	N	N	N	N
		bottom										N	N	N	N	N
		Is plugged?	N	N	N	N	N	N	N	N	N	N	N	N	N	N
77	front938	top	3	3	4	4			3	2	2	2			2	
		middle				2							2	3	2	2
		bottom														
		Is plugged?	1	1	1	1	0	0	1	1	1	1	1	1	1	1
78	front928	top	N	N	N	N	N	N	N	N	N	N	N	N	N	N
		middle	N	N	N	N	N	N	N	N	N	N	N	N	N	N
		bottom	N	N	N	N	N	N	N	N	N	N	N	N	N	N
		Is plugged?	N	N	N	N	N	N	N	N	N	N	N	N	N	N
79	front918	top		3	2		2						2		2	2
		middle												2	2	3
		bottom														
		Is plugged?	0	1	1	0	1	0	0	0	0	0	1	1	1	1
80	front908	top			2				2	3	3				2	
		middle										1		3		
		bottom														
		Is plugged?	0	0	1	0	0	0	1	1	1	0	0	1	1	0

Appendix B. Backpressure Model Derivation [19]

Variable Definitions

Note that the subscript "$\boldsymbol{i}$" in the definitions below, as in $\boldsymbol{u_i}$, is a dummy index that can be represented by any other symbol throughout this manuscript.

$\boldsymbol{A_1, A_2, B_1}$ – dimensionless groups in equations A.13, A.14, and A.15

$\boldsymbol{A_{1L}, A_{2L}, A_{3L}}$ – dimensionless groups in equations A.18, A.19, and A.20

$\boldsymbol{b_K}$ – width of empty channel

$\boldsymbol{b_{Lo}}$ – width of loaded channel

$\boldsymbol{c_1, c_2, c_3}$ – constants defined in equation A.21

$\boldsymbol{F}$ – friction coefficient

$\boldsymbol{f}$ – friction factor

$\boldsymbol{F_1}$ – channel friction coefficient along filtration length

$\boldsymbol{F_2}$ – channel friction coefficient along laminar channel length

$\boldsymbol{F_{ash\ binding}}$ – force affixing the particle to the DPF channel wall

$\boldsymbol{g_1, g_2}$ – constants defined in equations A.25 and A.26

$\boldsymbol{k_a}$ – permeability of ash layer

$\boldsymbol{k_s}$ – permeability of soot layer

$\boldsymbol{k_w}$ – permeability of wall layer

$\boldsymbol{L}$ – monolith channel length

$\boldsymbol{l_0}$ – characteristic ash particle diameter

$\boldsymbol{P^*}$ – characteristic pressure used to nondimensionalize channel flow pressures

$\boldsymbol{p_1(x), p_2(x)}$ – inlet and outlet channel pressure at axial position $\boldsymbol{x}$

$\boldsymbol{P_{atm}}$ – atmospheric pressure

$\boldsymbol{Q_i}$ – channel volumetric flow rate

$\boldsymbol{R_i}$ – channel flow resistance

$\boldsymbol{Re}$ – Reynolds number

$\boldsymbol{s_a}$ – ash layer thickness

$\boldsymbol{s_s}$ – soot layer thickness

$\boldsymbol{s_w}$ – substrate wall thickness

$\boldsymbol{U}$ – inlet channel entrance velocity

$\boldsymbol{u_1(x), u_2(x)}$ – inlet and outlet channel velocities at axial position $\boldsymbol{x}$

$\boldsymbol{u}$ – fluid flow velocity

$\boldsymbol{u_w(x)}$ – flow velocity through the filter wall substrate at axial position $\boldsymbol{x}$

$\boldsymbol{x}$ – channel axial coordinate

$\boldsymbol{x_{mcc}, m}$ – axial position of MCC plug

$\boldsymbol{\alpha}$ – fraction of channels with ash plugs

$\boldsymbol{\mu}$ – exhaust gas dynamic viscosity

$\boldsymbol{\rho}$ – exhaust gas density

$\Delta \boldsymbol{P}$ – pressure drop

$\boldsymbol{\mu}$ – exhaust gas dynamic viscosity

$\boldsymbol{\rho}$ – exhaust gas density

^ – dimensionless quantity

Relevant Acronym Definitions

CPSI – cells per square inch

DPF – diesel particulate filter

FIB – focused ion beam

HRSEM – high resolution scanning electron microscope

MCC – mid-channel collapse / mid-channel clogging / mid-channel congestion

nmcc – no mid-channel congestion

PM – particulate matter

ULSD – ultra-low-sulfur diesel fuel

X-Ray CT– X-Ray computed tomography

Derivation of Backpressure in the DPF

Mass balance in the inlet and outlet channels, respectively:

$$\rho \frac{du_1}{dx} = -\frac{4b_k}{{b_{Lo}}^2} \cdot \rho \cdot u_w \qquad (B.1)$$

$$\rho \frac{du_2}{dx} = \frac{4}{{b_k}^2} \cdot \rho \cdot u_w \qquad (B.2)$$

Likewise, the momentum balance in the inlet and outlet channels, respectively:

$$\rho \frac{d({u_1}^2)}{dx} = -\frac{dP_1}{dx} - F_1 \frac{\mu u_1}{{b_{Lo}}^2} \qquad (B.3)$$

$$\rho \frac{d({u_2}^2)}{dx} = -\frac{dP_2}{dx} - F_2 \frac{\mu u_2}{{b_k}^2}$$

It is understood that in equations B.3, B.4 above that the friction coefficient:

$$f = \frac{shear\ stress}{½ \cdot \rho \cdot velocity^2} \propto \frac{1}{Reynolds\ number} \qquad (B.4)$$

in the low Reynolds number regime, and $F_1 = F_2 \approx 28.5$ are built into the proportionality constants in the f varying with $\frac{1}{Re}$ relationship [59].

For simplicity, this derivation assumes true Darcian flow across the filter wall, where the pressure drop is proportional to the filter velocity only, i.e. dropping the Forchheimers non-linear velocity term. That is:

$$P_1 - P_2 = \mu \cdot u_w \cdot \frac{s_w}{k_w} + \mu \cdot u_w \cdot \frac{s_s}{k_s} + \mu \cdot u_w \cdot \frac{s_A}{k_A} \qquad (B.5)$$

The notations and symbols (as indicated in the Nomenclature section) are mostly similar to previous literature for easy cross reference [59]. The boundary conditions are, for the Mid-Channel Congestion (MCC) problem with inlet velocity U:

$$u_1\,(at\ x = 0) = \mathrm{U} \qquad (B.6)$$

$$u_2\,(at\ x = 0) = 0 \qquad (B.7)$$

$$P_2\,(at\ x = L) = P_{atm} \qquad (B.8)$$

Since the domain of x and the formulation apply only to the filtration region, x runs from $x = 0$ to $x = x_{mcc}$, the mid-channel plug location, then the boundary condition at the end of the inlet channel is:

$$u_1\,(at\ x = x_{mcc})\ = 0 \qquad (B.9)$$

It is easy to show from continuity, that in the outlet channel,

$$u_2(at\ x = x_{mcc}) = \frac{b_{Lo}^2}{b_k^2} \cdot U \qquad (B.10)$$

and maintains the same velocity thereafter from $x = x_{mcc}$ to the exit of the outlet channel, as there is no flow across the channel wall downstream of the mid-channel plug. Therefore, from momentum balance in the outlet channel, pressure decreases linearly to the P_{atm} at the channel exit. We now introduce the following nondimensional parameters:

$$\hat{x} = \frac{x}{L}\,\hat{u}_i = \frac{u_i}{U}\ \ \hat{u}_w = \frac{4L}{b_k U} \cdot\ u_w \qquad \text{(B.11a)}$$

$$\hat{P}_i = \frac{P_i\ -\ P_{atm}}{P^*}\ P^* = \frac{\mu \cdot U \cdot b_k \cdot s_w}{4 \cdot L \cdot k_w} \qquad (B.11b)$$

Where the subscript i = 1 refers to the inlet channel and i = 2 the outlet channel

Using the dimensionless variables in equations B.1-B.5, and defining the following quantities:

$$Re = \frac{\rho \cdot U \cdot b_k}{\mu} \qquad (B.12)$$

$$\mathrm{A_1}\ = \frac{k_w}{b_k \cdot s_w} \cdot \frac{4 \cdot L}{b_k} \cdot Re \qquad \text{(B.13)}$$

$$\mathrm{A_2}\ = 4 \cdot F_1 \cdot \frac{k_w}{b_k \cdot s_w} \cdot \left(\frac{L}{b_k}\right)^2 \qquad (B.14)$$

$$\mathrm{B_1}\ =\ 1\ \ +\ \ \frac{k_w}{s_w} \cdot \frac{s_s}{k_s}\ +\ \frac{k_w}{s_w} \cdot \frac{s_A}{k_A} \qquad (B.15)$$

and ultimately eliminating the variable $\hat{u}_1(x)$, and after a fair amount of algebra, we arrive at a single second order differential equation in $\hat{u}_2(x)$:

$$B_1 \frac{d^2\hat{u}_2}{d\hat{x}^2} - 2A_1 \frac{{b_k}^2}{{b_{Lo}}^2} \frac{d\hat{u}_2}{d\hat{x}} - A_2 \left(1 + \frac{{b_k}^4}{{b_{Lo}}^4}\right) \hat{u}_2 + A_2 \frac{{b_k}^2}{{b_{Lo}}^2} + 2A_1 \left(\frac{{b_k}^4}{{b_{Lo}}^4} - 1\right) \cdot \hat{u}_2 \cdot \frac{d\hat{u}_2}{d\hat{x}} = 0 \ (B.16)$$

which is close to (but not exactly the same as) equation A20 in Gaiser et al [59]. Dropping the last term in A16 as the coefficient in the non-linear velocity term is small compared to the coefficients of the rest of the terms, all of which are close to unity, equation B.16 simplifies to the following form:

$$\frac{d^2\hat{u}_2}{d\hat{x}^2} - 2A_{1L} \frac{d\hat{u}_2}{d\hat{x}} - 2A_{2L}\hat{u}_2 + A_{3L} = 0 \qquad (B.17)$$

Where A_{1L}, A_{2L}, and A_{3L} are coefficients independent of $\hat{x}$, given as follows:

$$A_{1L} = \frac{A_1}{B_1} \cdot \frac{{b_k}^2}{{b_{Lo}}^2} \qquad (B.18)$$

$$A_{2L} = \frac{A_2}{2B_1} \cdot \left(1 + \frac{{b_k}^4}{{b_{Lo}}^4}\right) \qquad (B.19)$$

$$A_{3L} = \frac{A_2}{B_1} \cdot \frac{{b_k}^2}{{b_{Lo}}^2} \qquad (B.20)$$

Following Konstandopoulos et al. [56, 57], equation B.17 can be solved using the method of characteristic solutions, except that in this case, this is done for loaded (with soot/ash) channels and for deposits which are lodged mid-channel (MCC). The boundary conditions are very different, so are the solutions. Details of the derivation are shown below:

Solving for c_1, c_2, and c_3 in the characteristic solution for $\hat{u}_2(x)$:

$$\hat{u}_2(\hat{x}) = c_1 e^{q_1\hat{x}} + c_2 e^{q_2\hat{x}} + c_3 \qquad (B.21)$$

Applying the boundary conditions, at $\hat{x} = 0$:

$$\hat{u}_2(0) = c_1 + c_2 + c_3 = 0 \qquad (B.22)$$

At $\hat{x} = \hat{x}_{mcc} (= m)$

$$\hat{u}_1(m) = 0 \tag{B.23}$$

And,

$$\hat{u}_2(m) = c_1 e^{q_2 m} + c_2 e^{q_2 m} + c_3 = \frac{b_{Lo}^2}{b_K^2} \tag{B.24}$$

Substituting B.21 into B.17 and equating coefficients of $e^{q_1 x}$, $e^{q_2 x}$, and setting the constant term to zero yields:

$$q_1 = A_{1L} - \sqrt{A_{1L}^2 + 2A_{2L}} \tag{B.25}$$

$$q_2 = A_{1L} + \sqrt{A_{1L}^2 + 2A_{2L}} \tag{B.26}$$

$$c_3 = \frac{A_{3L}}{2A_{2L}} \tag{B.27}$$

$$c_2 = \frac{\frac{b_{Lo}^2}{b_K^2} - c_3 + c_3 e^{q_1 m}}{e^{q_2 m} - e^{q_1 m}} \tag{B.28}$$

$$c_1 = -c_2 - c_3 \tag{B.29}$$

Applying B.25-B.29 to B.21 gives the closed-form solution of $\hat{u}_2(\hat{x})$ for $\hat{x} = 0 \; to \; m \; (= x_{mcc})$, and

$$\hat{u}_2(\hat{x}) = \frac{b_{Lo}^2}{b_K^2} \text{ for } \hat{x} \text{ from } m \; to \; 1 \; (x = L) \tag{B.30}$$

$$\hat{u}_1(\hat{x}) = 1 - \hat{u}_2(\hat{x}) \frac{b_K^2}{b_{Lo}^2} \text{ for } \hat{x} \text{ from } 0 \; to \; m \tag{B.31}$$

$$\therefore \hat{u}_1(\hat{x}) = 0 \text{ for } \hat{x} \text{ from } m \; to \; 1 \tag{B.32}$$

Considering pressures: Between $\hat{x} = m$ to 1, in the outlet channel, we have square-channel pipe flow:

$$\hat{P}_2(\hat{x}) = A_{2L}(1-\hat{x}) \qquad (B.33)$$

$$\hat{P}_2(\hat{x}=m) = A_{2L}(1-m) \qquad (B.34)$$

Integrating the momentum equation in the exit channel between $x = m$ and some point $x > m$:

$$\hat{P}_2(\hat{x}) = A_{2L}(1-m) + A_{1L}\left[\frac{b_{Lo}^4}{b_K^4} - \hat{u}_2^2(x)\right] - A_{2L}\int_m^{\hat{x}} \hat{u}_2 d\hat{x} \qquad (B.35)$$

The flow through the wall and deposit layers, given as $\hat{u}_w$ which is related to the pressure difference

$$\hat{P}(\hat{x}) \equiv \hat{P}_1(\hat{x}) - \hat{P}_2(\hat{x}) = \hat{u}_w = B_1\frac{d\hat{u}_2}{d\hat{x}} \qquad (B.36)$$

For the filter,

$$\hat{P}_{total} \equiv \hat{P}_1(\hat{x}=0) - \hat{P}_2(\hat{x}=1) = \hat{P}_2(\hat{x}=0) + \Delta\hat{P}(\hat{x}=0), \qquad (B.37)$$

since $\hat{P}_2(\hat{x}=1) = 0$ at the filter exit. Combining B.34-B.37 gives:

$$\Delta\hat{P}_{total} = A_{2L}(1-m) + A_{1L}\left(\frac{b_{Lo}^4}{b_K^4}\right) + A_{2L}\int_0^m \hat{u}_2 d\hat{x} + B_1\left.\frac{d\hat{u}_2}{d\hat{x}}\right|_{\hat{x}=0} \qquad (B.38)$$

Evaluating the integral and derivative in B.38, using B.21, gives:

$$\Delta\hat{P}_{total} = A_{1L}\frac{b_{Lo}^4}{b_K^4} + A_{2L}\left[\frac{c_1}{q_1}(e^{q_1 m}-1) + \frac{c_2}{q_2}(e^{q_2 m}-1) + c_3 m + 1 - m\right] + B_1(c_1 q_1 + c_2 q_2) \qquad (B.39)$$

For the special case of $m = 1$ (no mid-channel collapse plug) and a clean, unloaded filter where $b_{Lo} = b_k$ and $B_1 = 1$:

$$\Delta\hat{P}_{total} = A_1 + A_2\left[\frac{c_1}{q_1}(e^{q_1}-1) + \frac{c_2}{q_2}(e^{q_2}-1) + \frac{1}{2}\right] + c_1 q_1 + c_2 q_2 \qquad (B.40)$$

Appendix C. Regeneration Temperature History Model Parameter and Variable Definitions

Greek Constants

- $\alpha = 1.78 \cdot 10^{8}\ cm^{-2} = 1.78 \cdot 10^{12}\ m^{-2}$ constant for wall flow correlation
- $\beta = 5.75 \cdot 10^{6}\ cm^{-1} = 5.75 \cdot 10^{8}\ m^{-1}$ constant for wall flow correlation
- $\lambda_p = 2.0 \cdot 10^{-3}\ \frac{cal}{cm \cdot s \cdot K} = 0.8368\ \frac{W}{m \cdot K}$ deposit particle thermal conductivity
- $\lambda_s = 5.0 \cdot 10^{-3}\ \frac{cal}{cm \cdot s \cdot K} = 2.092\ \frac{W}{m \cdot K}$ substrate thermal conductivity
- $\mu(T_b) = a_2\sqrt{T_b}\ [\frac{g}{cm \cdot s}, \frac{kg}{m \cdot s}]$ viscosity approximation for $T = T_b$
- $\rho_0 = \frac{P_{atm}}{R \cdot T_b}\ \left[\frac{g}{cm^3}, \frac{kg}{m^3}\right]$ characteristic gas density
- $\rho_p = 0.55 \frac{g}{cm^3} = 550\ \frac{kg}{m^3}$ bulk density of deposit
- $\rho_s = 1.29 \frac{g}{cm^3} = 1290\ \frac{kg}{m^3}$ bulk density of the substrate
- $\omega_1 = 2.12 \cdot 10^{-4}\ cm = 2.12 \cdot 10^{-6}\ m$ wall thickness function constant
- $\omega_2 = 0.224\ cm = 2.24 \cdot 10^{-3}\ m$ wall thickness function constant
- $\omega_3 = 4.05 \cdot 10^{-2}\ cm = 4.05 \cdot 10^{-4}\ m$ wall thickness function constant

Roman Constants

- $a_1 = 8.57 \cdot 10^{-2}\ \frac{cal}{g \cdot K} = 359\ \frac{J}{kg \cdot K}$ parameter in gas thermal conductivity correlation
- $a_2 = 1.364 \cdot 10^{-5}\ \frac{g}{cm \cdot s \cdot \sqrt{K}} = 1.364 \cdot 10^{-6}\ \frac{kg}{m \cdot s \cdot \sqrt{K}}$ parameter in gas viscosity correlation
- $a_3 = 28.45$ parameter in square channel pressure drop correlation
- $A = 98\ cm^2 = 9.8 \cdot 10^{-3}\ m^3$ face area
- $B_1 = \frac{\rho_0 u_0^2}{P_0}$ equation constant
- $B_2 = \frac{a_3 u_0 L \mu(T_b)}{D^2 P_0}$ equation constant
- $B_3 = \frac{4NuL\mu(T_b)\left(1+\frac{a_1}{c_{pg}}\right)}{\rho_0 u_0 D^2}$ equation constant
- $B_4 = \frac{4\lambda_s w_s}{\rho_0 u_0 c_{pg} L D}$ equation constant

- $B_5 = \frac{\lambda_p w_0}{\lambda_s w_s}$ equation constant
- $B_6 = -\frac{\Delta H}{M_C C_{pg} T_b}$ equation constant
- $B_7 = \frac{\beta \rho_0 u_0 D}{4\alpha\mu(T_b)L}$ equation constant
- $B_8 = \frac{w_s}{\phi(w_0)}$ equation constant
- $c_1 = 0.256\ \frac{cal}{g \cdot K} = 1072 \frac{J}{kg \cdot K}$ constant in substrate heat capacity function
- $c_2 = 3.73 \cdot 10^{-5}\ \frac{cal}{g \cdot K^2} = 0.156\ \frac{J}{kg \cdot K^2}$ constant in substrate heat capacity function
- $c_3 = -8.21 \cdot 10^{-3}\ \frac{cal \cdot K}{g} = 34.4\ \frac{J \cdot K}{kg}$ constant in substrate heat capacity function
- $c_4 = 0.413\ \frac{cal}{g \cdot K} = 1729 \frac{J}{kg \cdot K}$ constant in deposit heat capacity function
- $c_5 = 2.31 \cdot 10^{-5}\ \frac{cal}{g \cdot K^2} = 9.67 \cdot 10^{-2}\ \frac{J}{kg \cdot K^2}$ constant in deposit heat capacity function
- $c_6 = -4.24 \cdot 10^{4}\ \frac{cal \cdot K}{g} = 1.78\ \frac{J \cdot K}{kg}$ constant in deposit heat capacity function
- $C_{pg} = 0.28\ \frac{cal}{g \cdot K} = 1172 \frac{J}{kg \cdot K}$ gas phase heat capacity
- $D = 0.211\ cm = 2.11 \cdot 10^{-3}\ m$ length of side of square channel cross section
- $\frac{E}{R} = 1.8 \cdot 10^4$ activation energy ÷ universal gas constant
- $G_f = 0.272 \frac{g}{cm^2 \cdot s} = 2.72 \frac{kg}{m^2 \cdot s}$ inlet mass velocity
- $\bar{G_f} = \frac{G_f}{\rho_0 u_0}$ nondimensional inlet mass velocity
- $-\Delta H = 9.4\ \cdot 10^4 \frac{cal}{mole} = 3.94 \cdot 10^5 \frac{J}{mole}$ heat of reaction of carbon oxidation
- $k_0 = 5.96 \cdot 10^4 \frac{cm}{s \cdot K} = 5.96 \cdot 10^2 \frac{m}{s \cdot K}$ pre-exponential factor in reaction
- $L = 10\ inches = 25.4\ cm = 0.254\ m$ length of monolith
- $M_C = 12.0 \frac{g}{mole} = 1.2 \cdot 10^{-2} \frac{kg}{mole}$ molecular weight of carbon
- $M_{Ox} = 32 \frac{g}{mole} = 3.2 \cdot 10^{-2} \frac{kg}{mole}$ molecular weight of oxygen
- $Nu = 2.975$ Nusselt number for square channels
- $P_{atm} = 1.013 \cdot 10^6 \frac{g}{cm \cdot s^2} = 1.013 \cdot 10^5 \frac{kg}{m \cdot s^2}$ atmospheric pressure
- $P_0 = \frac{u_0 D \alpha \phi(w) \mu(T_b)}{4L}$ characteristic pressure difference

- $\bar{R} = 2.87 \cdot 10^6 \frac{cm^2}{s^2 \cdot K} = 2.87 \cdot 10^2 \frac{m^2}{s^2 \cdot K}$ universal gas constant ÷ mass of air
- $S_p = 5.5 \cdot 10^5\ cm^{-1} = 5.5 \cdot 10^7\ m^{-1}$ specific area of deposit layer
- $T_b = 600\ K$ initial temperature prior to step increase
- $u_0 = \frac{G_f(t)}{\rho_0}\ \left[\frac{cm}{s}, \frac{m}{s}\right]$ characteristic channel velocity
- $w_0 = L^{-1} \int_0^L w_b(z)dz\ [cm, m] = w_b$ if w_b is constant, characteristic particle layer thickness
- $w_b = 1.117 \cdot 10^{-3}\ cm = 1.117 \cdot 10^{-5}\ m \approx 11\ \mu m$ initial deposit layer thickness
- $\bar{w}_b = \frac{w_b}{w_0} = 1$ dimensionless initial deposit layer thickness = 1 for uniform layer
- $w_s = 4.76 \cdot 10^{-2}\ cm = 4.76 \cdot 10^{-4}\ m$ thickness of substrate layer
- $Y_f = 0.154$ inlet oxygen mass fraction
- $\bar{Y}_f = \frac{Y_f(t) \cdot M_c}{M_{Ox}}$ dimensionless inlet oxygen mass fraction

Greek Variables

- $\mu(T) = a_2\sqrt{T}\ \left[\frac{g}{cm \cdot s}, \frac{kg}{m \cdot s}\right]$ gas viscosity approximation
- $\bar{\mu}(T) = \sqrt{\frac{T}{T_b}}\ \left[\frac{g}{cm \cdot s}, \frac{kg}{m \cdot s}\right]$ gas viscosity approximation
- $\rho_i\ \left[\frac{g}{cm^3}, \frac{kg}{m^3}\right]$ gas density in channel *i*
- $\bar{\rho}_i = \frac{\rho_i}{\rho_0}$ dimensionless gas density in channel *i*
- $\rho_w\ \left[\frac{g}{cm^3}, \frac{kg}{m^3}\right]$ gas density in the wall
- $\bar{\rho}_w = \frac{\rho_w}{\rho_0}$ dimensionless gas density in the wall
- $\phi(w) = \begin{cases} (2\omega_2 - \omega_3)\left(\frac{w}{\omega_1}\right) - (\omega_2 - \omega_3)\left(\frac{w}{\omega_1}\right)^2, & w < \omega_1 \\ \omega_2 + \omega_3\left(\frac{w}{\omega_1} - 1\right), & w \geq \omega_1 \end{cases}$ thickness function related to wall pressure drop
- $\bar{\phi}(w) = \frac{\phi(w)}{\phi(w_b)}$ thickness function related to wall pressure drop

Roman Variables

- $\overline{C_P}(\overline{w}, \overline{T_w}) = \left(1 + \overline{T_w}\frac{\partial}{\partial \overline{T_w}}\right)\left(\overline{C_{ps}}(\overline{T_w}) + \overline{w}\overline{C_{pp}}(\overline{T_w})\right)$ dimensionless effective wall heat capacity
- $C_{ps}(T) = c_1 + c_2 T + c_3 T^{-2}$ $\left[\frac{cal}{g \cdot K}, \frac{J}{kg \cdot K}\right]$ substrate layer heat capacity
- $\overline{C_{ps}}(T) = \frac{C_{ps}(T) \cdot \rho_S \cdot w_S}{C_{pg} \cdot \rho_P \cdot w_0}$ dimensionless substrate layer heat capacity
- $C_{pp}(T) = c_4 + c_5 T + c_6 T^{-2}$ $\left[\frac{cal}{g \cdot K}, \frac{J}{kg \cdot K}\right]$ particle layer heat capacity
- $\overline{C_{pp}}(T) = \frac{C_{pp}}{C_{pg}}$ dimensionless particle layer heat capacity
- $\bar{G}_i(\rho_i u_i) = \frac{\rho_i u_i}{\rho_o u_o}$ dimensionless mass velocity in channel *i*
- $h_i(T_i) = \left(\frac{Nu}{D}\right)\left(C_{pg} + a_1\right)\mu(T_i)$ $\left[\frac{cal}{cm^2 \cdot s \cdot K}, \frac{J}{m^2 \cdot s \cdot K}\right]$ heat transfer coefficient for channel *i*
- $k(T_w) = k_0 T_w e^{-\frac{E}{RT_w}}$ $\left[\frac{cm}{s}, \frac{m}{s}\right]$ reaction rate
- $\bar{k}(T_w) = \frac{4kLS_p w_0}{u_0 D}$ dimensionless reaction rate
- P_i $\left[\frac{g}{cm^2 \cdot s}, \frac{kg}{m^2 \cdot s}\right]$ pressure in channel *i*
- $\overline{P_i}(P_i) = \frac{P_i - P_{atm}}{P_0}$ dimensionless pressure in channel *i*
- t $[s]$ time
- $\bar{t}(t) = \frac{t\rho_0 u_0 D}{4L\rho_P w_0}$ dimensionless time
- T_f $[K]$ temperature of the inlet gas
- $\overline{T_f} = \frac{T_f}{T_b}$ dimensionless temperature of the inlet gas
- T_i $[K]$ temperature of the gas in channel *i*
- $\overline{T_i} = \frac{T_i}{T_b}$ dimensionless temperature of the gas in channel *i*
- T_w $[K]$ temperature of the wall
- $\overline{T_w} = \frac{T_w}{T_b}$ dimensionless temperature of the wall
- u_i $\left[\frac{cm}{s}, \frac{m}{s}\right]$ gas velocity in channel *i*
- $\bar{u}_i$ dimensionless gas velocity in channel *i*

- u_w $\left[\frac{cm}{s}, \frac{m}{s}\right]$ superficial velocity in wall
- $\bar{u}_w = \frac{4u_w L}{u_0 D}$ dimensionless superficial velocity in wall
- w $[cm, m]$ particle layer thickness
- $\bar{w} = \frac{w}{w_0}$ dimensionless particle layer thickness
- x $[cm, m]$ distance through wall system
- Y_i oxygen mass fraction in channel *i*
- Y_w oxygen mass fraction in the wall
- z $[cm, m]$ axial distance
- $\bar{z} = \frac{z}{L}$ dimensionless axial distance

Appendix D. Regeneration Temperature Model Parameter Values over Time

Note that the order of colors for variables is blue, then red, then yellow. For example, p_1 is blue, p_2 is red, and v_w is yellow.

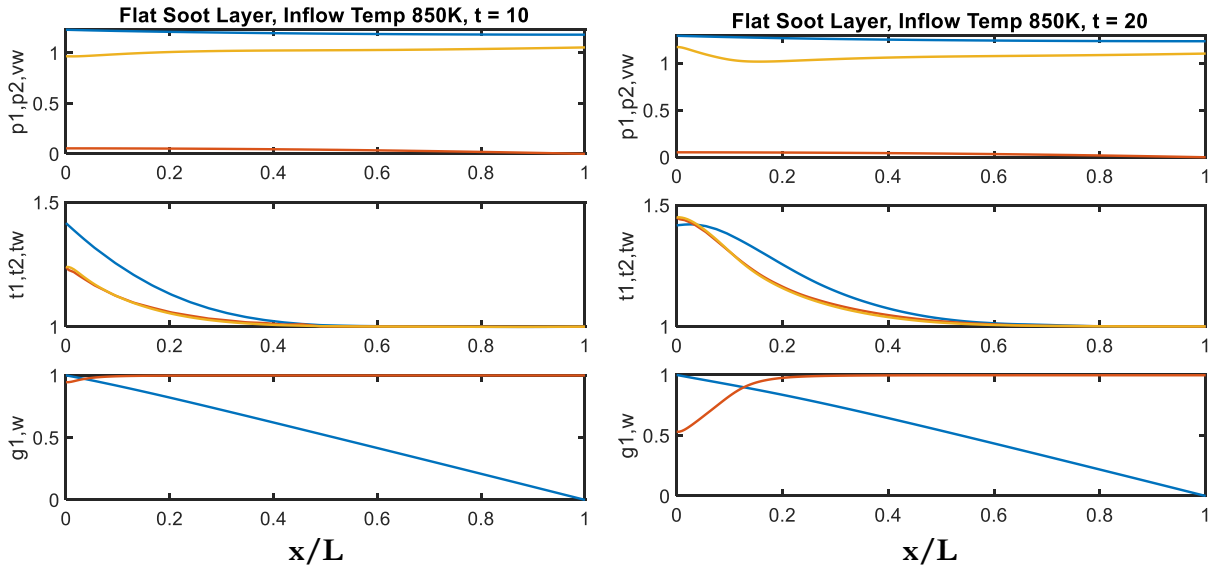

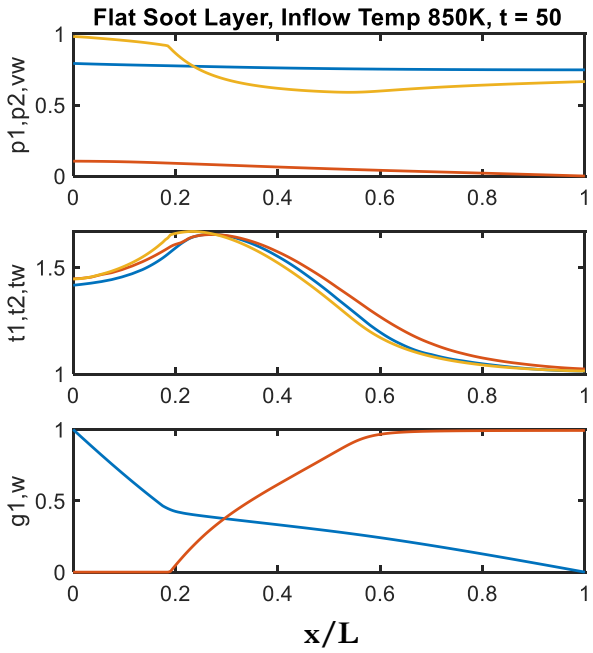

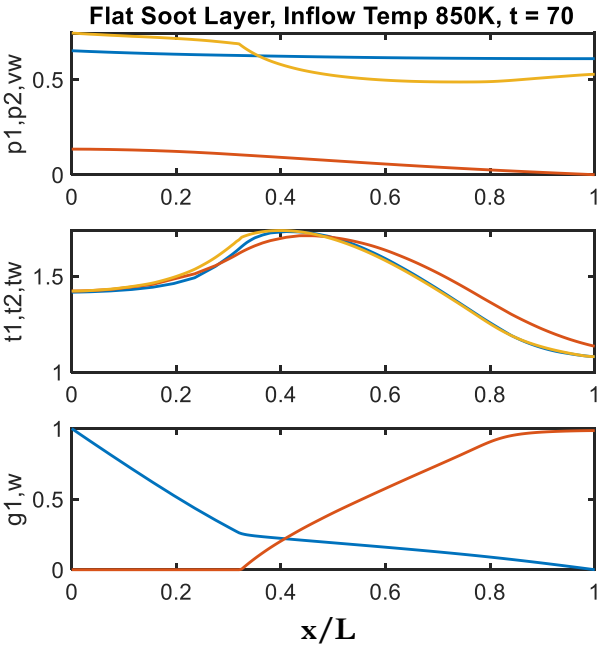

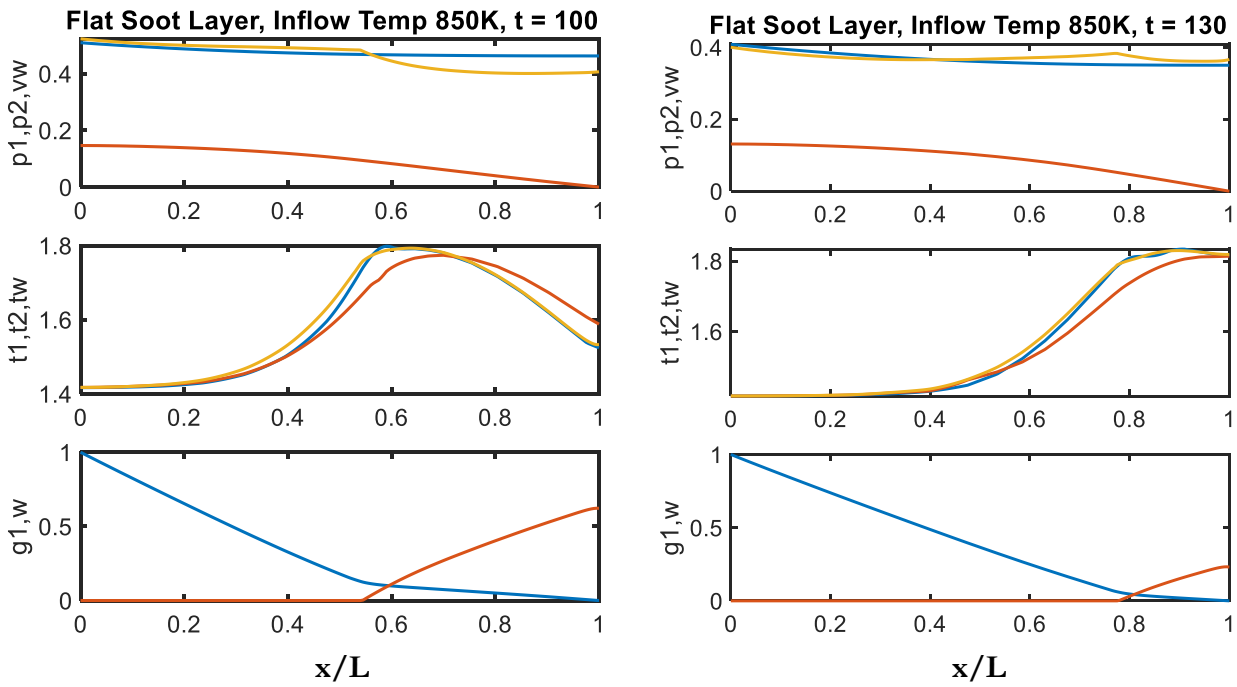
Flat Soot Layer, Inflow Temp 850K, t = 100
p1,p2,vw
t1,t2,tw
g1,w
x/L
Flat Soot Layer, Inflow Temp 850K, t = 130
p1,p2,vw
t1,t2,tw
g1,w
x/L

Appendix E. Regeneration Temperature Model Parameter Values with Variable Initial Soot Deposit Layer Geometry

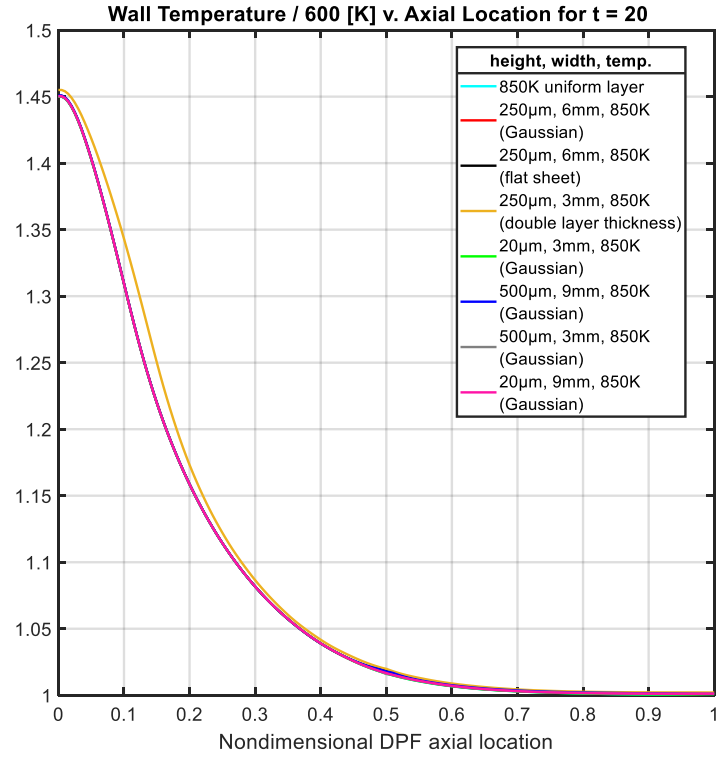

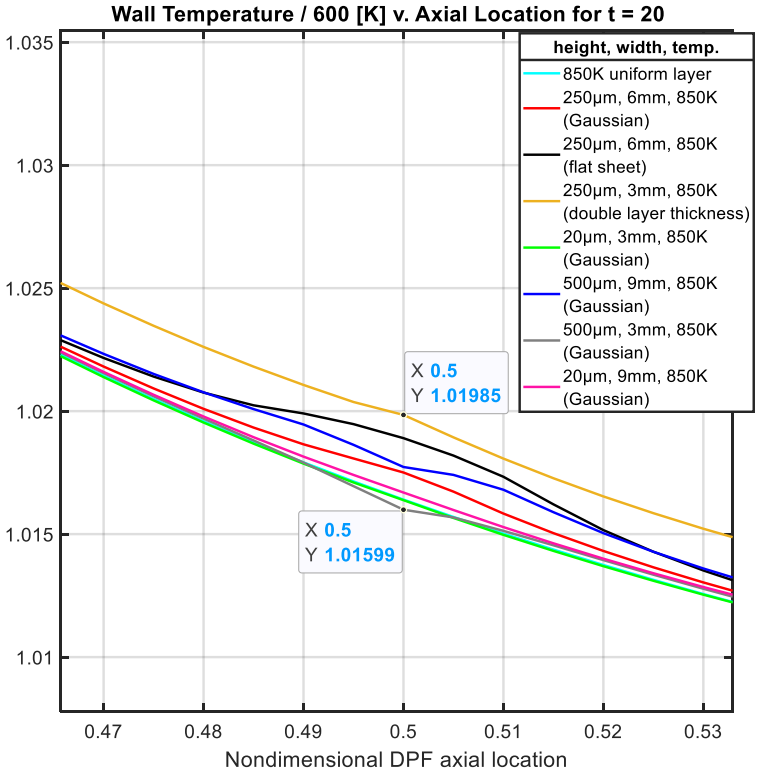

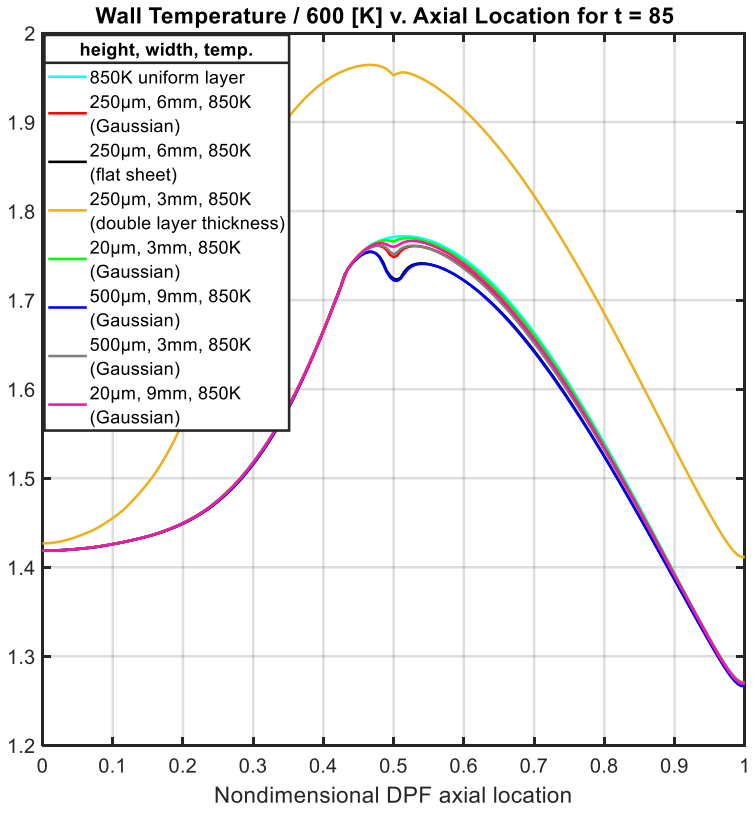
Wall Temperature / 600 [K] v. Axial Location for t = 85
height, width, temp.
850K uniform layer
250μm, 6mm, 850K (Gaussian)
250μm, 6mm, 850K (flat sheet)
250μm, 3mm, 850K (double layer thickness)
20μm, 3mm, 850K (Gaussian)
500μm, 9mm, 850K (Gaussian)
500μm, 3mm, 850K (Gaussian)
20μm, 9mm, 850K (Gaussian)
2
1.9
1.8
1.7
1.6
1.5
1.4
1.3
1.2
0
0.1
0.2
0.3
0.4
0.5
0.6
0.7
0.8
0.9
1
Nondimensional DPF axial location

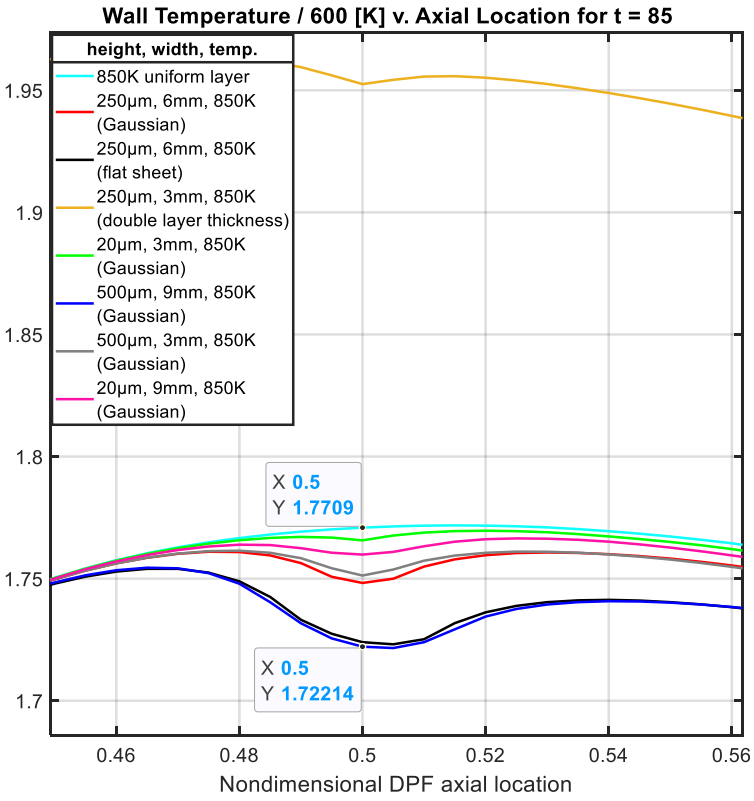
Wall Temperature / 600 [K] v. Axial Location for t = 85
height, width, temp.
850K uniform layer
250μm, 6mm, 850K (Gaussian)
250μm, 6mm, 850K (flat sheet)
250μm, 3mm, 850K (double layer thickness)
20μm, 3mm, 850K (Gaussian)
500μm, 9mm, 850K (Gaussian)
500μm, 3mm, 850K (Gaussian)
20μm, 9mm, 850K (Gaussian)
X 0.5
Y 1.7709
X 0.5
Y 1.72214
1.95
1.9
1.85
1.8
1.75
1.7
0.46
0.48
0.5
0.52
0.54
0.56
Nondimensional DPF axial location

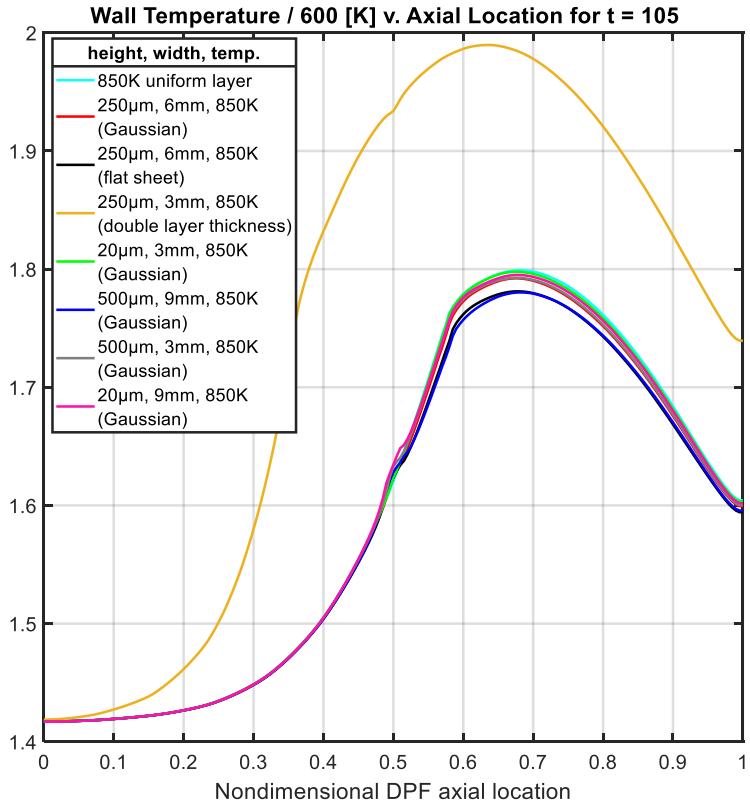
Wall Temperature / 600 [K] v. Axial Location for t = 105
height, width, temp.
850K uniform layer
250μm, 6mm, 850K (Gaussian)
250μm, 6mm, 850K (flat sheet)
250μm, 3mm, 850K (double layer thickness)
20μm, 3mm, 850K (Gaussian)
500μm, 9mm, 850K (Gaussian)
500μm, 3mm, 850K (Gaussian)
20μm, 9mm, 850K (Gaussian)
2
1.9
1.8
1.7
1.6
1.5
1.4
0
0.1
0.2
0.3
0.4
0.5
0.6
0.7
0.8
0.9
1
Nondimensional DPF axial location

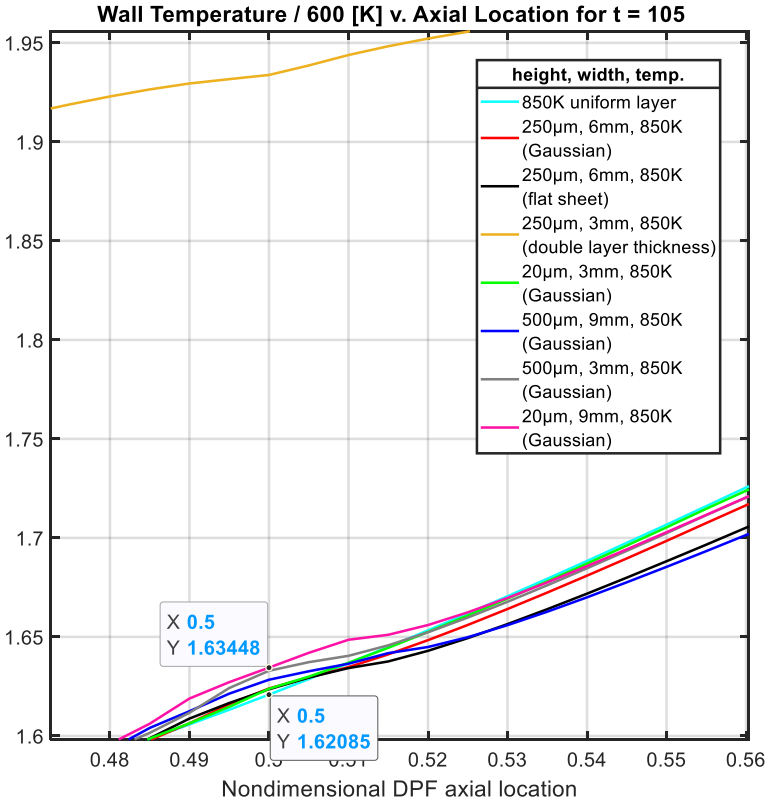
Wall Temperature / 600 [K] v. Axial Location for t = 105
height, width, temp.
850K uniform layer
250μm, 6mm, 850K (Gaussian)
250μm, 6mm, 850K (flat sheet)
250μm, 3mm, 850K (double layer thickness)
20μm, 3mm, 850K (Gaussian)
500μm, 9mm, 850K (Gaussian)
500μm, 3mm, 850K (Gaussian)
20μm, 9mm, 850K (Gaussian)
X 0.5
Y 1.63448
X 0.5
Y 1.62085
1.95
1.9
1.85
1.8
1.75
1.7
1.65
1.6
0.48
0.49
0.52
0.53
0.54
0.55
0.56
Nondimensional DPF axial location

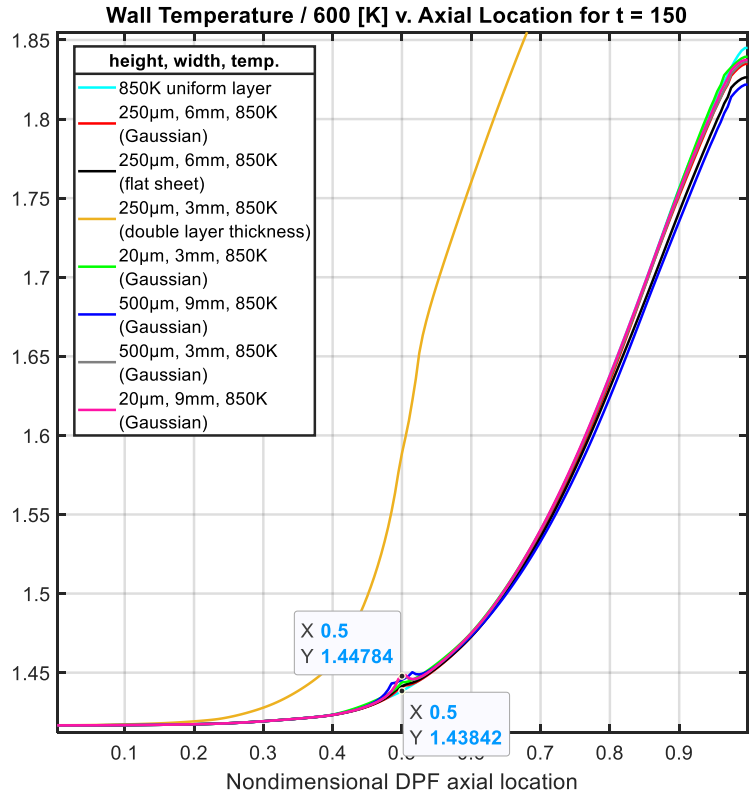
Wall Temperature / 600 [K] v. Axial Location for t = 150
height, width, temp.
850K uniform layer
250μm, 6mm, 850K (Gaussian)
250μm, 6mm, 850K (flat sheet)
250μm, 3mm, 850K (double layer thickness)
20μm, 3mm, 850K (Gaussian)
500μm, 9mm, 850K (Gaussian)
500μm, 3mm, 850K (Gaussian)
20μm, 9mm, 850K (Gaussian)
X 0.5
Y 1.44784
X 0.5
Y 1.43842
1.85
1.8
1.75
1.7
1.65
1.6
1.55
1.5
1.45
0.1
0.2
0.3
0.4
0.7
0.8
0.9
Nondimensional DPF axial location

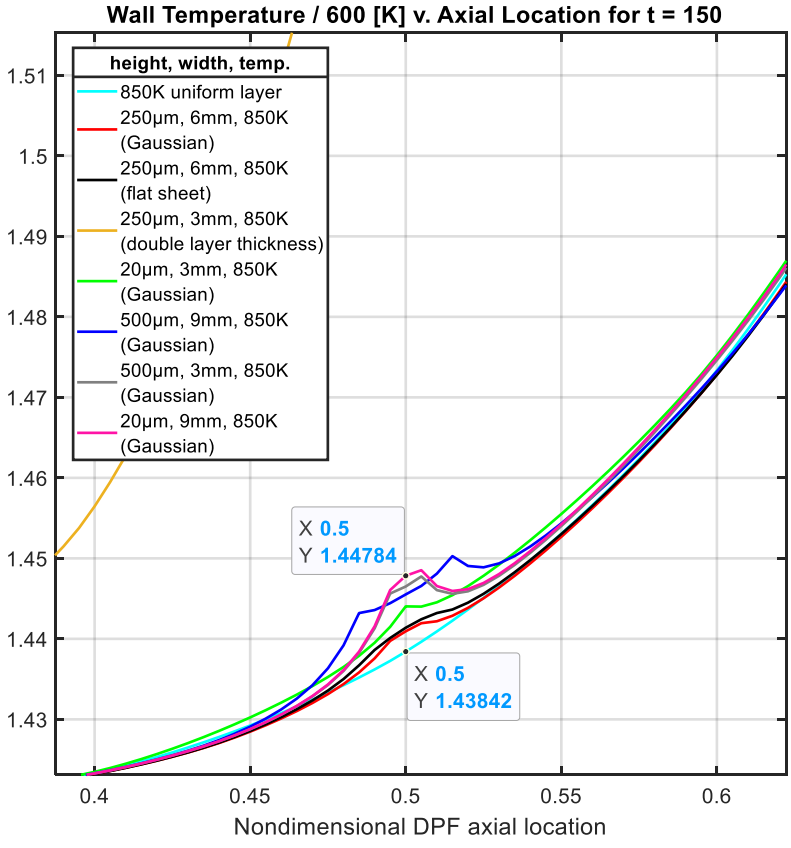
Wall Temperature / 600 [K] v. Axial Location for t = 150
height, width, temp.
850K uniform layer
250μm, 6mm, 850K (Gaussian)
250μm, 6mm, 850K (flat sheet)
250μm, 3mm, 850K (double layer thickness)
20μm, 3mm, 850K (Gaussian)
500μm, 9mm, 850K (Gaussian)
500μm, 3mm, 850K (Gaussian)
20μm, 9mm, 850K (Gaussian)
X 0.5
Y 1.44784
X 0.5
Y 1.43842
1.51
1.5
1.49
1.48
1.47
1.46
1.45
1.44
1.43
0.4
0.45
0.5
0.55
0.6
Nondimensional DPF axial location

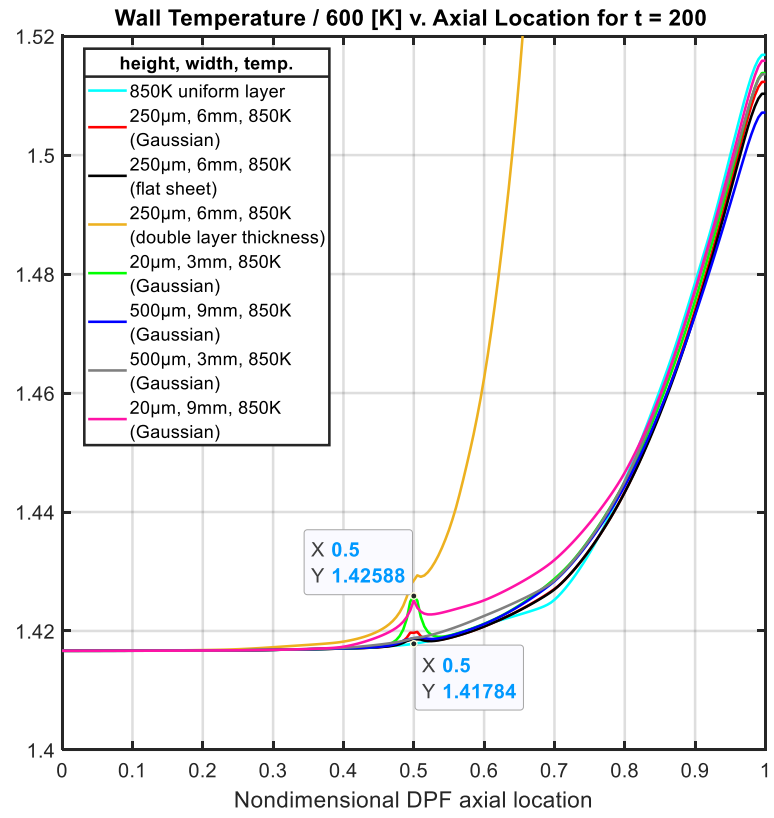
Wall Temperature / 600 [K] v. Axial Location for t = 200
height, width, temp.
850K uniform layer
250μm, 6mm, 850K (Gaussian)
250μm, 6mm, 850K (flat sheet)
250μm, 6mm, 850K (double layer thickness)
20μm, 3mm, 850K (Gaussian)
500μm, 9mm, 850K (Gaussian)
500μm, 3mm, 850K (Gaussian)
20μm, 9mm, 850K (Gaussian)
X 0.5
Y 1.42588
X 0.5
Y 1.41784
1.52
1.5
1.48
1.46
1.44
1.42
1.4
0
0.1
0.2
0.3
0.4
0.5
0.6
0.7
0.8
0.9
1
Nondimensional DPF axial location

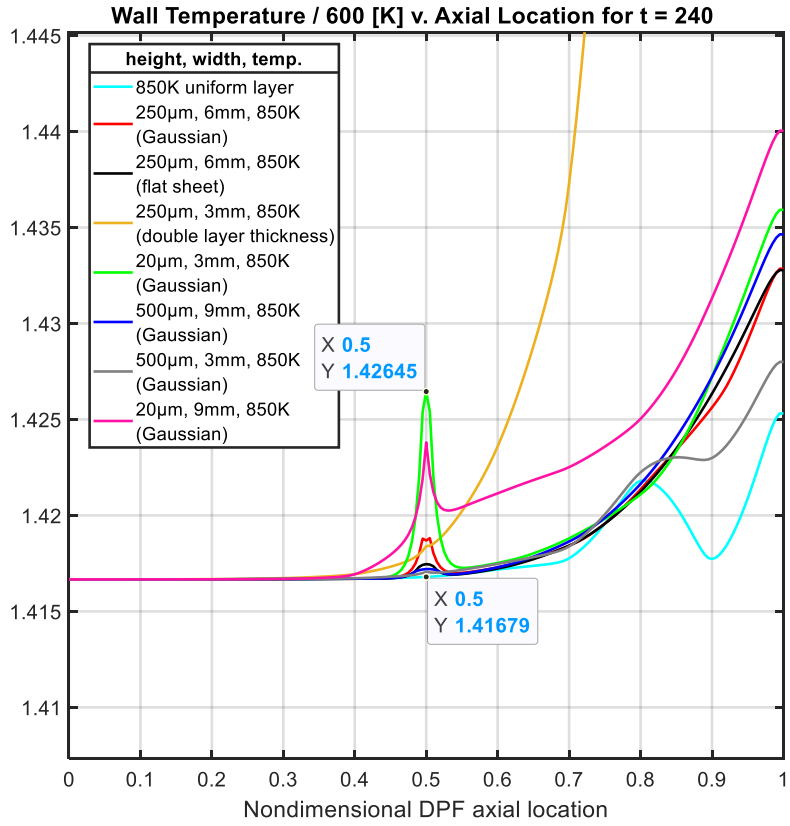
Wall Temperature / 600 [K] v. Axial Location for t = 240
height, width, temp.
850K uniform layer
250μm, 6mm, 850K (Gaussian)
250μm, 6mm, 850K (flat sheet)
250μm, 3mm, 850K (double layer thickness)
20μm, 3mm, 850K (Gaussian)
500μm, 9mm, 850K (Gaussian)
500μm, 3mm, 850K (Gaussian)
20μm, 9mm, 850K (Gaussian)
X 0.5
Y 1.42645
X 0.5
Y 1.41679
1.445
1.44
1.435
1.43
1.425
1.42
1.415
1.41
0
0.1
0.2
0.3
0.4
0.5
0.6
0.7
0.8
0.9
1
Nondimensional DPF axial location

References

[1] NASA, "Global Climate Change Vital Signs of the Planet: Global Temperature," 16 November 2020. [Online]. Available: https://climate.nasa.gov/vital-signs/global-temperature/. [Accessed 16 November 2020].

[2] A. Buis, "Global Climate Change: Vital Signs of the Planet," NASA Jet Propulsion Laboratory, 8 September 2020. [Online]. Available: https://climate.nasa.gov/blog/3017/making-sense-of-climate-sensitivity/.

[3] N. Climate.gov, "Climate Change: Atmospheric Carbon Dioxide," 14 August 2020. [Online]. Available: https://www.climate.gov/news-features/understanding-climate/climate-change-atmospheric-carbon-dioxide. [Accessed 16 November 2020].

[4] U. S. E. P. Agency, "Global Greenhouse Gas Emissions Data," 2020. [Online]. Available: https://www.epa.gov/ghgemissions/global-greenhouse-gas-emissions-data. [Accessed 14 October 2020].

[5] U. S. E. P. Agency, "Sources of Greenhouse Gas Emissions," 13 October 2020. [Online]. Available: https://www.epa.gov/ghgemissions/sources-greenhouse-gas-emissions.

[6] Our World in Data, "Share of the population exposed to air pollution levels above WHO guidelines, 2016," [Online]. Available: https://ourworldindata.org/grapher/share-above-who-pollution-guidelines?time=2016.

[7] W. A. Majewski, "What Are Diesel Emissions," ECOpoint Inc., August 2012. [Online]. Available: https://dieselnet.com/tech/emi_intro.php.

[8] J. B. Heywood, Internal Combustion Engine Fundamentals, New York: McGraw-Hill Companies, Inc., 1988, pp. 571-660.

[9] K. L. Hoag and D. E. Foster, "The Effect of Mixing Intensity and Degree of Premix on Soot Formation in a Backmixed Combustor," *SAE Transactions,* vol. 92, no. 3, pp. 858-871, 1983.

[10] W. A. Majewski, "What are Diesel Emissions?," ECOpoint Inc., August 2012. [Online]. Available: https://dieselnet.com/tech/emi_intro.php.

[11] A. Cornet, R. Hensley, C. Hirschberg, P. Schaufuss, A. Tschiesner, A. Venus and J. Werra, "Reboost: A comprehensive view on the changing," McKinsey Center for Future Mobility.

[12] D. C. Hammond, Jr. and P. T. Vickers, "Wall-Flow Monolith Filter". United States Patent US4390355A, 28 June 1983.

[13] S. Viswanathan, S. George, M. Govindareddy and A. Heibel, "Advanced Diesel Particulate Filter Technologies for Next Generation Exhaust Aftertreatment Systems," *SAE International,* vol. 01, no. 1434, pp. 1-9, 2020.

[14] A. G. Konstandopoulos, M. Kostoglou, E. Skaperdas, E. Papaioannou, D. Zarvalis and E. Kladopoulou, "Fundamental Studies of Diesel Particulate Filters: Transient Loading, Regeneration and Aging," *SAE International,* vol. 01, no. 1016, pp. 1-23, 2000.

[15] E. Ohara, Y. Mizuno, Y. Miyairi, T. Mizutani, K. Yuuki, Noguchi Y., T. Hiramatsu, M. Makino, A. Takahashi, H. Sakai, M. Tanaka, A. Martin, S. Fujii, P. Busch, T. Toyoshima, T. Ito, I. Lappas and C. D. Vogt, "Filtration Behavior of Diesel Particulate Filters (1)," *SAE International,* vol. 01, no. 0921, 2007.

[16] R. Sanui and K. Hanamura, "Scanning Electron Microscopic Visualization of Bridge Formation inside the Porous Channels of Diesel Particulate Filters," *SAE International,* vol. 01, no. 9079, pp. 725-733, 2016.

[17] Y. Wang, C. Kamp, Y. Wang, T. Toops, C. Su, R. Wang, J. Gong and V. Wong, "The origin, transport, and evolution of ash in engine particulate filters," *Applied Energy,* vol. 263, 2020.

[18] O. Salvat, P. Marez and G. Belot, "Passenger Car Serial Application of a Particulate Filter System on a Common Rail Direct Injection Diesel Engine," *Society of Automotive Engineers,* vol. 01, no. 0473, p. 7, 2000.

[19] Y. Wang, Y. Obuchi, J. Zhang, I. Tracy and V. Wong, "Experiments and Analyses on Stability/MidChannel Collapse of Ash-Deposit Wall Layers and Pre-Mature Clogging of Diesel Particulate Filters," *SAE International,* vol. 01, no. 0972, pp. 1-20, 2019.

[20] R. Fukui, Y. Okamoto and M. Nakao, "Experimental Analysis of Sudden Pressure Increase Phenomenon by Real-Time Internal Observation of Diesel Particulate Filter," *Journal of Enginering for Gas Turbines and Power,* vol. 138, no. 10, pp. 1-7, 2016.

[21] A. Sappok, I. Govani, C. Kamp, Y. Wang and V. Wong, "In-Situ Optical Analysis of Ash Formation and Transport in Diesel Particulate Filters During Active and Passive DPF Regeneration Processes," *Society of Automotive Engineers,* vol. 01, no. 0519, pp. 336-349, 2013.

[22] C. Kamp, S. Bagi and Y. Wang, "Phenomenological Investigations of Mid-Channel Ash Deposit Formation and Characteristics in Diesel Particulate Filters," *Society of Automotive Engineers,* vol. 01, no. 0973, 2019.

[23] A. Sappok, M. Santiago, T. Vianna and V. W. Wong, "Characteristics and Effects of Ash Accumulation on Diesel Particulate Filter Performance: Rapidly Aged and Field Aged Results," *Society of Automotive Engineers,* vol. 01, no. 1086, 2009.

[24] A. Sappok and V. Wong, "Sensitivity Analysis of Ash Packing and Distribution in Diesel Particulate Filters to Transient Changes in Exhaust Conditions," *SAE International Journal of Fuels and Lubricants,* vol. 5, no. 2, pp. 733-750, 2012.

[25] A. Jiang, N. Awasthi, A. Kolmogorov, W. Setyawan, A. Börjesson, K. Bolton, A. R. Harutyunyan and S. Curtarolo, "Theoretical study of the thermal behavior of free and alumina-supported Fe-C nanoparticles," *Physical Review B,* vol. 75, no. 205, p. 205426, May 2007.

[26] E. J. Bissett, "Mathematical Model of the Thermal Regeneration of a Wall-Flow Monolith Diesel Particulate Filter," *Chemical Engineering Science,* vol. 39, pp. 1233-1244, 1984.

[27] M. Srilomsak and K. Hanamura, "Time-lapse visualization of shrinking soot in diesel particulate filterduring active-regeneration using field emission scanning electronmicroscopy," *Journal of Microscopy,* vol. 279, no. 2, pp. 85-97, 2020.

[28] C. J. Kamp, A. Sappok, Y. Wang, W. Bryk, A. Rubin and V. Wong, "Direct Measurements of Soot/Ash Affinity in the Diesel Particulate Filter by Atomic Force Microscopy and Implications for Ash Accumulation and DPF Degradation," *SAE International,* vol. 01, no. 1486, pp. 307-316, 2014.

[29] Y. Shao, Physics and modeling of wind erosion, 2 ed., Netherlands: Springer, 2008.

[30] U. S. E. P. Agency, "Diesel Particulate Filter General Information," 2010.

[31] A. Sydbom, A. Blomberg, S. Parnia, N. Stenfors, T. Sandström and S.-E. Dahlén, "Health effects of diesel exhaust emissions," *European Respiratory Journal,* vol. 17, pp. 733-746, 2001.

[32] A. Buis, "A Degree of Concern: Why Global Temperatures Matter," 19 June 2019. [Online]. Available: https://climate.nasa.gov/news/2865/a-degree-of-concern-why-global-temperatures-matter/. [Accessed 14 October 2020].

[33] M. Z. Jacobson, "Strong radiative heating due to the mixing state of black carbon in atmospheric aerosols," *Nature,* vol. 409, no. 6821, 2001.

[34] T. C. Bond, S. J. Doherty and D. W. Fahey, "Bounding the role of black carbon in the climate system: A scientific assessment," *Journal of Geophysical Research: Atmospheres,* vol. 118, no. 11, 2013.

[35] J. Quaas, "The soot factor," *Nature,* vol. 471, pp. 456-457, 2011.

[36] U. S. E. P. Agency, "Fast Facts on Transportation Greenhouse Gas Emissions," 2018. [Online]. Available: https://www.epa.gov/greenvehicles/fast-facts-transportation-greenhouse-gas-emissions. [Accessed 14 October 2020].

[37] U. S. E. I. Administration, "Diesel fuel explained: Diesel and the environment," 2018. [Online]. Available: https://www.eia.gov/energyexplained/diesel-fuel/diesel-and-the-environment.php. [Accessed 14 October 2020].

[38] E. Hannon, T. Nauclér, A. Suneson and F. Yüksel, "The zero-carbon car: Abating material emissions is next on the agenda," McKinsey & Company, 18 September 2020. [Online]. Available: https://www.mckinsey.com/business-functions/sustainability/our-insights/the-zero-carbon-car-abating-material-emissions-is-next-on-the-agenda. [Accessed 15 October 2020].

[39] California Air Resources Board (CARB) Research Division, "Overview: Diesel Exhaust and Health," [Online]. Available: https://ww2.arb.ca.gov/resources/overview-diesel-exhaust-and-health.

[40] California Air Resources Board (CARB), "Summary: Diesel Particulate Matter Health Impacts," 2020. [Online]. Available: https://ww2.arb.ca.gov/resources/summary-diesel-particulate-matter-health-impacts. [Accessed 22 November 2020].

[41] W. H. Organization, "Health Effects of Particulate Matter: Policy Implications for Countries in Eastern Europe, Caucasus, and Central Asia," WHO Regional Office for Europe, Copenhagen, 2013.

[42] T. I. C. o. C. Transportation, "CHINA'S CLEAN DIESEL ACTION PLAN: 2018–2020," 2019.

[43] D. Meng, L. Wu and Y. Yang, "Predict the Particulate Matter Concentrations in 128 cities of China," *Air Quality, Atmosphere & Health,* pp. 399-407, 2020.

[44] Y.-L. Zhang and F. Cao, "Fine Particulate Matter (PM2.5) in China at a City Level," *Scientific Reports,* 15 October 2015.

[45] J. B. Heywood, International Combustion Engine Fundamentals, New York: The McGraw-Hill Companies, Inc., 1988, pp. 25-27.

[46] J. B. Heywood, Internal Combustion Engine Fundamentals, New York: The McGraw-Hill Companies, Inc., 1988, pp. 148-149.

[47] A. Sappok, R. Rodriguez and V. Wong, "Characteristics and Effects of Lubricant Additive Chemistry on Ash Properties Impacting Diesel Particulate Filter Service Life," *Society of Automotive Engineers,* vol. 01, no. 1213, pp. 705-722, 2010.

[48] G. A. Merkel, W. A. Cutler and C. J. Warren, "Thermal Durability of Wall-Flow Ceramic Diesel Particulate Filters," *Society of Automotive Engineers,* vol. 01, no. 0190, 2001.

[49] T. Ishizawa, H. Yamane, H. Satoh, K. Sekiguchi, M. Arai, N. Yoshimoto and T. Inoue, "Investigation into Ash Loading and Its Relationship to DPF Regeneration Method," *Society of Automotive Engineers,* vol. 01, no. 2882, pp. 164-175, 2009.

[50] A. Gurupatham and Y. He, "Architecture Design and Analysis of Diesel Engine Exhaust Aftertreatment System and Comparative Study with Close-coupled DOC-DPF System," *Society of Automotive Engineers,* vol. 01, no. 1756, 2008.

[51] "Diesel Particulate Filter Market Size, Share, Trend, Forecast, & Competitive Analysis," Strateview Research, 2020.

[52] W. Cutler and G. Merkel, "A New High Temperature Ceramic Material for Diesel Particulate Filter Applications," *Society of Automotive Engineers,* vol. 01, no. 2844, 2000.

[53] A. Dittler, "The Application of Diesel Particle Filters—From Past to Present and Beyond," *Topics in Catalysis,* vol. 60, pp. 342-347, 2017.

[54] A. Sappok and V. Wong, ""Detailed Chemical and Physical Characterization of Ash Species in Diesel Exhaust Entering Aftertreatment Systems," *Society of Automotive Engineers,* vol. 01, no. 0318, 2007.

[55] J. B. Heywood, Internal Combustion Engine Fundamentals, New York: The McGraw-Hill Companies, Inc., 1988, pp. 51-52.

[56] A. G. Konstandopoulos and J. H. Johnson, "Wall-Flow Diesel Particulate Filters—Their Pressure Drop and Collection Efficiency," *SAE International,* no. 890405, 1989.

[57] A. G. Konstandopoulos and E. Skaperdas, "Optimized Filter Design and Selection Criteria for Continuously Regenerating Diesel Particulate Traps," *SAE International,* vol. 01, no. 0468, 1 March 1999.

[58] M. Masoudi, A. G. Konstandopoulos, M. S. Nikitidis, E. Skaperdas, D. Zarvalis, E. Kladapoulou and C. Altiparmakis, "Validation of a Model and Development of a Simulator for Predicting the Pressure Drop of Diesel Particulate Filters," *SAE International,* vol. 01, no. 0911, 2001.

[59] G. Gaiser and P. Mucha, "Prediction of Pressure Drop in Diesel Particulate Filters Considering Ash Deposit and Partial Regenerations," vol. 01, no. 0158, 8 March 2004.

[60] C. Zhao, Y. Zhu and S. Huang, "Pressure Drop and Soot Accumulation Characteristics through Diesel Particulate Filters Considering Various Soot and Ash Distribution Types," *SAE International,* vol. 01, no. 0959, 2017.

[61] A.-M. Stamatellou and A. Stamatelos, "Overview of Diesel particulate filter systems sizing approaches," *Applied Thermal Engineering,* vol. 121, pp. 537-546, 2017.

[62] P. Versaevel, H. Colas, C. Rigaudeau, R. Noirot, G. C. Koltsakis and A. M. Stamatelos, "Some Empirical Observations on Diesel Particulate Filter Modeling and Comparison Between Simulations and Experiments," *SAE International,* vol. 01, no. 0477, pp. 1-11, 2000.

[63] O. A. Haralampous, I. P. Kandylas, G. C. Koltsaki and Z. C. Samaras, "Diesel particulate filter pressure drop Part 1: modelling and experimental validation," *International Journal of Engine Research,* vol. 5, no. 2, pp. 149-162, 2004.

[64] Z. N. Mogaka, V. W. Wong and S. M. Shahed, "Performance and Regeneration Characteristics of a Cellular Ceramic Diesel Particulate Trap," *SAE International,* no. 820272, pp. 65-87, 1982.

[65] J. Yang, M. Stewart, G. Maupin, D. Herling and A. Zelenyuk, "Single wall diesel particulate filter (DPF) filtration efficiency studies using laboratory generated particles," *Chemical Engineering Science,* vol. 64, no. 8, pp. 1625-1634, 2009.

[66] M. A. Barris, D. R. Monson, T. M. Weik and J. W. Schaefer, "Material Characterization of Diesel Particulate Trap Alternatives," *SAE International,* no. 872246, pp. 1-12, 1987.

[67] C. N. Opris and J. H. Johnson, "A 2-D Computational Model Describing the Flow and Filtration Characteristics of a Ceramic Diesel Particulate Trap," *SAE International,* no. 980545, 1998.

[68] E. A. Kladapoulou, S. L. Yang, J. H. Johnson, G. G. Parker and A. G. Konstandopoulos, "A Study Describing the Performance of Diesel Particulate Filters During Loading and Regeneration - A Lumped Parameter Model for Control Applications," *SAE International,* vol. 01, no. 0842, 2003.

[69] K. W. Lee and J. A. Gieseke, "Collection of aerosol particles by packed beds," *Environmental Science & Technology,* vol. 13, 1979.

[70] G. A. Merkel, W. A. Cutler, T. Tao, A. Chiffey, P. Phillips, M. V. Twigg and A. Walker, "New Cordeirite Diesel Particulate Filters for Catalyzed and Non-Catalyzed Application," in *9th Diesel Engine Emissions Reduction Conference*, Newport, RI, 2003.

[71] Y. Wang, V. Wong, A. Sappok and S. Munnis, "The Sensitivity of DPF Performance to the Spatial Distribution of Ash Inside DPF Inlet Channels," *Society of Automotive Engineers,* vol. 01, no. 1584, 2013.

[72] C. Gehrke, H. Sivadas, T. Bazyn and D. Milam, "The Role of Advanced Combustion in Improving Thermal Efficiency," in *DEER Conference*, Dearborn, 2008.

[73] G. Muntean, "How Exhaust Emissions Drive Diesel Engine Fuel Efficiency," Pacific Northwest National Laboratory, 30 August 2004. [Online]. Available:

https://www1.eere.energy.gov/vehiclesandfuels/pdfs/deer_2004/session1/2004_deer_muntean.pdf. [Accessed 1 December 2020].

[74] W. A. Majewski, "Diesel Filter Systems," ECOpoint Inc., October 2020. [Online]. Available: https://dieselnet.com/tech/dpf_sys.php. [Accessed 1 December 2020].

[75] Y. Wang and C. Kamp, "The Effects of Mid-Channel Ash Plug on DPF Pressure Drop," *SAE International,* vol. 01, no. 0966, 2016.

[76] O. R. K. Montedo, F. J. Floriano, J. d. O. F. Filho, E. Angolette and A. M. Bernardin, "Sintering Behavior of LZSA Glass-Ceramics," *Materials Research,* vol. 12, no. 2, pp. 197-200, 2009.

[77] K. Kim, R. Mital, T. Higuchi, S. Chan and C. H. Kim, "An Investigative Study of Sudden Pressure Increase Phenomenon Across the DPF," *Society of Automotive Engineers,* vol. 01, no. 1516, 2014.

[78] Y. Wang, *Modeling and interpreting the observed effects of ash on diesel particulate filter performance and regeneration,* Cambridge: Department of Mechanical Engineering. Massachusetts Institute of Technology, 2014.

[79] D. M. Young, D. L. Hickmann, G. Bhatia and N. Gunasekaran, "Ash Storage Concept for Diesel Particulate Filters," *SAE International,* vol. 01, no. 0948, 2004.

[80] A. Sappok and V. Wong , "Detailed Chemical and Physical Characterization of Ash Species in Diesel Exhaust Entering Aftertreatment Systems," *SAE International,* vol. 01, no. 0318, 2007.

[81] National Institute of Standards and Technology, "Engineering Statistics Handbook," National Institute of Standards and Technology, [Online]. Available: https://www.itl.nist.gov/div898/handbook/prc/section2/prc222.htm. [Accessed 30 November 2020].

[82] J. Cohen, "Quantitative Methods in Psychology: A Power Primer," *Psychological Bulletin,* vol. 112, no. 1, pp. 155-159, 1992.

[83] "Unpaired (Two Sample) t Test," StatsDirect Limited, 2016. [Online]. Available: https://www.statsdirect.co.uk/help/parametric_methods/utt.htm. [Accessed 1 December 2020].

[84] Y. Wang and V. Wong, "Quantitative Analysis of Ash Density and Ash Distribution inside DPF Honeycomb Channels Based on X-ray Computed Tomography," *SAE International,* vol. 01, no. 0979, 2019.

[85] A. G. Konstandopoulos, M. Kostoglou and P. Housiada, "Spatial Non-Uniformities in Diesel Particulate Trap Regeneration," *SAE International,* vol. 01, no. 0908, 05 March 2001.

[86] A. Atangana, "Chapter 2 - Principle of Groundwater Flow," in *Fractional Operators with Constant and Variable Order with Application to Geo-Hydrology*, Academic Press, 2018, pp. 15-47.

[87] A. G. Konstandopoulos, M. Kostoglou, P. Housiada, . N. Vlachos and D. Zarvalis, "Multichannel Simulation of Soot Oxidation in Diesel Particulate Filters," *SAE International,* vol. 01, no. 0839, 2003.

[88] S. Ghosal, Electrokinetic Flow and Ion Transport in Nanochannels, Boston: Springer, 2008.

[89] P. K. Kundu, I. M. Cohen and D. R. Dowling, Fluid Mechanics, 5 ed., Elsevier, 2012, p. 342.

[90] KRÜSS GmbH, "Bubble pressure tensiometer," KRÜSS GmbH, 2020. [Online]. Available: https://www.kruss-scientific.com/services/education-theory/glossary/bubble-pressure-tensiometer/.

[91] B. E. Rapp, "Chapter 22 - Measuring Surface Tension and Free Surface Energy," in *Microfluidics: Modelling, Mechanics and Mathematics*, Elsevier, 2017, pp. 453-465.

[92] P.-G. d. Gennes, F. Brochard-Wyart and D. Quéré, Capillarity and Wetting Phenomena: Drops, Bubbles, Pearls, Waves, Springer, 2003.

[93] H. Liu and G. Cao, "Effectiveness of the Young-Laplace equation at nanoscale," *Scientific Reports,* vol. 6, no. 23936, 2016.

[94] A. D. Sediako, C. Soong, J. Y. Howe, M. R. Kholgy and M. J. Thomson, "Real-time observation of soot aggregate oxidation in an Environmental Transmission Electron Microscope," *Proceedings of the Combustion Institute,* vol. 36, no. 1, pp. 841-851, 2017.

[95] S. R. Turns, An Introduction to Combustion: Concepts and Applications, 3 ed., New York: McGraw-Hill, 2012.

[96] A. Sappok, Y. Wang, R. Wang, C. Kamp and V. Wong, "Theoretical and Experimental Analysis of Ash Accumulation and Mobility in Ceramic Exhaust Particulate Filters and Potential for Improved Ash Management," *SAE International,* vol. 01, no. 1517, pp. 511-524, 2014.

[97] A. B. Chhetri and K. C. Watts, "Surface tensions of petro-diesel, canola, jatropha and soapnut biodiesel fuels at elevated temperatures and pressures," *Fuel,* vol. 104, pp. 704-710, 2013.

[98] W. R. Jones and L. D. Wedeven, "Surface-Tension Measurements in Air of Liquid Lubricants to 200° C by the Differential-Maximum-Bubble-Pressure Technique," NASA, Washington D.C., 1971.

[99] D. K. Thakur and K. Hickman, "Surface tension of water at 100°C," *Journal of Colloid and Interface Science,* vol. 50, no. 3, pp. 525-531, 1975.

[100] R. Shekhar, P. S. Dhugga and K. Malik, "CFD analysis of Back Pressure due to bend in exhaust Pipe of 4 stoke petrol engine," *International Journal of Aerospace and Mechanical Engineering,* vol. 3, no. 4, pp. 1-3, 2016.

[101] D. Nitschke and E. Schmidt, "A New Approach to Model the Re-Entrainment of Settled Particles Based on Film Theory of Fluid Mass Transfer Processes," *Particle & Particle Systems Characterization,* vol. 26, no. 1-2, pp. 58-68, 2009.

[102] F. M. White, Appendix A: Physical Properties of Fluids, 6 ed., New York: McGraw-Hill, 2008, p. 816.

[103] Y. Koizumi, M. Shoji, M. Monde, Y. Takata and N. Nagai, "Chapter 4 - Minimum Heat Flux-Film Boiling," in *Boiling*, Elsevier, 2017, pp. 369-410.

[104] R. L. Panton, Incompressible Flow, 4 ed., Hoboken: John Wiley & Sons, Inc., 2013, p. 640.

[105] M. D. Mikhailov and A. P. Silva Freire, "The drag coefficient of a sphere: An approximation using Shanks transform," *Powder Technology,* vol. 237, pp. 432-435, March 2013.

[106] G. Ahmadi, "Introduction to Aerosols," Department of Mechanical and Aeronautical Engineering, Potsdam, NY.

[107] R. M. Wham, O. A. Basaran and C. H. Byers, "Wall Effects on Flow Past Solid Spheres at Finite Reynolds Numbers," *Industrial & Engineering Chemistry Research,* vol. 35, no. 3, pp. 864-874, 1996.

[108] O. H. Faxen, "Die bewegung einer starren kugel langs der achse eines mit zaher flussigkeit gefullten rohres," *Ark. Mat. Astron. Fys.,* vol. 17, no. 1, 1923.

[109] D. Tabor, "Surface forces and surface interactions," *Journal of Colloid and Interface Science,* vol. 58, no. 1, pp. 2-13, 1977.

[110] J. N. Israelachvili, Intermolecular and surface forces, 3 ed., Oxford: Elsevier Academic Press, 2011.

[111] E. M. Lifschitz, "The theory of molecular attractive forces between solids," *Sov. Phys. JETP,* vol. 2, no. 1, pp. 73-83, 1956.

[112] E. Hadjittofis, S. C. Das, G. Z. Zhang and J. Y. Heng, "Chapter 8 - Interfacial Phenomena," in *Developing Solid Oral Dosage Forms*, 2 ed., Academic Press, 2017, pp. 225-252.

[113] H. C. Hamaker, "The London—van der Waals attraction between spherical particles," *Physica,* vol. 4, no. 10, pp. 1058-1072, 23 November 1937.

[114] M. Corn, "The adhesion of solid particles to solid surfaces. I. A review.," *Journal of the Air Pollution Control Association,* vol. 11, no. 11, pp. 523-528, 1961.

[115] J. Visser, "als and other cohesive forces affecting powder fluidization," *Powder Technology,* vol. 58, no. 1, pp. 1-10, 1989.

[116] M. Lu, M. Fang, M. He, S. Liu and Z. Luo, "Insights into agglomeration and separation of fly-ash particles in a sound wave field," *RSC Advances,* vol. 9, pp. 5224-5233, 2019.

[117] F. L. Leite, C. C. Bueno, A. L. Da Róz, E. C. Ziemath and O. N. Oliviera Jr., "Theoretical Models for Surface Forces and Adhesion and Their Measurement Using Atomic Force Microscopy," *International Journal of Molecular Sciences,* vol. 13, pp. 12773-12856, 2012.

[118] G. Ahmadi, "London-van der Waals Force," Clarkson University, 2005. [Online]. Available: https://webspace.clarkson.edu/projects/crcd/public_html/me437/downloads/5_vanderWaals.pdf.

[119] S. You and P. Wan, "Mathematical Models for the van der Waals Force and Capillary Force between a Rough Particle and Surface," *Langmuir,* vol. 29, pp. 9104-9117, 2013.

[120] The Editors of Encyclopaedia Britannica, "Brownian motion," Encyclopædia Britannica, 2017.

[121] M. D. Knotter and F. Wali, "Particles in Semiconductor Processing," in *Developments in Surface Contamination and Cleaning*, R. Kohli and K. L. Mittal, Eds., William Andrew Publishing, 2010, pp. 81-120.

[122] I. L. Mostinsku, "Diffusion Coefficient," Thermopedia, 10 February 2011. [Online]. Available: http://www.thermopedia.com/content/696/. [Accessed 4 December 2020].

[123] M. M. Hoffman, M. D. Too, T. Gutmann and G. Buntkowsky, "Breakdown of the Stokes−Einstein Equation for Solutions of Water in Oil Reverse Micelles," *Journal of Physical Chemistry B,* vol. 124, no. 41, pp. 9115-9125, 2020.

[124] J. T. Edward, "Molecular Volumes and the Stokes-Einstein Equation," *Journal of Chemical Education,* vol. 47, no. 4, pp. 261-270, 1970.

[125] C. F. Schadt and R. D. Cadle, "Thermal Forces on Aerosol Particles," *Journal of Physical Chemistry,* vol. 65, no. 10, pp. 1689-1694, 1 October 1961.

[126] L. Waldmann, "Uber die Kraft eines inhomogenen Gases auf kleine suspendierte Kugeln," *Z. Naturforsch,* vol. 14a, pp. 589-599, 1959.

[127] R. L. Saxton and W. E. Ranz, "Thermal Force on an Aerosol Particle in a Temperature Gradient," *Journal of Applied Physics,* vol. 23, no. 8, pp. 917-923, 1952.

[128] J. R. Brock, "On the theory of thermal forces acting on aerosol particles," *Journal of Colloid Science,* vol. 17, pp. 768-780, 1962.

[129] J. B. Young, "Thermophoresis of a Spherical Particle: Reassessment, Clarification, and New Analysis," *Aerosol Science and Technology,* vol. 45, pp. 927-948, 2011.

[130] C. J. Kamp, A. Sappok and V. Wong, "Soot and Ash Deposition Characteristics at the Catalyst-Substrate Interface and Intra-Layer Interactions in Aged Diesel Particulate Filters Illustrated using Focused Ion Beam (FIB) Milling," *SAE International Journal of Fuels and Lubricants,* vol. 5, no. 2, pp. 696-710, 2012.

[131] J. D. Anderson, Fundamentals of Aerodynamics, 4 ed., New York: McGraw-Hill, 2007, pp. 163-409.

[132] D. P. Debrincat, C. B. Solnordal and J. J. Van Deventer, "Characterisation of inter-particle forces within agglomerated metallurgical powders," *Powder Technology,* vol. 182, no. 3, pp. 388-397, 2008.

[133] H. Yang, X. Li, Y. Wang, M. Mu, X. Li and G. Kou, "Experimental investigation into the oxidation reactivity and nanostructure of particulate matter from diesel engine fuelled with diesel/polyoxymethylene dimethyl ethers blends," *Scientific Reports,* vol. 6, 2016.

[134] D. B. Kittelson, Y. H. Pui and K. C. Moon, "Electrostatic Collection of Diesel Particles," *SAE International,* pp. 19-30, 1 March 1986.

[135] H. Rumpf, Particle Technology, London: Chapman and Hall, 1990.

[136] C. Kanaoka, M. Hata and H. Makino, "Measurement of adhesive force of coal flyash particles at high temperatures and different gas compositions," *Powder Technology,* vol. 118, no. 1-2, pp. 107-112, 2001.

[137] J. Frenkel, "Viscous flow of crystalline bodies under the action of surface tension," *Journal of Physics,* vol. 9, pp. 385-391, 1945.

[138] H. Namkung, X. Hu, H.-T. Kim, F. Wang and G. Yu, "Evaluation of sintering behavior of ash particles from coal and rice straw using optical heating stage microscope at high temperature fouling conditions," *Fuel Processing Technology,* vol. 149, pp. 195-208, 2016.

[139] F. Wakai, K. Katsura, S. Kanchika, Y. Shinoda, T. Akatsu and K. Shinagawa, "Sintering force behind the viscous sintering of two particles," *Acta Materialia,* vol. 109, pp. 292-299, 2016.